

PROCEEDINGS OF SPIE



SPIE—The International Society for Optical Engineering

FG1725-98-WE027

~~ESP~~ 98-1028-2
CSP

Laser Optics '98

Solid State Lasers

Vladimir I. Ustyugov
Editor

22-26 June 1998
St. Petersburg, Russia

Organized by

Institute for Laser Physics, S.I. Vavilov State Optical Institute
General Physics Institute, Russian Academy of Sciences
P.N. Lebedev Physical Institute, Russian Academy of Sciences
Institute for Fine Mechanics and Optics, Technical University
Russian National Center of Laser Physics, St. Petersburg State University
Scientific Council on Coherent and Nonlinear Optics, Russian Academy of Sciences
SPIE—The International Society for Optical Engineering
SPIE Russia Chapter
OSA—Optical Society of America
EOS—European Optical Society
ROS—Rozhdestvensky Optical Society
Government of St. Petersburg

DISTRIBUTION STATEMENT A
Approved for Public Release
Distribution Unlimited



Volume 3682

19990702 027

DTIC QUALITY INSPECTED 4

AQF99-10-1696



PROCEEDINGS OF SPIE

SPIE—The International Society for Optical Engineering

Laser Optics '98

Solid State Lasers

Vladimir I. Ustyugov

Editor

22–26 June 1998

St. Petersburg, Russia

Organized by

Institute for Laser Physics, S.I. Vavilov State Optical Institute • General Physics Institute, Russian Academy of Sciences • P.N. Lebedev Physical Institute, Russian Academy of Sciences • Institute for Fine Mechanics and Optics, Technical University • Russian National Center of Laser Physics, St. Petersburg State University • Scientific Council on Coherent and Nonlinear Optics, Russian Academy of Sciences • SPIE—The International Society for Optical Engineering • SPIE Russia Chapter • OSA—Optical Society of America • EOS—European Optical Society • ROS—Rozhdestvensky Optical Society • Government of St. Petersburg

Supported by

Ministry of Science and Technical Policy of Russia • Ministry for Economics of Russia • Ministry for Education of Russia • Russian National Foundation for Basic Research • SPIE—The International Society for Optical Engineering • Lawrence Livermore National Laboratory (USA) • USAF European Office of Aerospace Research and Development • OSA—Optical Society of America

Sponsored by

Technische Zentrum Nord (Germany)
Thomson-CSF (France)
JENOPTIK Technologie GmbH (Germany)

Published by

SPIE—The International Society for Optical Engineering



Volume 3682

SPIE is an international technical society dedicated to advancing engineering and scientific applications of optical, photonic, imaging, electronic, and optoelectronic technologies.



The papers appearing in this book comprise the proceedings of the meeting mentioned on the cover and title page. They reflect the authors' opinions and are published as presented and without change, in the interests of timely dissemination. Their inclusion in this publication does not necessarily constitute endorsement by the editors or by SPIE.

Please use the following format to cite material from this book:

Author(s), "Title of paper," in *Laser Optics '98: Solid State Lasers*, Vladimir I. Ustyugov, Editor, Proceedings of SPIE Vol. 3682, page numbers (1998).

ISSN 0277-786X
ISBN 0-8194-3156-7

Published by
SPIE—The International Society for Optical Engineering
P.O. Box 10, Bellingham, Washington 98227-0010 USA
Telephone 360/676-3290 (Pacific Time) • Fax 360/647-1445

Copyright ©1998, The Society of Photo-Optical Instrumentation Engineers.

Copying of material in this book for internal or personal use, or for the internal or personal use of specific clients, beyond the fair use provisions granted by the U.S. Copyright Law is authorized by SPIE subject to payment of copying fees. The Transactional Reporting Service base fee for this volume is \$10.00 per article (or portion thereof), which should be paid directly to the Copyright Clearance Center (CCC), 222 Rosewood Drive, Danvers, MA 01923. Payment may also be made electronically through CCC Online at <http://www.directory.net/copyright/>. Other copying for republication, resale, advertising or promotion, or any form of systematic or multiple reproduction of any material in this book is prohibited except with permission in writing from the publisher. The CCC fee code is 0277-786X/98/\$10.00.

Printed in the United States of America.

Contents

vii *Conference Committees*

SESSION 1 DIODE-PUMPED SOLID STATE LASERS

- 2 **Design considerations for high-power TEM₀₀ operation of end-pumped solid state lasers [3682-01]**
W. A. Clarkson, Univ. of Southampton (UK)
- 13 **High-power laser diodes, laser diode modules, and their applications [3682-02]**
F. X. Daiminger, F. Dorsch, D. Lorenzen, JENOPTIK Laserdiode GmbH (Germany)
- 24 **1.5- μ m diode-pumped erbium-ytterbium glass lasers [3682-03]**
P. Laporta, S. Taccheo, S. Longhi, O. Svelto, C. Svelto, G. Sorbello, INFN (Italy) and Politecnico di Milano (Italy)
- 36 **Yb:YAG disk laser pumped by a stacked diode array [3682-04]**
N. Kugler, T. Brand, I. Schmidt, Laser- und Medizin-Technologie gmbH (Germany); C. Gao, H. Weber, Technische Univ. Berlin (Germany)
- 47 **Requirements of pump diodes for diode-pumped solid state lasers [3682-05]**
H. Gempel, BremLas Lasertechnik Bremen GmbH (Germany); N. I. Katsavets, A. L. Ter-Martirosyan, ATC-Semiconductor Devices (Russia); C. von Kopylow, E. Pfeifer, BremLas Lasertechnik Bremen GmbH (Germany)
- 50 **Nd:CSB laser pumped by laser diode array [3682-06]**
O. V. Kuzmin, S. A. Kutovoi, V. L. Panyutin, SPA Firm (Russia); S. T. Durmanov, Yu. P. Rudnitskiy, G. V. Smirnov, TRINITI (Russia); A. J. Abazadze, M. N. Grudin, J. M. Kolbatskov, J. P. Koval, Polyus Research and Development Institute (Russia)
- 53 **Polarization dynamics of Nd:YAG laser with weakly anisotropic Fabry-Perot cavity [3682-07]**
P. A. Khandokhin, Institute of Applied Physics (Russia); N. D. Milovsky, Nizhny Novgorod State Univ. (Russia); Yu. A. Mamaev, E. Ovchinnikov, E. Y. Shirokov, Institute of Applied Physics (Russia)
- 63 **Diode-pumped solid state laser with 2D intracavity beam scanning using liquid crystal spatial light modulator [3682-08]**
A. F. Kornev, S.I. Vavilov State Optical Institute (Russia); A. P. Onokhov, Peterlab Ltd. (Russia); V. P. Pokrovskiy, L. N. Soms, V. K. Stupnikov, S.I. Vavilov State Optical Institute (Russia)

SESSION 2 GAIN MEDIA

- 76 **Up-conversion in YLF:Yb³⁺, Tm³⁺ laser crystals [3682-09]**
A. M. Tkachuk, I. K. Razumova, S.I. Vavilov State Optical Institute (Russia); M.-F. Joubert, Univ. Lyon I (France); R. Moncorge, Univ. de Caen (France)

- 83 **Energy transfer and lasing in $\text{LiYbF}_4\text{:Ho}$, $\text{LiYbF}_4\text{:Ho,Tm}$, and $\text{Krb(WO}_4)_3$ crystals** [3682-10]
A. V. Sandulenko, V. A. Sandulenko, A. M. Tkachuk, A. N. Titov, V. M. Reiterov, V. N. Ivanov, S.I. Vavilov State Optical Institute (Russia)
- 92 **Spectroscopic and laser properties of $\text{LaSc}_3(\text{BO}_3)_4\text{:Cr,Yb,Er}$ crystals** [3682-11]
O. V. Kuzmin, S. A. Kutovoi, V. L. Panyutin, SPA Firm (Russia); S. T. Durmanov, Yu. P. Rudnitskiy, G. V. Smirnov, TRINITI (Russia)
- 99 **Effect of temperature on absorption and fluorescence spectra of Er-doped laser glasses** [3682-12]
S. G. Lunter, S.I. Vavilov State Optical Institute (Russia); N. V. Nikonorov, Corning Scientific Ctr. (Russia); A. K. Przhvuskii, S.I. Vavilov State Optical Institute (Russia)

SESSION 3 LASER APPLICATIONS FOR HIGH-PRECISION MEASUREMENTS

- 108 **LINGRAN-100: laser middle-base interferometric gravitational antenna** [3682-13]
V. N. Rudenko, V. K. Milyukov, V. V. Kulagin, A. V. Gusev, A. Kopaev, M.V. Lomonosov Moscow State Univ. (Russia)
- 117 **Wideband laser interferometer for monitoring Earth strains** [3682-14]
V. K. Milyukov, V. N. Rudenko, B. S. Klyachko, A. M. Kart, A. V. Myasnikov, M.V. Lomonosov Moscow State Univ. (Russia)
- 126 **Observation of variations of long-period microseismic noise by precision laser interferometry** [3682-15]
S. N. Bagayev, V. A. Orlov, S. V. Panov, Institute of Laser Physics (Russia)
- 131 **Contrast enhancement of ESPI addition fringes using real-time electronic filtering** [3682-16]
R. Rodriguez Vera, C. Perez Lopez, F. Mendoza Santoyo, B. Barrientos, Ctr. de Investigaciones en Optica AC (Mexico)

SESSION 4 LASER CHARACTERISTICS CONTROL

- 138 **Transverse mode pattern in distorted resonators** [3682-17]
V. V. Lyubimov, S.I. Vavilov State Optical Institute (Russia)
- 145 **High-power Nd:YAG laser with birefringence compensation and adaptive HR mirror** [3682-18]
N. Kugler, S. Seidel, Laser- und Medizin-Technologie gGmbH (Germany); H. Weber, Technische Univ. Berlin (Germany)
- 155 **Compensation of thermo-optical distortions in the active elements of high-power cw Nd:YAG lasers** [3682-19]
S. T. Durmanov, V. V. Lyubimov, Yu. P. Rudnitskiy, G. V. Smirnov, TRINITI (Russia); M. A. Kurin, Ya. I. Malashko, A. S. Rumjantsev, SIC Systema (Russia)
- 163 **Kinetics of laser processes in multicascade optical schemes** [3682-20]
S. G. Grechin, Moscow State Technical Univ. (Russia); E. V. Raevsky, Polyus Research and Development Institute (Russia); V. N. Rojdestvin, E. A. Sharandin, Moscow State Technical Univ. (Russia)

- 170 **Feedback timing approach to pulse energy stabilization in the actively mode-locked laser**
[3682-21]
V. A. Zaporozhchenko, B.I. Stepanov Institute of Physics (Belarus)

SESSION 5 LASER COMPONENTS

- 176 **Liquid crystal modulators with improved laser damage resistance** [3682-22]
F. L. Vladimirov, N. I. Pletneva, I. E. Morichev, L. N. Soms, V. P. Pokrovskiy, S.I. Vavilov State
Optical Institute (Russia)
- 183 **Passive shutter based on nonlinear total internal reflection for laser pulse shortening**
[3682-23]
A. N. Rubinov, I. M. Korda, A. I. Bibik, B.I. Stepanov Institute of Physics (Belarus)
- 187 **Biaxial nonlinear crystals for laser radiation harmonic generation** [3682-24]
V. G. Dmitriev, Polyus Research and Development Institute (Russia); S. G. Grechin, Moscow
State Technical Univ. (Russia)
- 196 **Broadband spectrum selective coatings for laser systems** [3682-25]
E. Kotlikov, E. Khonineva, State Univ. of Aerospace Instrument Manufacturing (Russia)
- 201 **Fullerene-based nonlinear optical devices for fast control of spatial, power, and temporal
characteristics of laser radiation** [3682-26]
I. M. Belousova, V. P. Belousov, E. A. Gavronskaya, V. A. Grigorev, O. B. Danilov,
A. G. Kalintsev, V. E. Krasnopol'sky, V. A. Smirnov, E. N. Sosnov, S.I. Vavilov State Optical
Institute (Russia)
- 210 *Author Index*

Conference Committees

Conference Honorary Chairs

Alexander M. Prokhorov, General Physics Institute, Russian Academy of Sciences
Charles H. Townes, University of California/Berkeley (USA)

Organizing Committee

Arthur A. Mak, *Chair*, Institute for Laser Physics, S.I. Vavilov State Optical Institute
Alexander A. Andreev, *Cochair*, Institute for Laser Physics, S.I. Vavilov State Optical Institute
Vladimir M. Arpishkin, *Cochair*, ROS—Rozhdestvensky Optical Society
E.I. Akopov, SPIE Russia Chapter
T. Fujioka, Tokai University (Japan)
O.D. Gavrilov, Institute for Laser Physics, S.I. Vavilov State Optical Institute
A.S. Gorshkov, Institute for Laser Physics, S.I. Vavilov State Optical Institute
V.B. Kryuchenkov, International Science Technology Center
H. Lowdermilk, Lawrence Livermore National Laboratory (USA)
E.I. Makurov, S.I. Vavilov State Optical Institute
V.B. Smirnov, St. Petersburg State University
E. Spitz, Thomson-CSF (France)
Yu.A. Straus, S.I. Vavilov State Optical Institute
B.S. Zykov, International Science Technology Center

Program Committee

Arthur A. Mak, *Chair*, Institute for Laser Physics, S.I. Vavilov State Optical Institute
Alexander A. Andreev, *Cochair*, Institute for Laser Physics, S.I. Vavilov State Optical Institute
Leonid N. Soms, *Scientific Secretary*, Institute for Laser Physics, S.I. Vavilov State Optical Institute
P.A. Apanasevich, B.I. Stepanov Institute of Physics (Belarus)
S.N. Bagaev, Institute of Laser Physics
N.G. Basov, P.N. Lebedev Physical Institute
V.I. Bespalov, Institute of Applied Physics
F.V. Bunkin, General Physics Institute
Yu.D. Golyaev, Polyus Research and Development Institute
V.M. Gordienko, M.V. Lomonosov Moscow State University
V.P. Kandidov, M.V. Lomonosov Moscow State University
Ya.I. Khanin, Institute of Applied Physics
O.A. Kocharovskaya, Institute of Applied Physics
N.I. Koroteev, M.V. Lomonosov Moscow State University
V.I. Kovalev, P.N. Lebedev Physical Institute

V.I. Kovalev, P.N. Lebedev Physical Institute
I.B. Kovsh, Laser Association
V.V. Lyubimov, Institute for Laser Physics, S.I. Vavilov State Optical Institute
A.A. Manenkov, General Physics Institute
Yu.T. Mazurenko, S.I. Vavilov State Optical Institute
A.P. Napartovich, TRINITI
A.N. Oraevsky, P.N. Lebedev Physical Institute
V.Ya. Panchenko, NICTL Laser Research Center
P.P. Pashinin, General Physics Institute
G.T. Petrovskiy, S.I. Vavilov State Optical Institute
L.A. Rivlin, Moscow State Institute of Radio Engineering, Electronics
 and Automation
N.N. Rosanov, Institute for Laser Physics, S.I. Vavilov State Optical Institute
A.S. Rubanov, B.I. Stepanov Institute of Physics (Belarus)
V.A. Serebryakov, Institute for Laser Physics, S.I. Vavilov State Optical Institute
I.A. Shcherbakov, General Physics Institute
V.E. Sherstobitov, Institute for Laser Physics, S.I. Vavilov State Optical Institute
A.P. Shkadarevith, Peleng (Belarus)
V.B. Smirnov, St. Petersburg State University
M.S. Soskin, Institute of Physics (Ukraine)
A.P. Sukhorukov, M.V. Lomonosov Moscow State University
V.I. Ustyugov, Institute for Laser Physics, S.I. Vavilov State Optical Institute
V.V. Valuev, GPO Almaz
E.A. Viktorov, Institute for Laser Physics, S.I. Vavilov State Optical Institute
G.M. Zverev, Polyus Research and Development Institute

American Local Committee

Howard Lowdermilk, *Chair*, Lawrence Livermore National Laboratory (USA)
Sherene Goulart, *Secretary*, Lawrence Livermore National Laboratory (USA)

Asian Local Committee

Sadao Nakai, *Chair*, Osaka University (Japan)
Tomoo Fujioka, *Cochair and Scientific Secretary*, Tokai University (Japan)

European Local Committee

Erich Spitz, *Chair*, Thomson SA (France)
Arnaud Brignon, *Scientific Secretary*, Thomson-CSF (France)
Henri Rajbenbach, *Scientific Secretary*, European Commission (Belgium)

SESSION 1

Diode-Pumped Solid State Lasers

DESIGN CONSIDERATIONS FOR HIGH-POWER TEM₀₀ OPERATION OF END-PUMPED SOLID-STATE LASERS

W. A. Clarkson

Optoelectronics Research Centre
University of Southampton
Southampton, SO17 1BJ
United Kingdom

ABSTRACT

A resonator design strategy for high-power end-pumped solid-state lasers is described, which reduces the beam distortion due to thermally-induced lens aberrations. The approach is based on a resonator design satisfying two criteria: firstly, the laser mode radius must be appreciably smaller than the pump beam radius, and secondly, the laser mode size must decrease with decreasing power (increasing focal length) of the thermal lens. Experimental results are presented for diode-bar-pumped Nd:YAG lasers confirming the validity of this approach. A simple technique, employing a single quarter-wave plate, for reducing the depolarisation loss due to thermally-induced birefringence is also described. Using this approach, the depolarisation loss for a diode-bar-pumped Nd:YAG laser operating at 946nm has been reduced from ~1.7% to <0.001%, resulting in 2.9W of linearly-polarised output for 14.3W of incident pump power.

1. INTRODUCTION

Recent advances in semiconductor laser technology have led a very significant increase in the available output power from diode-bar sources, and as a result there has been growing interest in using high-power diode-bars as pump sources for power-scaling of solid-state lasers. At relatively low pump powers (<few watt), the use of end-pumped rather than side-pumped geometries has been the preferred route owing to the much higher efficiencies achievable, the relative ease with which fundamental transverse mode operation can be selected and the enormous flexibility in cavity design and operating wavelength. Many of these attractive features stem from the relative ease with which low power diodes can be focused to small beam sizes, combined with their relatively narrow emission linewidths allowing short absorption lengths (typically ~few mm) in the laser material.

Progress in scaling diode-end-pumped solid-state lasers to high powers, whilst retaining these attractive features, has been hindered by two main problems. The first of these has been the unfriendly and highly elliptical nature of the output from high-power diode-bars, which is nearly diffraction-limited in the plane perpendicular to the array, but is typically ~2000 times diffraction-limited in the array plane. This large mismatch in the M^2 beam quality factors for orthogonal planes makes it difficult to focus to the small diameter beams required for efficient end-pumping of solid-state lasers.

To allow focusing to small beam diameters it is necessary to use a beam delivery scheme which equalises the M^2 values in orthogonal planes without significantly decreasing the brightness. Recently, a number beam delivery schemes which attempt to solve this problem have been reported (e.g. ref.1), offering the attractive prospect of efficient high-power operation even on relatively low gain or quasi-three-level transitions².

However, the availability of high power and high intensity pump sources has further exacerbated thermal effects such as thermal lensing and thermally-induced stress-birefringence, which are particularly pronounced in end-pumped lasers owing to the high thermal loading density. One of the main problems encountered in end-pumped lasers is beam distortion due to the highly aberrated thermal lens, making it extremely difficult to simultaneously achieve high efficiency and good beam quality. To overcome this problem a number of approaches have been reported including the use of apertures to select the

TEM₀₀ beam³, and aspheric lenses as compensators⁴. More recently, an alternative approach has been reported⁵, which uses face-cooling to achieve axial heat flow in a thin disc of laser material, and hence a significant decrease in the strength of the thermal lensing. Unfortunately, the latter approach has the disadvantage that it is only applicable to laser materials with a short absorption length for the pump light and/or laser transitions with a high gain cross-section. This is necessary to ensure that the pumped region has a high aspect ratio of pump beam size to disc thickness to minimise radial heat flow.

In this paper we describe an alternative resonator design strategy to reduce the beam distortion resulting from strong thermally-induced aberrations without using compensating components. The underlying basis of this approach is that the aberrations which result from the Gaussian-like pump beam are most pronounced in the wings of the pumped region. Hence by using a resonator with a TEM₀₀ mode which is smaller than the pump beam it is possible to achieve a near-diffraction-limited output beam. However, a consequence of the smaller mode size there is unused inversion in the wings of the pumped region which may provide sufficient gain for simultaneous oscillation on higher-order transverse modes. Suppression of higher-order transverse modes can be achieved by applying a second condition to the resonator design, namely that the TEM₀₀ beam size in the laser rod should decrease with increasing focal length of the thermal lens. The rationale for this design is presented below, together with experimental results for a diode-bar-pumped Nd:YAG laser which confirm the benefits of this approach. Finally, a simple technique, using a single quarter-wave plate, for reducing the depolarisation loss due to thermally-induced birefringence in resonators employing a single laser rod is also described. Results for a diode-bar-pumped Nd:YAG laser operating at 946nm which demonstrate the advantages of this approach are presented.

2. THERMAL LENSING IN END-PUMPED SOLID-STATE LASERS

In the work described here we are restricting our consideration to end-pumped lasers with side-cooled rods of cylindrical geometry. The attraction of side cooling is the relative simplicity of its implementation, but due to the predominantly radial heat flow it has the disadvantage of strong thermal lensing. One of the main problems is that the thermal lens is highly aberrated, due to the Gaussian-like intensity profile of the pump beam, leading to a very pronounced degradation in beam quality. In laser materials, such as Nd:YAG, with its high stress-fracture limit, it is generally the aberrated thermal lens which presents the most difficult obstacle to simultaneously achieving both high efficiency and a diffraction-limited TEM₀₀ output in high-power end-pumped lasers.

To enable the formulation of an appropriate resonator design strategy to minimise degradation in beam quality, and hence obtain the optimum TEM₀₀ performance at high pump powers, it is necessary to know the focal length of the thermal lens and determine the effect of the non-parabolic phase aberrations on beam quality. For an edge-cooled laser rod of radius a , length l mounted in a heat-sink with its outer curved surface maintained at a constant temperature and end-pumped by a diode-laser with pump intensity $I_p(r)$, the phase difference, $\Delta\phi(r)=\phi(0)-\phi(r)$, which results from thermal loading and the temperature dependence of the refractive index is given by the approximate expression^{6,7}:

$$\Delta\phi(r) = - \frac{2\pi}{\lambda} \int_0^l \int_0^r \frac{h(r',z)}{K_c} \cdot \frac{dn}{dT} dr' dz \quad (1)$$

where K_c is the thermal conductivity and $h(r,z)$ is the heat flux (assumed to be purely radial) given by

$$h(r,z) = \frac{\alpha_p \gamma \exp(-\alpha_p z)}{r} \int_0^r r' I_p(r') dr' \quad (2)$$

where α_p is the absorption coefficient for the pump and γ is the fraction of absorbed pump converted to heat. If the pump beam has a uniform transverse intensity profile, then $\Delta\phi(r) \propto r^2$ and the resulting thermal lens has no phase aberration. However, in general the pump beam has a Gaussian-like intensity profile hence it is more appropriate to consider the resulting aberrated thermal lens as one whose focal length varies radially. For a thin thermal lens with radially varying phase difference $\Delta\phi(r)$ an approximate expression for the focal length $f(r)$ of the thermal lens is given by

$$f_t(r) = \frac{2\pi r}{\lambda \frac{d\Delta\phi(r)}{dr}} \quad (3)$$

Substituting equation (1) into equation (3) yields the following expression for $f_t(r)$:

$$f_t(r) = \frac{K_c r^2}{\eta_{abs} \gamma \frac{dn}{dT} \int_0^r r' I_p(r') dr'} \quad (4)$$

where η_{abs} is the fraction of pump light absorbed. It can be seen from the above expression that the focal length of the thermal lens at $r=0$ and its variation with r , and hence the phase aberration, is strongly dependent on the transverse intensity profile $I_p(r)$ of the pump beam. For a pump beam with a 'top-hat' intensity profile ($I_p = P_p/\pi w_p^2$ for $r \leq w_p$ and $I_p = 0$ for $r > w_p$, where P_p is the incident pump power), the focal length of the thermal lens is given by the following expression:

$$f_t(r) = \frac{2\pi K_c w_p^2}{P_p \gamma \eta_{abs} \frac{dn}{dT}} \quad (r \leq w_p) \quad (5)$$

$$f_t(r) = \frac{2\pi K_c r^2}{P_p \gamma \eta_{abs} \frac{dn}{dT}} \quad (r > w_p)$$

and for a pump beam with a Gaussian transverse intensity profile, $I_p(r) = (2P_p/\pi w_p^2) \exp(-2r^2/w_p^2)$ the focal length is given by

$$f_t(r) = \frac{2f_{t0}}{w_p^2} \left(\frac{r^2}{1 - \exp(-2r^2/w_p^2)} \right) \quad (6)$$

where f_{t0} is the focal length on axis at $r=0$, given by

$$f_{t0} = \frac{\pi K_c w_p^2}{P_p \gamma \eta_{abs} \frac{dn}{dT}} \quad (7)$$

Thus from comparison of equations (5) and (6), it can be seen that for a Gaussian pump profile the thermal lensing on axis ($r=0$) is approximately a factor-of-two stronger than for a pump beam with a 'top-hat' intensity distribution. In addition, a Gaussian pump results in a thermal lens which is much more highly aberrated with only a small region in the centre ($r \ll w_p$) having essentially constant focal length. In contrast the 'top-hat' pump beam, produces a lens which is essentially unaberrated over the entire pumped region ($r \leq w_p$). Thus, the intensity profile of the pump beam is a very important factor in determining the thermal lens power and its phase aberration.

3. MEASUREMENT OF THERMAL LENSING

In order to determine the thermal lens focal length in an actual diode-bar-pumped Nd:YAG laser we have made a measurement of the phase difference as a function transverse position using a Mach-Zehnder interferometer. The experimental set-up (shown in fig.1) consisted of an antireflection coated 10mm long Nd:YAG rod mounted in a water-cooled copper heat-sink, end-pumped by a 20W diode-bar (Opto Power Corporation OPC-AO20-mm-CS). The diode-bar output beam was re-formatted using a two-mirror beam shaper¹, to roughly equalise the M^2 factors in orthogonal planes, and was focused with an arrangement of standard lenses similar to that described in ref.8. The resulting focused beam was nearly

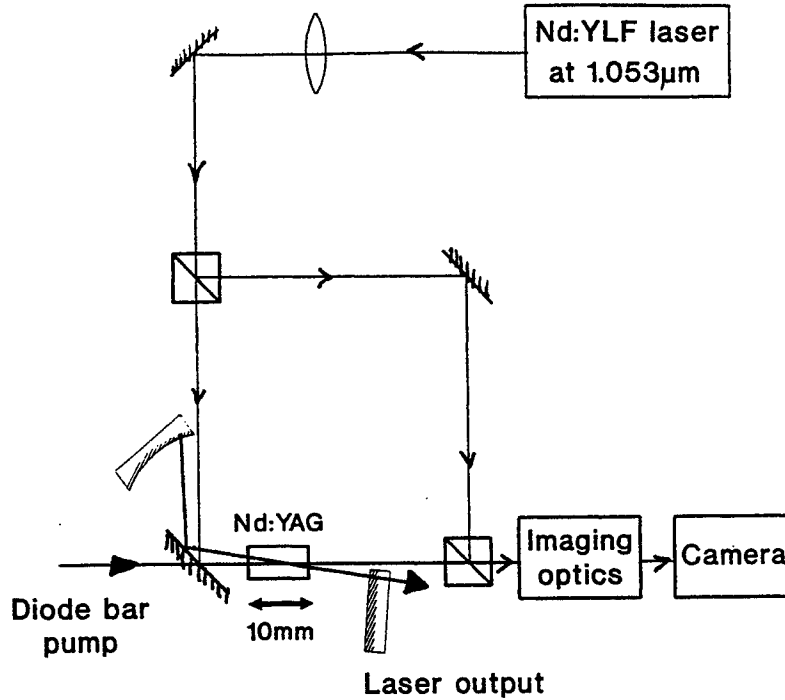


Figure 1: Mach-Zehnder interferometer for measuring the thermally-induced phase difference

circular with radii; $w_{px}=227\mu\text{m}$ and $w_{py}=224\mu\text{m}$ and beam quality factors; $M_x^2\approx 78$ and $M_y^2\approx 63$ in orthogonal planes. This choice of beam size is typical of that required for efficient operation on some of the lower gain Nd:YAG transitions (e.g. at 946nm and 1.32μm). The Mach-Zehnder interferometer arrangement used permitted measurements of the phase difference $\Delta\phi(r)$ under both non-lasing and lasing conditions. At the maximum pump power incident on the laser rod of 14.2W, the Nd:YAG laser produced ~6W of output at 1.064μm in a multi-transverse-mode beam. Under lasing conditions and at the maximum pump power the measured phase difference as a function of radial position is shown in fig.2(a). The solid line in fig.2(a) is the parabolic curve which is the best fit to the phase difference data close to the centre of the pumped region. This indicates the phase difference profile that would be measured for a perfect (unaberrated) lens, and corresponds to a focal length of ~60mm. By comparison, the thermal lens at the centre of the pumped region, under non-lasing conditions had a focal length ~24mm - a factor-of-two shorter than the measured focal length under lasing conditions. The explanations for this difference is thought to be additional thermal loading due to upconversion effects. This clearly illustrates the importance of making thermal lens measurements under the appropriate operating conditions. The deviation of phase difference from the ideal parabolic phase difference profile, shown in fig.2(b), reveals the highly aberrated nature of the thermal lens with the phase aberration becoming increasingly pronounced for $r>w_p$. The resulting radial variation in focal length, calculated from the experimental data, is compared with predicted variation in focal length for a Gaussian pump beam given by equation (6), where it is assumed that $K_c=13\text{Wm}^{-1}\text{K}^{-1}$, $dn/dT=9.86\times 10^{-6}\text{K}^{-1}$ for YAG, $\gamma\approx 0.32$ for 1.064μm operation, $w_p=235\mu\text{m}$, and $\eta_{abs}=0.94$. The result of this comparison are shown in fig.3, where the predicted values for focal length (dashed line) correspond to a slightly weaker lens than was measured in practice. This can be easily explained since the theoretical model does not take into account the extra contribution to lensing which arises from end-face bulging and the stress dependence of the refractive index, which are included in the experimental measurements. From independent measurements of the stress-induced birefringence, using the Mach-Zehnder interferometer, and the end-face curvature, using a Michelson interferometer, we were able to show that the relative contributions to thermal lensing are; ~86% due to temperature dependence of refractive index, ~8% due to end-face curvature and ~6% due to radial stress dependence of refractive index. Taking into account these additional contributions and simply multiplying equation (5) by 0.86 results in a predicted focal length given by the dotted line in fig.3, which is in good agreement with the experimental data.

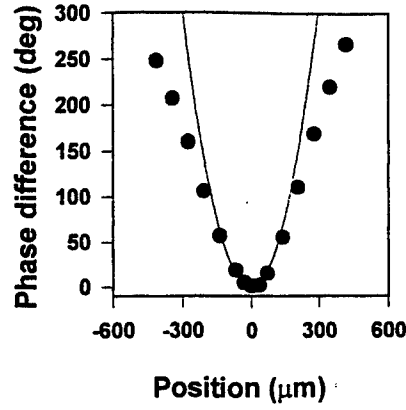


Figure 2(a): Phase difference as a function of radial position under lasing conditions.

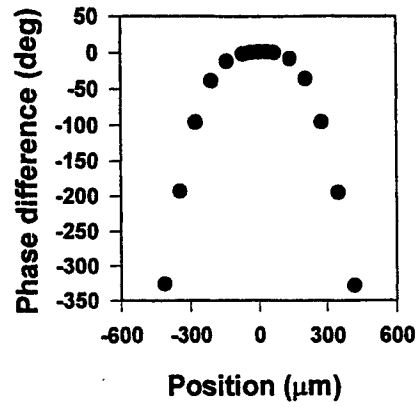


Figure 2(b): Deviation of phase difference from the ideal parabolic phase difference profile.

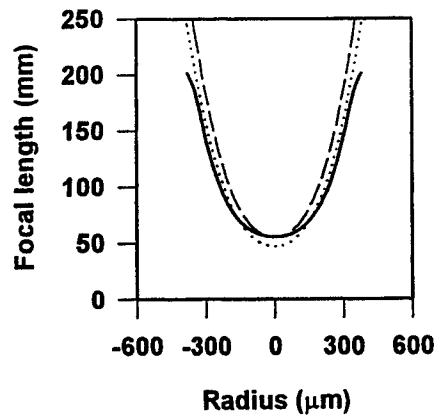


Figure 3: Radial dependence of the thermal lens focal length. (The solid line was calculated from the measured phase difference data. The dashed line represents the predicted radial dependence of focal length for a Gaussian pump beam taking into account the contribution due to the temperature dependence of refractive index only. The dotted line represents the predicted radial variation in focal length, modified to take into account the measured contributions to lensing from the stress dependence of refractive index and end-face bulging.

4. BEAM QUALITY DEGRADATION

The highly aberrated nature of the thermal lens can lead to significant beam distortion. To investigate this we have performed a simple experiment to measure the increase in M^2 for a diffraction-limited probe laser beam after a single-pass through an end-pumped Nd:YAG rod. The experimental set-up (not shown) uses the same end-pumping arrangement described in the previous section on thermal lens measurement with the probe beam, from a low-power diode-pumped Nd:YLF laser aligned to be collinear with the high-power diode-bar pump. The M^2 factor was measured using a Coherent Modemaster for a series of different probe beam sizes in the Nd:YAG rod at the maximum available pump power of 14.2W. The results, for both lasing and non-lasing conditions (fig.4) indicate a marked increase in the M^2 value and hence degradation in beam quality with probe beam size. It is also apparent that the M^2 values measured under non-lasing conditions are significantly worse than those measured under lasing conditions, implying that the thermal loading is significantly greater under non-lasing conditions. This is believed to be due to upconversion processes which lead to multiphonon decay and an increase in heat dissipation, which is especially pronounced at high inversion densities.

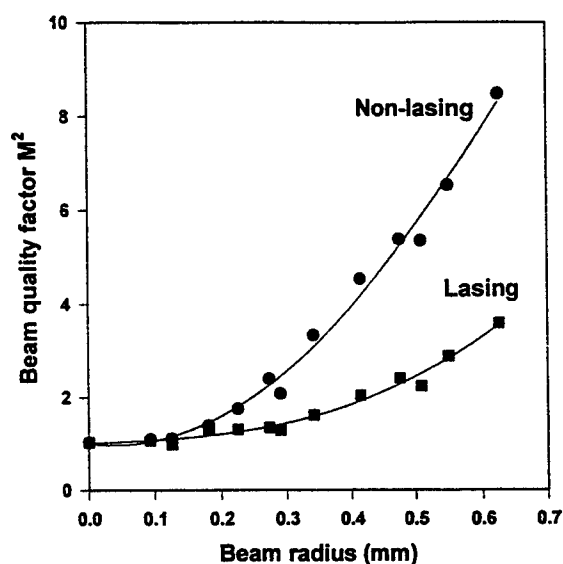


Figure 4: Single-pass degradation in beam quality versus probe beam size.

5. RESONATOR DESIGN STRATEGY

Clearly, in order to avoid significant degradation in beam quality and depolarisation loss for the TEM_{00} mode at high pump power, it is necessary to use a resonator with a TEM_{00} radius in the laser rod which is significantly smaller than the pump beam radius. This is in contrast to the situation at low powers where it is generally accepted that one should use a resonator design with $w_L \geq w_p$ for efficient TEM_{00} operation. At high pump powers, the smaller the ratio w_L/w_p the lower the depolarisation loss and the smaller the degradation in beam quality. Unfortunately one can not simply choose a resonator with an arbitrarily small laser mode size, since there will then be a significant amount of undepleted inversion in the pumped region not occupied by the laser mode, leading to multi-transverse mode oscillation and hence a non-diffraction-limited laser output. In practice therefore, it is necessary to use the largest possible laser mode size without significantly increasing the M^2 value and the depolarisation loss. The upper limit on the TEM_{00} size that can be used for laser operation with for example, $M^2 < 1.1$, is difficult to calculate, but a rough value can be estimated from the experimental data on single-pass beam degradation and the discussion of the preceding section. It is clear from the previous section that the laser mode must still be appreciably smaller than the pump beam to avoid significant beam distortion, hence there is still the problem of some undepleted inversion in the wings of the pumped region which can lead to lasing on higher-order transverse modes. One solution to this problem is to simply use an aperture to discriminate against the unwanted higher-order modes. However, this has the disadvantage that it can significantly increase the loss for the fundamental mode and hence be detrimental to

the efficiency. An alternative approach is to make use of the radially varying focal length of the thermal lens to provide the required discrimination. This is based on the principle that higher-order transverse modes, by virtue of their larger beam size than the TEM_{00} mode, will see a thermal lens with an effective focal length which is longer than that seen by the TEM_{00} beam. Hence, choosing a resonator design where the mode size decreases with increasing focal length of the thermal lens, will effectively decrease the ratio of beam sizes of the higher-order transverse modes to the TEM_{00} mode. This results in a decrease in available gain for higher-order modes by virtue of their stronger spatial overlap with the fundamental mode, hence suppressing their oscillation.

To verify the benefits of this approach we have performed a number of experiments on a Nd:YAG laser end-pumped by a high-power diode-bar. The pumping scheme used is identical to that described in earlier sections, delivering a maximum of 14.2W in a beam of radius $w_p \approx 225\mu m$. The resonator design employed was a simple folded cavity (fig. 5), with the 10mm long Nd:YAG laser rod was mounted, as before, in a water-cooled copper heat-sink. The use of two output couplers (with transmissions of 5% and 2% at $1.064\mu m$ facilitated simultaneous monitoring of the laser output power, beam quality factor and transverse intensity profile of the output beam, whilst having the additional advantage of allowing easy determination of the laser mode size at the pump input mirror, and hence in the laser rod, without requiring a knowledge of the resonator design and the effect of the thermal lens.

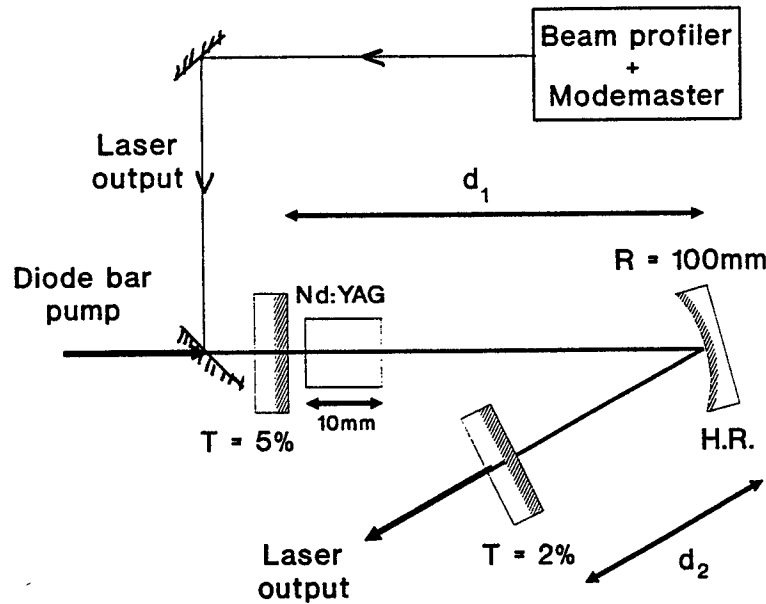


Figure 5: Resonator design for Nd:YAG laser experiments.

Using the standard ABCD matrix formalism it can be shown that a decrease in laser mode size in the rod with increasing focal length of the thermal lens can be realised by choosing an effective optical length for arm 1 to be just less than the sum of the focal lengths of the curved high reflector and the thermal lens focal length ($\sim 60mm$ at the maximum pump power). In our experiment the length d_1 was set to 109mm with the angle of incidence on the curved mirror made small ($< 5^\circ$) to render the effects of astigmatism negligible. The required TEM_{00} size in the laser rod can be obtained by simply adjusting the arm length d_2 . Calculated values for the TEM_{00} beam radius at the laser rod are plotted as a function of thermal lens

focal length for different values of d_2 in fig.6. Without a polariser present in the cavity and at the maximum available pump power of 14.2W, it was found that TEM_{00} operation ($M^2 \leq 1.1$) could be achieved for a small range of values d_2 of approximately (70 ± 0.5) mm, resulting in a maximum output power of 6.2W (fig.7). Inserting a Brewster-angled plate into the cavity resulted in a linearly polarised, TEM_{00} output ($M^2 < 1.1$) of slightly lower output power 5.5W, the reduction caused

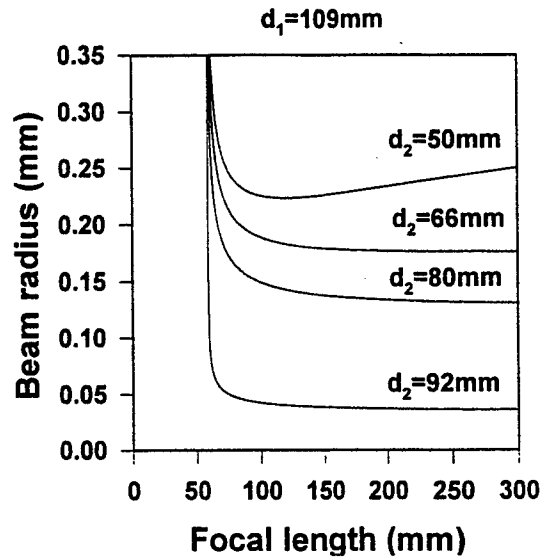


Figure 6: TEM_{00} radius versus thermal lens focal length.

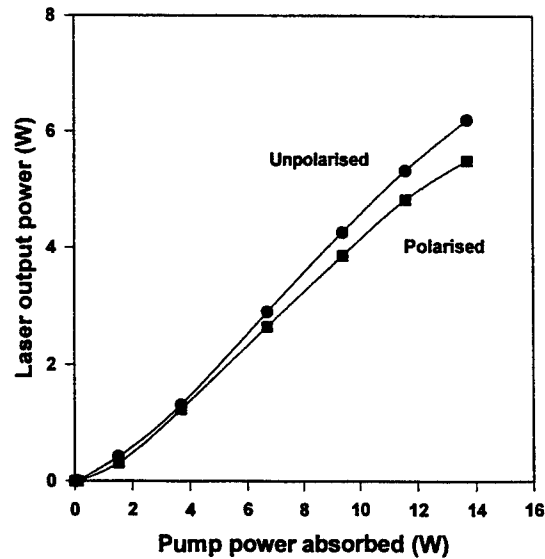


Figure 7: Nd:YAG output power at $1.064\mu\text{m}$ versus absorbed pump power.

by an additional cavity loss of $\sim 1\%$ due to thermally-induced stress birefringence. One interesting observation was that the reliability of TEM_{00} operation was improved as a result of including a polariser in the cavity and additionally, had the benefit of extending the range of arm lengths d_2 , and hence the range of laser mode sizes, over which near diffraction-limited operation can be maintained. This can be attributed to the additional transverse mode discrimination provided by the polariser by virtue of the fact that higher-order transverse modes with larger beam sizes see, on average, a larger stress-induced birefringence and hence experience increased depolarisation loss at the polariser compared to the smaller fundamental mode.

To provide additional confirmation of the benefits of this resonator design approach, and in particular, to demonstrate the importance of using a resonator with a laser mode size which decreases with increasing thermal lens focal length, we have also investigated the behaviour of a similar folded cavity, but this time with arm lengths d_1 and d_2 selected to give a laser mode radius similar to that used in the previous experiment (i.e. $\sim 165\mu m$), but one which does not vary appreciably with rod focal length. At the maximum pump power, a folded cavity with $d_1 \approx 80mm$ and $d_2 \approx 50mm$ roughly satisfies these requirements. The minimum M^2 beam quality factor attainable for this resonator was >2 , thus serving to illustrate the importance of using a resonator which satisfies both of our design criteria.

This design strategy has been successfully applied to other diode-bar-end-pumped Nd:YAG lasers operating on lower gain transitions at $946nm$ and at $1.3\mu m$, yielding diffraction-limited performance up to power levels of $3.1W$ and $3.2W$ respectively. However, due to their relatively low gain, both of these lasers when operated with Brewster plate polarisers, provided significantly lower powers due to the depolarisation loss resulting from thermally-induced birefringence. In the case of the $946nm$ Nd:YAG laser a maximum polarised output of $2.1W$, and for $1.3\mu m$ operation, a maximum linearly polarised output of $\sim 1.75W$ were achieved. In the latter case the much higher heat loading density, which results from the larger quantum defect, makes it more difficult to achieve an efficient, linearly polarised TEM_{00} output.

6. SIMPLE TECHNIQUE FOR COMPENSATION OF THERMALLY-INDUCED BIREFRINGENCE

For applications such as nonlinear frequency conversion, requiring a linearly polarised output, the most serious problem is often the depolarisation loss resulting from stress-induced birefringence which dramatically reduces the efficiency of low gain lasers at high pump powers. Various techniques for compensating stress-induced birefringence have been described^{9,10}, but which are not well-suited for low gain end-pumped lasers employing a single laser rod.

In this section, we describe an alternative technique for reducing the depolarisation loss due to stress-induced birefringence, which is well-suited for use in end-pumped solid-state lasers. The benefits of this approach have been investigated for a diode-bar-end-pumped Nd:YAG laser operating on the low gain transition at $946nm$. Our approach employs only a single quarter-wave plate located in the small gap between the pump incoupling mirror and the Nd:YAG rod shown in fig.8. The quarter-wave plate is aligned with its fast or slow axis parallel to the desired plane of polarisation, in this case defined by a Brewster-angled plate polariser as the x-direction. The principle of operation can be explained by considering the transit of linearly-polarised light from the polariser to the pump incoupling mirror and back to the polariser. Rays which propagate along the laser rod in the x-z or y-z planes will not experience any change in polarisation state after a double-pass of the Nd:YAG and quarter-wave plate, since the radial and tangential components of stress are parallel or perpendicular to the x,y axes for these rays. The rays which would normally experience the largest change in polarisation state, and hence loss at the polariser, propagate along planes inclined 45° to the x-z and y-z planes, where the radial and tangential stress components are inclined at 45° to the x,y axes. With the quarter-wave plate present in the cavity, the radial and tangential polarisation components, after a single-pass of the laser rod, will subsequently be rotated by 90° on double-passing the quarter-wave plate, thus emerging after a second transit of the laser rod, with no net change in the polarisation state, and hence experience negligible loss at the polariser. Some degree of birefringence compensation will also occur for rays propagating along other sectors of the laser rod, with the net overall result that depolarisation loss is substantially reduced.

To demonstrate the effectiveness of this technique we have compared the performances of our diode-bar-pumped $946nm$ Nd:YAG laser with and without the quarter-wave plate present in the cavity. The results shown in fig.9 indicate that the maximum linearly-polarised output (without the quarter-wave plate) was limited by the effects of thermally-induced

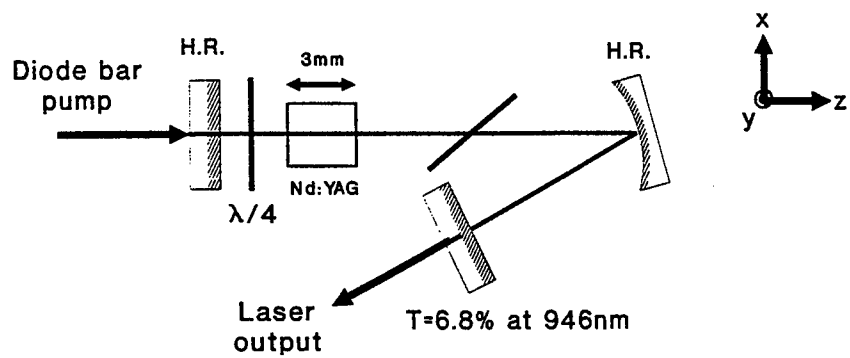


Figure 8: Diode-pumped Nd:YAG laser with a quarter-wave plate for compensating stress-induced birefringence.

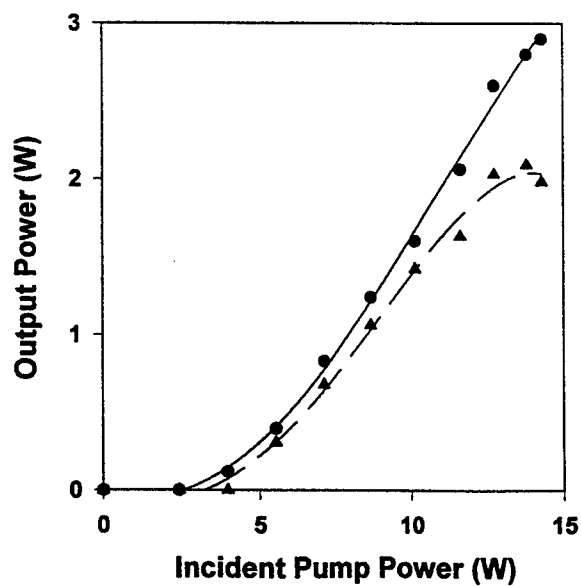


Figure 9: Laser output power versus incident pump power with the quarter-wave plate (solid-line) and without the quarter-wave plate (dotted line).

birefringence to $\sim 2.1\text{W}$. In contrast, with the quarter-wave plate present, the maximum output power was $\sim 2.9\text{W}$, limited only by the maximum available pump power of 14.3W incident on the laser rod. The output beam was also nearly diffraction-limited with $M^2 < 1.2$. A measurement of the power reflected from the Brewster-angled polariser plate indicated that the contribution to cavity loss arising from stress-induced birefringence was $< 0.001\%$, compared with a depolarisation loss of $\sim 1.7\%$ for the laser without the quarter-wave plate. These results clearly demonstrate the potential of this simple technique for compensation of thermally-induced birefringence, which should now allow further power-scaling of a various end-pumped lasers with linearly polarised output beams.

7. CONCLUSIONS

An alternative resonator design strategy has been described, which reduces the degradation in beam quality arising from thermally-induced lens aberrations in high-power end-pumped lasers. The design strategy is based on the resonator satisfying two requirements which are namely; that the TEM_{00} mode size must be significantly smaller than the pump beam size and that the TEM_{00} size must decrease with increasing thermal lens focal length. Using this approach Nd:YAG lasers, end-pumped by a 20W diode bar, have been operated efficiently with multiwatt output powers and near-diffraction-limited beam quality at $1.064\mu\text{m}$, 946nm and $1.3\mu\text{m}$. In addition, a simple technique for reducing the depolarisation loss due to thermally-induced birefringence has also been described, which is suitable for use in low gain and quasi-three-level end-pumped lasers. The combination of this resonator design strategy and technique for compensating thermally-induced birefringence should facilitate further brightness scaling of end-pumped solid-state lasers with a linearly-polarised output.

8. ACKNOWLEDGEMENTS

This work was funded by the Engineering and Physical Sciences Research Council.

9. REFERENCES

1. W. A. Clarkson and D. C. Hanna, "Two-mirror beam-shaping technique for high-power diode bars," *Optics Letters*, Vol. 21, pp375-377, 1996.
2. W. A. Clarkson, R. Koch and D. C. Hanna, "Room-temperature diode-bar-pumped Nd:YAG laser at 946nm ," *Optics Letters*, vol. 21, pp737-739, 1996.
3. W. L. Nighan, D. Dudley and M. Keirstead, "Diode-bar-pumped Nd:YVO₄ lasers with $>13\text{W}$ TEM_{00} output at $>50\%$ efficiency," *Conference on Lasers and Electro-Optics*, Vol. 15, OSA Technical Digest Series, (Optical Society of America, Washington, D.C.), p17, 1995.
4. S. C. Tidwell, J. F. Seamens, M. S. Bowers and A. Cousins, "Scaling cw diode-end-pumped Nd:YAG lasers to high average powers," *IEEE Journal of Quantum Electronics*, vol 28, pp997-1009, (1992).
5. U. Brauch, A. Giesen, M. Karszewski, C. Stewe and A. Voss, "Multiwatt diode-pumped Yb:YAG thin disc laser continuously tunable between 1018 and 1053nm ," *Optics Letters*, vol. 20, pp713-715, 1995.
6. M. E. Innocenzi, H. T. Yura, C. L. Fincher and R. A. Fields, "Thermal modeling of continuous-wave end-pumped solid-state lasers," *Applied Physics Letters*, vol. 56, pp1831-1833, 1990.
7. W. A. Clarkson and D. C. Hanna, "Resonator design considerations for efficient operation of solid-state lasers end-pumped by high-power diode-bars," in *NATO Advanced Workshop Series; Optical Resonators*, (Kluwer Academic Publishers, The Netherlands), 1998.
8. M. A. Kern, W. A. Clarkson and D. C. Hanna, "Resonator design considerations for high-power TEM_{00} operation of a Nd:YAG laser at $1.3\mu\text{m}$ end-pumped by a diode-bar," in *Technical Digest of Conference on Lasers and Electro-Optics* (Optical Society of America, Washington, DC), vol. 11, paper CTuE4, p479, 1997.
9. W. C. Scott and M. de Wit, "Birefringence compensation and TEM_{00} mode enhancement in a Nd:YAG laser," *Applied Physics Letters*, vol. 18, p3, 1971.
10. W. Koechner, *Solid-State Laser Engineering*, Springer-Verlag, New York, p.409, 1996.

High power laser diodes, laser diode modules and their applications

F. Daiminger, F. Dorsch, D. Lorenzen

JENOPTIK Laserdiode GmbH, Prüssingstr. 41, D-07745 Jena (Germany)

ABSTRACT

High power laser diodes and especially high power laser diode modules made enormous progress in the last few years. Different aspects of high power laser diodes are treated starting from general description of high power laser diodes and their mounting techniques, characterising the electro-optical behaviour of single laser bars and finally presenting beamshaping optics for the collimation of large modules. The later technique allows for symmetrical focal spots in the kilowatt range with a beam quality of about 170 mm*mrad. Different aspects of current applications of high power laser diodes are presented.

Keywords: Diode laser, laser beam shaping, fibre coupling, micro optics, heatsink, stack

1. INTRODUCTION

In recent years the improvement of the performance of high power diode lasers has been enormous. The output power of commercially available diode lasers increased by nearly a factor of three in the last three years accompanied by an increase of the reliability. Both developments lead to a strong decrease of the prices for high power diode lasers. Along with the advantages of high efficiency, small size and easy operation they get more and more attractive for commercial applications. The substitution of flash lamps for pumping of solid state lasers was one of the main applications of high power diode lasers in the last years. But as the output power increases and new techniques for beam shaping of the strongly asymmetric beam profile of high power diode lasers are developed direct applications are more and more of interest like in medicine or in material processing.

One of the main problems one faces when dealing with high power diode lasers are removing thermal heat and at the same time applying high electrical currents. Special actively cooled heatsinks had to be developed to handle thermal heat flow densities of about 2 kW/cm². In order to achieve optical output powers of several hundreds up to some kilowatts necessary for direct application in material processing techniques have been developed to arrange several heatsinks as a stacked array. Still the power densities obtained by this architecture would be too low for material processing. A complex system of beam shaping optics is necessary in order to focus the output power of several tens of laser bars down to one focus point gaining power densities in the range of several kW/cm² even at cw operation.

2. DESCRIPTION OF HIGH POWER DIODE LASERS

Although there is no unique definition of high power diode lasers in this paper we restrict to diode lasers having the form of so called laser bars. Here several tens of emitters are arranged in a monolithic semiconductor element as shown in Fig. 1. which has a length of about 10 mm. The width of each emitter usually ranges between 60 µm and 200 µm. Each emitter itself may be designed as a broad area laser or a phase coupled striped array laser. The stripes are in the range of some µm. Filling factors of the emitters on the laser bar range between 30 % and 50 % for cw operation and are increased to 90 % for qcw operation. The total height of the laser bar is about 100 µm with a resonator length between 600 µm and 1 mm.

The active region of the emitters consist of single or double quantum well structures mainly based on GaAs, emitting laser radiation in the wavelength range between 790 nm and 980 nm. Visible high power diode lasers in the form of laser bars are already under investigation but have not yet entered commercial applications due to reliability problems¹. The total height of the emitting region (perpendicular to the pn-junction) is approximately 1 µm (Fig. 1) and the radiation is nearly single-mode in respect to this direction which is generally called the fast axis. Due to diffraction at this roughly 1 µm high output window the radiation is highly divergent with angles up to 100°. In the other direction parallel to the pn-junction

(slow axis) the emitted radiation is highly multi-mode with angles in the range of 10° . The single emitters on a laser bar are optically isolated and superimpose incoherently in the farfield. Thus the emitted radiation of high power diode lasers is highly asymmetric with different dimensions and divergence angles in the fast and slow axis.

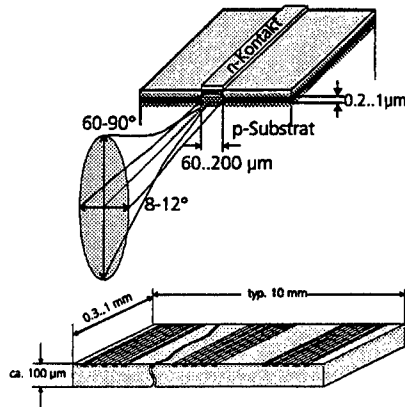


Fig.:1 Scheme of a high power diode laser. The emitted radiation is highly asymmetric in the slow and fast axis. The active region has a width of about $1 \mu\text{m}$.

On a laser bar with a typical width of about 10 mm several tens emitters are arranged.

3. MOUNTING OF HIGH POWER DIODE LASERS

The specific problems that arise when mounting high power diode lasers are due to the large geometry of the laser bar and the fact that at the same time one has to remove large quantities of dissipation heat and apply high currents through the same interface with a flux density of about 2 kA/cm^2 for commercial 30 W lasers. Dissipation heat for such lasers lies in the range of 50 - 60 W resulting in a heat flux density of about 2 kW/cm^2 . Currently only soldering techniques can provide the quality that is needed for thermal and electrical contact between laser bar and heatsink. In order to get the best thermal contact laser bars have to be mounted junction side down. This causes special problems since the active region in the laser bar is as close as about $3 \mu\text{m}$ to the soldered interface. The solder materials that are used can be divided into two categories namely soft solders like In or PbSn and hard solders like AuSn. Using the latter one great care has to be taken that the thermal expansion coefficient of the heatsink is similar to that of the laser bar. Otherwise the large geometry of the laser bar would lead to high stress which would cause defect growth resulting in reduced lifetime of the laser. Heatsink materials like CuW, CuMo which fulfil these requirements have low thermal conductivity (170 W/mK for both) and limit the performance of high power diode lasers. Soft solders on the other side allow some differences between the thermal expansion coefficients of both constituents. So copper differing significantly in its expansion coefficient (16.5 ppm/K) from that of GaAs (6.5 ppm/K), with a much better thermal conductivity (400 W/mK) can be used as heatsink material.

Mounting a laser bar on a pure copper block with a height of about 5 mm which is attached to some cooling plate with constant temperature would result in an overall thermal resistance of about 0.8 k/W . That means for lasers with output powers of 30 W the junction temperature would increase for about 44 K. To get high reliability with high power diode lasers the operating junction temperature should be about 50°C . To improve the thermal resistance micro channel techniques first developed for silicon heatsinks², can be applied to copper³. The principle of such a design is shown in Fig.2. Small micro channels with a width between $100 \mu\text{m}$ and $300 \mu\text{m}$ and a height between $300 \mu\text{m}$ and $600 \mu\text{m}$ are located closely below the laser bar. Such micro channel coolers can be used with and without heatspreaders. In the latter case a final copper layer of some 100 microns acts as a heatspreader.

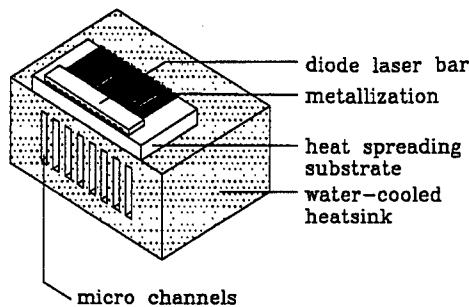
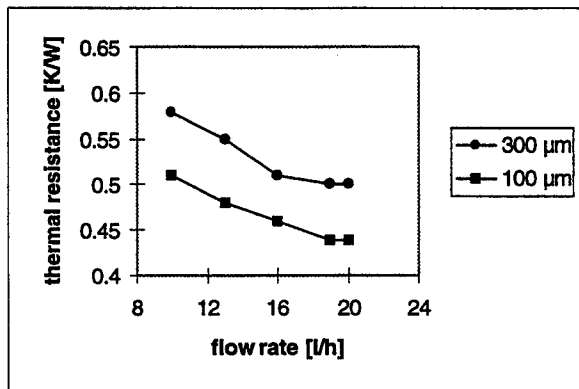


Fig. 2: Principle of a copper micro channel heatsink. The width of the channels is between $100\ \mu\text{m}$ and $300\ \mu\text{m}$. The height of the fins are between $300\ \mu\text{m}$ and $600\ \mu\text{m}$. Copper micro channel coolers can also be used without heatspreaders. In this case a final copper layer serves for that purpose.

In Fig. 3 the dependence of the thermal resistance on the water flow rate is shown for two different widths of the micro channels, namely $100\ \mu\text{m}$ and $300\ \mu\text{m}$. For all flow rates the thermal resistance of the smaller micro channels is lower by about $0.6 - 0.7\ \text{K/W}$. Increasing the flow rate from $10\ \text{l/h}$ to $20\ \text{l/h}$ leads to a reduction in the thermal resistance by about 15% . For both structures there is a saturation of the thermal resistance at flow rates of about $20\ \text{l/h}$. The lowest value obtained for the $100\ \mu\text{m}$ broad micro channel heatsink is $0.44\ \text{K/W}$.

Fig. 3: Dependence of the thermal resistance of a copper micro channel cooler on the flow rate for two different channel widths ($100\ \mu\text{m}$ and $300\ \mu\text{m}$).



For special applications, e.g. in printing industry, single addressing of the different emitters on a laser bar is of great interest⁴ to increase printing speed by parallel processing. Supposed that the p-side metallization of the laser bar is electrically isolated between single emitters single addressing can be achieved by a structured metallization of the heatsink as shown in Fig. 4. The structured metallization is attached to an AlN substrate that allows for an electrical isolation between the metal stripes and which is soldered onto a copper heatsink. A laser bar with 25 emitters was soldered in that way that each emitter was electrically contacted with one metal stripe. The overall thermal resistance of such a module is a function of the number and the location of the emitters which are turned on. As long as emitters are far away from one another and have no exchange the thermal resistance simply decreases with the number of turned on emitters n by $1/n$. As soon as the emitters get so close that an emitter heats its neighbour and vice versa, called the thermal cross talk, this simple relation does no more hold true. Fig. 5 shows the result of an experiment where different numbers of emitters were switched on in that way that they were equally spaced across the laser bar. That means with increasing number of switched on emitters the spacing between neighbouring emitters got smaller. For comparison the theoretical curve giving the expected thermal resistance in the case of no thermal cross talk is included as a solid line. It is clearly seen that already for four emitters switched on there is a significant thermal cross talk. For more than 10 emitters there is even a saturation in the thermal resistance.

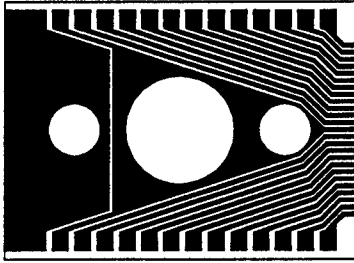


Fig.4 Structured metallization on an AlN substrate, which is soldered on a copper heatsink. Thus it is possible to address single emitter son a laser bar which is mounted p-side down

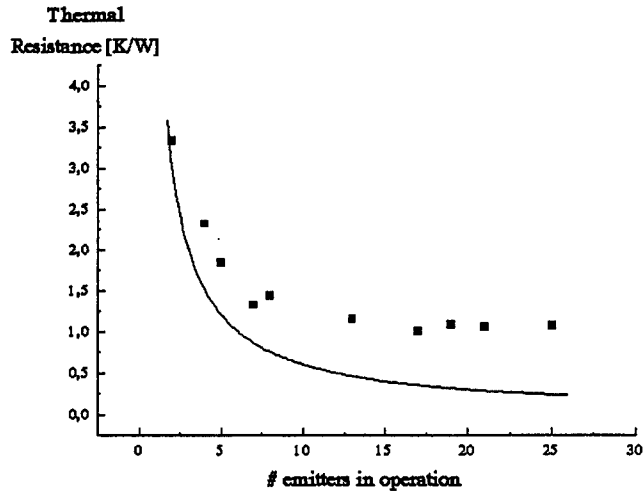


Fig.5 Total thermal resistance of a single addressable laser bar in dependence of the number of emitters which are switched on. The switched on emitters were equally spaced across the laser bar. The solid line represents a theoretical caculation assuming no crosstalk.

4. ELECTRO-OPTICAL CHARACTERISTICS OF HIGH POWER LASER DIODES

Currently commercially available high power diode lasers in the wavelength range between 800 nm and 980 nm have output powers in the range of 30 W if lifetimes beyond 10.000 h are required. For lower reliability requirements of only some thousands of hours it is possible to drive commercial high power diode lasers at optical output powers in the range of 50 W.

In Fig. 6a the P-I characteristics for an GaInAsP/GaInP high power laser diode at 808 nm with a filling factor of 30% (150 μm emitter width, 500 μm spacing) is given. The laser is mounted on an actively cooled copper heatsink with a thermal resistance of 0.42 K/W. At a water cooling temperature of 25 $^{\circ}\text{C}$, which is a common one in commercial applications, a maximum output power of 103 W was obtained at a current of 120 A with a wall plug efficiency of about 50 %. The external quantum efficiency is constant for currents up to 60 A with a value of 1.07 W/A. The bending of the P-I characteristics for higher characteristics is a pure thermal effect and can be modelled with a T0 value of 110 K and a T1 value of 360 K which are characteristic for this material. The optical density at the output facets was 8.6 MW/cm^2 and no COD (catastrophic optical damage) could be observed. So by better cooling the output power could be shifted to even higher powers.

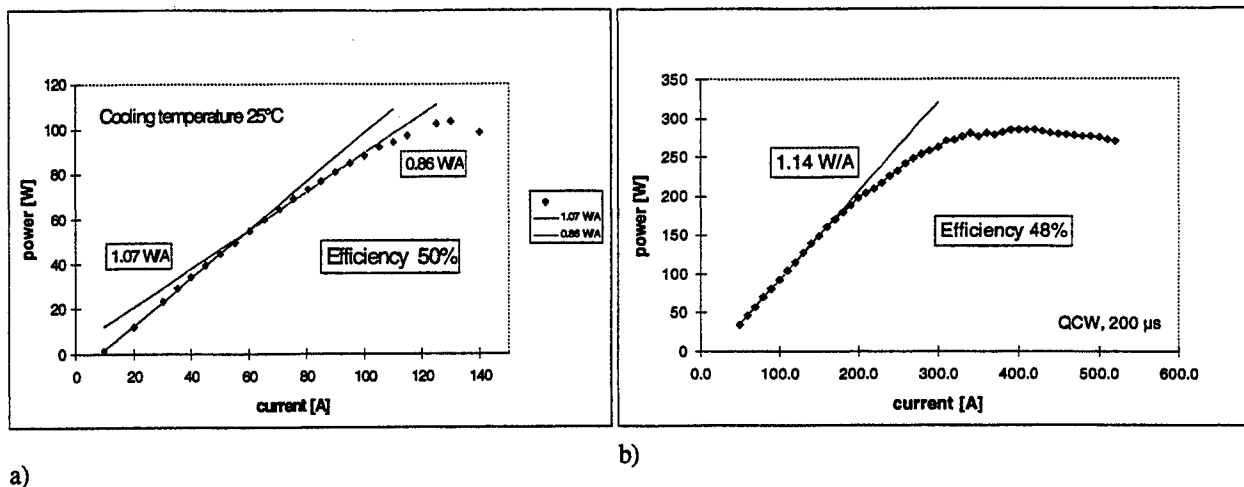


Fig. 6 a) P-I characteristics in cw mode of a GaInAsP/GaInP high power diode laser at 808 nm with a filling factor of 30% (150 μm emitter width, 500 μm spacing), mounted on a copper micro channel cooler. b) P-I characteristic of a similar laser as in a) except that the filling factor is 30 %.

In Fig. 6b the P-I characteristics of a qcw laser bar with a filling factor of 90% also based on GaInAsP/GaInP with the 150 μm wide emitters is shown. The maximum power achieved is 280 W at a current of about 350 A at pulses of 200 μs and a repetition rate of 3 Hz. The slope up to 200 A is linear with a value of 1.14 W/A. The bending for higher currents was not due to degradation and could be reproduced several times.

The serial resistance for high power diode lasers lies between about 2.7 mOhm and up to 8 mOhm. As the operation current is increasing more and more the serial resistance may represent a substantial heat source limiting the lifetime of the laser.

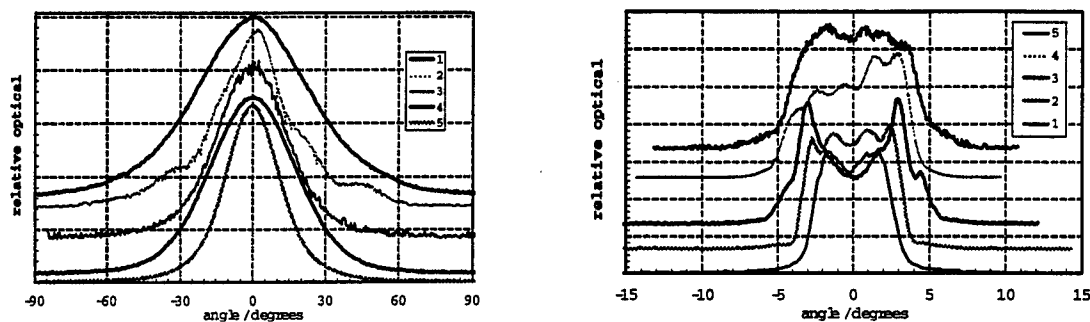
The spectral width of the emitted radiation typically lies between 1.5 nm and 3 nm FWHM for broad area high power lasers. As the centre wavelength of diode lasers is temperature dependent, with rates of 0.25 - 0.33 nm/K for high power diode lasers, inhomogeneities in the thermal contact along the laser bar will be directly represented in the spectral width of the emission.

The far field of the emission from high power diode lasers is very complicated and still there exists no standardisation for this characteristic feature. Usually the far field is described by the angular distribution of the emission, but there is no unique definition for the parameter 'angular width'. In the following part of the paper we will describe the angular distribution by using essentially three different types of possible definitions. (1) The angular width is given by the second moment width for the angular distribution in analogy to the beam width in ISO11146. (2) Two different level-dependent widths definitions may be used based on the full width at half maximum (FWHM) and the full width at $1/e^2$ -level. (3) The width may be determined by different power contents (86.5 %, 95% and 99%) calculated by integrating the recorded curves.

In Fig. 7a. the angular distribution along the fast axis is shown for different types of high power diode lasers. The height of the light emitting zone in this direction is small (approx. 1 μm) and often the radiation is assumed to be diffraction limited. In practice there seem to be contributions from higher modes and the shape deviates from Gaussian or Lorentzian. From each data set different types of 'widths' are calculated as defined above and the results are summarised in table 1a. In general, there is no unique relationship between the commonly given level-based widths and the power content or the 2nd moment width. Only for Gaussian-shaped distributions (e.g. no. 1 in fig. 7a) 2nd moment width, 95%-power content width and $1/e^2$ -width are equal. As soon as the shape deviates from a Gaussian this does not hold true any more. From the often used FWHM one cannot predict the angle that includes a certain percentage of the emitted power. In most cases the 95% width is larger than expected from a Gaussian profile of the same FWHM.

In Fig. 7b. the angular distribution of the emission along the slow axis is given for the same lasers as in Fig. 7a. As the emission is multi-mode in this direction and the emitter is wide, the radiation is not diffraction-limited but a superposition of many modes. (For laser bars that consist of many individual emitters it is even an incoherent superposition of the radiation of the emitters.) The shape of the profile may vary strongly: from near flattop to the typical double lobe pattern of single phase-coupled arrays (no. 3 in fig. 8). But in any case it is somewhat 'rectangular-shaped' with slopes of different steepnesses.

Level-dependent widths do not vary very much with the selected level for profiles of this shape (ref. tab. 1b). The FWHM is close to the 86.5% power content width, whereas the $1/e^2$ -width is generally larger than the 86.5 %-width. But again, there is no unique correlation and without knowledge of the shape the power content cannot be derived from a level based width.



a)

b)

Fig. 7 Angular distributions of the fast axis emission (a) and for the slow axis (b) for different types of high power diode laser bars.

N	2nd moment	power content		width at level	
		86.5%	95%	FWHM	$1/e^2$
1	104.5°	75.0°	101°	53.5°	101.5°
2	90.0°	65.7°	89.1	30.7°	75.4°
3	85.6°	55.2°	85.9	33.2°	65.7°
4	80.5°	55.5°	75.0	41.0°	74.0°
5	65.4°	40.5°	60.0	25.5°	50.0°

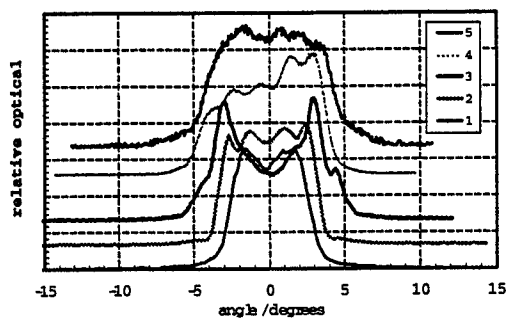
a)

N	2nd moment	power content		width at level	
		86.5%	95%	FWHM	$1/e^2$
1	12.5°	8.4°	11.5°	8.4°	11.8°
2	11.1°	7.6°	9.0°	7.8°	9.7°
3	13.1°	8.4°	10.2°	7.3°	10.5°
4	9.1°	5.4°	6.4°	6.2°	7.2°
5	9.2°	4.8°	6.4°	5.0°	6.8°

b)

Table 1 Comparison of different fast axis widths (a) and slow axis widths (b) of various diode lasers given in Fig. 7.

Especially the emission characteristics of the slow axis of a diode laser may strongly depend on the operating current or the output power, respectively. Fig. 8 shows an example for the variation of shape as well as for the variation of the widths with the driving current. As a consequence the usable fraction of optical power within an aperture might depend on the operating conditions. The supplier of diode lasers should give information on the operating current when specifying a slow axis width.



current A	2nd moment	power content			width at level	
		86.5%	95%	99%	FWHM	1/e ²
15	7.8°	4.4°	5.2°	6.0°	5.4°	6.2°
25	9.9°	6.0°	7.2°	8.8°	6.8°	8.6°
30	10.9°	7.0°	8.6°	10.0°	7.8°	9.8°
35	11.6°	7.4°	8.8°	10.4°	8.2°	10.2°
40	11.8°	8.0°	9.0°	11.0°	9.2°	10.6°

Fig. 8 Angular slow axis profile of one diode laser at different operating currents. The corresponding widths are listed in the table on the right side.

5. STACKED HIGH POWER DIODE LASER ARRAYS AND BEAMSHAPING

Up to now only single laser bars were treated. A wide field of application will be open if the output power of high power diode laser modules could be increased to some kilowatts with power densities in the range of 4-20 kW/cm². A technique to reach that goal is to stack several diode lasers one above the other as shown schematically in Fig. 9. The power densities without any additional optics depends on the height of the heatsink which currently lies between 1.2 mm and 2 mm. Stacking techniques for cw high power diode lasers currently can only be carried out with actively cooled heatsinks. It is then possible to connect the heatsinks in parallel concerning the cooling water, so that each laser gets cooling water with the same temperature. At the moment it is possible to stack up to 25 lasers without any visible influence on the performance and the homogeneity of the cooling.

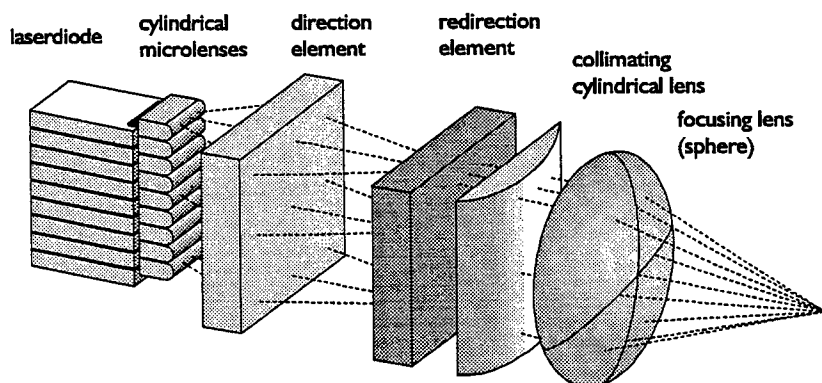


Fig. 9 Schematic view of the beamshaping of high power laser diode stacks. First cylindrical microlenses collimate the radiation of each single laser diode in the stack. The director and the succeeding redirector element make a beam transformation which improves the BPP of the slow axis and make that of the fast axis worse (see text). Finally with a macroscopic cylindrical lens and a spherical lens the laser radiation is focused.

For certain applications (chapter 4) power densities achieved with simple stacking of the laser diodes are not sufficient. A simple collimation of the radiation of the stack by macroscopic lenses would not lead to an optimum result, as the 'dark lines' between the single laser bars given by the height of the heatsinks and the 'dark gaps' between the single emitters on a laser bar strongly increase the Beam Parameter Product (BPP) of the whole stack. The best result could be obtained by an optical scheme which first rearranges the emitters all over the stack so that all dark areas are removed, collimates each single emitter in both axis and finally collimates the shaped beam with macroscopic optics. As the BPP for each emitter in the laser stack is strongly different in the fast (nearly diffraction limited) and the slow axis (about 450 mm*mrad), a refined rearrangement of the emitters has to be realised in order to receive a symmetrical beam.

The realisation of any beamshaping of diode laser stacks always starts with the collimation of the highly divergent radiation in the fast axis by a cylindrical micro lens (Fig.9). Currently best results are obtained with high refractive index aspheric lenses which allow the collimation of the fast axis to 5 to 10 mrad at a beam height of 0.6 mm with high efficiency (> 90 %), equivalent to a BPP of 0.8 to 1.5 mm*mrad. In a second step the rearrangement of the emitters has to be carried out. In the following we will describe a variation of a method originally designed for beamshaping of single laser bars⁵. The principle of this design is shown in Fig. 10a where the nearfield after collimation of the fast axis is schematically depicted. Each laser bar in the stack is divided into three parts which undergoes special rearrangement. The left and the right part are relocated above and below to the middle part respectively. Calculating the BPP in the slow axis shows that it is improved by a factor of three. At the same time in the fast axis it is degraded by a factor of three. Thus the resulting beam is more symmetrical. Supposed now that the pitch in the stack between individual laser bars is three times the height of the beam after collimation the 'dark lines' in the transformed stack are removed.

Technically the transformation is achieved by two succeeding elements called director and redirector as shown schematically in Fig. 10 b. The director is made of two macroscopic prisms and one parallel plate causing different deflecting for the left, inner and right part of all laser bars in the stack. At the redirector all the deflected beams overlap but have different incident angles, so that without additional optics the beam would strongly diverge. The redirector element which consists of an array of prisms deflects each single beam in such a way that all beams are parallel after the redirector. After this transformation optics a macroscopic cylindrical lens collimates the slow axis and a final spherical lens focuses the laser beam.

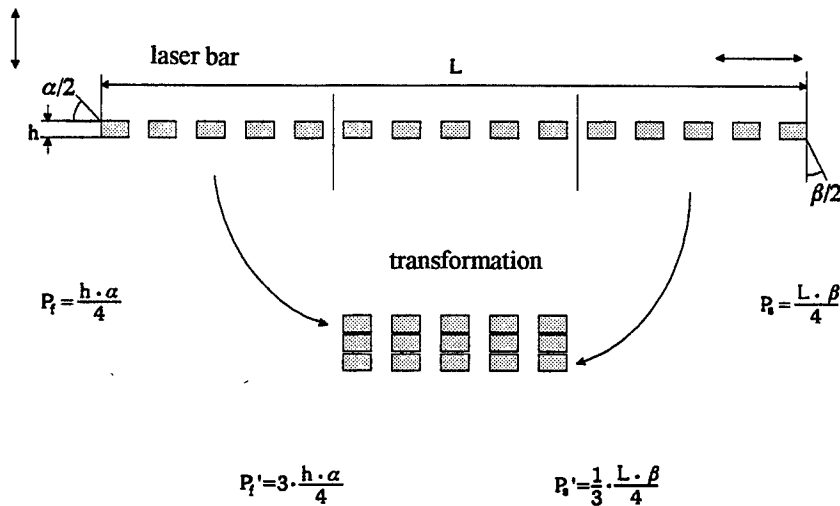


Fig. 10 Principle of the beam transformation that improves the BPP of slow axis and make that of the fast axis worse. The rectangular shaped boxes represent the nearfield of the single emitters after the fast axis collimation with microlenses. The beam transformation relocates the left part of the bar above and the right part of the bar below the inner part of the laser bar.

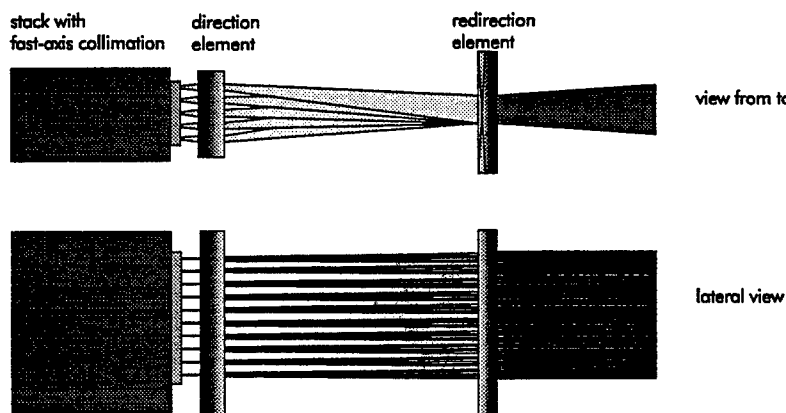


Fig. 10b Application of the principle shown in Fig. 10a to a laser stack. Instead of deviding the laser bar into three pieces as in Fig. 10a here the technique is varied and devides each laser bar into fife parts. The director and the redirector are technically realised by prisms.

In Fig. 11 the beam propagation of a stacked device with 25 elements using the above described transformation optics is shown. The final focusing lens had a focal length of 250 mm. In both axis the width of the spot was about 4 mm at a similar divergence angle of about 85 - 90 mrad for both axis. So for both axis a symmetric BPP of about 170 mm*mrad is obtained. The output power of this system lies in the range of 600-700 W with. The efficiency of the beam transformation optics is in the range of 65%.

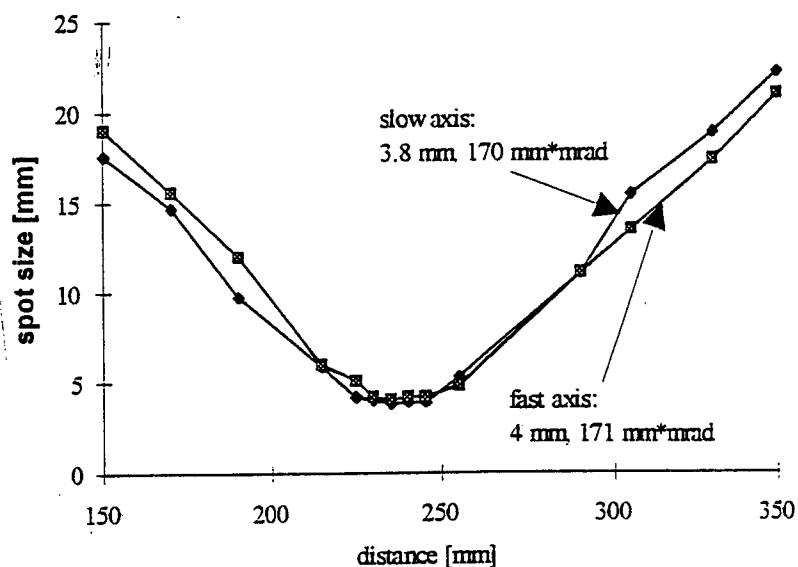


Fig. 11 The beam propagation of a stack with 25 elements being focused after the above described beam transformation optics. The final focusing spherical lens has a focal length of 250 mm. The spot obtained has a diameter of about 4 mm in both directions and a BPP of about 170 mm which is also nearly equal in both direction.

In order to increase the output power of diode laser modules polarisation coupling of two beamshaped modules is possible. In Fig. 12 the P/I characteristics of such a module consisting of two 25 element stacks is shown which has the same BPP as the single stack module shown above. The P/I characteristics is linear and a maximum output power of about 1350 W was obtained at a current of 53 A after a circular pinhole with 5 mm diameter.

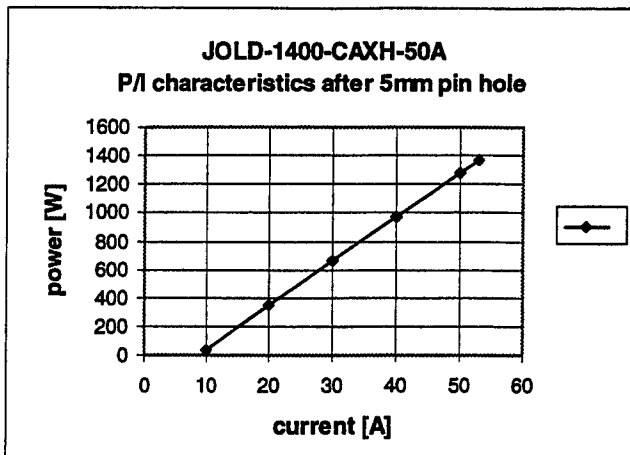


Fig. 12 P-I characteristics of a module consisting of two 25 diode laser stacks being polarisation coupled. The radiation of each stack was beam shaped with the above described optics. The power was measured after a pinhole with a diameter of 5 mm.

6. APPLICATION OF HIGH POWER DIODE LASERS

The main areas for application of high power diode lasers are medical applications, material processing and pumping of solid state lasers. The later one being the largest in volume in the last few years. The intention was mainly to simply substitute flash lamps in existing designs of solid state lasers and to take advantage of better overall electro-optical efficiencies and ease of operation. More and more special designs of solid state lasers emerge which take care of the characteristics of high power diode lasers and some of them even can only be pumped with diode lasers. A design using low loss diffuse reflectivity pumping chamber^{6,7} is perfectly adapted to the easy to scale stacked array technique for high power diode lasers and combines this with the proved rod laser geometry. Another solid state laser design which can only be pumped with diode lasers is the new concept of the thin-disk laser⁸ which provides high efficiency, good beam quality and easy scalability. Due to the thin absorbing disk of only about 300 μm the pump beam must transmit the crystal several times. Thus good beam quality of the pump source is required.

As the output power increases and due to refined beam shaping techniques beam quality of high power diode lasers improve direct material processing becomes more and more important as an application of high power diode lasers. Applications here are printing and marking, soldering, welding of plastics and hardening of metals. The applications given are listed according to the required optical power and beam quality which is highest for the latter one. The highest requirements will be for applications in the field of metal sheet welding and metal sheet cutting, where output powers of some kilowatts at a beam quality of about 10 mm*mrad are needed.

A special application for direct material processing is surface treatment. With pulsed high power diode systems of 1.3 kW, focused down to a spot of 1mm it is possible to remove oxidised aluminium, or to remove dispersion colours or red lead oxide from calcium sulphate. Even burned in screen print colours on motor car safety glasses could be removed⁹.

7. SUMMARY

It was shown that using refined cooling techniques with copper micro channel coolers cw output powers as high as 103 W and qcw output powers of 280 W per bar are possible. Special mounting techniques allow for single addressing of the

emitters of high power laser diode bars. The angular distribution of the emitted radiation of high power diode lasers was investigated and different possibilities for characterising the farfield behaviour was presented. A new beamshaping technique for high power laser diode modules was described which allows for symmetrical focal spots with optical powers of 1300 W and a beam quality of about 170 mm*mrad.

ACKNOWLEDGEMENT

We would like to thank our colleagues at JENOPTIK Laserdiode for their support.

REFERENCES

1. P. Savolainen, M. Pessa, S. Heinemann, F. Daiminger, 'High power visible laser diode arrays', Proceed. LEOS'96, p. 276, 9th. annual meeting, 18.-21. Nov. 1996, Boston.
2. R. Beach, 'Modular microchannel cooled heatsinks for high power laser diode arrays', IEEE J. Quant. Electr., vol.28, no4, pp 966-976, 1992.
3. T. Ebert, H. Treusch, P. Loosen, R. Poprawe, 'Optimization of microchannel heatsinks for high-power diode lasers in copper technology', SPIE Proc. vol. 3285, pp. 25 - 29.
4. R. Bringans, 'Lasers for printing', Technical Digest Conference on Lasers and Electro-Optics, May 18-23, 1997, p. 174.
5. R. Göring, P. Schreiber, T. Poßner, 'Microoptical beam transformation system for high-power laser diode bars with efficient brightness conservation', SPIE Proc. 3008 (M.E. Motamedi, L.J. Hornbeck, K.S. Pister, eds.), pp. 202-210, 1997.
6. T. Brand, Opt. Lett. 20 (1995), p. 1776.
7. T. Brand, I. Schmidt, 'Design and performance of a compact 600 W cw Nd:YAG rod laser system pumped by microchannel-cooled stacked diode laser arrays', Technical Digest Conference on Lasers and Electro-Optics Europe, Sept. 8-13, 1996, p. 4.
8. A. Giesen, U. Brauch, I. Johannsen, M. Karszewski, C. Stewen, A. Voss, Advanced Solid State Lasers, S.A. Payne, C. Pollock, eds., Vol. 1 of OSA Trends in Optics and Photonics Series (Optical Society of America, Washington, D.C., 1996), Vol. 1, pp.11ff.
9. Fraunhofer Institut, Werkstoff- und Strahltechnik, Winterbergstr. 28, Dresden, Rochler et. al., private communications.

1.5- μ m Diode-Pumped Erbium-Ytterbium Glass Lasers

P. Laporta ^{a*}, S. Taccheo ^a, S. Longhi ^a, O. Svelto ^a, C. Svelto ^b, and G. Sorbello ^b,

^a INFM - Dipartimento di Fisica del Politecnico di Milano
Centro di Elettronica Quantistica e Strumentazione Elettronica del CNR
Piazza Leonardo da Vinci 32, 20133 Milano, Italy

^b INFM - Dipartimento di Elettronica e Informazione del Politecnico di Milano
Centro di Studio sulle Telecomunicazioni Spaziali del CNR
Piazza Leonardo da Vinci 32, 20133 Milano, Italy

ABSTRACT

In this paper we present recent results obtained by our group on diode-pumped bulk erbium-ytterbium lasers. Modeling of the active material is first presented to outline design criteria for the optimization of laser cavities. Different operating regimes and particular properties of these novel laser devices are subsequently analyzed and discussed, including single-frequency operation, frequency tuning, intensity and frequency stabilization, mode-locking and frequency-modulation operation. Due to the high performance in terms of emission characteristics, these lasers are attractive for a large number of applications and, in particular, for optical communications in 1530-1570 nm wavelength region.

Keywords: Erbium laser, Diode-pumped lasers, Single-frequency tunable lasers, Microchip lasers, Frequency-stabilized lasers, Picosecond-pulse generation, Mode-locked Er-Yb laser, Intracavity frequency modulation, Optical communications.

1. INTRODUCTION

The erbium glass laser attracted much interest since its first operation in the pulsed regime in 1965¹, in particular for telemetry and laser ranging applications, due to its emission at the eye-safe wavelength of 1530 nm. More recently, with the development at the end of 1980s of the InGaAs laser diodes emitting at 980-nm wavelength², laser physicists have in particular been actively considering continuous wave laser oscillators based on Er³⁺ doped glasses and optical fibers. This interest was also stimulated by the successful operation of the erbium-doped fiber amplifier (EDFA) pumped at 980 nm wavelength³, which rapidly turned out to be a key component in all modern optical

* Correspondence: P. Laporta; Email: Paolo.Laporta@PoliMi.IT; Telephone: +39-02-2399-6151; Fax: +39-02-2399-6128. Other author information: S. T.; Email: Taccheo@axp7000.cdc.PoliMi.IT; Telephone: +39-02-2399-6167; Fax: +39-02-2399-6128. S. L.; Email: Stefano.Longhi@PoliMi.IT; Telephone: +39-02-2399-6156; Fax: +39-02-2399-6128. O. S.; Email: Orazio.Svelto@PoliMi.IT; Telephone: +39-02-2399-6143; Fax: +39-02-2399-6128. C. S.; Email: Cesare.Svelto@PoliMi.IT; Telephone: +39-02-2399-3610; Fax: +39-02-2399-3413. G.S.; Email: Gino.Sorbello@PoliMi.IT; Telephone: +39-02-2399-6114; Fax: +39-02-2399-6126. Partially supported by a grant from the Italian National Research Council under «Progetto Finalizzato Tecnologie Elettroottiche» and «Progetto Strategico Materiali e Dispositivi per Optoelettronica».

transmission systems. In the last few years many authors have successfully demonstrated pulsed as well as continuous wave (cw) operation of erbium ion in different hosts; the best laser performance has been obtained so far with erbium-doped and ytterbium sensitized doped glasses⁷.

In this paper we present recent results of the work done by our group on diode-pumped bulk Er-Yb lasers, with particular emphasis toward devices of potential interest for optical communication applications. Different operating regimes of this novel laser will be described and discussed. The paper is organized as follows. In Section 2 we discuss a simplified model, based on a rate equation analysis, useful for design and optimization of end-pumped miniaturized cavities. In Section 3 we present the experimental results obtained with different devices in continuous-wave operation, under the single frequency regime, and we analyze the tuning properties of these Er-Yb lasers. Section 4 is devoted to the study of Er-Yb lasers in pulsed operation under different operating regimes suitable to generate high-bit-rate picosecond pulse trains. In Section 5 we analyze the amplitude noise properties of these optical oscillators, we report on active intensity noise suppression, and we describe frequency stabilization and locking of Er-Yb lasers to molecular lines of acetylene, to obtain absolute frequency references for wavelength division multiplexing applications.

2. MODELING OF THE ACTIVE MATERIAL

Spectroscopic properties of the erbium ion in several glass hosts have been the object of extensive investigations^{8,9}. Erbium-doped glasses act as three-level systems at 1.5 μm and codoping with ytterbium is the most effective way to enhance the absorption and pumping efficiencies^{6,10}, particularly in the case of very short cavity length devices (e.g. bulk microlasers or particular fiber lasers). In fact, this indirect pumping process, which is based on an energy-transfer mechanism from ytterbium to erbium ions, allows for very short absorption lengths, obtained by increasing Yb concentrations, still keeping low pump thresholds. In this section we will focus on the erbium-ytterbium doped phosphate glass, which appears to be the best active material for bulk lasers having a very high phonon energy and, consequently, a higher energy-transfer efficiency.

Figure 1 shows a simplified energy level diagram of the Er-Yb laser system and the processes of main interest for pumping in the 980-nm band and for laser action. A complete list of these phenomena include radiative absorption and emission, with absorption arising both from ground (GSA) and excited state (ESA)⁸, energy-transfer and non-radiative decay^{10,11}, cooperative up-conversion¹¹, ions pair formation and clusterization¹². Most of these processes have been carefully investigated by several authors and many rates have been theoretically as well as experimentally determined in different glass hosts^{12,13}. As already analyzed in a previous work¹⁴, a rate-equation system which takes into account all the above processes is heavy to be managed. It can be shown, however, that a few phenomena can be neglected on the basis of their weak influence on the behaviour of Er-Yb bulk laser devices, namely clustering, ion pair formations and ESA. According to the lettering of the scheme in Fig. 1, the processes which are thus of major concern for modeling the Er-Yb laser systems are the following: (a, b) Radiative absorption and emission of a pump photon from $F_{7/2}$ and $F_{5/2}$ ytterbium levels, respectively. (c) Spontaneous decay from $F_{5/2}$ ytterbium level. (d) The Yb to Er, $\text{Yb}(F_{7/2}) + \text{Er}(I_{15/2}) \rightarrow \text{Yb}(F_{5/2}) + \text{Er}(I_{11/2})$, transfer process, that acts as indirect pumping of Er ions. (e) Erbium non-radiative decay from the $I_{11/2}$ level to the $I_{13/2}$ upper laser level. (f, g) Stimulated emission and absorption between $I_{13/2}$ upper and $I_{15/2}$ ground Er laser levels. (h) Erbium spontaneous decay from $I_{13/2}$ level. (i) Cooperative up-conversion (UC) process between two excited Er ions that promotes one ion to the $I_{9/2}$ upper level, while the

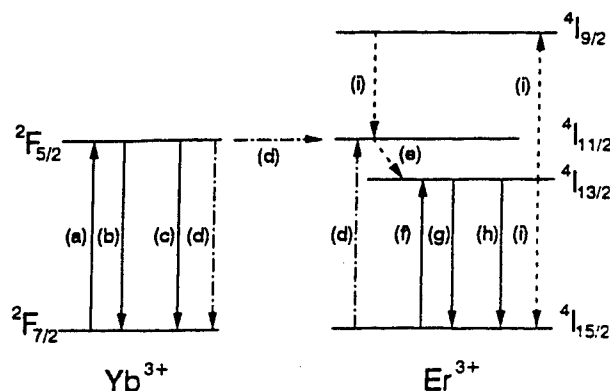


Fig. 1 Energy level diagram of the erbium-ytterbium system. The letters refer to the processes discussed in the text. The solid-line arrows refer to radiative phenomena, the dashed-dot arrows to Er-Yb energy transfer process and the dashed arrows to non-radiative transitions.

second ion decays to the ground level. The first ion then relaxes, through a fast non-radiative decay, to its original $I_{13/2}$ state so that the overall effect is the loss of one, $I_{13/2}$, excited ion. Note that a uniform UC can be assumed¹⁴.

On the basis of the assumptions and approximations previously discussed, a simplified system of rate-equations can readily be written¹⁴. Further simplifications can be introduced to make more manageable this system: (i) Due to its fast non-radiative decay, the $I_{11/2}$ level is assumed empty for cw operation. (ii) The $I_{9/2}$ level can be also considered empty due to its fast non-radiative decay. It follows that the sum, $N_{1Er} + N_{2Er}$, of erbium populations in the lower and upper laser levels reduces to the total Er concentration, N_{Er} . (iii) Direct absorption of pump radiation by ground state Er ions is neglected, due to its negligible rate compared to the energy-transfer rate from Yb ions. The resulting set of rate equations is:

$$\frac{dN_{2Yb}}{dt} = (\sigma_{a,Yb} N_{1Yb} - \sigma_{e,Yb} N_{2Yb}) F_p - K N_{2Yb} N_{1Er} - \frac{N_{2Yb}}{\tau_{Yb}} \quad (1a)$$

$$\frac{dN_{2Er}}{dt} = (\sigma_{a,Er} N_{1Er} - \sigma_{e,Er} N_{2Er}) F_L + K N_{2Yb} N_{1Er} - \frac{N_{2Er}}{\tau_{Er}} - C N_{2Er}^2 \quad (1b)$$

where N_{1Yb} , N_{2Yb} , N_{1Er} , N_{2Er} are the populations of the $F_{7/2}$, and $F_{5/2}$ levels of Yb and of the $I_{15/2}$, $I_{13/2}$ levels of Er, respectively; $\sigma_{a,Yb}$, $\sigma_{e,Yb}$, $\sigma_{a,Er}$, and $\sigma_{e,Er}$ are the absorption and emission cross sections for the $F_{7/2}$ - $F_{5/2}$ Yb pump and $I_{15/2}$ - $I_{13/2}$ Er laser transitions; τ_{Yb} and τ_{Er} are the lifetimes of the $F_{7/2}$ and $I_{13/2}$ states of Yb and Er; F_L and F_p are the total laser and pump photon flux; K and C are the energy-transfer and the UC coefficients. The K coefficient is assumed to be independent of Er concentration and it ranges between 1×10^{-16} and 5×10^{-16} cm³/s depending on Yb concentration¹⁰. The C coefficient can be calculated and, in phosphate glass, it is of the order of 1×10^{-18} cm³/s.

It should be noticed that (1a) and (1b) have to be considered as spatially dependent because, in typical microlaser cavities, the pump intensity as well as the pump and laser mode sizes change both with longitudinal and radial coordinates inside the active material. Even by taking into account for these spatial variations, a simplified solution can, near threshold, be found analytically¹⁵. From these calculations some important conditions to minimize threshold pump power were worked out, providing useful guidelines to laser design and optimization. A numerical solution of the pump and laser field equations, using (1a) and (1b) to evaluate the local populations, can be obtained by an iterative process using a Runge-Kutta method by an approach similar to that used for optical amplifiers¹⁶. To simplify the iterative solution we also assumed two further approximations¹⁴: (i) Negligible depletion of ground-state Yb population, so that the pump power is exponentially attenuated. (ii) Negligible UC rate compared to the spontaneous decay rate. Assuming a value for C of about of 1×10^{-18} cm³/s, we obtain that UC becomes negligible for Er concentration lower than 3×10^{19} ions/cm³. Upon using the two previous assumptions, (1a) and (1b) give a second order characteristic polynomial and the computational time is consistently reduced.

3. CONTINUOUS WAVE LASER OPERATION

Quasi-continuous-wave laser operation of bulk erbium in glass was achieved by end-pumping with a Nd:YAG laser at 1064 nm wavelength¹⁷; cw operation was subsequently demonstrated by pumping with a cw diode-pumped Nd:YAG laser⁴ and, contemporary, by pumping at 980 nm both with a Ti:sapphire laser and with an InGaAs diode laser by our group^{5,6}. For any practical application, the InGaAs diode-pumped configuration is by far the most interesting one. In the following of this paragraph we review the experimental results obtained with diode-pumped laser configurations in continuous wave regimes, including single-frequency operation and laser tunability.

In absence of any particular contrivance, the bulk Er-Yb:glass laser generally exhibits multi-longitudinal and transverse mode operation. A typical cavity configuration of an end-pumped, Er-Yb microlaser operating in the multi-longitudinal mode regime is shown in Fig. 2^{6,18}. The cavity consists of a plane-plane, erbium-doped phosphate glass disk, codoped with ytterbium, and of a curved output mirror. One face of the glass disk is coated for high reflectivity (>99.9%) in the wavelength range 1530-1560 nm and for high transmission at the pump wavelength, the other face being antireflection coated at the laser wavelength to avoid undesirable etalon effects. The radius of

curvature of the output mirror may range between 5 and 10 mm, with a transmission at the laser wavelength typically between 0.5% and 2%. Depending on the desired gain and laser central wavelength, the Er concentration may vary between 1×10^{19} and 2×10^{20} ions/cm³, and the disk thickness between 1 and 2.5 mm; the Yb concentration is $\approx 1 \times 10^{21}$ ions/cm³. The disk is end-pumped by a broad-area InGaAs laser diode at 980 nm wavelength, and a suitable collimating and reshaping optics is used to partially compensate for the astigmatism of the pump beam and to focus it into the glass disk with a spot-size ranging typically from 30 μ m to 60 μ m. This pumping configuration enables an effective selection of the single transverse mode without the use of any intracavity pin-hole.

Typical output power versus incident pump power characteristics show threshold values between 10 and 80 mW and slope efficiencies which range between 15% and 40%, depending on the particular values of the resonator parameters and on pumping configurations. The maximum output power we achieved with the Er-Yb laser is of the order of 150 mW with an incident pump power of ~ 750 mW using the new QX-Er glass host (Kigre Inc.) with improved thermal properties.

Without any frequency selective element, the Er-Yb laser typically oscillates on many longitudinal cavity modes due to the wide bandwidth of the active medium. Although the laser linewidth is mainly homogeneously broadened, multimode oscillation spontaneously arises because of the spatial hole burning phenomenon. Typically, the frequency separation between modes that fill the available spatial holes increases as the gain region is moved from the middle of the cavity to the end of the cavity¹⁹. In our case, the length of the resonator is quite short, typically of the order of a few mm, and we practically observed an interesting and stable multimode regime characterized by the simultaneous oscillation of a few longitudinal modes, up to 8-10 when pumping the laser far above threshold, spaced by the free spectral range of the laser cavity (~ 10 GHz to ~ 100 GHz), without mode-hopping or other dynamic instabilities. The linewidth of each mode, as measured by a self-homodyne technique, is found to be less than 50 kHz.

To overcome problems arising from mechanical vibrations, and, in particular, to reduce the intensity noise induced by external perturbations, a compact monolithic cavity was also designed and demonstrated^{14,20}. This laser cavity is simply made of an active disk, 1-mm to 2.5-mm long, with one plane face and one convex spherical face, both faces being coated by multilayer coatings to form the resonator ends. The spherical surface, coated for 0.5%-1% transmission at the laser wavelength and for maximum reflectance at the pump wavelength, forms the output coupler. In this case pumping was simply provided by a fiber-coupled 980-nm InGaAs laser diode through a graded index (GRIN) lens. For this monolithic device (2.5-mm length), five or six longitudinal modes, spaced by 40 GHz, were found to steadily oscillate around 1533 nm wavelength with an overall output power of 13 mW at 80 mW pump power²⁰.

Multi-longitudinal mode operation appears to be very appealing for applications in high capacity wavelength division multiplexing (WDM) systems, where each mode can be singularly modulated and can thus act as an independent channel. We have demonstrated, using the Er-Yb microlaser in a four channel transmission experiment, a transmission capability up to 4x2.5 Gbit/s²¹.

3.1 Single mode operation and laser tunability

To achieve single longitudinal mode operation and laser tunability wavelength over a wide range, a Fabry-Perot (FP) etalon, made of BK7 glass and of suitable thickness (100-300 μ m), or of an anisotropic absorptive Polarcor etalon (~ 50 μ m), is inserted in the laser cavity (see Fig. 2) and the output mirror is mounted on a piezoelectric (PZT) transducer^{21,22,23}. Etalons are typically left uncoated since the Fresnel reflections at the bare surfaces provide for

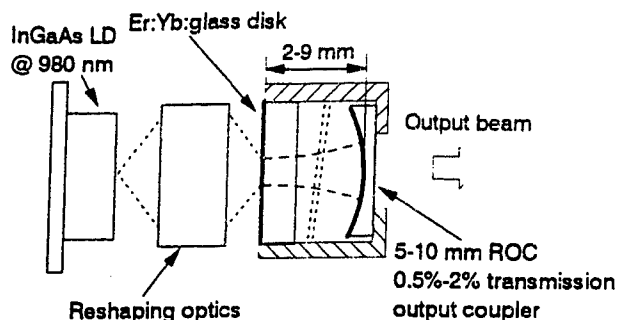


Fig. 2 Schematic diagram of the Er-Yb phosphate glass microlaser

sufficient band limitation to allow single mode operation. The special Polarcor etalon is fabricated from a borosilicate glass containing elongated silver particles aligned along a common axis; resonant absorption by the conduction electrons inside the silver introduces a strong absorption for light polarized along this axis. The use of this etalon thus provides, at the same time, single frequency operation and linearly polarized output beam over a wide tuning range. The purpose of the PZT transducer is to finely tune a cavity mode to the transmission peak of the etalon. In the following, we will focus on the microlaser which makes use of the Polarcor etalon, due to its outstanding performance. With reference to the laser configuration of Fig. 2, the thickness of the laser disk is, in this case, 1 mm and the Er and Yb concentrations are chosen to be 10^{20} ions/cm³ and 2×10^{21} ions/cm³, respectively. The resonator length is 5 mm, resulting in a longitudinal mode separation of ~ 30 GHz. We used mirrors with two different radii of curvature (7.5 and 10 mm) and with three different values of transmission (0.5, 1 and 2%). Depending on the cavity length and on the radius of curvature of the output mirror, the mode spot-size ranges between 40 and 50 μm . The laser is pumped by a tunable, external-cavity laser diode with a nearly diffraction limited beam ($M^2=1.2$) tuned at 978 nm wavelength.

The behavior of the laser output power versus the emission wavelength, obtained upon rotating the Polarcor etalon, is shown in Fig. 3. The laser wavelength first follows the blueshift of the etalon transmission peak over one free spectral range, from 1564 to 1547; upon further increasing the tilting angle, the laser wavelength jumps back to 1564 and then is continuously tuned down to 1528 nm. These tuning characteristics were explained in Ref. 17 as arising from a detailed balance between gain and absorption in the Er ions. By using the QX Er glass base with higher thermal load, output powers in excess of 100 mW at several wavelengths between 1530 nm and 1560 nm were recently demonstrated with a maximum output power of 130 mW at 1533 nm. Single longitudinal operation is ascertained by a scanning Fabry-Perot interferometer (Burleigh Model IR-110) and, in all cases, mode suppression is found to be larger than 25 dB, the limit being established by the resolution of our measuring apparatus. The laser linewidth, as measured by the self-homodyne technique, is narrower than 50 kHz.

This single-mode widely-tunable Er-Yb laser may find important applications as a high power, low intensity noise oscillator for cable television transmission with external analog modulation in the whole 1530-1565 nm spectral range.

3.2 Microchip laser

Erbium-ytterbium microchip lasers^{24,25} represent monolithic, miniaturized devices showing extremely interesting operating characteristics (such as single longitudinal and transverse mode operation, low threshold, high efficiency and intrinsic stability) of potential importance in many applications where coherent light sources around 1530 nm wavelength are required. These microchips consist of a monolithic cavity formed by a thin disk (typically 100-300- μm thickness, 3-mm diameter) of Er-Yb doped phosphate glass with plane parallel faces, dielectrically coated to obtain a high finesse, standing-wave laser cavity. The short thickness of the cavity, which corresponds to a frequency separation between consecutive modes from a few hundreds GHz to ~ 1 THz, ensures single longitudinal mode operation, still permitting enough gain to reach threshold for continuous-wave laser operation²⁵. The concentrations of Er and Yb ions are $\approx 1 \times 10^{20}$ ions/cm³ and $\approx 2 \times 10^{21}$ ions/cm³, respectively. These values have been chosen on the basis of a space-dependent rate equation model of laser operation^{15,24}. The microchip is longitudinally pumped by a InGaAs diode laser at 980 nm wavelength through a suitable reshaping optical system. The pump face of the microchip is coated for high reflectivity at 1530 nm ($R > 99.9\%$) and for high transmission at the pump wavelength

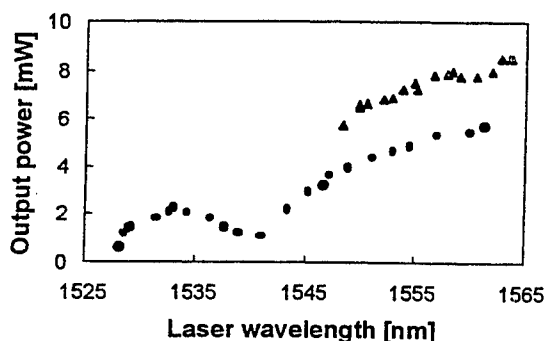


Fig. 3 Linearly polarized laser output power versus oscillating wavelength. Upper curve (triangles) refers to laser wavelength tuning over the first Polarcor etalon free spectral range; lower curve (circles) refers to subsequent wavelength tuning obtained by further etalon tilting.

($T > 96\%$); the other face, which is the output coupler, is coated for high reflectivity at 980 nm ($R > 96\%$) and for 1% transmission at the laser wavelength. For a focusing condition corresponding to $\sim 40\text{ }\mu\text{m}$ pump beam spot size into a 200- μm thickness microchip, more than 25 mW (at a pump power of 150 mW) in a TEM_{00} , 33 μm circular mode size with excellent beam quality ($M^2=1.06$) were obtained, with a low threshold condition ($\sim 40\text{ mW}$) and a high slope efficiency ($\approx 22\%$)²⁵. The laser output spectrum, measured by a grating-type optical spectrum analyzer (Anritsu Model MS 9001-A1), is shown in Fig. 4 on a logarithmic scale. As it can be seen, the laser oscillates on a single longitudinal mode at the peak wavelength of the Er emission spectrum ($\approx 1533\text{ nm}$), the adjacent longitudinal modes (which would be located at $\sim 4\text{ nm}$ apart from the peak emission) being not visible on the scale of the figure. This indicates single longitudinal mode operation with more than 40-dB suppression of lateral modes. The laser linewidth, measured by a self-homodyne technique, is estimated to be narrower than $\sim 1\text{ kHz}$ ²⁵, and a frequency tunability with temperature of $2.1\text{ GHz}/^\circ\text{C}$ was also demonstrated. The transverse laser mode is mainly determined by waveguiding effects induced by the pump beam, and therefore a careful control of the focusing conditions is needed to keep a low threshold condition. A detailed experimental and theoretical analysis of self-guiding effects in Er-Yb microchip lasers and on the effects of the pump spot size on the operating microchip characteristics is given in Ref. 24.

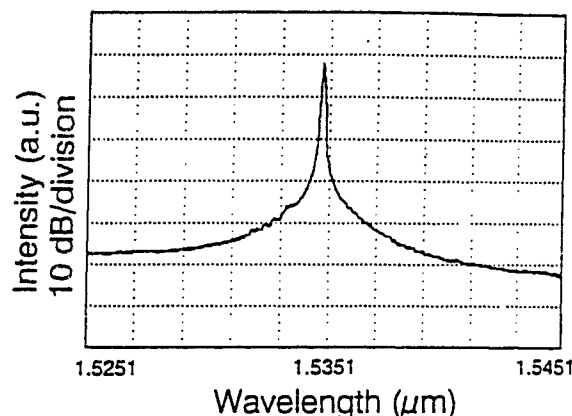


Fig. 4 Optical spectrum of the Er-Yb:glass microchip laser in single-longitudinal mode operation.

4. PULSED LASER OPERATION

Bulk erbium-ytterbium lasers have been successfully demonstrated to operate in pulsed regimes generating either pulses in the picosecond scale at high repetition rates by active mode-locking techniques²⁶⁻²⁸ and in the nanosecond scale at low repetition rates by active and passive Q-switching techniques^{29,30}. Both pulsed regimes appear to be of great importance for several applications. In particular, nanosecond pulses around 1530 nm emitted from a compact source are of potential interest in eye-safe long range distance measurements, where high peak powers are required. On the other hand, high-repetition-rate picosecond pulses around 1500 nm wavelength are extremely interesting for their potential use in soliton-based optical communication systems. In this paragraph we present the results obtained with the Er-Yb laser in mode-locking and frequency modulation regimes.

4.1 Mode-locking operation

Conventional techniques for ultrashort pulse generation are based on active mode-locking concept, where either an intracavity amplitude- (AM) or frequency modulation (FM) at a frequency equal to an integer number of the cavity axial mode separation is externally imposed by use of a modulator. Although active mode-locking of erbium-doped fiber lasers has been demonstrated to be capable of generating high-quality pulse trains at high repetition rates, these lasers usually fail in producing pulse trains with long-term stability, and generally stable operation requires some form of active stabilization. The instability inherent to mode-locked fiber lasers is mainly due to the higher harmonic order in which they are operated, which causes supermode competition in the spectral domain. We have recently demonstrated the operation at a fundamental or at a low harmonic order of a compact bulk erbium-ytterbium laser^{27,28} by frequency-modelocking at 2.5 GHz achieved by an intracavity LiNbO_3 electro-optic phase modulator. A schematic diagram of the diode-pumped, FM mode-locked cavity in the third-harmonic configuration is shown in Fig. 5. The laser source consists of a one-folded, 18-cm long linear cavity composed by a 1-mm thick

disk of active material placed at the end of the short cavity arm, by a folding mirror (62-mm radius of curvature), and by a plane output mirror (1% output coupling). For this configuration, stable pulse trains with durations from a few picoseconds up to few tens of picoseconds with an average power up to 20 mW were generated, with a stability to frequency detunings of the order of few tens of kHz²⁷. The time-bandwidth product measured for these pulses is typically close to 0.65, in agreement with the value predicted by FM mode-locking theory indicating that the pulses are chirped; to obtain chirp-free pulses, if needed, the mode-locked pulse train should be sent to a suitable dispersion line.

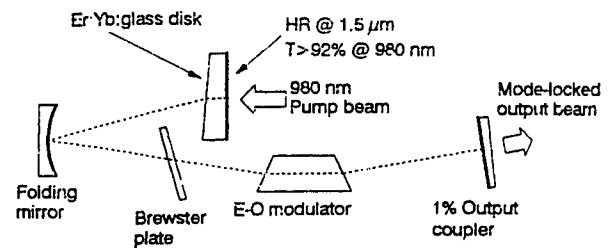


Fig. 5 Schematic diagram of the third-order harmonic FM mode-locked Er-Yb:glass laser.

4.2 Frequency modulation operation

An interesting regime of operation of the Er-Yb:glass laser, which sets in when the modulation frequency is detuned by few MHz from the natural repetition rate as imposed by the laser cavity, is the frequency modulation regime, which corresponds to a signal with a nearly constant intensity but with a large sinusoidal sweep of the instantaneous frequency. In the spectral domain, the laser exhibits a characteristic FM Bessel spectrum whose bandwidth may be increased by suitable cavity length adjustments up to the entire gain bandwidth of the cavity. Although this kind of operation has not been considered of particular interest for applications and it was mainly regarded as a fundamental topic on phase-modulated laser dynamics, we have recently shown a possible application of this operating regime to the generation of chirp-free picosecond pulses from our bulk Er-Yb:glass laser³¹. Generation of high-repetition-rate picosecond pulses from spectral filtering of a phase-modulated beam emitted by an externally-modulated single-mode semiconductor laser was recently proposed and experimentally demonstrated in Ref. 32. The key idea of this method is that, when the red-shifted (Stokes) or the blue-shifted (anti-Stokes) groups of modes in a purely FM optical signal are filtered out from the entire FM spectrum, a train of symmetric and transform-limited pulses at a repetition frequency equal to the modulation frequency can be generated. Furthermore, if both Stokes and anti-Stokes bands are filtered out from the FM spectrum, a dual-wavelength pulse train can be produced, with doubling of the pulse repetition frequency. We have recently demonstrated that the FM laser spectrum obtained from our Er-Yb:glass laser by an *intracavity* phase modulation is well suited for the nonresonant generation of low duty-cycle pulse trains with high long-term stability against environmental perturbations, as well as for the generation of a dual-wavelength pulse train. With respect to conventional mode-locking techniques, the main advantage of this technique is that no strict constraint on cavity length stability is necessary. The laser cavity for the operation of the Er-Yb:laser in the FM regime is the same as that shown in Fig. 5 and used for mode-locking operation. A 100-μm thick uncoated BK7 etalon is inserted in the cavity in order to control, by etalon tilting, the carrier frequency of the FM spectrum. The laser output is coupled into a single-mode fiber and it is sent to a fiber Bragg grating through a three-port optical circulator. In a first set of experiments, the fiber grating was designed to work as a bandpass filter with a reflectivity larger than 99% over 21.5 GHz bandwidth centered at 1535.284 nm wavelength. In this case, by a suitable adjustment of the carrier frequency of the FM signal, only the first (or the last) group of modes in the frequency spectrum (anti-Stokes and Stokes bands,

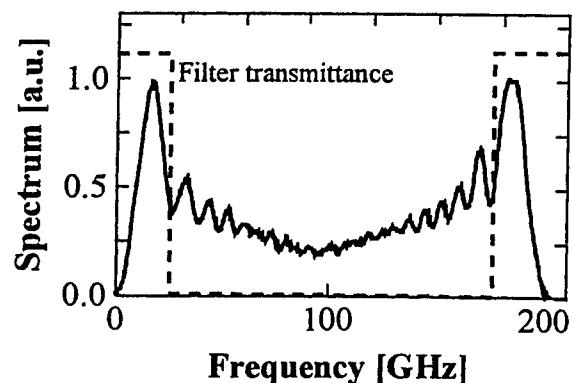


Fig. 6 Spectrum of the FM laser output corresponding to an effective modulation index of 33. The dashed line in the figure shows the transmittance of the fiber Bragg grating.

respectively) are reflected and available at a port of the circulator. In the time domain, this signal corresponds to a train of pulses at a repetition rate of 2.5 GHz. Measurements of the pulse duration by a non-collinear autocorrelation technique indicates that pulses as short as 40 ps are generated, corresponding to a measured oscillating bandwidth of ~11 GHz. A time-bandwidth product of 0.44 and a duty cycle of ~0.1 are hence obtained, the former indicating that the pulses are nearly transform limited and the latter ensuring weak pulse interactions. In order to generate a dual-wavelength pulse train, in a second set of experiments³³ we designed the fiber Bragg grating to operate in the transmission configuration as a notch filter with a wide high-reflectivity (99 %) over a bandwidth of 1.2 nm centered at 1533.866 nm characterized by sharp edges. With a suitable cavity length adjustment and after tuning the carrier frequency of the FM spectrum close to the center wavelength of the fiber grating, the optical field transmitted throughout the filter is composed solely by the Stokes and anti-Stokes bands (see Fig.6). The average optical power carried by the filtered signal is 1 mW, which corresponds to $\approx 22\%$ of the overall power in the FM signal. In the time domain, the transmitted optical field corresponds to a dual-wavelength pulse train at 5 GHz repetition frequency. A typical trace of the pulse train, measured by a fast photodiode connected to a sampling oscilloscope, is shown in Fig. 7(a). The pulse duration was measured by a noncollinear autocorrelation technique after sending the fiber grating output to an erbium-doped fiber amplifier which increases the average power of the pulse train up to 15 mW. A typical autocorrelation trace is shown in Fig.7(b); the pulse duration, assuming a sech-like pulse shape, is 48 ps, and the corresponding time-bandwidth product is 0.48, indicating that the pulses are nearly transform-limited.

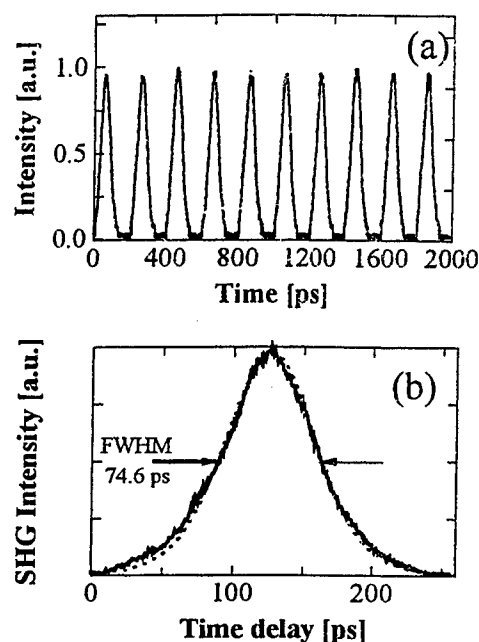


Fig. 7 Dual-wavelength pulse train at 5 GHz repetition rate as measured by a fast photodiode connected to a sampling oscilloscope (a), and corresponding autocorrelation trace of the pulse (b). In (b) the dashed line is the best fit autocorrelation function obtained by assuming a sech-like pulse shape.

5. AMPLITUDE AND FREQUENCY STABILIZATION

In this paragraph we discuss amplitude and frequency stabilization of diode-pumped bulk Er-Yb microlasers discussed in Sect. 3.1 due to their importance for several applications to optical communications as well as to metrology, where stability of the laser source is of particular concern.

5.1 Amplitude stabilization

A fundamental prerequisite of optical sources for optical communication applications is the occurrence of low relative intensity noise (RIN). In particular, this requirement is of the upmost importance for analog modulation applications (such as common antenna television, CATV) for which any spurious modulation of the carrier has to be avoided. Intensity noise in solid-state lasers may be induced by acoustical, mechanical and thermal noise as well as by pump power fluctuations. Whatever the origin of the perturbation is, the RIN is strongly enhanced at around the relaxation oscillation frequency, which for a typical microlaser is located between a few tens of kilohertz to about 1 MHz^{34,35}. To suppress the RIN peak at the relaxation oscillation frequency a feedback circuit acting on the pump power is usually used³⁴. We demonstrated that in a three-level codoped system such as the Er-Yb laser, the main RIN cause is due to intrinsic spurious modulation of cavity losses³⁵, differently from what typically happens for lasers with direct pumping, such as Nd:YAG or Er:glass, where the intensity noise is mainly induced by pump power

fluctuations. To gain some further insight into the laser responses to external perturbations, it is worth considering the corresponding transfer function (TF) obtained by the Fourier transforms of the linearized rate equations. This TF is hence useful to describe, in the frequency domain, the response of the laser system to the perturbations of pump rate and cavity loss. The peculiar behaviour of the Er-Yb laser is strictly related to the energy-transfer process in the pumping scheme, which acts as a low-pass filter introducing an additional low-frequency pole in the pump rate TF. The cut-off frequency is related to the overall ytterbium $F^{7/2}$ lifetime³⁵, which typically ranges from ~150 Hz (for low-doped material) to a few kHz (for highly-doped material). The most relevant features introduced by the energy transfer process are the following: (a) All noise sources acting on Yb (like pump power fluctuations) show an additional low-frequency pole with respect to noise sources directly acting on the erbium inversion (like cavity loss modulation and cavity length modulation). (b) Pump noise effects are strongly reduced due to the filtering action of the low-frequency pole. (c) A feedback circuit acting on the pump power must therefore provide very high gain at the relaxation oscillation frequency to overcome the attenuation introduced by the Er-Yb laser system itself.

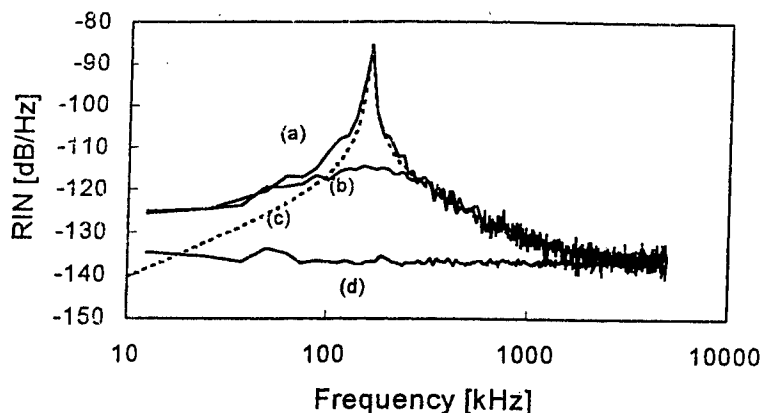


Fig.8 RIN spectra: (a) Experimental spectrum in free running regime. (b) Experimental laser spectrum with feedback circuit on. (c) Theoretical prediction of the free running spectrum assuming a white noise source for the cavity losses with spectral density of -167 dB/Hz. (d) Background noise of the experimental apparatus.

Pump power and cavity loss TFs were investigated using a microlaser³⁵ similar to the one discussed in section 3.1. Both amplitude and phase of TFs were measured by means of a network analyzer, finding a good agreement with the theoretical predictions³⁵. On the basis of these results, was designed a suitable feedback circuit and operated. The experimental set-up used for amplitude stabilization is reported in Ref. 35. A small fraction (~5%) of the output power is sent to a low-noise photodiode as feedback signal. The output of the photodiode is sent to a suitable noise reduction circuit³⁸ (NRC) that provides a high gain at the relaxation oscillation frequency. The ac voltage signal from the NRC is then fed into the current driver of the pump laser diode. The resulting open loop gain is ~33 dB at the RIN peak frequency of 160 kHz. Figure 8 shows the measured RIN spectra of the free running oscillator (curve *a*) and of the laser when the feedback loop is operating (curve *b*). The free running spectrum exhibits a -120 dB/Hz RIN level at low frequency values, an increase to -84 dB/Hz at the relaxation oscillation peak and a -20 dB/decade slope after the peak. We also report in Fig. 8, as curve *c*, the theoretical prediction for the RIN assuming a white input noise with a suitable value of the spectral density function for loss modulation of -167 dB/Hz. When the feedback circuit is turned on, we note that, as expected, the peak RIN suppression is ~30 dB, from -84 dB/Hz to -114 dB/Hz, and the NRC does not introduce any appreciable extra noise either at lower or higher frequencies³⁵.

5.2 Frequency stabilization.

Laser frequency stabilization in the 1500 nm region is of great interest for many of the proposed optical communication applications involving wavelength-division multiplexing, such as multiwavelength transport networks and passive optical networks. In addition, absolute frequency reference lines in this region are important for metrological applications and high-resolution spectroscopy. To date, several studies have been devoted to absolute 1.5 μ m frequency stabilization of semiconductor lasers using various atomic³⁹ or molecular^{40,41} absorption lines. The multi-mode or single-mode devices of sections 3.1 can be frequency stabilized by locking the oscillation frequency, or one of the oscillation frequencies for multi-mode operation, to an external frequency reference. In particular, the widely tunable Er-Yb bulk microlaser²³ can be frequency stabilized to any of the C_2H_2 and $^{13}C_2H_2$ absorption lines in the wavelength range from 1530 nm to 1550 nm to obtain a narrow-linewidth absolute frequency reference in this spectral region.

In a first set of experiments⁴², two single-mode Er-Yb:QE7-glass microlasers have been frequency stabilized to the P(13), P(14) and P(15) absorption lines of C₂H₂ at 1532.828 nm, 1533.458 nm and 1534.097 nm, respectively. The stabilization set-up, based on the fringe-side locking technique, is reported in Ref. 42. The Er-Yb microlasers are first wavelength tuned to the side of the desired acetylene absorption line, by tilting the intracavity etalon, and then frequency locked to the molecular reference, by means of an electronic control loop acting on the PZT transducer. The beam passing through the acetylene cell experiences in fact a frequency dependent absorption. In this way, frequency fluctuations of the laser source are transformed into amplitude fluctuations to be used as the feedback signal. This signal is integrated, amplified and then sent to the PZT for active frequency control. The resulting laser frequency stability has been measured performing a beat note signal analysis both in the time and frequency domains, between two stabilized laser sources. The C₂H₂-P(15)-line stabilized lasers showed a beat-note frequency stability of ± 1 MHz over a 4 hours observation time and a 1-ms beat-note linewidth of ~ 95 kHz. The single Er-Yb laser thus reached a long- and short-term relative frequency stability of $\Delta\nu/\nu \equiv 5 \times 10^{-9}$ and $\Delta\nu/\nu \equiv 2.5 \times 10^{-10}$, respectively.

In further experiments⁴³ on frequency stabilization, two Er-Yb microlasers, based on a heavily Er-doped phosphate glass, have been successfully tuned to match the P(13)-P(29) absorption lines of the ¹³C₂H₂ molecule in the wavelength range 1540-1550 nm, allowing for a finely resolved laser spectroscopy of all the 9 odd molecular transitions. Also in this case the microlasers have been frequency stabilized, with a fringe-side locking technique, to several absorption lines of the isotopic acetylene molecule. The resulting frequency stability showed comparable results to the ones obtained in Ref. 42. Figure 9 shows beat-note experiments when locking to P(13) and P(29) lines. Root mean square frequency stabilities of 330 kHz and 700 kHz over 5-h time interval were measured in both cases; the laser linewidth observed over 1 ms was less than 50 kHz.

More recently, looking for a frequency reference of higher accuracy and stability, two new laser cavities with more rigid and mechanically stable mounts have been constructed. Low-voltage and higher-excursion PZT actuators have also been added to allow for low-noise driving electronics⁴⁴. The resulting two, QE7-based, Er-Yb microlasers have been frequency stabilized by a Pound-Drever-Hall technique to the peak of the P(15) absorption line of C₂H₂. External phase modulation, at 100 MHz modulation frequency, and synchronous detection after the resonance showed loop error signals located around zero value and a corresponding r.m.s. frequency fluctuation of ~ 200 kHz ($\Delta\nu/\nu \equiv 1 \times 10^{-9}$). A beat note signal analysis confirms the stiffness of the locking with beat frequency fluctuations below 400 kHz. The two-sample standard deviation $\sigma(2,\tau)/\nu$ (Allan deviation) was measured to be $< 10^{-10}$ for integration times between 0.01 s and 1 s, and below 4×10^{-11} for 0.1 s integration time.

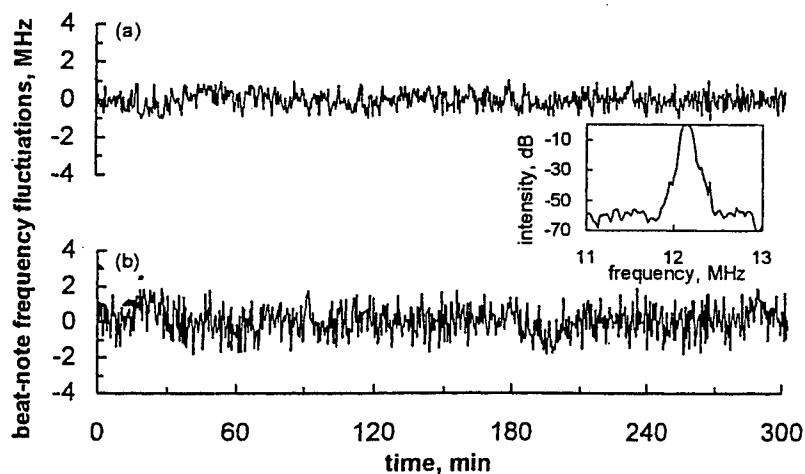


Fig. 9 Beat-note signal between the two frequency stabilized Er-Yb microlasers: time analysis of the beat frequency fluctuations for (a) P13 line and P(25) line. Etherodyne beat spectrum over 1 ms (inset).

6. CONCLUSIONS

We presented a review of recent work done by our group on diode-pumped bulk Er-Yb lasers. Different operating regimes and peculiar properties of this novel device have been discussed, namely multi-mode and single-frequency operation, frequency tuning and stabilization, intensity stabilization, mode-locking and frequency modulation operation. Due to high performance in terms of emission characteristics and potential low cost, this miniaturized

laser device compares quite favorably with alternative sources emitting in the 1530-1570 nm range, such as DFB and DBR semiconductor lasers and Er-doped fiber lasers and appears to be particularly suitable for optical communication applications.

REFERENCES

- [1] E. Snitzer and R. Woodcock, *Appl. Phys. Lett.* **6**, 45 (1965).
- [2] M. Okayasu, T. Takeshita, M. Yamada, O. Kogure, M. Horiguchi, M. Fukuda, A. Kozen, K. OE, and S. Uehara, *Electron. Lett.* **25**, 1563 (1989).
- [3] R. J. Mears, L. Reekie, I. M. Jauncey, and D. N. Payne, *Electron. Lett.* **23**, 1026 (1987).
- [4] D. W. Anton, T. J. Pier and P. A. Leilabody, *Digest of Conference on Optical Fiber Communications*, 1991 (Optical Society of America, Washington DC, 1991) paper FB6, 206.
- [5] P. Laporta, S. De Silvestri, V. Magni, L. Pallaro and O. Svelto, *Digest of Conference on Lasers and Electro-Optics*, 1991 (Optical Society of America, Washington DC, 1991) paper CthR1.
- [6] P. Laporta, S. De Silvestri, V. Magni and O. Svelto, *Opt. Lett.* **16**, 1952 (1991).
- [7] J. A. Hutchinson and T. H. Allik, *Appl. Phys. Lett.* **60**, 1424 (1992).
- [8] W. J. Miniscalco in «Rare Earth Doped Fiber Lasers and Amplifiers» edited by J.F.Digonnet, Marcel Dekker, New York 1993.
- [9] E. Desurvire, «Erbium-Doped Fiber Amplifiers», John Wiley & Sons Inc. 1994.
- [10] V. P. Gapontsev, S. M. Matisin, A. A. Iseneev and V. B. Kravchenko, *Opt. and Laser Technology*, **14**, 189 (1982).
- [11] J. C. Wright, *Topics in Applied Physics, Radiationless Processes in Molecules and Condensed Phases*, F. K. Fong Ed., **15**, Springer-Verlag (1976).
- [12] J. L. Wagener, P. F. Wysocki, M. J. F. Digonnet and H. J. Shaw, *Opt. Lett.* **18**, 2014 (1993).
- [13] P. Blixt, J. Nilsson, T. Carlnas and B. Jaskorzynska, *IEEE Photon. Technol. Lett.* **3**, 996 (1991).
- [14] S. Taccheo, P. Laporta, S. Longhi, O. Svelto and C. Svelto, *Appl. Phys. B* **63**, 425 (1996).
- [15] P. Laporta, S. Longhi, S. Taccheo and O. Svelto, *Opt. Commun.* **100**, 311 (1993).
- [16] G. R. Giles and E. Desurvire, *IEEE J. Ligth. Technol.* **9**, 271 (1991).
- [17] D.C. Hanna, A. Kazer, and D. P. Sheperd, *Opt. Commun.* **63**, 147 (1987).
- [18] P. Laporta, S. Taccheo and O. Svelto, *Electron. Lett.* **28**, 490 (1992).
- [19] B. Braun, K.J. Weingarten, F. X. Kartner, and U Keller, *Appl. Phys. B* **61**, 429 (1995).
- [20] G. Sacchi, S. Cecchi, G. Chiaretti, G. Randone, P. Laporta, S. Taccheo, F. Salina and O. Svelto, *IEEE Photon. Technol. Lett.* **4**, 98 (1994).
- [21] S. Taccheo, P. Laporta and C. Svelto, *Appl. Phys. Lett.* **68**, 2621 (1996).
- [22] P. Laporta, S. Longhi, S. Taccheo, O. Svelto and G. Sacchi, *Opt. Lett.* **18**, 31 (1993).
- [23] S. Taccheo, P. Laporta and O. Svelto, *Appl. Phys. Lett.* **69**, 3128 (1996).
- [24] S. Taccheo, P. Laporta, S. Longhi and C. Svelto, *Opt. Lett.*, **20**, 889 (1995).
- [25] P. Laporta, S. Taccheo, S. Longhi and O. Svelto, *Opt. Lett.* **18**, 1232 (1993).
- [26] G. Cerullo, S. De Silvestri, P. Laporta, S. Longhi, V. Magni, S. Taccheo and O. Svelto, *Opt. Lett.* **16** 272 (1994).
- [27] S. Longhi, P. Laporta, S. Taccheo and O. Svelto, *Opt. Lett.* **19**, 1985 (1994).
- [28] S. Longhi, S. Taccheo, P. Laporta and C. Svelto, *Electron. Lett.* **31**, 368 (1995).
- [29] E. Tanguy, J.P. Pocholle, G. Feugnet, C. Larat, M. Schwarz, A. Brun and P. Georges, *Electron. Lett.* **31**, 458 (1995).
- [30] R. Fluck, B. Braun, U. Keller, E. Gini, H. Melchior. *CLEO '97*, paper CThK3, p. 355.
- [31] S. Longhi, S. Taccheo, P. Laporta, *Opt. Lett.* **22**, 1642 (1997).
- [32] P.V. Mamyshev, *Opt. Lett.* **19**, 2074 (1994).
- [33] S. Longhi, G. Sorbello, S. Taccheo and P. Laporta, *Opt. Lett.* (Submitted, 1998).
- [34] J. T. Kringlebotn, J. L. Archambault, J. E. Townsend, G. G. Vienne and D. N. Payne, *Electron. Lett.* **30**, 972 (1994).
- [35] S. Taccheo, P. Laporta, O. Svelto and G. de Geronimo, *Opt. Lett.* **21**, 1747 (1996).

- [36] T. J. Kane, IEEE Phot. Technol. Lett. **2**, 244 (1990).
- [37] S. Taccheo, P. Laporta, O. Svelto and G. de Geronimo, App. Phys. B **66**, 19 (1998).
- [38] G. De Geronimo, S. Taccheo and P. Laporta, Electron. Lett. **33**, 1336 (1997).
- [39] Y.C. Chun, C.B. Boxio, Electron. Lett. **24**, 1048 (1988).
- [40] T. Yanagawa, S. Saito, Y Yamamoto, Appl. Phys. Lett. **45**, 826 (1984).
- [41] M. de Labachellerie, K. Nakagawa, Y. Awaji and M. Ohtsu, Opt. Lett. **20**, 572 (1995).
- [42] S. Taccheo, S. Longhi, L. Pallaro, P. Laporta, C. Svelto and E. Bava, Opt. Lett. **29**, 2420 (1995).
- [43] S. Taccheo, G. Sorbello, P. Laporta and C. Svelto, Electron. Lett. **34**, 81 (1998).
- [44] C. Svelto, E. Bava, S. Taccheo and P. Laporta, Electron. Lett. **34**, 461 (1998).

Yb:YAG Disk Laser Pumped by a Stacked Diode Array

N. Kugler^a, T. Brand^a, I. Schmidt^a, C. Gao^b and H. Weber^b

^aLaser- und Medizin-Technologie Berlin gGmbH, Rudower Chaussee 6, D-12489 Berlin

^bOptisches Institut der Technischen Universität Berlin, Straße des 17. Juni 135, D-10623 Berlin

ABSTRACT

A major problem using laser diodes for longitudinal pumping of solid state lasers is the poor beam quality and the non symmetric beam profile of the diodes as the astigmatic beam emitted from the array of diodes exhibits a limited focusability in the direction of the slow axis of the diodes. To overcome this problem an optic which turns the astigmatic beam of a stacked diode array into a radially symmetric (stigmatic) beam has been designed. This symmetric beam is then focused into an axially water cooled disk laser to serve as a longitudinal pump source. Up to now different laser crystals have been investigated as laser source. Using Yb:YAG an output power of 60 W in qcw operation has been realised whereas Nd:YVO₄ delivers a qcw power of 113 W. The optical to optical efficiencies are 18% and 32.3% respectively.

Key words: Disk Laser, diode pumped, Yb:YAG laser, beam transformation

1. INTRODUCTION

Diode pumping of high power lasers has gained more interest recently since output power and reliability of the laser diodes increased while their price decreased. For side pumped solid state lasers stacked diode arrays have been used as well as fibre coupled laser diodes¹⁻³. Stacked diode arrays offer a higher efficiency and a lower price compared to fibre coupled devices but have the disadvantage of a very low beam quality and therefore limited focusability in the plane of the diode bar (slow axis, later referred to as x-axis). Therefore longitudinally pumped lasers are often realized with fibre coupled diode lasers to get a homogeneous and radially symmetric pump light distribution. Alternatively the emission of a diode bar or a stack of diode bars (stacked array) can be symmetrized by a transformation optic. The principle of these optics bases on reflection - as in the case of step mirrors or the beam shaper with two mirrors shifted against each other^{4,5} - or on transmission. This paper deals with a beam transformation optic based on cylindrical lenses which transform an astigmatic beam emitted from a stacked diode array into a radially symmetric beam^{6,7}. The symmetric beam is then focused into a disk laser (Fig. 1).

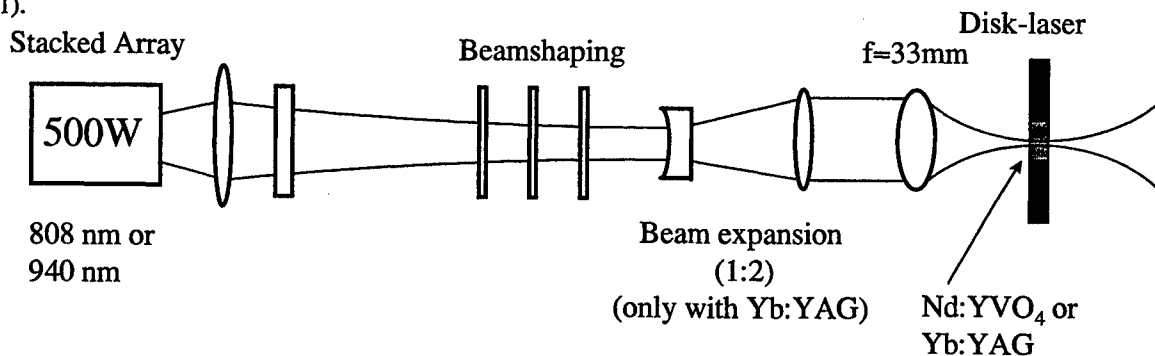


Figure 1. Sketch of the experimental set-up of the pump source used for the axially water cooled disk laser.

Correspondence: Nicolas Kugler, Tel.: +49 / 30 / 67053-440; Fax.: +49 / 30 / 67053-440.

The concept of a thin disk laser offers several advantages over a conventional rod- or slab-laser. Due to the heat flow parallel to the beam propagation direction thermal lensing and thermally induced aberrations are widely reduced. Therefore the mode volume for the TEM₀₀ mode can be matched with the pumped volume. As a result a very good beam quality can be obtained with a considerable high efficiency. The thin active medium leads to a high damage threshold with regard to the pump power densities.

2. BEAM TRANSFORMATION

The pump source for the disk laser consists of a stack of 20 Cu-microchannel cooled diode bars each collimated in the fast axis by a cylindrical microlens. The light emitted from the stack has remaining divergence of 5° half angle in the fast axis (perpendicular to the bar, later referred to as x-axis) and a divergence of 20° half angle in the slow axis (y-axis). The radiation of the stack is then formed by a spherical and a cylindrical lens to generate a common beam waist for both, x- and y-direction, having an equal rayleigh length at the same time. This is an important prerequisite transforming the astigmatic beam of the stack into a stigmatic one. The transformation itself is done by three cylindrical lenses with focal lengths of $f_1=104\text{mm}$, $f_2=2\cdot f_1$ and $f_3=f_1$. The lenses are separated by f_1 and the distance to the beam waist mentioned above is f_1 as well. A crucial point of the transformation optic is the orientation of the cylindrical lenses. The first and the last lens is tilted by +45° with regard to the co-ordinate system given by the diode-stack, whereas the second lens is tilted by -45°, i.e. 90° to the first and the last lens (Fig. 2).

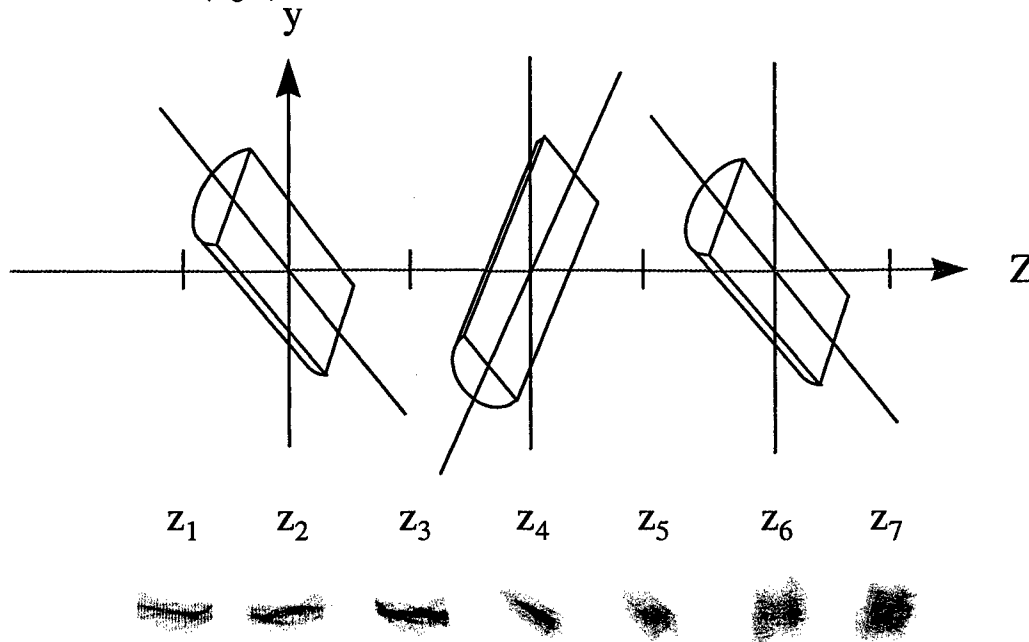




Figure 2. Set-up of the beam transformation optic („Beam Twister“) and beam shape of the emission from the stacked diode array while propagating through the transformer.

Passing through the set of cylindrical lenses the beam changes its shape. For $z > z_6$ the beam is radially symmetric in terms of second moment radii* (Fig. 2). The beam parameter product of the transformed beam is independent of the direction and it is equal to the arithmetic average of the beam parameter product in x- and y-direction before the beam was transformed (Table 1).

* A beam may be radially symmetric in terms of 2nd moment radii without „looking“ round, because the eye does not integrate intensity weighed by the square of the distance to the centre.

Table 1. Comparison of the beam quality and the focus shape with and without beam transformation by the „Beam Twister“.

	Not transformed	transformed by the „Beam Twister“
Beam Quality (second moment radii)	$M_x^2 \gg M_y^2$	$M_x^2 \approx M_y^2 \approx M_r^2 = \frac{1}{2}(M_x^2 + M_y^2)$
Focus shape		

This radially symmetric beam is then focused into an Yb:YAG disk laser by a corrected objective with a focal length of $f_f=33\text{mm}$. The radius of the focus is approximately 1 mm.

3. DISK LASER

The principle of the disk laser is shown in Fig. 3. The laser crystal is pumped longitudinally by the transformed and focused beam mentioned in chapter 2. The laser is cooled by a turbulent water flow over both surfaces of the crystal. The surface of the crystal facing the pump source is high reflecting coated for laser emission and high transmission coated for the pump light. The opposite crystal face is low transmission coated for the pump light and anti reflection coated for the laser light. Both coatings are designed for the transition between YAG and water. The windows are made of quartz glass. They are broad band anti reflection coated (around the wavelength of $1\text{ }\mu\text{m}$) on the outside and uncoated on the inside facing the water. As the refractive indices of water is $n_{\text{water}}=1.33$ and of quartz glass $n_{\text{qg}}=1.45$ ($\lambda \approx 1\text{ }\mu\text{m}$), the losses at the uncoated faces are small. The laser resonator is formed by the coated crystal as HR mirror and an external output coupler. Some of the measurements were made with Nd:YVO₄ as active medium. In this case the coatings for the laser resonator and the pump light were on the outside of the windows while the crystal was broadband anti reflection coated. The turbulent water flow does not influence the laser radiation, as was proved by interferometric measurement. The heat transfer from the crystal to the coolant is expected to be much higher than in contact cooled Yd:YAG disk laser configurations⁸.

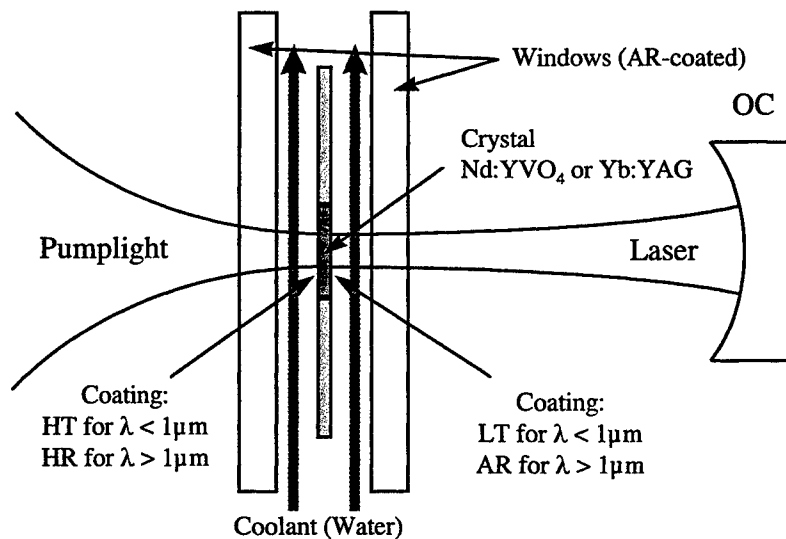


Figure 3. Scheme of the set-up of the disk laser cavity and resonator.

3.1 Thermal Management

To calculate thermal effects in the crystal disk the stationary heat equation in cylindrical co-ordinates has to be solved. The thermal conductivity is assumed to be constant^{9,10}.

$$\nabla^2 T + \frac{h}{\kappa} = \frac{1}{r} \frac{\partial}{\partial r} \left(r \frac{\partial T}{\partial r} \right) + \frac{1}{r^2} \frac{\partial^2 T}{\partial \varphi^2} + \frac{\partial^2 T}{\partial z^2} + \frac{h}{\kappa} = 0 \quad (1)$$

κ is the thermal conductivity [W/(m·K)], T is the temperature [K] and h is the heat dissipated in the crystal [W/m³]. The differential equations of the tensions and compressions are given by (no external force is assumed):

$$\frac{\partial \sigma_r}{\partial r} + \frac{1}{r} \frac{\partial \tau_{rt}}{\partial \varphi} + \frac{\partial \tau_{rz}}{\partial z} + \frac{\sigma_r - \sigma_t}{r} = 0 \quad (2)$$

$$\frac{\partial \tau_{rz}}{\partial r} + \frac{1}{r} \frac{\partial \tau_{tz}}{\partial \varphi} + \frac{\partial \sigma_z}{\partial z} + \frac{\tau_{rz}}{r} = 0 \quad (3)$$

$$\frac{\partial \tau_{rt}}{\partial r} + \frac{1}{r} \frac{\partial \sigma_t}{\partial \varphi} + \frac{\partial \tau_{tz}}{\partial z} + \frac{2\tau_{rt}}{r} = 0 \quad (4)$$

where $\sigma_r, \sigma_t, \sigma_z$ stand for the stress in radial, tangential and axial direction and $\tau_{rt}=\tau_{tr}, \tau_{zt}=\tau_{tz}, \tau_{rz}=\tau_{rz}$ represent the shear stress in the crystal [N/mm²]. The strains e_r, e_t and e_z (normal) and $g_{rt}=g_{tr}, g_{zt}=g_{tz}, g_{rz}=g_{rz}$ (shear) [-] are related to the expansions u, v and w in radial, tangential and axial direction [m] by

$$e_r = \frac{\partial u}{\partial r} \quad e_t = \frac{u}{r} + \frac{\partial v}{r \partial \varphi} \quad e_z = \frac{\partial w}{\partial z} \quad (5-7)$$

$$g_{rt} = g_{tr} = \frac{\partial u}{r \partial \varphi} + \frac{\partial v}{\partial r} + \frac{v}{r} \quad g_{tz} = g_{zt} = \frac{\partial v}{\partial z} + \frac{\partial w}{r \partial \varphi} \quad g_{rz} = g_{rz} = \frac{\partial u}{\partial z} + \frac{\partial w}{\partial r} \quad (8-10)$$

Taking the rotational symmetry into account, all angular derivatives vanish as well as the shear stress τ_{tr} and τ_{tz} and the tangential displacement v . Hence the stress equations (2) and (3) simplify to

$$\frac{\partial \sigma_r}{\partial r} + \frac{\partial \tau_{rz}}{\partial z} + \frac{\sigma_r - \sigma_t}{r} = 0 \quad \frac{\partial \tau_{rz}}{\partial r} + \frac{\partial \sigma_z}{\partial z} + \frac{\tau_{rz}}{r} = 0 \quad (11,12)$$

and equation (4) vanishes completely. The normal and the shear strains simplify to

$$e_r = \frac{\partial u}{\partial r} \quad e_t = \frac{u}{r} \quad e_z = \frac{\partial w}{\partial z} \quad g_{rz} = g_{rz} = \frac{\partial u}{\partial z} + \frac{\partial w}{\partial r} \quad (13-16)$$

The generalized Hooke's law with the module of elasticity E [N/mm²], the Poisson ratio ν [-] and the expansion coefficient α [1/K] reads

$$e_r = \frac{1}{E} [\sigma_r - \nu(\sigma_t + \sigma_z)] + \alpha \Delta T \quad (17)$$

$$e_t = \frac{1}{E} [\sigma_t - \nu(\sigma_z + \sigma_r)] + \alpha \Delta T \quad (18)$$

$$e_z = \frac{1}{E} [\sigma_z - \nu(\sigma_r + \sigma_t)] + \alpha \Delta T \quad (19)$$

These equations can be solved for the normal stresses in radial, tangential and axial direction $\sigma_r, \sigma_t, \sigma_z$ (including Eqs. (13) to(16))

$$\sigma_r = C_1 \frac{d}{dr} u + C_2 \frac{u}{r} + C_2 \frac{d}{dz} w - b \cdot \Delta T \quad (20)$$

$$\sigma_t = C_1 \frac{u}{r} + C_2 \frac{d}{dr} u + C_2 \frac{d}{dz} w - b \cdot \Delta T \quad (21)$$

$$\sigma_z = C_1 \frac{d}{dz} w + C_2 \frac{d}{dr} u + C_2 \frac{u}{r} - b \cdot \Delta T \quad (22)$$

with the constants

$$C_1 = \frac{E}{1+\nu} \cdot \frac{1-\nu}{1-2\nu} \quad C_2 = \frac{E}{1+\nu} \cdot \frac{\nu}{1-2\nu} \quad b = \frac{E}{1+\nu} \cdot \frac{1+\nu}{1-2\nu} \cdot \alpha \quad (23-25)$$

and for the shear stress τ_{rz}

$$\tau_{rz} = G \left(\frac{d}{dz} V + \frac{d}{dr} U \right) \quad (26)$$

with

$$G = \frac{E}{2(1+\nu)} \quad (27)$$

The boundary conditions are given by the cooling geometry. The inhomogeneity h of the heat equation (1) is determined by the distribution of the pump power, its absorption and the heat efficiency. In case the pump light propagates in the direction of the (positive) z -axis, enters the crystal at $z = -d/2$ and is reflected at the back of the crystal at $z = d/2$, d being the thickness of the crystal. The heat deposition is given by

$$h = \frac{\eta_h a P_p}{\pi w^2} \exp\left\{-\frac{r^2}{w^2}\right\} \times \left(\exp\left\{-a\left(\frac{3d}{2} - z\right)\right\} + \exp\left\{-a\left(\frac{d}{2} + z\right)\right\} \right) \quad (28)$$

where η_h is the heat efficiency, P_p is the total pump power, w is the pump spot radius in the crystal and a is the absorption coefficient. The maximum local tensile stress in the crystal is given by the maximum of the local stress components

$$\sigma_{\max} = \max(\sigma_r, \sigma_t, \sigma_z, \tau_{rz}). \quad (29)$$

The temperature distribution, the thermal expansion, the normal and shear stresses were calculated by a finite element program (FEM). The following values for the geometrical and thermal constants of the Yb:YAG were assumed (Table 2):

Table 2. Constants of Yb:YAG and parameters used for the calculation of thermal effects in the pumped crystal disk.

Name	Letter	Value	Unit
Thermal conductivity	κ	13.0	W/(m·K)
Thermal expansion	α	$9.3 \cdot 10^{-6}$	1/K
Module of elasticity	E	$280 \cdot 10^9$	N/m ²
Poisson ratio	ν	0.27	-
Heat efficiency	η_h	0.15	-
Coolant temperature	T_k	20.0	°C
Yb concentration	n	10.0	at %
Absorption coefficient [†]	a	0.83 (for $n=10$ at %)	1/mm
Diameter of the disk	D	5.0	mm
Thickness of the disk	d	0.75	mm
Radius of the pump spot	w	1.0	mm
Pump power	P_p	500	W

With these parameters the resultant heat deposition (Fig. 4) was calculated. As the assumed pump intensity profile is gaussian with a $1/e^2$ spot radius of 1 mm the heat is essentially dissipated in the central region of the crystal.

Thermal Properties of a 500 W diode-pumped Yb:YAG Disk
Heat deposition [W/mm³]

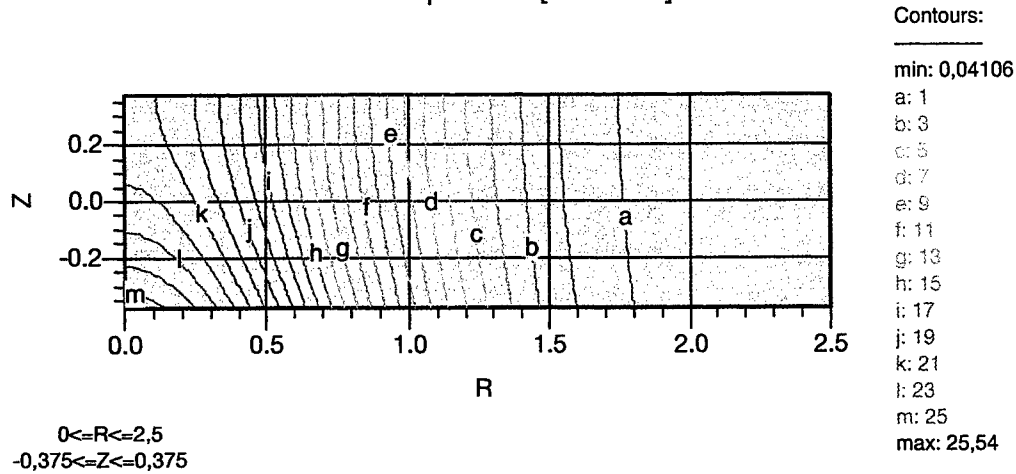


Figure 4. Calculated heat deposition in the Yb:YAG disk pumped with 500 W cw.

The temperature distribution in the axially cooled Yb:YAG disk laser is shown in Fig. 5. The inhomogeneous pumping light distribution results in a radial gradient and therefore leads to thermal effects on a beam propagating through the crystal. But as the gradient is small compared to the gradient along the beam propagation axis and as the crystal is very thin, the optical path difference between a central ray and a marginal ray is much smaller than in laser rods. Therefore the effect of thermal lensing in the disk laser is also very small. The optical path difference caused by higher order terms in the radial dependence is much smaller than the wavelength used and can be neglected.

[†] The absorption coefficient is given by the product of the absorption cross section $\sigma_{abs} = 6.0 \cdot 10^{-21}$ cm² and the density n of the active ions. ($n = 1.38 \cdot 10^{20}$ cm⁻³ per at% Yb concentration in YAG.)

Thermal Properties of a 500 W diode-pumped Yb:YAG Disk Temperature [C]

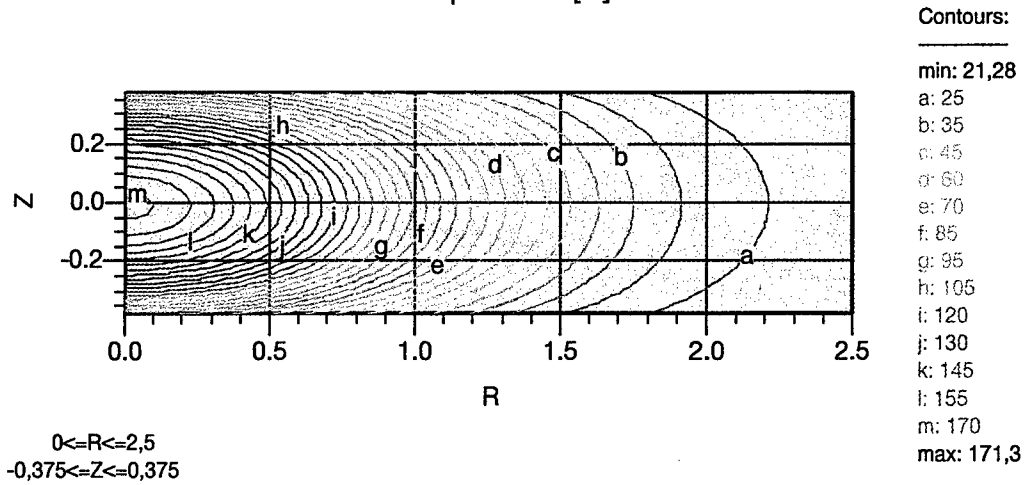


Figure 5. Calculated temperature distribution in the Yb:YAG disk pumped with 500 W cw.

In Fig. 6 the expansion behaviour of the pumped Yb:YAG disk is shown. As the pump light is concentrated in the centre of the disk and the crystal can expand nearly free in the z direction it takes a lenslike shape in inner region. The effect is small though as the physical difference of thickness (centre to rim) of the disk is approximately 1 μm (Fig. 7). The optical effect is much smaller because the refractive index of water is 3/4 of that of YAG.

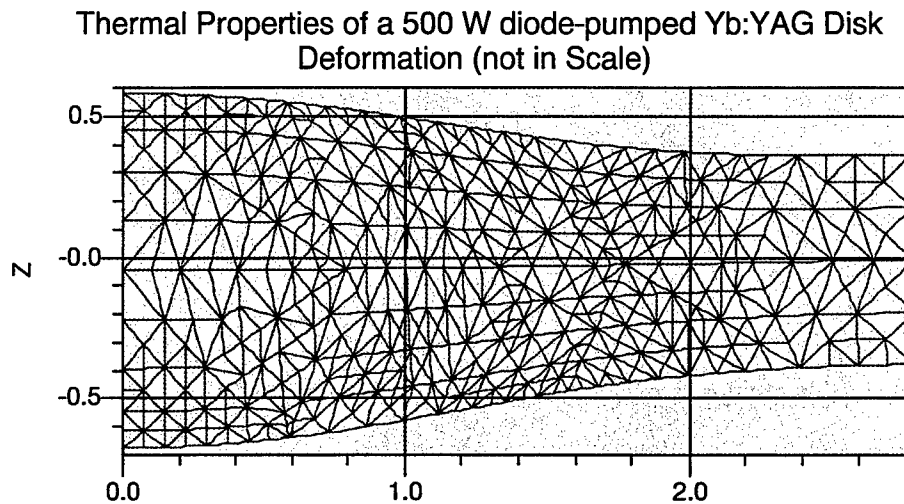


Figure 6. Calculated heat deformation of the Yb:YAG disk pumped with 500 W cw.
The expansion is exaggerated in this representation.

The axial expansion is displayed in detail in Fig. 7. Even though the temperature of the centre of the disk can be quite high, the overall expansion is small because of the small thickness of the disk.

Thermal Properties of a 500 W diode-pumped Yb:YAG Disk Axial Displacement [mm]

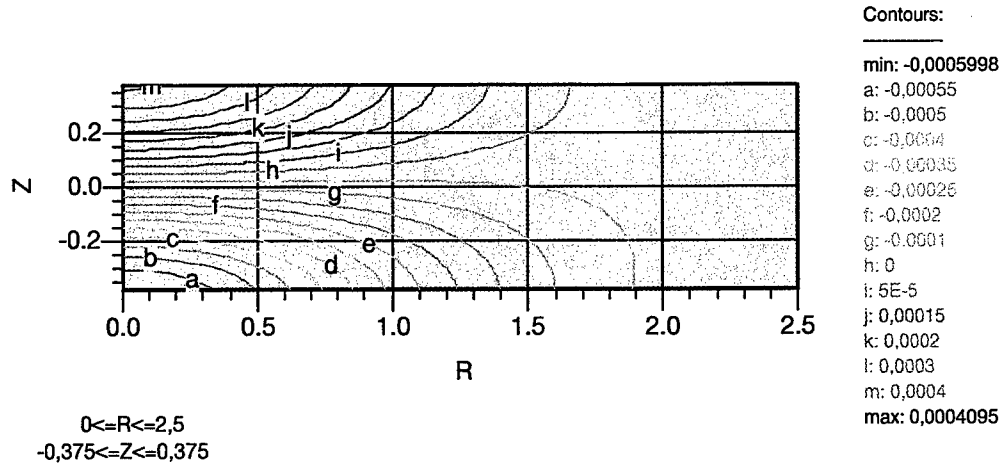


Figure 7. Calculated axial expansion of the Yb:YAG disk pumped with 500 W cw.

The upper limit of pump power is given by the fracture limit of the disk. The maximum local stress within the disk is given by the maximum of the local normal and the local shear stresses (see Equation (29)). The fracture limit of a crystal strongly depends on the crystal quality and its surface properties. As a rough estimate the tensile stress that leads to rupture is of the order of (150 ± 50) MPa.

Thermal Properties of a 500 W diode-pumped Yb:YAG Disk Maximum Stress [N/mm mm]

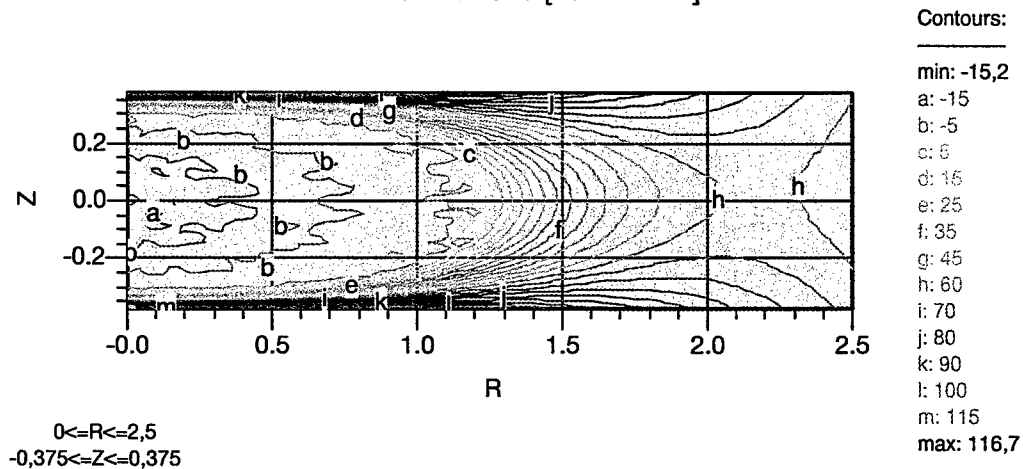


Figure 8. Calculated maximum stress in the Yb:YAG disk pumped with 500 W cw.

The maximum stress calculated for the Yb:YAG disk pumped by a cw power of 500 W is $\sigma_{\max} = 117 \text{ MPa}$ which is within the tolerances of the fracture limit. To apply a higher pump power would require a different concept for save operation. To reduce the stress the pump spot radius can be increased or the thickness of the disk can be decreased.

3.2 Quasi-Continuous-Wave-Operation with Yb:YAG and Nd:YVO₄

The configuration of the Yb:YAG laser is sketched in Fig. 9. The Yb concentration is 11 at % and the thickness of the crystal is 1.6 mm. The output coupler has a reflectivity of 81 % and a radius of curvature of 250 mm concave. The length of the resonator is 150 mm.

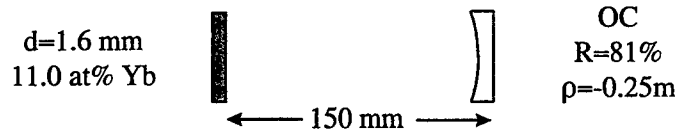


Figure 9. Set-up of the resonator for qcw operation with Yb:YAG

With this resonator an output power of 60 W in quasi continuous wave operation was realized. Due to the thickness of the crystal, a real cw operation would have led to a high temperature in the centre of the crystal and maybe to crystal fracture. As Yb:YAG is a quasi three level system the population of the lower laser level increases dramatically with the temperature. Therefore an efficient and save operation in real cw can only be realized with crystals thinner than 1 mm. The optical efficiency of 18 % in qcw operation can be further increased by reducing the temperature of the coolant.

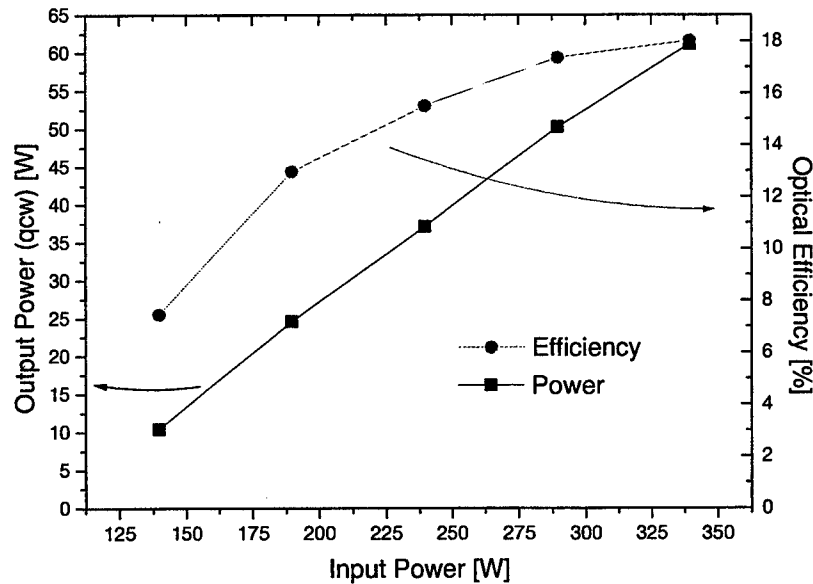


Figure 10. Measured output power and optical efficiency of the axially water-cooled Yb:YAG disk laser in qcw operation.

For the Nd:YVO₄ laser a crystal with a thickness of 0.6 mm and a Nd concentration of 3 at% is used. The output coupler has a reflectivity of 80.2 % and a radius of curvature of 250 mm concave. The resonator length L was varied between 125 and 240 mm. The pump pulse duration was $\tau_p=1\text{ms}$, i.e. the pump energy of 350 mJ equals a qcw pump power of 350 W and the maximum output energy of 113 mJ equals a qcw power of 113 W.

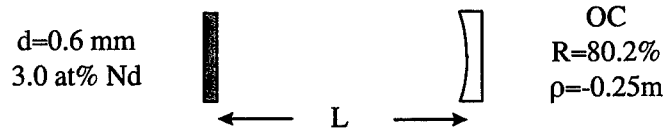


Figure 11. Set-up of the resonator for qcw operation with Nd:YVO₄

Comparing Fig. 12 to Fig. 10 the advantage of Nd:YVO₄ over Yb:YAG is quite obvious. With Nd:YVO₄ being a four level system the reabsorption losses are much smaller than in Yb:YAG and therefore the optical efficiency is much higher (32%). With approximately the same pump power the output power is about twice as high. A disadvantage of the Nd:YVO₄ system is that the heat efficiency is also higher but the fraction limit of the crystal is lower than it is in YAG. Therefore Nd:YVO₄ does not seem to be a good alternative to Yb:YAG or Nd:YAG in the high average power regime.

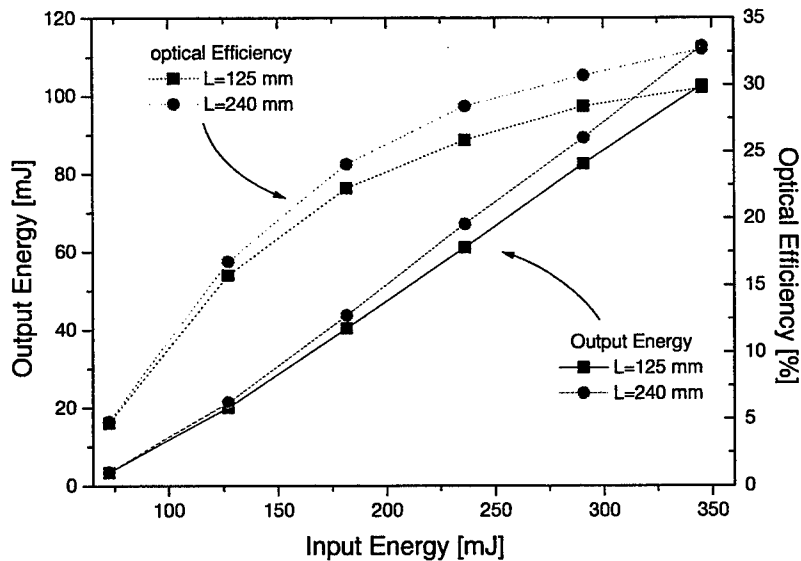


Figure 12. Measured output energy and optical efficiency of the axially water-cooled Nd:YVO₄ disk laser in qcw operation. The pump pulse duration was $\tau_p=1\text{ms}$.

The variation of the resonator length shows only little influence on the output energy. This is (as discussed in chapter 3.1) because thermal effects in the disk laser are much smaller than they are in rod lasers.

4. CONCLUSION

The beam shaping technique of the „Beam Twister“ proved to be a simple and straight forward concept of a transformation system to turn the astigmatic emission of a stacked diode array into a radially symmetric beam. This stigmatic beam then served as a stable and reliable pump source for an axially cooled disk laser. The disk laser was operated with Yb:YAG or Nd:YVO₄ crystals. With the Yb:YAG a qcw output power of 60 W at an optical efficiency of 18 % was realized. The Nd:YVO₄ laser emitted 113 mJ within 1 ms at an optical efficiency of 32 %. At this time there are still some limitations due to insufficient cooling, but we believe a real cw output power in the order of 60 W can be realized with an axially cooled Yb:YAG disk laser. The step hereafter will be the investigation of a side pumped disk laser as scaling the output power of the laser is much easier in a side pumped system than in an end pumped one.

ACKNOWLEDGEMENTS

This work was supported by the German Ministry of Education, Science, Research and Technology (BMBF) under the contract numbers 13 N 6802 and 13 N 7294.

REFERENCES

1. T. Brand, B. Ozygus and H. Weber, „Diode-Pumped Solid-State Lasers in the kW Range“, *Laser Physics*, Vol. 8, pp. 1-5, 1998
2. T. Brand, „Compact 170-W continuous-wave diode-pumped Nd:YAG rod laser with a cusp-shaped reflector“, *Opt. Lett.*, Vol. 20, pp. 1776-1778, 1995
3. D. Golla, S. Knoke, W. Schöne, A. Tünnermann and H. Welling, „300 W cw Diode-Laser Side-Pumped Nd:YAG Laser“, *Opt. Lett.* Vol. 20, pp. 1148, 1995
4. W. A. Clarkson, A. B. Neilson and D. C. Hanna, „Diode laser bar beam shaping technique“, *Digest of CLEO Europe 94*, CFH 6
5. W. A. Clarkson and D. C. Hanna, *Opt. Lett.*, Vol. 21, pp. 375, 1996
6. J. K. Jabczynski, „Laser diode beam shaping for end pumped lasers“, *Proc SPIE*, Vol. 2772, pp 238-249, 1996
7. A. Friberg, C.Gao, B. Eppich and H. Weber, „Generation of Partially Coherent Fields with Twist“, in *Optical Engineering in Israel*, I. Shladov and S. R. Rotman, eds., *Proc SPIE*, Vol. 3110 (1), pp 317-328, 1997
8. C. Hönninger, I. Johannsen, M. Moser, G. Zhang, A. Giesen and U. Keller, „ Diode pumped thin disk Yb:YAG regenerative amplifier“, *Appl. Phys. B*, Vol. 65, pp. 423-426 (1997)
9. S. Timoshenko and J. N. Googier, *Theory of Elasticity*, McGraw-Hill, New York, 1951
10. A. K. Cousins, „Temperature and Thermal Stress in Finite-Length End-Pumped Laser Rods“, *IEEE J. Quantum Electron.*, Vol. QE-28, pp. 1057-1069, 1992

Requirements on pump-diodes for diode-pumped solid state lasers

Hermann Grempel^b, Nikolay I. Katsavets^a, Alexander L. Ter-Martirosyan^a, Christoph v. Kopylow^b, Egon Pfeifer^b

^aATC-SEMICONDUCTOR DEVICES, P.O. BOX 29, ST. PETERSBURG, 194156
RUSSIA

^bBremLas Lasertechnik Bremen GmbH, Fahrenheitstrasse 1, D-28359 Bremen,
Germany

ABSTRACT

We report on the influence of the different specifications of a single emitter laser diode (type A) and a laser diode (LD) of the partially phase locked type (type B), on some characteristics of our diode pumped solid state lasers (DPSSL). We find that the use of the type B LD is preferable to that of type A with respect to smaller M^2 of the DPSSL-beam, superior noise behavior, and smaller full width at half maximum (FWHM) of the LD emission.

Keywords: DPSSL, LD, beam quality, M^2 , intra cavity frequency doubling

1. INTRODUCTION

In the recent years, diode pumped solid state lasers (DPSSL) have gained an important role in the laser market. This is because of the unique advantages that DPSSLs offer compared to e.g. gas lasers. In the fields where DPSSLs are applied, the demands on the performance of the lasers are quite high. Life time of the DPSSL should be well above 10,000 hours, the beam should be Gaussian-shaped with an M^2 smaller than 1.2, and noise has to be lower than 1 %.

Besides the construction of the cavity and the elements building the cavity, the characteristics of the pumping diode has a significant influence on the performance of the DPSSL.

2. DESCRIPTION OF THE LASER SYSTEM

The DPSSL under consideration is an end-pumped intra cavity frequency doubled micro chip laser. The radiation of the LD is focused into the laser crystal by pump optics. The cavity consists of a Nd:LSB laser crystal and a KTP-crystal for frequency doubling. The mirrors of the cavity are built by dielectric layers on the outer side of the LSB- and KTP-crystal, which are high reflective for the fundamental wavelength at 1064 nm. To couple out the second harmonic, the dielectric layer at the outer side of the KTP-crystal is high-transmittive at 532 nm.

Some characteristics of the LDs are shown in Table 1.

	Type A	Type B
emitting surface	200 μm x 1 μm	150 μm x 1 μm
optical output power	1 W	1 W
expected life time	> 10,000 h	> 10,000 h
type	single emitter	partially phase-locked laser array

Table 1: characteristics of LDs of type A and type B

3. DESIRED AND ACTUAL CHARACTERISTICS OF THE LDs AND THEIR INFLUENCE ON THE PERFORMANCE OF THE DPSSL

3.1 Spectral characteristics of the LDs

To pump the laser crystal effectively, the center wavelength of the emission spectrum of the LDs should coincide with the absorption maximum of Nd:LSB at 808 nm. The FWHM of emission spectrum should be smaller than the FWHM of the Nd:LSB-crystal, which is 3 nm. In Table 2, some of the emission characteristics of the LDs are shown. The emission spectra of about 40 pieces of each LD-type have been taken into account.

	Type A	Type B
average deviation of the center wavelength of emission from 808 nm, LD temperature: 20 C	+/- 0.14 nm	+/- 0.53 nm
average FWHM	(2.50 +/- 0.81) nm	(1.49 +/- 0.62) nm
relative number of LDs with FWHM > 3nm	20.93 %	0 %

Table 2: Some characteristics of the LD's emission spectra. Type B is superior to type A with respect to its smaller FWHM.

From Table 2 it can be seen, that the average deviation of the center wavelength of the LD emission from the desired center wavelength at 808 nm is bigger for type B than for type A. In any case, it has been possible to tune the center wavelength of the diodes to 808 nm by adjusting the their temperature between 15 C and 35 C. With respect to their smaller FWHM, the type B LDs are superior to the type A LDs.

3.2 The influence of the LD-type on the DPSSL beam quality

To achieve a Gaussian beam-shape, the pump-volume should lie within the volume of the TEM₀₀-cavity mode. The better this requirement is fulfilled, the closer will the value of M^2 be to 1. In Table 3, the average M^2 of the beam of the DPSSL is evaluated for DPSSLs pumped by type A and type B laser diodes.

	Type A	Type B
M^2 of the DPSSL-beam	1.36 +/- 0.29	1.24 +/- 0.13

Table 3: Average M^2 -value of the DPSSL-beam for DPSSLs pumped by type A of by type B laser diodes. Type B is superior to type A because smaller M^2 -values can be achieved.

For pumping with type B LDs, the average value of M^2 is lower. We ascribe this to the smaller emitting area of the type B LDs. Furthermore, if we tried to achieve an M^2 -value smaller 1.2 for an DPSSL pumped by a LD of type A, this was only possible if the pump-beam impinged near the edge of the laser crystal. We presume that part of the pump beam is cut by the holder in this case and the pumping volume is reduced in that way.

Usually, the quality of the crystal and the layer is reduced near the edge of the crystal. Therefore, in the manufacturing process, it takes a lot of time, to find an area with acceptable quality of layers and crystal. Moreover, these areas are usually rather small. In consequence, just very small disalignment, e.g. induced by thermal expansion, may be enough to enhance the M^2 -value or to reduce the output power of the DPSSL. Therefore, we expect the DPSSLs pumped by type B LDs to show superior stability.

3.3 Comparison of the noise behavior of type A and type B LDs

For many applications, the output noise of the DPSSL has to be lower than 1 %. In the kind of DPSSL laser considered here, one of the main contributions to noise arises from mode competition. It is therefore desirable, to minimize all additional contributions to noise. Because of this reason, we examined the noise behavior of type A and type B LDs. While scanning temperature and pumping current of the LDs, the noise has been measured. In the case of type A LDs, broad areas with noise up to 6 % were detected. In the case of type B LDs, the noise has been smaller than 0.5 % nearly in the whole scanning region.

4. SUMMARY

We compared some characteristics of a single emitter LD to that of a partially-phase locked laser array. The partially-phase locked laser array LD showed a smaller FWHM of its emission spectrum and lower amount of noise in its optical output power. If we pumped our DPSSLs by the partially-phase locked laser array LD, the average value of M^2 of the DPSSL-beam was closer to 1, compared to the case that we used the single emitter LD-type as a pumping source.

In conclusion, we prefer the partially-phase locked laser array for the production of our DPSSLs.

5. ACKNOWLEDGMENTS

BremLas would like to thank ATC SEMICONDUCTOR DEVICES for providing the type B LDs.

Nd:CSB-laser pumped by laser diode array

O.V.Kuzmin, S.A.Kutovoi, V.L.Panyutin -

SPA "FIRN" Krasnodar, Russia

S.T.Durmanov, J.P.Rudnitskiy, G.V.Smirnov -

TRINITI, Troitsk Moscow reg., Russia

A.J. Abazadze, M.N.Grudin, J.M.Kolbatskov, J.P.Koval -

R&D Institute «Polyus», Moscow

In present research we investigated laser performance of Czochralski-grown $\text{CeSc}_3(\text{BO}_3)_4$ (CSB) crystals¹ with high levels of neodymium concentration 25 at.% and 20 at.%. For our experiments Nd:CSB bulks were fabricated 1.5x1.5 mm in pumping axes by 10 mm long. Quasi-CW laser diode 1-cm array with peak power up to 50 W manufactured by R&D Institute "Polyus" was used to pump Nd:CSB-crystal. The pump was close coupled to the polished side of the bulk (Fig.1). Our experiments were carried with resonator consisted of a 20 cm concave high reflector and a flat output coupler separated by 12 cm, the calculated TEM_{00} diameter at the $1/e^2$ -intensity value was 0.13 mm.

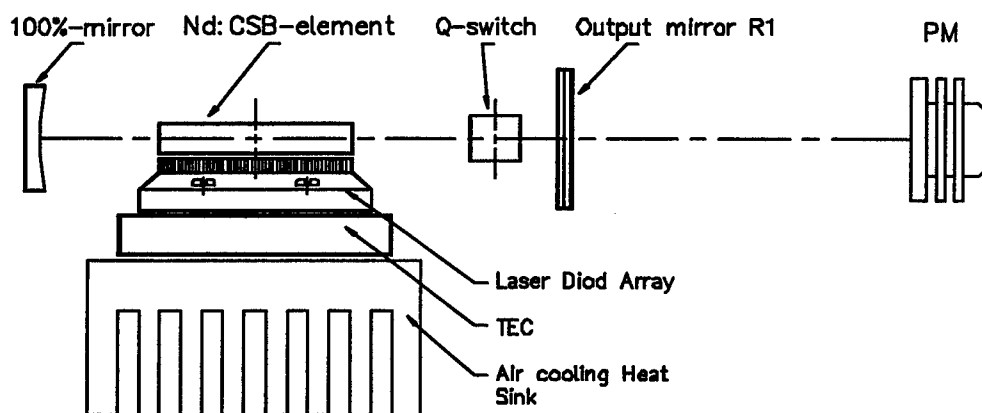


Fig.1: Layout of the Q-switched Nd:CSB-laser.

We measured Nd:CSB laser output versus pumping energy in 200- μsec -long pulses using output couplers with different transmissions 7, 12 and 24 at.% near 1.0625 μm . Under the most effective performance conditions Nd:CSB (25 at.%) and Nd:CSB (20 at.%) lasers output of about 2 mJ per pulse with an optical efficiency of 22% was demonstrated (Fig.2,a and b). Nd:CSB (25 at.%) laser output was TEM_{00} , because of the overlap of pump light and fundamental mode was better than for other modes case² (Fig.3,a). But output of Nd:CSB (20 at.%) laser was more effective for beam consisted of higher transverse modes (Fig.3,b). Maximum output 1.0625 μm pulse energy was observed when laser-diode output was at near 801.5 nm - for Nd:CSB (25 at.%) crystal, and at near 806.5 nm - for Nd:CSB (20 at.%) crystal. Stability of Nd:CSB (25 at.%) laser output was of $\leq 10\%$ according to environment temperature varying of 5°C (Fig.4). Comparison of fundamental mode operated diode-laser side-pumped Nd:YAG and Nd:CSB (25 at.%) lasers showed that the second is sufficiently more effective than the first one (Fig.5).

In Q-switched operation of Nd:CSB (25 at.%) an output of 220 μJ in a 30 ns (FWHM) a TEM_{00} - mode pulse was obtained using GSGG:Cr³⁺ saturable absorber with a small signal transmission of about 80% in a 20 cm concave-flat resonator.

Acknowledgments: This work was supported by ISTC under the project #251-96.

References:

1. O.V.Kuzmin, G.M.Kuzmicheva, S.A.Kutovoi, A.A.Martinov, V.L.Paniutin, V.I.Chizhikov, *Sov. J. Quantum Electr.* 24, No. 1, (1998)
2. P.Meyn, T.Jensen, and G. Huber, *IEEE J. Quantum Electron* 30, 913, (1994)

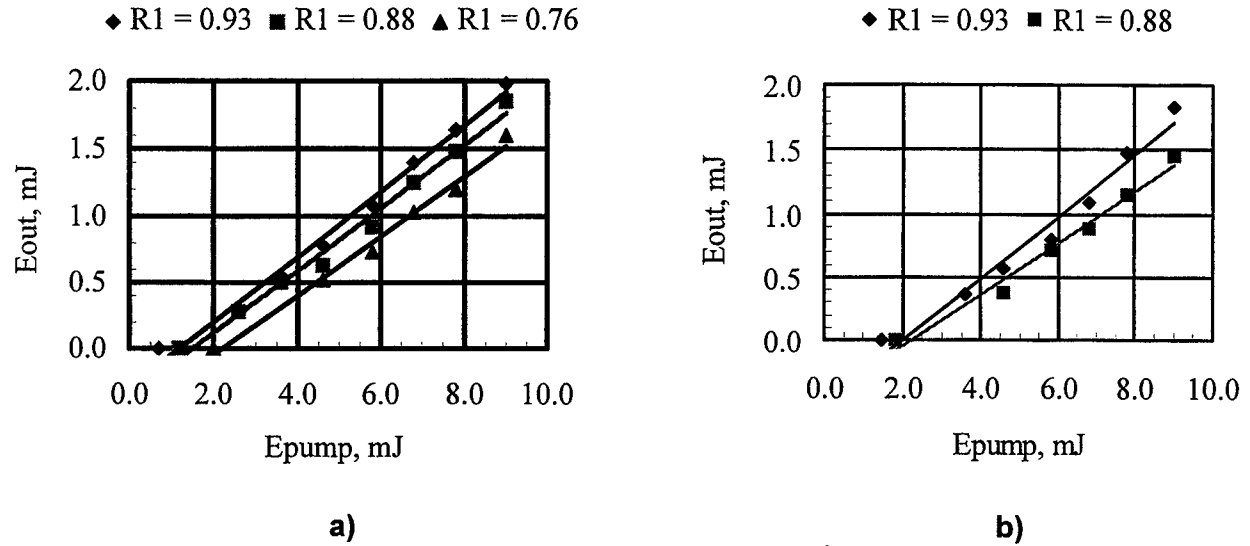


Fig.2. Output energy versus pump energy for Nd:CSB-laser: a) Nd³⁺[25 at.%], $\lambda_p=801-802$ nm, b) Nd³⁺[20 at.%], $\lambda_p=806-807$ nm.

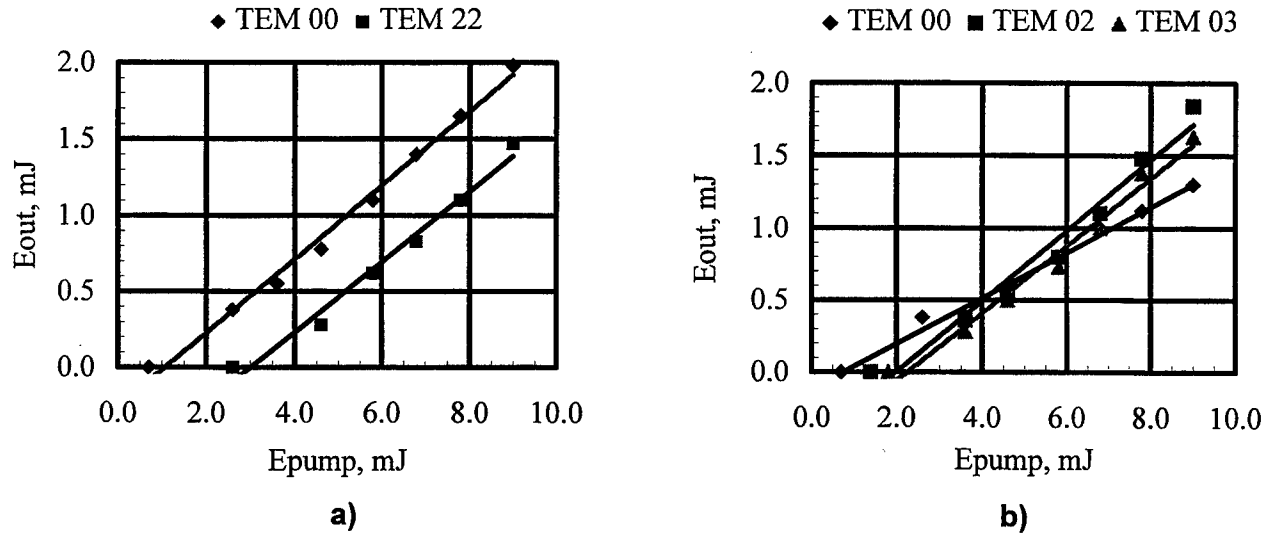


Fig. 3 Comparison of Nd:CSB-laser outputs for TEM₀₀- and TEM₁₁-transverse modes, R1= 0.93: a) Nd³⁺[25 at.%], b) Nd³⁺[20 at.%].

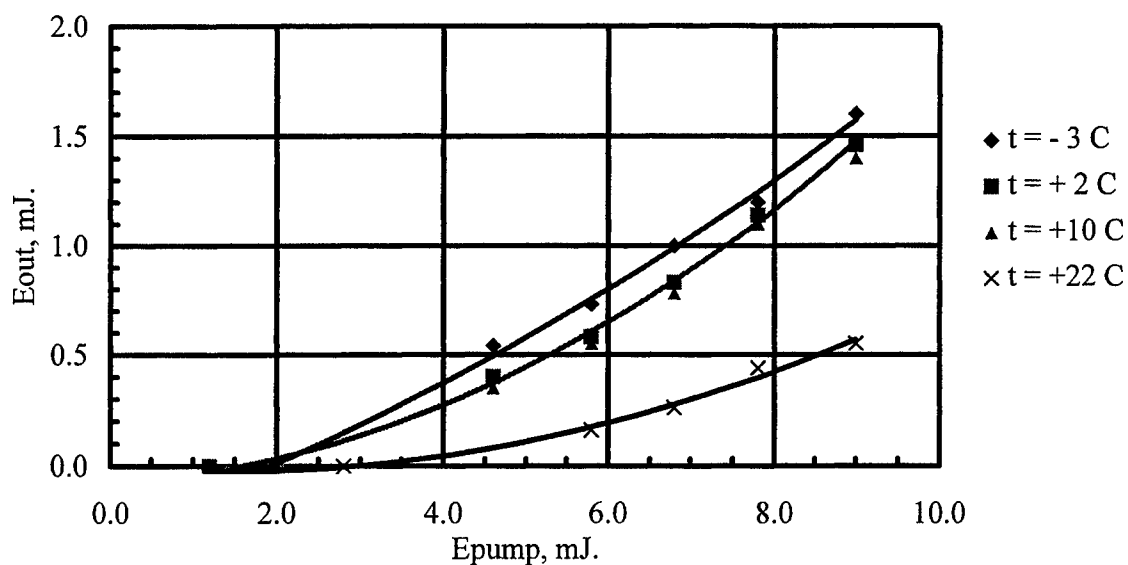


Fig. 4. Temperature dependence of CSB:Nd³⁺[25at.%]-laser output. Output coupler R1 = 0.76, TEM₀₀-mode operation.

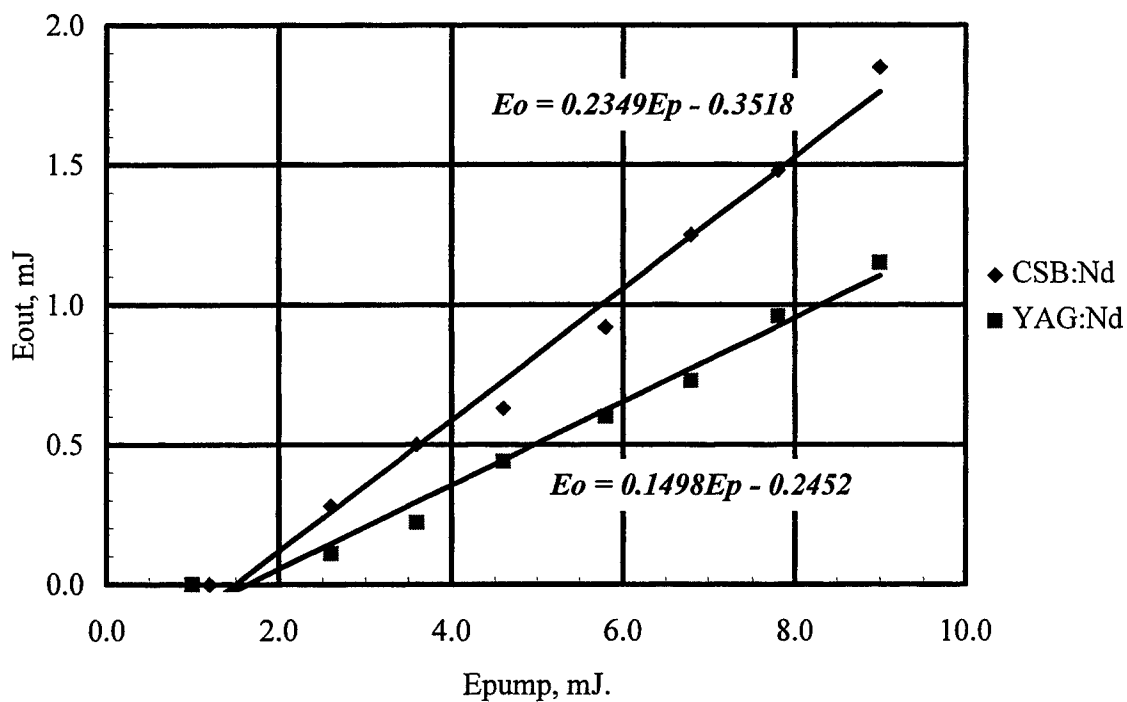


Fig. 5. Comparison of single transverse TEM₀₀-mode outputs of CSB:Nd³⁺[25 at.%]- and Nd:YAG lasers. R1 = 0.88

Polarization dynamics of Nd:YAG laser with weakly anisotropic Fabry-Perot cavity

P. Khandokhin^a, N. Milovsky^b, Yu. Mamaev^a, E. Ovchinnikov^a, E. Shirokov^a

^aInstitute of Applied Physics, Russian Academy of Science, 46 Ulyanov Street,
603600 Nizhny Novgorod, Russia

^bDepartment of Radiophysics, Nizhny Novgorod State University, 23 Gagarin
Ave., 603600 Nizhny Novgorod, Russia

ABSTRACT

Orthogonally polarized modes have been operated in a Nd:YAG laser with weakly anisotropic cavity. Different intensity dependences of the orthogonal modes on the orientation of the pump polarization plane are discovered. The power spectrum of each polarization mode reveals three relaxation peaks in a good agreement with predictions of the laser model modified to include polarization effects.

1. INTRODUCTION

The polarization of laser emission is known to be determined by both the cavity anisotropy (birefringence, anisotropy of losses) as well as by the anisotropy of active medium gain (crystals with definite direction of dipole moments of active centers, active media in magnetic field, lasers with polarized pump laser). The absence of such a strong factor as anisotropy of losses for orthogonally polarized modes leads to joint lasing of these modes. It was found ^[1-3] that in the weakly anisotropic cavity the excitation thresholds of fiber laser orthogonally-polarized modes and their intensities depend on the orientation of the polarization plane of a pump laser. It was shown in papers ^[4,5] using a dye laser as the example (a laser with inertialess active medium – so called class *A* laser) that the use of the pump laser source with linearly polarized emission leads to the gain anisotropy. This, in its turn, causes the experimentally discovered effect of the orientation of the pump polarization plain on the intensities of polarized modes. The model of the bipolarized class *B* laser with Fabry-Perot cavity was developed in papers ^[2,3] to explain the observed effects in lasers with inertial active medium. Unlike the class *A* lasers here we should take into account the differential connection between the laser field and the population inversion. Therefore we cannot apply directly the results of investigations ^[4,5] to solid-state lasers. In the mentioned papers ^[2,3] gain anisotropy was taken into account phenomenologically via the pump parameter depending on the orientation of the pump polarization plane. When choosing the type of this dependence it was taken into account that the number of active centers is maximum for collinearly-oriented dipoles and has the minimum for orthogonally-oriented dipoles. Following the ideas of papers ^[4,5], the attempt was made in paper ^[6] to perform a more consistent quantum-mechanic derivation of the expression for the pump parameter. But here the authors did not take into account the effect of saturation in the orientation distribution of active centers due to the pump intensity leading to the decrease of the gain anisotropy with the increase of the pump intensity predicted in papers ^[4,5].

The present paper discusses the theoretical investigation and experiments performed to study the effect of pump polarization on dynamical and fluctuation parameters of a solid-state Nd:YAG laser with a weakly anisotropic Fabry-Perot cavity. The developed model is shown to be suitable to describe the specific features of polarization dynamics observed in the experiments. In the given equations, the expression for the pump parameter, which takes into account the influence of the emission intensity of the pump laser on the gain anisotropy, is used.

2. EXPERIMENTAL SETUP

The experimental setup is shown in Fig. 1. The pump source is a semiconductor laser at $0.81 \mu\text{m}$

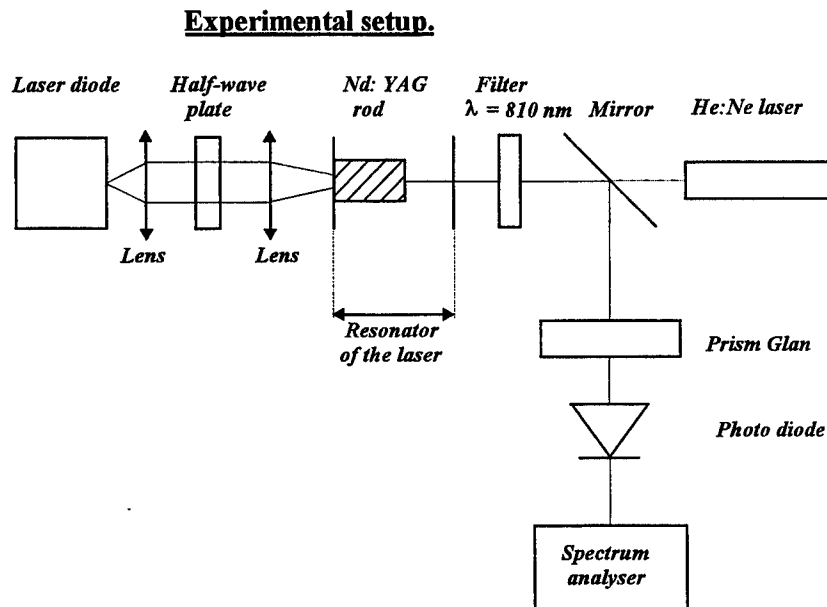


Figure 1.

wavelength. Polarization is linear. A half-wave plate located between two focusing lenses was used to rotate the direction of pump polarization. We employed a Nd:YAG crystal 1 cm long and 0.6 cm in diameter as the active laser medium. One crystal face with dichroic coating acted as an input cavity mirror ensuring high reflection at $1.06 \mu\text{m}$ operating wavelength and high transparent light at pump wavelength. The other crystal face with antireflection coating was transparent at $1.06 \mu\text{m}$ close to unity. We used an isotropic mirror with 99.5% reflection at $1.06 \mu\text{m}$ as an output cavity mirror. The cavity was 2.3 cm long. As the refraction index of Nd:YAG crystal n equaled 1.8, then the length corresponded to the optical length of 3.1 cm and to the interval between adjacent longitudinal cavity modes about 5 GHz. A filter was placed at the cavity output to block the stray pump laser radiation. The Glan prism was employed as an analyzer of laser output. The Nd:YAG laser signal was given to a photodiode whose output was connected with a spectroanalyzer. The maximum output power of the Nd:YAG laser was 2 mW. A He:Ne laser was used for alignment.

3. EXPERIMENTAL RESULTS

In the experiment we studied the effect of pump polarization on the intensity of polarization modes in a Nd:YAG laser. The strong polarization mode corresponded to such position of the analyzer when its transmission was maximal. The minimum analyzer transmission corresponded to a weak mode whose polarization was orthogonal relative to the strong mode. Rotation of the pump polarization direction Ψ_0 led to antiphase change in photocurrents I_1, I_2 with period $\Delta\Psi_0 = 180^\circ$. Fig. 2 shows

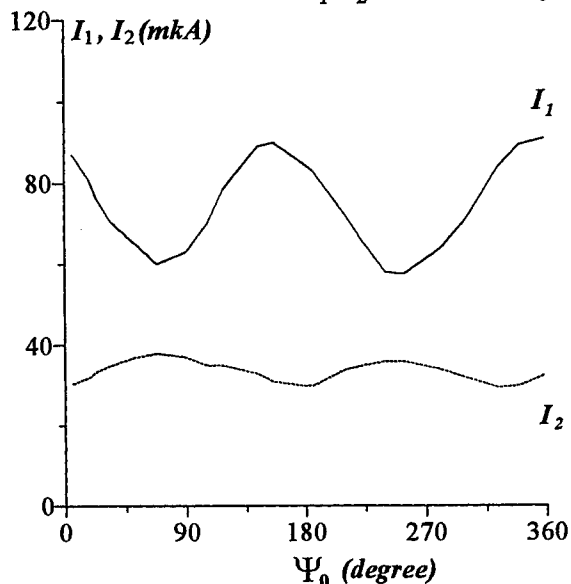


Figure 2. The dependence of the intensities I_1, I_2 on the direction Ψ_0 of the pump polarization at $A=1.2$

the dependence of the intensities I_1, I_2 on the pump polarization direction Ψ_0 when pump parameter $A=1,2$ is constant. The dependence of I_1, I_2 on the pump parameter in two fixed positions of the half-wave plate $\Psi_0=0^\circ$ and $\Psi_0=90^\circ$ is presented in Fig. 3.

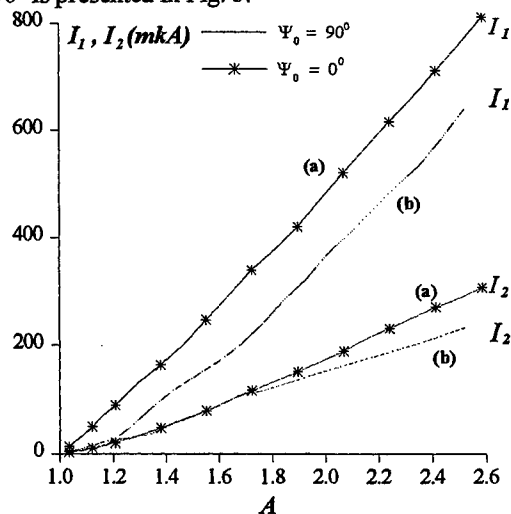


Figure 3. The dependencies of I_1, I_2 on the pump parameter at (a) $\Psi_0=0^\circ$ and (b) $\Psi_0=90^\circ$

The power spectra of the polarization modes I_1 , I_2 are shown in Fig.4. Along with a high-frequency peak at Ω_0 that corresponds to the main relaxation oscillation, there are two low frequency peaks at Ω_1 , Ω_2 in the spectra. The same figure shows the power spectrum I_{PR} obtained in some intermediate position of the analyzer. The low frequency peaks are not present in this case indicating

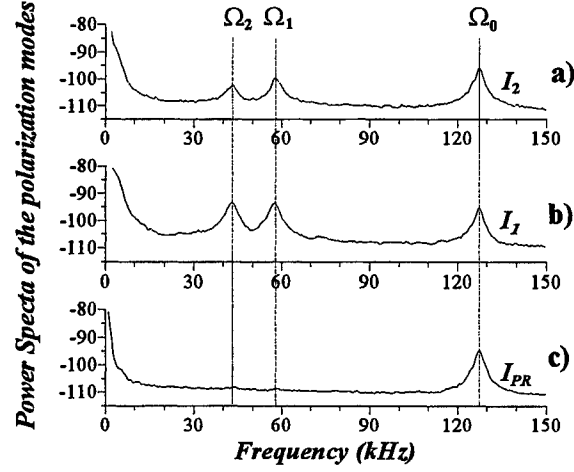


Figure 4. The power spectra of the polarization modes at $A=1.4$.
Here $I_{PR} \sim I_1 + I_2$

antiphase character of relaxation oscillations at Ω_1 , Ω_2 . Fig. 5 presents the dependence of relaxation frequencies $\Omega_{0,1,2}$ on pump parameter when position of the half-wave plate is fixed.

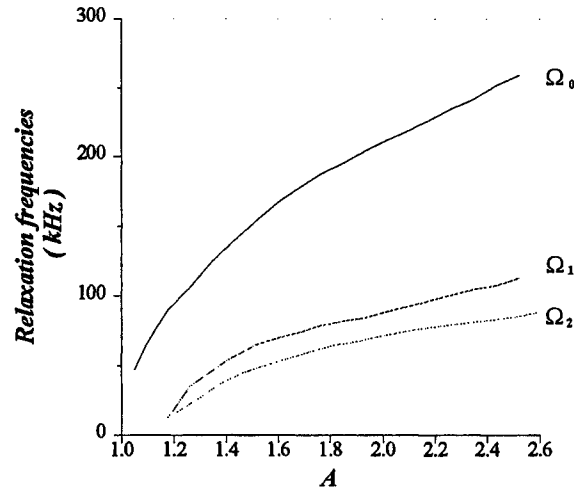


Figure 5. The dependence of relaxation frequencies on pump parameter
at $\Psi_0 = 0^\circ$

Here we studied also the effect of orientation of pump polarization plane on mode lasing thresholds I_1 , I_2 (Fig. 6). It is clearly seen in Fig. 6 that one of the polarization modes dominates over other mode with respect to the lasing threshold.

The problem of how pump polarization affects the intensity of spontaneous emission was studied on an experimental setup where there was no output cavity mirror. During rotation of the half-wave plate, the azimuth of maximum of spontaneous emission intensity also rotated. When the position of the half-wave plate was fixed, the maximum and minimum of spontaneous emission were shifted at an angle close to 90° on the analyzer scale. The ratio I^{\min}/I^{\max} of spontaneous emission is close to 0.7.

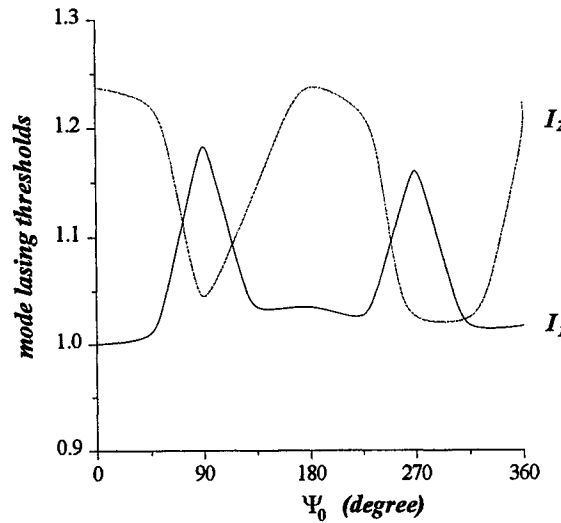


Figure 6. The dependence of the polarization mode thresholds on the direction of the pump polarization plane.

The main experimental results are as follows:

- 1) A strong dependence of the intensities of polarization modes on the direction of pump polarization is observed.
- 2) Two additional low frequency relaxation peaks, along with the high frequency relaxation peak, are observed in the power spectrum of each polarization mode.
- 3) There is a certain position of an analyzer when the low frequency relaxation peaks are absent indicating the antiphase character of these relaxation oscillations.
- 4) Maximum of spontaneous emission follows the rotation of the pump polarization plane.

4. MODEL OF THE BIPOLARIZED LASER

An important factor in the dynamical behavior of solid-state lasers with a weakly anisotropic cavity is a collective interaction of all longitudinal modes of one polarization (first polarized mode) with the whole ensemble of modes of the orthogonal polarization (second polarized mode). So, when constructing a model to adequately describe the key features of laser dynamics we have to consider the interaction of two orthogonally-polarized modes. Let us consider the field as decomposition in two orthogonally-polarized cavity eigenmodes. The total field inside the laser cavity E is of the form

$$E = (E_1 U_1 + E_2 U_2) e^{i\omega t} + c.c. \quad (1)$$

Here $U_{1,2}$ are the orthogonal eigenmodes of the laser cavity, $E_{1,2}$ are the slowly varying amplitudes of fields with orthogonal polarizations, ω is the carrier optical frequency. Eigenmodes $U_{1,2}$ are defined by the expression

$$U_m = \sqrt{2} e_m^0 \sin k_m z, \quad m=1, 2 \quad (2)$$

where e_m^0 are unit eigenvectors of the cavity

$$e_1^0 = x^0 \cos R + y^0 \sin R, \quad (3)$$

$$e_2^0 = x^0 \sin R - y^0 \cos R,$$

x^0, y^0 are the Cartesian unit vectors, R is an angle between vectors x^0 and e_1^0 (see Fig.7).

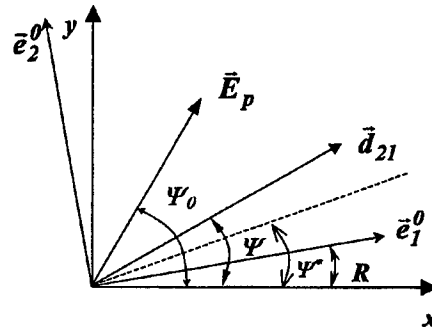


Figure 7. The disposition of the eigenvectors, the pump field vector, and the vector of active dipoles in the Cartesian coordinates

In crystals, active ions take quite definite positions inside the cell unit of crystal lattice. In Nd:YAG crystal there are 3 such equally likely positions. Therefore we may expect that the dipole moments of the active ions will be oriented around several definite directions in space yet preserving the isotropic properties of the crystal as a whole. Depending on the technology used to fabricate the active element its axis (that usually coincide with the cavity axis) may not coincide with the axis of isotropic dipole distribution. We will therefore assume for simplicity that active dipoles are linearly polarized and part of them is randomly oriented in the plane orthogonal to the laser axis

$$d_{21}^0 = d_{21} / |d_{21}| = (x^0 \cos \Psi + y^0 \sin \Psi) \quad (5)$$

(the angle- Ψ value ranges from 0 to π) and the rest part of dipoles is oriented along Ψ^* direction

$$d_{21}^0 = (x^0 \cos \Psi^* + y^0 \sin \Psi^*) \quad (6)$$

Let us present the angular distribution of dipoles as a sum of isotropic and anisotropic parts:

$$f_{or}^0(\Psi) = \Phi_1/\pi + \Phi_2 \delta(\Psi - \Psi^*). \quad (7)$$

The linearly polarized pumping oriented along the direction Ψ_0 modifies the angular distribution of active dipoles ^[4,5] as follows:

$$f_{or}(\Psi) = f_{or}^0(\Psi)F(\Psi - \Psi_0)$$

$$F(\Psi - \Psi_0) = b \cos^2(\Psi - \Psi_0) / (1 + b \cos^2(\Psi - \Psi_0)). \quad (8)$$

Here $b = E_p^2 \tau_2 \mu_p^2 / \hbar^2$, E_p^2 is the intensity of pump field, μ_p is the dipole moment of the absorption line of the active ion and τ_2^{-1} is the homogeneous absorption line halfwidth of the pump emission.

The laser model, which takes into account the interaction of the laser field (1) with the dipoles that have the angular distribution (8), is described by a set of equations [7]:

$$\frac{dE_m}{d\tau} = i \frac{\Delta_{cm}}{2} E_m - \frac{G}{2} E_m + \frac{G}{2\pi L} \iint d_{21}^0 (d_{21}^0 E) (N + D) U_m^* dz d\Psi,$$

$$\frac{dN}{d\tau} = A_1 - N \left(1 + |d_{21}^0 E|^2 \right), \quad A_1 = \Phi_1 A F(\Psi - \Psi_0) / \pi$$

$$\frac{dD}{d\tau} = A_2 - D \left(1 + |d_{21}^0 E|^2 \right), \quad A_2 = \Phi_2 A F(\Psi^* - \Psi_0) \quad (9)$$

Here $m=1, 2$; $G=2\kappa/\gamma_{\parallel}$, $\tau=t\gamma_{\parallel}$, $\Delta_{cm} = (\omega - \omega_{cm})/\gamma_{\perp}$, where γ_{\parallel} , κ are the inversion and the field relaxation rates, respectively, γ_{\perp} is the homogeneous gain line halfwidth. The variables N , D describe the inversion of the randomly-oriented and unidirectionally-oriented dipoles of the active ions, respectively.

The interaction of the linearly polarized field with the ensemble of randomly oriented dipoles results in an azimuth-inhomogeneous distribution of inversion N (the effect of angular hole burning):

$$N = N^0 + 2N^c \cos 2\Psi + 2N^s \sin 2\Psi + \dots \quad (10).$$

Each angular harmonic of the inversion N^i ($i = 0, c, s$) and inversion D consist of a space-uniform component and spatial harmonics. The latter are determined by the individual action of each mode (spatial hole burning) and by the joint action of the modes whose wave numbers k_1 and k_2 are different:

$$N^i = N_0^i + 2N_1^i \cos(2k_1 z) + 2N_2^i \cos(2k_2 z) + 2N_{12}^{i-} \cos(k_1 - k_2)z + 2N_{12}^{i+} \cos(k_1 + k_2)z.$$

$$D = D_0 + 2D_1 \cos(2k_1 z) + 2D_2 \cos(2k_2 z) + 2D_{12}^- \cos(k_1 - k_2)z + 2D_{12}^+ \cos(k_1 + k_2)z. \quad (11)$$

In the present paper we will discuss only rate equation approximation that is quite sufficient to qualitatively explain the behavior of polarization mode intensities observed in the experiment. The studies where the phase-sensitive modal interaction is taken into account will be reported further. Besides, for simplicity we will neglect the angular harmonics of spatial gratings. Finally we yield the following 10th order rate equation model:

$$\dot{I}_1 = G I_1 \left[N_0^0 + N_1^0 + N_0^c \cos 2R + N_0^s \sin 2R + D_0 + D_1 - I \right]$$

$$\dot{I}_2 = G I_2 \left[N_0^0 + N_2^0 - N_0^c \cos 2R - N_0^s \sin 2R + D_0 + D_2 - I \right]$$

$$\dot{N}_0^0 = A_1 - N_0^0 (I + I_1 + I_2) - N_0^c (I_1 - I_2) \cos 2R - N_0^s (I_1 - I_2) \sin 2R - (N_1^0 I_1 + N_2^0 I_2)$$

$$\dot{N}_0^c = A_1^c - N_0^c (I + I_1 + I_2) - \frac{1}{2} N_0^0 (I_1 - I_2) \cos 2R - \frac{1}{2} (N_1 I_1 - N_2 I_2) \cos 2R$$

$$\begin{aligned}
\dot{N}_0^s &= -N_0^s(l + I_1 + I_2) - \frac{l}{2}N_0^0(I_1 - I_2)\sin 2R - \frac{l}{2}(N_1I_1 - N_2I_2)\sin 2R \\
\dot{N}_1 &= -N_1(l + I_1 + I_2) - \frac{l}{2}N_0^0I_1 - \frac{l}{2}N_0^cI_1\cos 2R - \frac{l}{2}N_0^sI_1\sin 2R \\
\dot{N}_2 &= -N_2(l + I_1 + I_2) - \frac{l}{2}N_0^0I_2 + \frac{l}{2}N_0^cI_2\cos 2R + \frac{l}{2}N_0^sI_2\sin 2R \\
\dot{D}_0 &= A_2 - D_0[l + I_1 + I_2 + (I_1 - I_2)T(\Psi^*)] - (D_1I_1 + D_2I_2) - (D_1I_1 - D_2I_2)T(\Psi^*) \\
\dot{D}_1 &= -D_1[l + I_1 + I_2 + (I_1 - I_2)T(\Psi^*)] - \frac{l}{2}D_0I_1(l + \cos 2(\Psi^* - R)) \\
\dot{D}_2 &= -D_2[l + I_1 + I_2 + (I_1 - I_2)T(\Psi^*)] - \frac{l}{2}D_0I_2(l - \cos 2(\Psi^* - R)) \quad (12) \\
A_1 &= A\Phi_1 \\
A_1^c &= [A\Phi_1(\sqrt{1+2b_0} - 1)/2b_0]\cos 2\Psi_0 \\
A_2 &= A\Phi_2\left\{1 + \frac{(\sqrt{1+2b_0} - 1)}{2b_0}\cos 2(\Psi_0 - \Psi^*)\right\}
\end{aligned}$$

5. THEORETICAL RESULTS AND DISCUSSION

We seek the nontrivial steady-state solution by numerical integration of the basic model (12). Fig.8 and fig.9 displays the behavior of the modes intensities I_1 and I_2 versus pump polarization direction Ψ_0 and versus pump parameter A respectively.

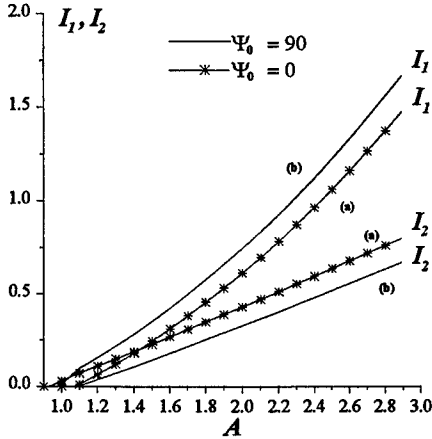


Figure 8. Theoretical dependencies of I_1, I_2 on the pump parameter at (a) $\Psi_0=0^\circ$ and (b) $\Psi_0=90^\circ$
 $G=1000; b=100\cdot A; \Psi^*=R=0^\circ$

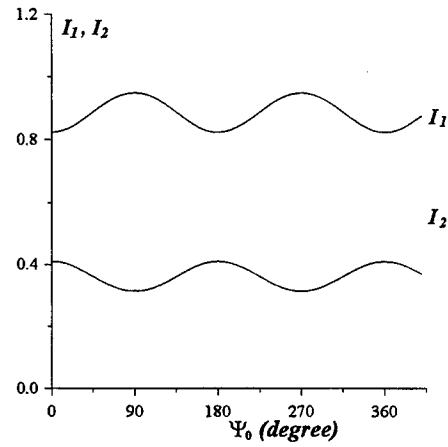


Figure 9. Theoretical dependencies of I_1, I_2 on the direction Ψ_0 of the pump polarization at
 $A=1.5 G=1000; b=100\cdot A; \Psi^*=R=0^\circ$
 $\Phi=0.5; \Phi_2=0.5$

Comparison of these data with the experimental results (Fig.2,3) proves that the model in question provides a good description of the behavior of the fiber laser intensity.

It should be noted that the division of modes into a strong and a weak one observed in the experiment is provided in the present model by matching parameters Φ_1 and Φ_2 that determine the proportion of isotropically and anisotropically distributed dipoles of active medium.

A linear stability analysis leads to the tenth-order characteristic equation whose roots were found by numerical methods. According to our calculations, it has two pairs of complex-conjugate roots defining relaxation oscillations. Fig.10 offers the dependence of the relaxation oscillations frequencies on a pump parameter.

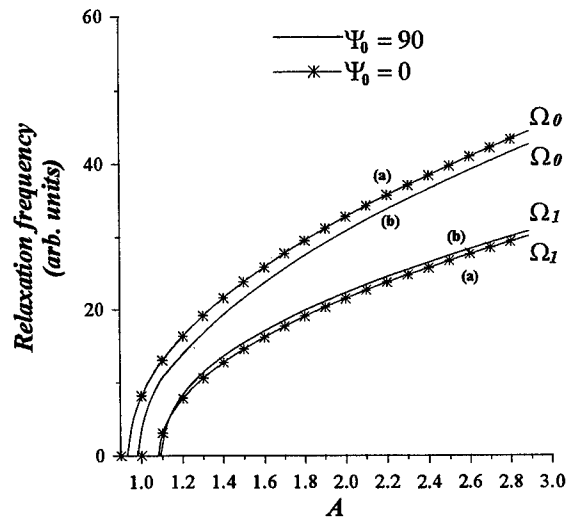


Figure 10. Theoretical dependencies of relaxation frequencies on pump parameter at (a) $\Psi_0=0^\circ$ and (b) $\Psi_0=90^\circ$ $G=1000$; $b=100 \cdot A$; $\Psi=R=0^\circ$

The developed rate equation model (12) describes only two relaxation oscillation. As mentioned in paper [3], in order to describe the third low frequency relaxation oscillation it is necessary to consider phase-sensitive interaction of modes via inversion grating that is recorded in the active medium by joint action of polarization modes. This problem will be discussed in further papers.

6. ACKNOWLEDGMENTS

The work was supported by RFBR grants No 96-02-19274 and No 96-15-96742.

7. REFERENCES

1. R. Leners, P.L. Francois, G. Stephan, "Simultaneous effects of gain and loss anisotropies on the thresholds of a bipolarization fiber laser", *Optics Letters* vol.19, N4, pp275-277, 1994.
2. P. Khandokhin, Ya. Khanin, Yu. Mamaev, N. Milovsky, E. Shirokov, S. Bielawski, D.Derozier, P. Glorieux, "Low-frequency dynamics of class B laser with two elliptically-polarized modes", *Kvan.. Elektron. (Moscow)* v. 25, N.6, 1998
3. P.A. Khandokhin, Ya.I. Khanin, N.D. Milovsky, E.Yu. Shirokov, S. Bielawski, D. Derozier, P. Glorieux, "Polarization dynamics of a fiber Fabry-Perot laser with feedback", *Quantum and Semiclassical Optics, JEOS* part B, v.10, p.97, 1998.
4. K.C. Reyzer, L.W. Casperson, "Polarization characteristics of dye-laser amplifiers I. Unidirectional molecular distributions", *J.Appl.Phys.* vol.51, N12, pp6075-6082, 1980.
5. K.C. Reyzer, L.W. Casperson, "Polarization characteristics of dye-laser amplifiers II. Isotropic molecular distributions", *J.Appl.Phys.* vol.51, N12, pp6083-6090, 1980.
6. H. Zeghlache, A. Boulnois, "Instability in lasers.I.nModel and steady states of neodymium-doped fiber lasers", *Phys. Rev. A*, v.52, p.4229, 1995
7. Ya.I. Khanin, *Principles of Laser Dynamics*, (North-Holland/Elsevier, Amsterdam, 1995).

Diode Pumped Solid State Laser With 2D Intracavity Beam Scanning Using Liquid Crystal Spatial Light Modulator

A Kornev, A.Onokhov(*), V.Pokrovskiy, L.Soms, V.Stupnikov

Institute for Laser Physics, (*) PETERLAB LTD, St.Petersburg, Russia

e-mail: soms@ilph.spb.su

1. Introduction

The problem of swift steering of laser beams is important for many applications, (projection, marking, engraving, etc.). An approach of intracavity laser beams spatial control was proposed and developed by several teams [1 - 9, 14]. Laser beam movement is provided, with this approach, by the positioning of the "ruling diaphragm" across the surface of one of mirrors of conjugate laser cavity. The "ruling diaphragm" can be done as a Spatial Light Modulator (SLM). Such modulators are based on various physical effects and can use various modulating media: electrooptical crystals [2,10], thin semiconductor layers [11], ferro-electrical ceramics [12-14], or liquid crystals [6,8]. The electrically-addressed intracavity Spatial Light Modulators (SLMs) were experimentally shown to provide computer-controlled beam addressing to any pixel inside laser Field Of View (FOV) [12, 13,14]

In the presented article the following aspects are treated of such laser development: (a) design and properties of intracavity LC SLMs with random addressing to arbitrary pixel in 2D field, and (b) some peculiarities of DPSSL with intracavity beam scanning, in terms of SLM operation inside the cavity, and thermal lens influence on the laser FOV.

2. 2D Electrically-addressed LC SLMs

The list of requirements to intracavity LC SLMs is given in the Table 1.

Table 1 Requirements to 2D Electrically Addressed LC SLMs

Requirement	Characteristics	Comment
- fast response time	$\sim 10^{-4}$ s	FLC, nematic LC
- low refresh time	$< 5 \cdot 10^{-4}$ s	FLC
- direct access to $\{x_i, y_k\}$	optical effects linear to electric field	FLC
- low open-state losses	round trip $< 1\%$	scattering
- contrast ratio	$> 3:1$	intracavity read-out provides increase of contrast ratio
- laser damage resistance	$\sim 1 \text{ J/cm}^2$ @ 30 ns	ITO electrodes are the weakest layers
Operation stability		

2.1. Modulation Effect Choice.

Let us note that, while the switch-on time about $\sim 10^{-4}$ s can be obtained both with nematic and ferroelectric LC (FLC), the fast switch-off time is not available with nematics. Only FLC, which are exhibiting linear to the driving electric field optical effects, can provide the necessary refresh time of the LC device.

Several types of FLC were studied and tested in order to select the most appropriate one for the LC SLM manufacturing. The summary of our studies is given in Table 2.

Table 2. The choice for the Type of Modulation Effect in FLC

Effect type	Switch time	Losses	Contrast ratio	Operation stability
Electroclinic	+++	-	-	-
DHF	+	---	+	+
SS FLC	++	-	+	+

The electroclinic effect is the fastest of all the others. We reached the repetition rate $F_{rep} \sim 100$ kHz with a linear array LC SLM using this effect. The devices using the electroclinic effect exhibit relatively low losses (about 3-4% comprising ~2% losses due to the scattering outside the TEM_{00} mode angular zone). Nonetheless, this effect was rejected because of the strong temperature dependence of the contrast ratio: in order to get a satisfactory contrast ratio, the temperature of LC device was to be maintained within $\Delta t \sim 1^\circ C$.

The DHF LC cells showed high losses: 6-10% of light passing through the LC cell were scattered out of the TEM_{00} mode angular zone.

So, the SS FLC mixtures were selected as working media for SLM development. This effect is slower than the electroclinic effect, but the repetition rate about 3 kHz was easily available. The LC cells losses were about 2-4%, and the contrast ratio was better than 3:1 for all samples.

The phase modulation mechanism in LC cells using SS FLC is shown in the Fig. 1. The orientation of the LC director D is changed to the angle θ with the change of the electrical field applied (vectors E_1 and E_2 in the figure). For the LC mixture used, the angle $\theta = 49^\circ$. Thus, if the thickness h of the LC cell is chosen to provide the relation $k \Delta n h = \lambda/2$, here k – the wave number, Δn – difference between ordinary and extraordinary refractive indices of LC, λ – wavelength, then the LC cell will operate as electrically-driven quarter wave plate. For the LC mixture used the cell thickness was about $\sim 1 \mu$.

The next important requirement is the availability of the direct random access to any pixel inside the LS SLM cross section. Here, once again, the optical effects in FLC that are linear to the electric field applied help to fulfill this requirement. The scheme of the voltage application to 2D matrix of electrodes is shown in the Fig 2.

In the state A all pixels are under the same voltage equal to difference between “column voltage” U_i and “row voltage” V_k . In order to switch on the pixel $\{i, k\}$, the other voltage $\{U'_i, V'_k\}$ is applied to the i -th column and k -th row, so as to change the direction of the effective electrical field to the opposite. At the same time, the values of $\{U'_i, V'_k\}$ must be chosen so that to leave LC director orientation for the adjacent pixels (e.g. $\{i-1, k\}$ or $\{i, k-1\}$) in the initial state. This can be done taking into account the bistable character of LC director behavior under electrical field change.

Using this approach, the 2D random addressing LC SLM was manufactured and tested, with the following characteristics:

- ◆ number of pixels 32x32
- ◆ pixel size 475x475 micron
- ◆ gap between the pixels 25 micron
- ◆ repetition rate up to 3 kHz
- ◆ level of voltage applied $\square 12V, =18V$ bias
- ◆ LC mixture SS FLC (Felix, manufactured by Hoechst)

2.2. Laser Damage Resistance

The summary of results on the LC SLM laser damage resistance is shown on the Fig.3. The weakest layers in the whole SLM sandwich-like structure are the ITO transparent electrodes. A number of studies were performed to get reliable values of laser damage resistance of ITO layers that were deposited using various methods and were subjected to additional annealing to reduce absorption. The best results were obtained with the laser deposition method with the subsequent annealing in the oxygenating atmosphere. The left three curves in Fig.3 are relating to the ITO deposited directly on the blank while the right curve – to the ITO layer deposited on the mirror. The difference of about the order in the laser damage threshold can be explained by the following. For the ITO layer deposited onto the mirror, it was possible to put the ITO layer into the nod of the standing electromagnetic wave produced by the incident and reflected waves. As for the other electrode that is separated from the mirror by LC layer, the exact location of ITO layer in the standing wave nod was technically impossible, and the effective relative intensity of laser wave was greater, thus leading to lower laser damage threshold value. Taking into account the requirements of several millions shots, the reliable operational laser energy at the SLM was found not exceeding ~ 0.5 J/cm² at pulse duration $\tau = 15$ ns. Let us notice that under this energy density the average

power density tolerable for LC SLM is about 200 W/cm^2 (experimentally: repetition rate $F=400 \text{ Hz}$, spot square $2 \cdot 10^{-3} \text{ cm}^2$, pulse energy 10^{-4} J , no damage indicated after 2 hours of work).

It is quite clear that the relatively low value of the LC SLM laser damage resistance puts a serious impact to the optical schematics of laser resonator providing the required output power/energy.

3. Laser Optical Scheme and Operation.

The optical scheme of DPSSL used in our studies is shown on the Fig.4. Two lenses with focal lengths $f=12.1 \text{ cm}$ are located at the distance $L=2f$, so the left mirror ($R=100\%$) located at the distance f is imaged onto the right mirror – electrically-addressed LC SLM. The laser rod (Nd:YAG $\varnothing 4 \times 5 \text{ mm}$ with water cooling of the cylindrical surface) is located in the centre of the resonator and is pumped by the radiation of three LD bars. The radiation of LD bars is combined by a combiner [15] and is focused inside the optical fibre $\varnothing 660 \mu$. The output end of the fibre is imaged into the laser rod producing the pumped zone $\varnothing 600\text{--}700 \mu$. The repetitive pumping of laser rod caused its thermal lensing. In order to compensate for the thermal lens, one of laser rod faces was spherical, with the curvature radius $R=29 \text{ cm}$.

A special signal generator driven by a computer generated the LC SLM driving voltage. The computer software provided generation of sweeps, addressing to arbitrary pixels, or moving pictures. The switch-on/off times were $\tau_{\text{on}}=150 \mu\text{s}$ and $\tau_{\text{off}}=200 \mu\text{s}$.

The electrooptical Q-switch (KD*P crystal with cross section $23 \times 23 \text{ mm}$) was used to get the necessary time characteristic of the laser pulse. The output fraction of the laser energy circulating inside the resonator was reflected by the dielectric polarizer. The voltage at EO Q-switch was applied different from the exact $U_{\lambda/4}$, so two orthogonal polarisation components presented between the polariser and EO Q-switch. One polarisation component of the laser beam travelled to the LC SLM while the orthogonal component was emitted out of the resonator. This scheme provides a diminishing of laser beam density on the LC SLM. The fraction of the output energy can be determined from the following considerations. The laser energy density w inside the laser rod must be more than the saturated energy density for the laser medium: $w > w_{\text{sat}} \approx 2h\nu/\sigma$, $h\nu$ is the energy of the quanta, σ is the radiation cross section (for Nd:YAG $w_{\text{sat}} \sim 1 \text{ J/cm}^2$). At the same time, the energy density at the SLM must not exceed $w_{\text{SLM}} \sim 0.5 \text{ J/cm}^2$. The “unbending” coefficient K provided by the polariser is expressed as $K = (w_{\text{SLM}}/w_{\text{sat}})(D_{\text{pump}}/D_{\text{SLM}})^2$; for our case K must be about $K=4$, and the effective reflection coefficient $R_{\text{eff}}=0.2$. Of course, the gain per pass in laser rod must exceed the value of K . The curves on the Fig. 5 represent the output energy E_{out} , energy density at the LC SLM w_{SLM} , and the unbending coefficient K as function of the ratio of the operation voltage at the EO Q-switch U to the quarter wave voltage $U_{\lambda/4}$. Inside the working zone of the operation voltage $0.2 < U/U_{\lambda/4} < 0.3$ the energy density at the LC SLM is lower than $w_{\text{SLM}} \sim 0.5 \text{ J/cm}^2$ while the output energy $E_{\text{out}} \geq 0.85 E_{\text{out}}(\text{max})$.

The curves on the Fig.6b represent the scanlaser field of vision. At the ordinate axis, the output energy E_{out} (AU) is plotted as the function of the pixel position d . The parameter of the curves is the distance δ between the focal planes of the intracavity lenses: the condition $\delta=0$ corresponds to the confocal adjustment, while $\delta>0$ – to unstable resonators, and $\delta<0$ – to stable resonators.

For the confocal resonators, $\delta=0$, the energy drop with the pixel movement out of the axis is connected primarily with the violation of so-called telecentric condition: the optical ray coming from the focal point and refracted at the peripheral zone of the lens, becomes not parallel to the resonator axis. This is equivalent to the tilt of the flat mirror, and leads to the losses increase. The Fig.6b shows the sensitivity of the output energy to such tilts.

If the distance between lenses $\delta>0$, for a certain distance from the axis in the plane of the lens, the violation of telecentric condition due to the spherical aberration can be compensated by the divergent character of beams in unstable resonators. This lead to the restoration of perfect telecentric conditions for an annular zone, with the corresponding output energy restoration (see Fig.6a, curves 3,4). In a whole, if we admit a certain ravine in the curve $E_{\text{out}}(d)$ (say, 80%), the FOV of laser can be significantly increased pulling the resonator lenses out. Let us note that the FOV can be increased using two-component objective lenses corrected for these aberrations [16].

The thermal lensing influence to the laser FOV is shown on the Fig.7. The parameter of curves is the thermal lens focal length. The strongest thermal lens ($f_{\text{th}}=25 \text{ cm}$) is equivalent to the wave aberration 0.24λ placed in the waist of laser resonator mode. The relative variation of the output energy inside laser FOV drops as optical strength of the thermal lens increases, which can be explained by the compensation for the violations of telecentric conditions by the thermal lens. At the same time, the overall energy decreases. Thus, an optimal value of thermal lens can be found; our experiments gave the corresponding value of the wave aberration about 0.1λ . The radius of the laser rod spherical surface must be calculated taking into account this condition together with the thermal focal length at the required operation mode (pump power, pulse repetition rate). For our case ($P_{\text{pump}}=12.6 \text{ W}$, pump pulse duration $\tau_{\text{pump}}=300 \mu\text{s}$, repetition rate $F_{\text{pump}}=1 \text{ kHz}$), the sphere radius $R=29 \text{ cm}$. The output energy was measured as $E_{\text{out}} \geq 0.8 \text{ mJ}$.

References

1. W.A.Hardy - Active image formation in laser - IBM Journ. R&D, 1965, v.9, p.31
2. R.A.Myers, R.V.Pole - Electron beam scanlaser - IBM Journ. R&D, 1967, v.11, #5, 502-510
3. A.B.Welch, B.Burzlaff, W.Cunningham - Electronically scanned CO-2 radar techniques - Proc. SPIE, (1981) v.300, 153-162
4. J.S.Chivian, H.W.Scott, W.E.Case, N.J.Krasutsky, IEEE QE-21, (1985) p.383; 5. J.S.Chivian, H.W.Scott, A.E.Hill, A.Gedault, IEEE QE-21, (1985) p.1135
6. F.L.Vladimirov, M.A.Groznov, V.P.Pokrovskij, L.N.Soms, et al., Kvant. elektr., 1985, #12, p.2061
7. F.L.Vladimirov, M.A.Groznov, A.F.Kornev, V.P.Pokrovskij, L.N.Soms et al. - in "Trudy GOI (Optika zhidkikh kristallov)", L.:GOI, 1986, v.60, #.194, s.73-81 (Proc. Vavilov GOI, in Russian).
8. V.V.Danilov, D.A.Savel'ev - in "Trudy GOI, (Optika zhidkikh kristallov)", L.:GOI, 1986, v.60.#194, p.81-91 (Proc. Vavilov GOI, in Russian)
9. I.B.Vitrischak, S.Yu.Orlov, V.P.Pokrovskij, L.N.Soms - Kvant. elektr., 1988, v.15, #.1, 177-179 (in Russian)
10. S.L.Hou, D.S.Oliver - Pockels Readout Optical Memory using BSO - Appl.Phys.Lett, 1971, v.18, #4, 325-328
11. A.A.Bugaev, B.P.Zakharchenya, F.A.Chudnovskiy, - Phase Transition Metal-Semiconductor and its applications (in Russian) - L.,Nauka, 1979 y, 184pp.
12. V.Alekseev, V.Liber, A.Anspoks, E.Auzins, E.Klotins and J.Kotleris, Abstr. of 7-th Europ. Meeting on Ferroelectricity, Dijon, 1991, p.542
13. V.N.Alekseev, M.B.Svechnikov, V.N.Chernov, - Kvantovaya Elektronika, v.12, s.729-738, 1985 y.
14. A.F.Kornev, V.P.Pokrovskij, L.N.Soms, V.K.Stupnikov - Laser Systems with Internal Scanning - Journ. of Opt. Techn.,#1, p..10-25, (1994)
15. M.M.Khaleev, A.A.Mak, A.V.Mikhailov, G.E.Novikov, O.A.Orlov, V.I.Ustyugov, G.Hollemann, H.Voelkel: Techn, Dig. CLEO/EUROPE'96, paper #CTuA2, p.55
16. A.F.Kornev, V.P.Pokrovsky, L.N.Soms, V.K.Stupnikov, V.Yu.Venediktov. in the book: Optical Resonators - Science and Engineering. NATO ASI Series. Vol.3/45. Ed. by R.Kossowsky, M.Elinek and J.Novak, p.153-160 (1997)

Fig.1. Phase Modulation by Surface Stabilized FLC Cell

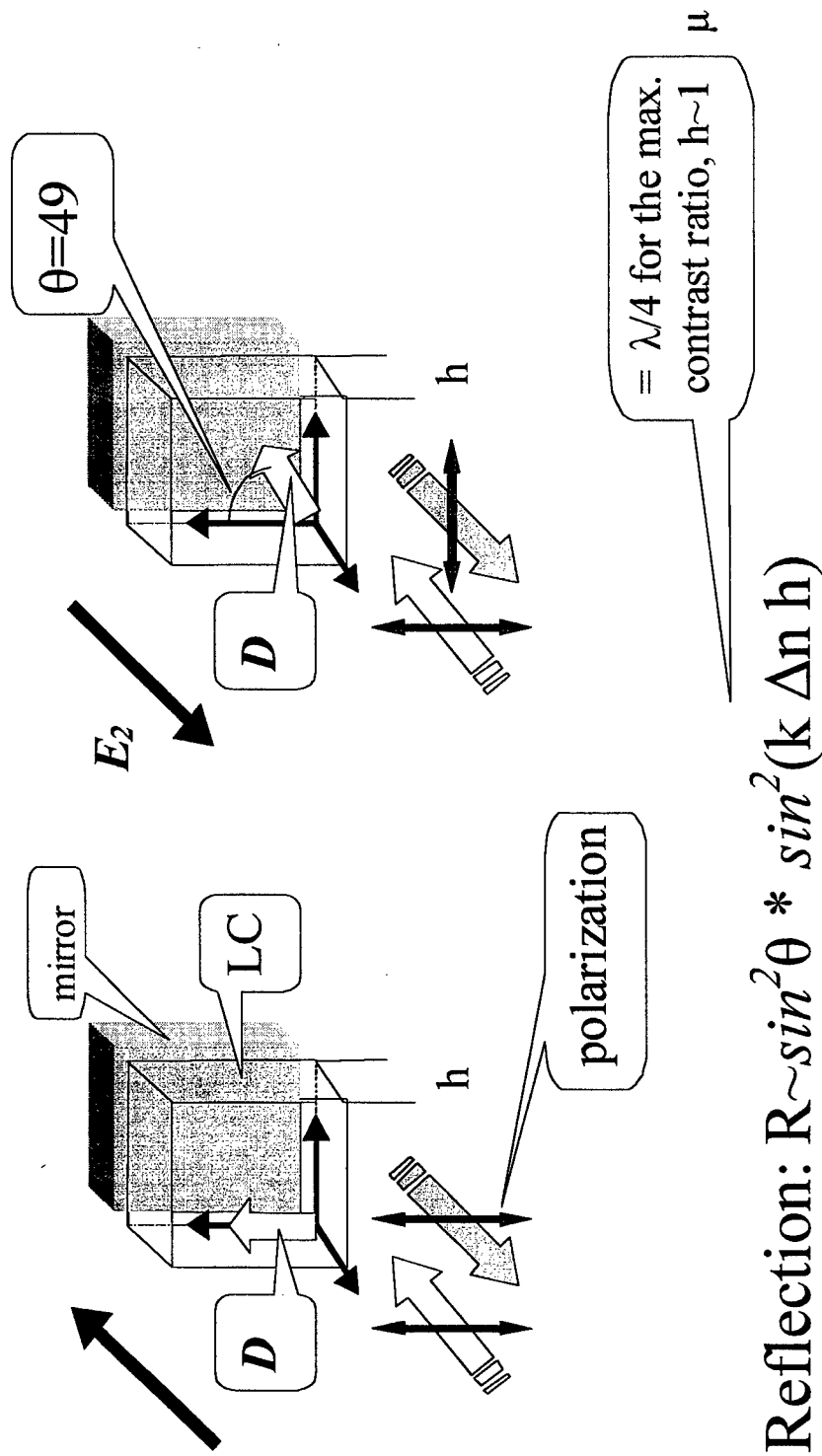


Fig.2. 2D Electrically Addressed LC SLM: Voltage Applying

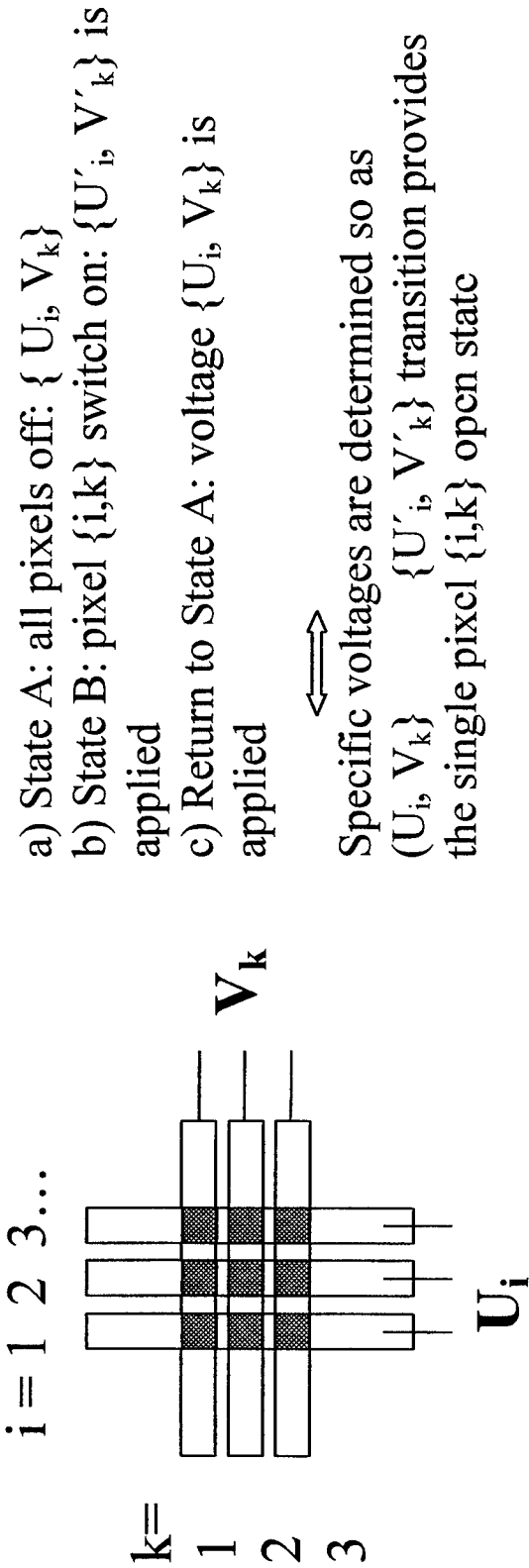
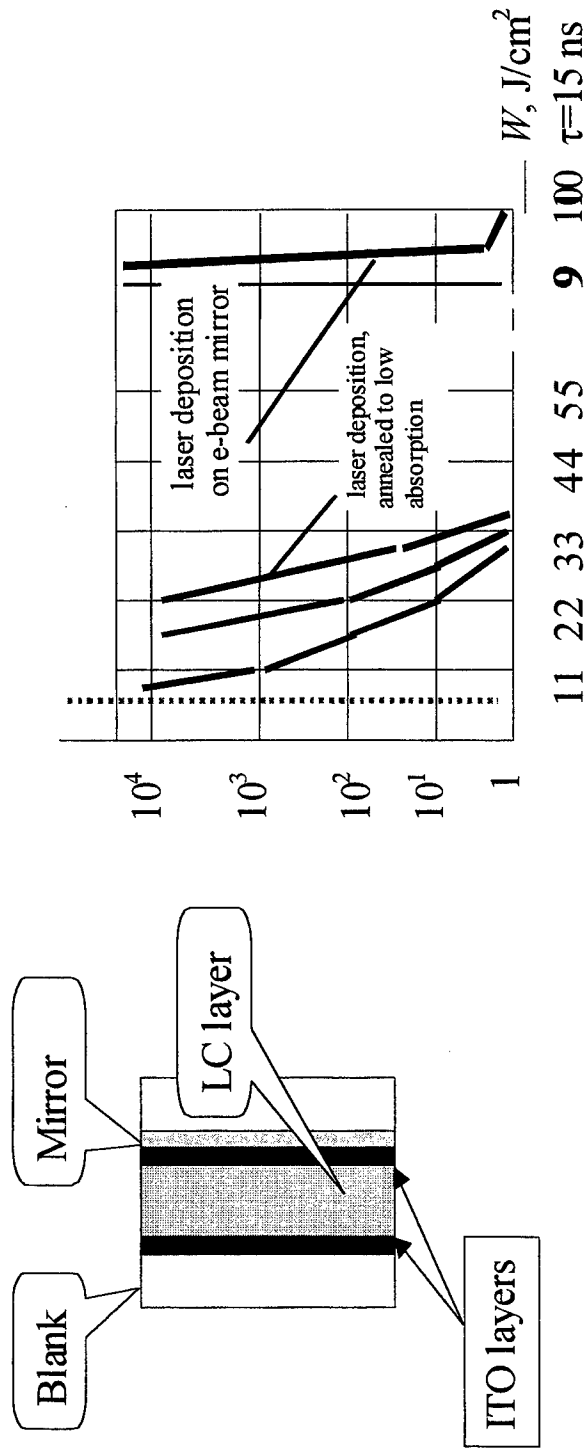


Fig.3. SLM Layers Laser Damage Resistance



***Operational laser energy density
at the SLM must not exceed
0.5 J/cm² (@ $\tau=15$ ns)***

Layers deposition methods:

Cathode sputtering

Laser evaporation

Electron beam evaporation

Fig.4 Scan Laser Resonator Schematics

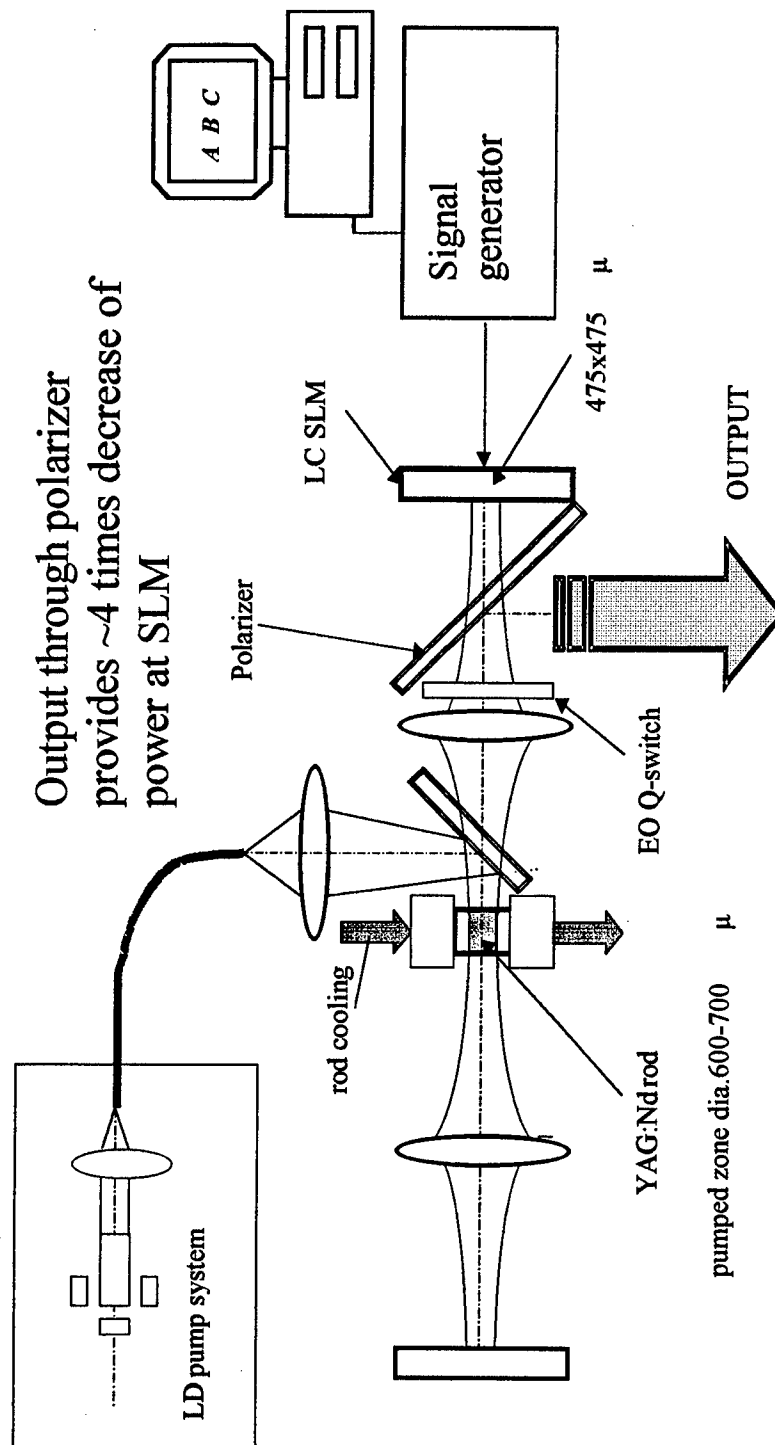


Fig.5. Polarizer Output.
Output Energy vs Resonator Unbending Coefficient.

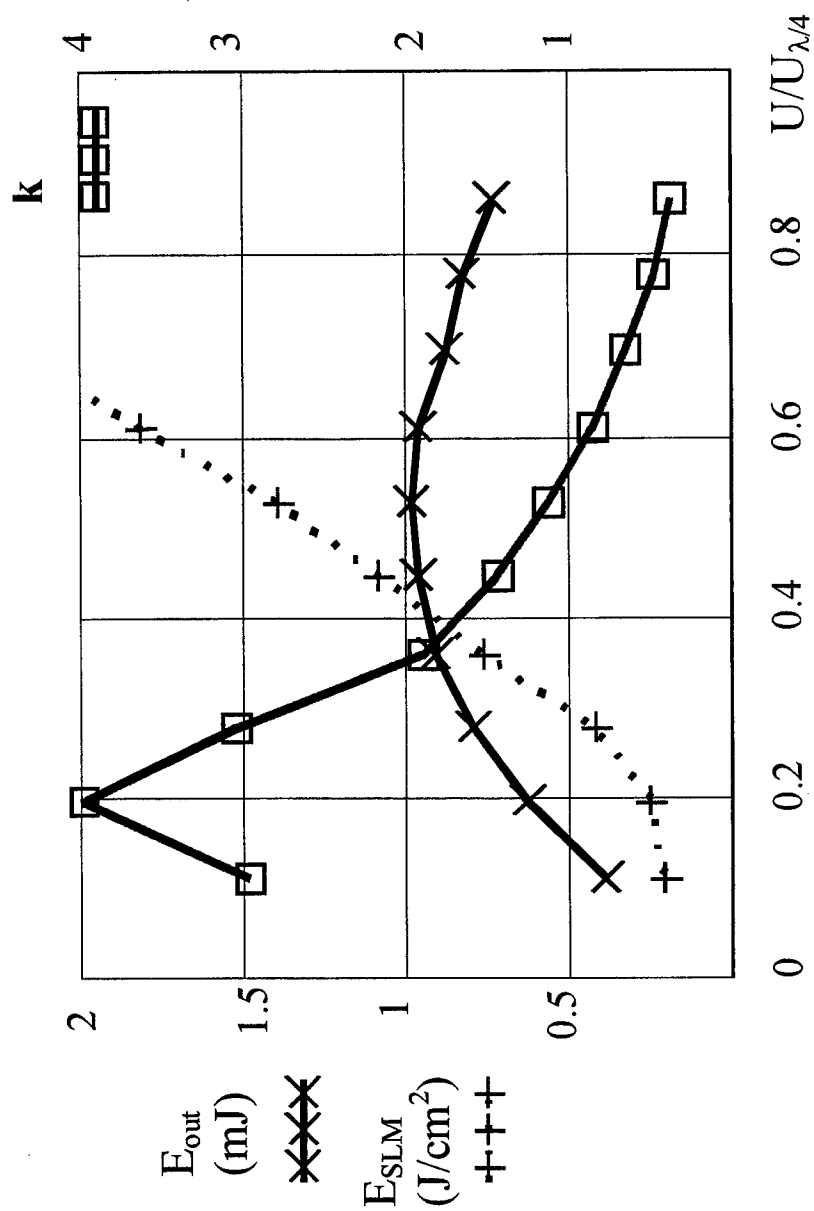
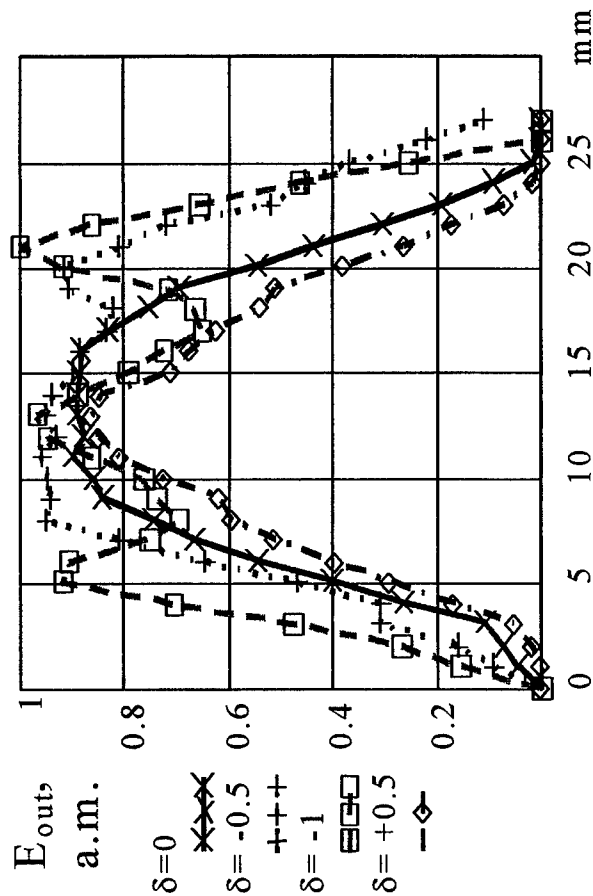
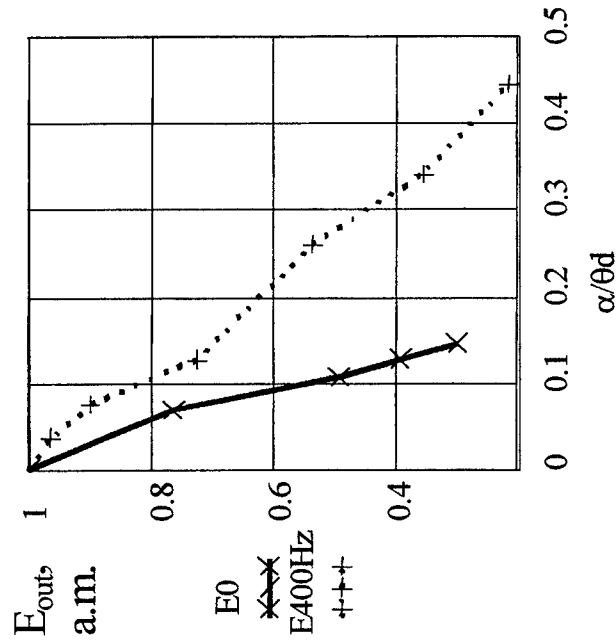


Fig.6. Energy per Pixel Across Laser FOV and Influence of Lenses Pull Out.

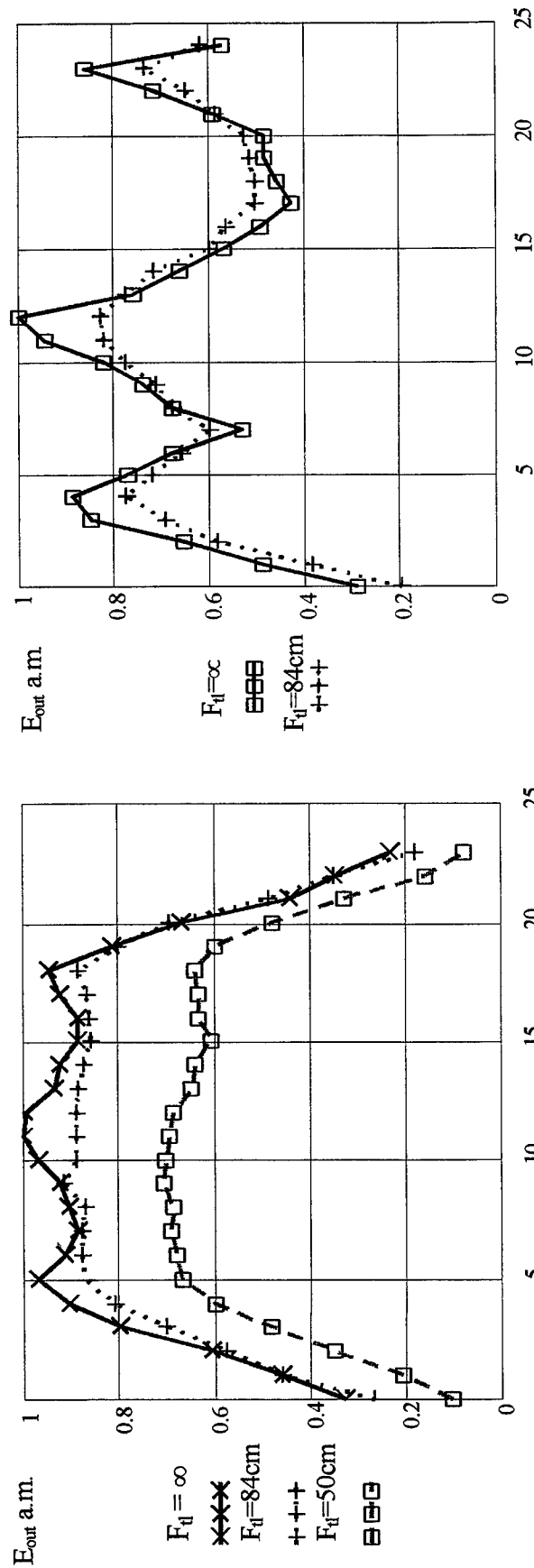


a. E_{out} per pixel vs pixel coordinate



b. E_{out} vs mirror tilt

**Fig.7. Energy per Pixel Across Laser FOV.
Influence of Thermal Lensing.**



a) $\delta = +1 \text{ mm}$. Wave aberration on the axis

$$\varepsilon = 0.07 \lambda \quad (F_{tl} = 84 \text{ cm})$$

b) $\delta = +0.5 \text{ mm}$. Wave aberration on the axis

$$\varepsilon = 0.07 \lambda \quad (F_{tl} = 84 \text{ cm})$$

$$\varepsilon = 0.12 \lambda \quad (F_{tl} = 50 \text{ cm})$$

SESSION 2

Gain Media

Up-conversion in YLF:Yb³⁺,Tm³⁺ laser crystals.

A.M.Tkachuk¹, I.K.Razumova¹, M.-F. Joubert², R.Moncorge³

¹ S.I.Vavilov State Optical Institute, St.Petersburg, 199034, Russia.

E-mail: alex@tkachuk.spb.su

² UMR CNRS 5620,Universite Lyon 1, F-69622 Villeurbanne Cedex, France

E-mail: joubert@pcml.univ-lyon1.fr

³Universite de Caen, 14050 Caen, France; E-mail: moncorge@spalp255.ismra.fr

ABSTRACT

We have studied the Yb³⁺ \leftrightarrow Tm³⁺ nonradiative energy transfer processes responsible for population of the ¹G₄ thulium level under Yb³⁺ or Tm³⁺ selective laser excitation of YLF:Tm³⁺,Yb³⁺ crystal. The microparameters and the rates of the energy transfer via cross-relaxation schemes are determined. It is concluded that the process of populating the ¹G₄ thulium level is greatly affected by up-conversion processes not only from the ³H₄ but also from the ³F₄ level, proceeding within the static decay model.

Keywords: crystal, doped ion, rare earth, energy transfer, kinetics, population.

1.INTRODUCTION

The YLF:Tm³⁺ and YLF:Tm³⁺,Yb³⁺ crystals are the well-known active media for lasing on a number of lines (from 0.450 to 2.35 μ m) upon selective laser, laser diode, and flash lamp pumping. As is known, the possibility of obtaining the inversion population in the higher-lying energy levels strongly depends on the ratio of the non-radiative energy transfer rates such as sensitization, selfquenching, and nonlinear interaction of the excited states of rare-earth ions. These processes are mostly important for selective pumping by laser diodes (LD), since they determine the rate of populating the working levels of laser transitions and limit the output laser characteristics. The knowledge of mechanisms of these processes and their efficiency permits one to describe behavior of crystal properties under different conditions.

1.1. Background

In this work we used results obtained in previous studies¹⁻⁴, where the intraionic transition probabilities and interionic energy transfer processes leading to luminescence selfquenching and up-conversion in YLF:Tm³⁺ were considered in a wide range of Tm concentrations (0.1 - 10 at%). There, we have studied both theoretically and experimentally the luminescence selfquenching processes for excited states of Tm³⁺ ions under low-power pumping. Good agreement between the experimental and calculated data was obtained in all cases. On the basis of experimental data and theoretical estimates, the predominant mechanisms of nonradiative selfquenching of ¹G₄, and ³H₄ levels were determined. It was shown that in these crystals the most efficient processes are selfquenching of ³H₄ (12640 cm⁻¹) and ¹G₄ levels and up-conversion from ³H₄ level. Selfquenching of ³H₄ level at low concentration (less than 5 at.%) can be described by the hopping model under dipole-dipole coupling, to describe the luminescence selfquenching of the ¹G₄ level, the static model should be used and dipole-quadrupole and quadrupole-quadrupole couplings have to be taken into account⁴.

Thus, from our studies we have concluded that the energy-transfer macrorates and microparameters obtained by the method of model quantum mechanical calculation⁵⁻⁷ provided good results in describing luminescence kinetic of YLF:Tm³⁺ crystals. So that, we supposed to get good results in describing YLF:Tm³⁺,Yb³⁺ system with the same set of calculated magnitudes of energy transfer microparameters and macrorates. We considered Tm³⁺ - Tm³⁺ selfquenching, cross-relaxation energy transfer between dopant ions, and the up-conversion processes upon Tm³⁺ - Tm³⁺ and Yb³⁺ - Tm³⁺ coupling.

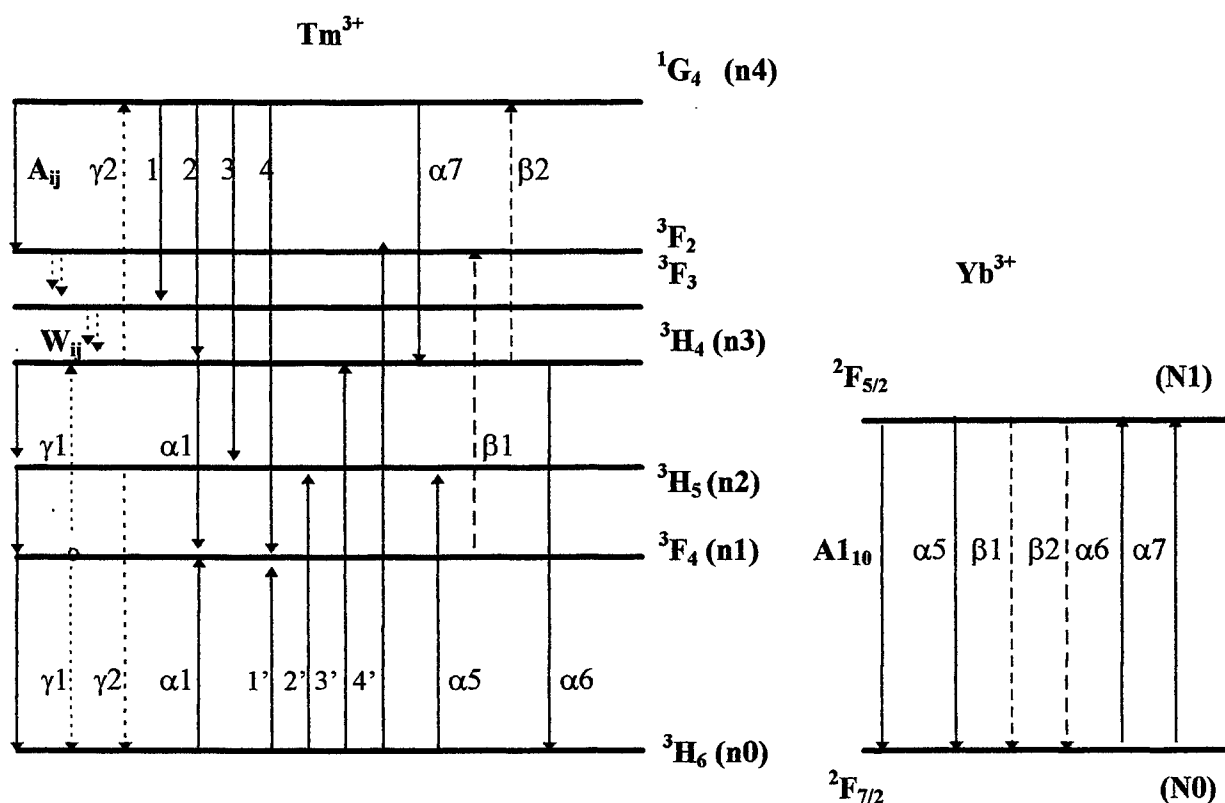


Fig. 1. Energy diagram and schemes of nonradiative coupling between doped ions in YLF:Tm³⁺, Yb³⁺ crystals. A_{ij} - radiative probability from level "i" to level "j", W_{ij} - nonradiative probability, α_i - constant of energy transfer (sensitization, selfquenching), β_i - constant of Tm-Yb nonlinear coupling (up-conversion at Tm³⁺-Yb³⁺ coupling), γ_i - constant of Tm³⁺-Tm³⁺ nonlinear coupling (up-conversion at Tm-Tm coupling).

2. EXPERIMENTAL METHODS

The luminescence kinetic was detected at the emission wavelength of ³H₄, ¹G₄ Tm and ²F_{5/2} Yb levels under selective laser excitation in the ³F₂, ³H₄ (796 nm) Tm or ²F_{5/2} (970 nm) Yb levels. To realize such selective excitation, a QUANTEL Nd:YAG laser (pulse length 10 ns and variable repetition rate 10Hz) followed by a dye laser and a Raman cell was used. The sample fluorescence was analyzed by a JOBIN YVON monochromator and detected by an RCA AsGa photomultiplier tube. The signal was processed by an ORTEC photon counting system. This experimental set-up was controlled by a PC. The decay time measurements were realized using a digital LECROY oscilloscope. The dynamic range of detection exceeded three orders of magnitude.

3. CALCULATIONS

3.1. Microparameters for Tm - Tm and Yb - Tm coupling.

Energy-level diagram of considered crystals and schemes of nonradiative coupling between doped ions are shown in Fig. 1. All processes involved into consideration, which take place under IR excitation of YLF:Tm³⁺, Yb³⁺ crystals are indicated by arrows and pointed as: A_{ij} - radiative probability from level "i" to level "j", W_{ij} - nonradiative probability, α_i - constant of energy transfer (sensitization, selfquenching), β_i - constant of Tm-Yb nonlinear coupling (up-conversion at Tm³⁺-Yb³⁺ coupling), γ_i - constant of Tm³⁺-Tm³⁺ nonlinear coupling (up-conversion at Tm-Tm coupling).

The energy transfer constants were estimated on the basis of experimental and theoretical studying Tm³⁺-Tm³⁺ selfquenching in YLF:Tm³⁺ crystals with different thulium concentration : from 0.5 to 10 at. %. Energy transfer

microparameters of migration (C_{DD}), selfquenching (C_{DA}) and up-conversion (C_{DA}) were estimated using the method of model quantum mechanical calculation^{6,7}. Results for YLF-Tm³⁺ crystals are summarized in Table 1. To determine the selfquenching macrorates in YLF-Tm³⁺ we studied the luminescence decay curves recorded for ³F₄, ³H₄ and ¹G₄

thulium levels after their resonant selective pumping by laser pulses with nanosecond duration. After comparison of experimental kinetics with theoretical curves calculated with pointed in Table 1 microparameters in framework of different energy transfer models, the mechanisms of Tm-Tm and Yb-Tm were established and effective values of α_i constant were determined. Energy transfer microparameters and macrorates for Tm - Yb energy transfer processes have been obtained by the method of model quantum-mechanical calculation. Results are listed in Table 2.

3.2. System of balance rate equations

We have considered the system LiYF₄:Tm³⁺, (1%), Yb³⁺ (10%), containing low concentration of Tm³⁺ ions and high concentration of Yb³⁺ ions, since we take into account not only Yb³⁺ - Tm³⁺ coupling, but also Tm³⁺ - Tm³⁺ coupling. Additional conditions were as follows: 1) under low pump density all constants describing nonlinear coupling were equal to zero, and 2) the parameters depending on the population of excited levels varied in reasonable limits as well as initial populations. We considered two cases of selective laser excitation of the crystal: 1) at ²F_{5/2} ytterbium level ($\lambda_{exc} = 914$ nm) and 2) at ³H₄ thulium level ($\lambda_{exc} = 796$ nm) with one and the same set of calculated parameters.

Table 1. Calculated microparameters of migration (C_{DD}), selfquenching (C_{DA}) and up-conversion (C_{DA}) in YLF-Tm³⁺ crystals.

Level	Process	$C_{DD}^{dd} \cdot 10^{40}$ cm ⁶ s ⁻¹	$C_{DA}^{dd} \cdot 10^{40}$ cm ⁶ s ⁻¹	$C_{DA}^{dq} \cdot 10^{54}$ cm ⁸ s ⁻¹	$C_{DA}^{qq} \cdot 10^{67}$ cm ¹⁰ s ⁻¹
³ F ₄	Migration 1. (³ F ₄ → ³ H ₆) : (³ H ₆ → ³ F ₄)	31.7			
	Up-conversion 2. (³ F ₄ → ³ H ₄) : (³ F ₄ → ³ H ₆) - 2hω		0.017	0.17	0.08
³ H ₄	Migration 1. (³ H ₄ → ³ H ₆) : (³ H ₆ → ³ H ₄)	17.3			
	Selfquenching 2. (³ H ₄ → ³ F ₄) : (³ H ₆ → ³ F ₄) + 2hω		0.93	9.3	4.2
	3. (³ H ₄ → ³ F ₄) : (³ H ₆ → ³ H ₅) - 2hω		0.01	0.06	0.01
			Σ0.94	Σ9.4	Σ4.2
	Up-conversion 4. (³ H ₄ → ¹ G ₄) : (³ H ₅ → ³ H ₆)		33.83	181.4	35.9
	5. (³ H ₄ → ¹ G ₄) : (³ H ₄ → ³ F ₄) + 2hω		0.26	2.0	0.76
			Σ34.1	Σ183.4	Σ36.7
¹ G ₄	Migration 1. (¹ G ₄ → ³ H ₆) : (³ H ₆ → ¹ G ₄)	0.93			
	Selfquenching 2. (¹ G ₄ → ³ F ₂) : (³ H ₆ → ³ F ₄)		9.3	61	25.7
	3. (¹ G ₄ → ³ F ₃) : (³ H ₆ → ³ F ₄) + hω		0.7	4.6	0.5
	4. (¹ G ₄ → ³ H ₄) : (³ H ₆ → ³ H ₅)		2.6	115	30
	5. (¹ G ₄ → ³ H ₅) : (³ H ₆ → ³ H ₄)		21.1	127	33
	6. (¹ G ₄ → ³ F ₄) : (³ H ₆ → ³ F ₂)		2.5	0.23	0
	7. (¹ G ₄ → ³ F ₄) : (³ H ₆ → ³ F ₃) + hω		0.8	0.07	0
			Σ37.0	Σ308	Σ69.2
	Up-conversion 8. (¹ G ₄ → ¹ D ₂) : (¹ G ₄ → ³ F ₃)		6.38	47.7	5.2

Table 2. Results of microparameter (C_{DD} , C_{DA}) calculations for Tm^{3+} - Tm^{3+} migration (DD), Yb^{3+} - Tm^{3+} energy transfer (ET), Tm^{3+} - Tm^{3+} selfquenching (SQ), and nonlinear coupling (NQ and NC) in $LiYbF_4:Tm^{3+}$.

No.	Cross-relaxation scheme	C_{DD}^* , C_{DA}^* $10^{-40} \text{ cm}^6 \text{ s}^{-1}$
DD	Tm – Tm migration ($^3H_4 \rightarrow ^3H_6$) : ($^3H_6 \rightarrow ^3H_4$) Yb – Yb migration ($^2F_{5/2} \rightarrow ^2F_{7/2}$) : ($^2F_{7/2} \rightarrow ^2F_{5/2}$)	34.2* 112*
ET1	Yb – Tm energy transfer ($^2F_{5/2} \rightarrow ^2F_{7/2}$) : ($^3H_6 \rightarrow ^3H_5$) + 2 $h\omega$	1.03
ET2 ET3	Tm – Yb energy transfer ($^3H_4 \rightarrow ^3H_6$) : ($^2F_{7/2} \rightarrow ^2F_{5/2}$) + 3 $h\omega$ ($^1G_4 \rightarrow ^3H_4$) : ($^2F_{7/2} \rightarrow ^2F_{5/2}$) – 2 $h\omega$	0.032 0.004
NQ1 NQ2	Tm – Tm up-conversion ($^3F_4 \rightarrow ^3H_4$) : ($^3F_4 \rightarrow ^3H_6$) – 2 $h\omega$ ($^3H_5 \rightarrow ^3H_6$) : ($^3H_4 \rightarrow ^1G_4$)	0.009 33.8
NC1 NC2	Yb – Tm up-conversion ($^2F_{5/2} \rightarrow ^2F_{7/2}$) : ($^3F_4 \rightarrow ^3F_2$) ($^2F_{5/2} \rightarrow ^2F_{7/2}$) : ($^3H_4 \rightarrow ^1G_4$) + 2 $h\omega$	61 0.74

The system of balance rate equations for normalized populations $n_i = n(Tm)_i / n(Tm)$, and $N_i = N(Yb)_i / N(Yb)$, where $n(Tm)$ and $N(Yb)$ are concentrations of Tm^{3+} and Yb^{3+} ions in crystal was:

$$dn_1/dt = -A_{10}n_1 + (A_{21} + W_{21})n_2 + A_{31}n_3 + A_{41}n_4 + 2\alpha_1 n_0 n_3 - \alpha_2 n_0 n_4 + \beta_1 n_1 N_1 - 2\gamma_1(n_1)^2$$

$$dn_2/dt = -(\sum_{j=0}^1 A_{2j} + W_{21})n_2 + A_{32}n_3 + A_{42}n_4 + (\alpha_3 + \alpha_4) n_0 n_4 + \alpha_5 n_0 N_1 - \gamma_2 n_2 n_3$$

$$dn_3/dt = -(\sum_{j=0}^2 A_{3j})n_3 + (A_{43} + W_{43})n_4 - \alpha_1 n_0 n_3 + (\alpha_2 + \alpha_3 + \alpha_4) n_0 n_4 - \alpha_6 n_3 N_0 + \alpha_7 n_4 N_0 + \beta_1 n_1 N_1 + \beta_2 n_3 N_1 + \gamma_1(n_1)^2 - \gamma_2 n_2 n_3$$

$$dn_4/dt = -(\sum_{j=0}^3 A_{4j} + W_{43})n_4 - (\alpha_2 + \alpha_3 + \alpha_4) n_0 n_4 - \alpha_7 n_4 N_0 + \beta_2 n_3 N_1 + \gamma_2 n_2 n_3$$

$$dN_1/dt = -(A_{56} + W_{56})N_1 - \alpha_1 n_0 N_1 + \alpha_6 n_3 N_0 + \alpha_7 n_4 N_0 - \beta_1 n_1 N_1 - \beta_2 n_3 N_1$$

$$n_0 + n_1 + n_2 + n_3 + n_4 = 1$$

$$N_0 + N_1 = 1$$

Initial conditions: 1) Pumping into 3H_4 Tm level ($\lambda = 796 \text{ nm}$): $n_0 = 0.6$; $n_1 = 0.065$; $n_2 = 0$; $n_3 = 0.335$; $n_4 = 0$; $N_0 = 1$; $N_1 = 0$.
2) Pumping into $^2F_{5/2}$ Yb level ($\lambda = 914 \text{ nm}$): $n_0 = 1$; $n_1 = 0$; $n_2 = 0$; $n_3 = 0$; $n_4 = 0$; $N_0 = 0.6$; $N_1 = 0.4$.

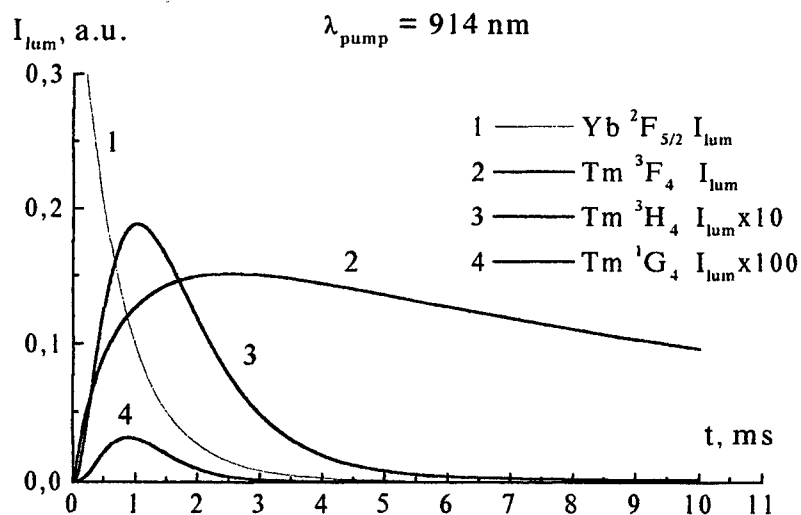
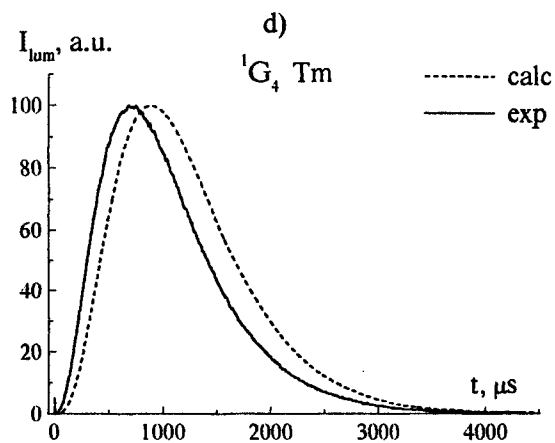
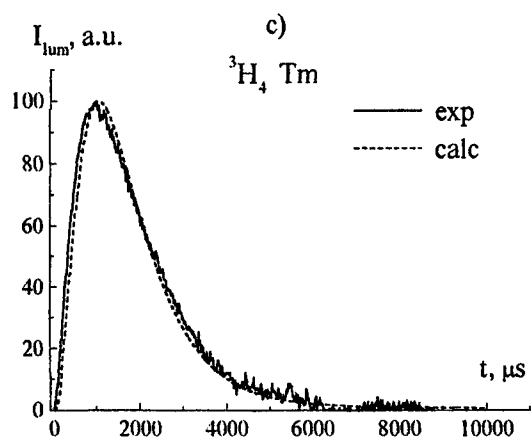
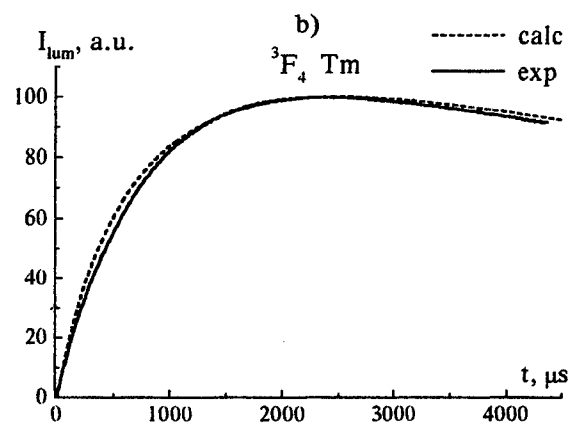
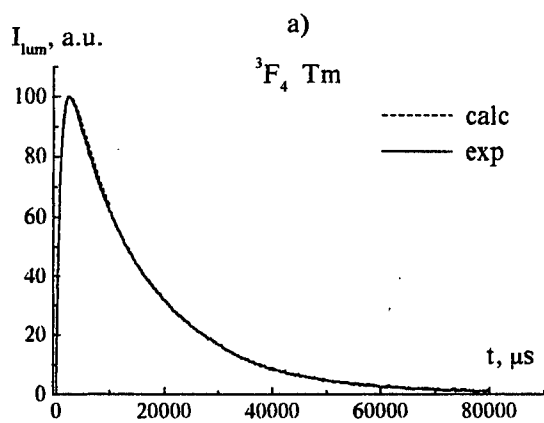


Fig. 2. Calculated luminescence kinetics of different levels in YLF:Yb³⁺(10%),Tm³⁺(1%) crystal. Pump in $^2F_{5/2}$ Yb³⁺ level ($\lambda_{pump} = 914 \text{ nm}$). Low pump power density.



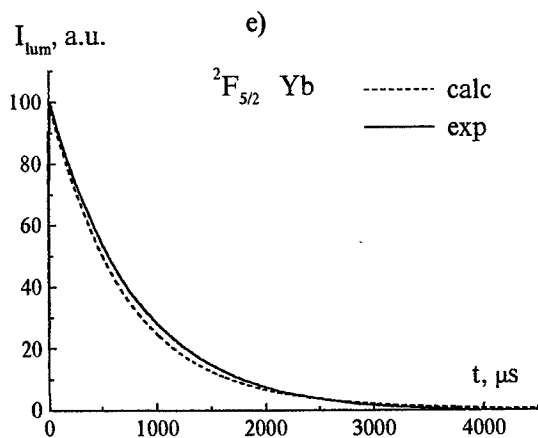


Fig. 3. Experimental (solid curves) and calculated (dashed curves) luminescence kinetics of different levels in YLF:Yb³⁺(10 %),Tm³⁺(1%) crystal. Pump in ²F_{5/2} Yb³⁺ level (914 nm). Low pumping density.
a) ³F₄ Tm³⁺ level, whole pulse,
b) ³F₄ Tm³⁺ level, increasing part of pulse,
c) ³H₄ Tm³⁺ level,
d) ¹G₄ Tm³⁺ level,
e) ²F_{5/2} Yb³⁺ level.

$\lambda_{\text{pump}} = 796 \text{ nm}$

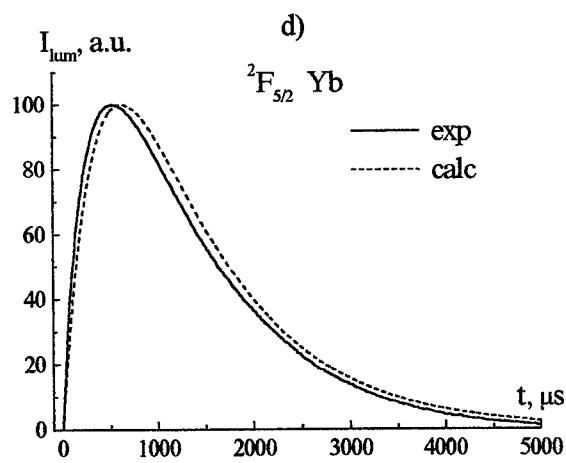
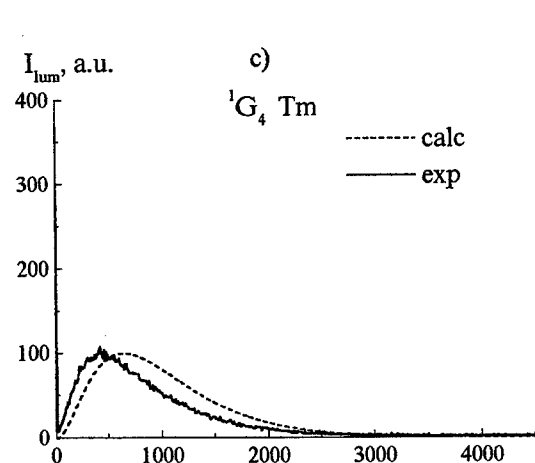
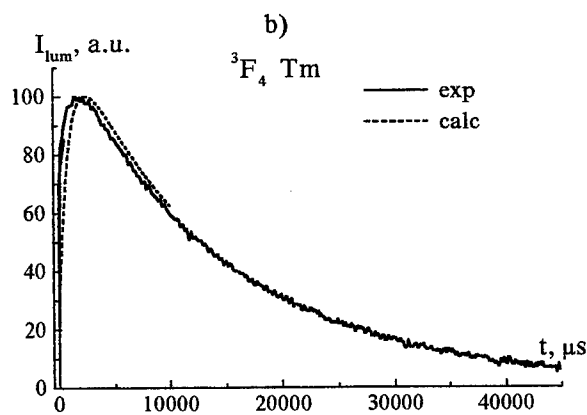
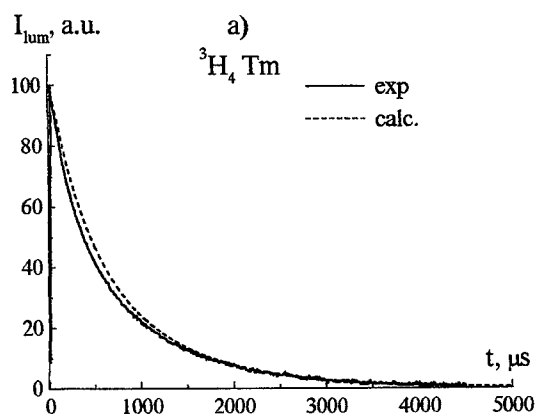


Fig.4. Experimental (solid curves) and calculated (dashed curves) luminescence kinetics in YLF:Tm³⁺ (1%), Yb (10%) crystal under pumping at ³H₄ Tm³⁺ level ($\lambda_{\text{pump}} = 796 \text{ nm}$). a) ³H₄ Tm³⁺ level, b) ³F₄ Tm³⁺ level, c) ¹G₄ Tm³⁺ level and d) ²F_{5/2} Yb³⁺ level. T=300⁰K.

4. RESULTS AND CONCLUSIONS

Results of calculations are shown in Fig. 2. Experimental (solid curves) and calculated (dashed curves) luminescence kinetics of 3F_4 , 3H_4 , 1G_4 thulium and $^2F_{5/2}$ ytterbium levels in YLF: Tm^{3+} (1%), Yb (10%) crystal under pumping in $^2F_{5/2}$ Yb $^{3+}$ level ($\lambda_{pump} = 914$ nm) and 3H_4 Tm^{3+} level ($\lambda_{pump} = 796$ nm) are shown in Fig. 3 and 4, respectively. Good agreement has been obtained under both types of excitation for all studied levels. A certain discrepancy can be observed for 1G_4 thulium level. Time delay for the 1G_4 Tm level indicates that some faster processes take place in the temporal range just after excitation, however, the general behavior repeats well the experimental curves.

It should be emphasized that one and the same set of calculated parameters and initial conditions were used in all cases.

Thus, it could be concluded that the luminescence of studied YLF:Tm: Yb crystal can be well described with the system of balance equations allowing for non-linear energy-transfer processes using the calculated transition probabilities and energy-transfer rates.

5. REFERENCES

1. Razumova I., Tkachuk A.M., Mironov D., Nikitichev A. *Opt. Spektrosk.* **81**, (2), pp. 230-239. 1996.
2. Guyot C.Li. Y., Linares C., Moncorge R., Jubert M.-F. *OSA Proc.* **15**, pp. 91-95. 1995.
3. Razumova I., Tkachuk A.M., Nikitichev A., Mironov D. *J. Alloys and Compounds.* **225**, pp. 129-132. 1995.
4. Tkachuk A.M., Razumova I.K., Mironov D.I., Nikitichev A.A., M.-F. Joubert M.-F., Moncorge R. *Opt. Spektrosk.* in press.
5. Tkachuk A.M. *Opt. Spektrosk.* **68**, (6), pp. 1324-1336. 1990. [*Opt. Spectrosc. (USSR)*. **68**, (6), pp. 775-783. 1990].
6. Klokishner S.I., Tkachuk A.M. *Opt. Spektrosk.* **68**, (4), pp. 745-751. 1990. [*Opt. Spectrosc. (USSR)*. **68**, (4), pp. 434-438. 1990].
7. Tkachuk A.M., Klokishner S.I. *Opt. Spektrosk.* **61**, (1), pp. 84-90. 1986. [*Opt. Spectrosc. (USSR)*. **61**, (1), pp. 55-61. 1986].

6. ACKNOWLEDGEMENTS

This work was supported by the Russian Foundation for Fundamental Research, Grant No. 97-02-16439.

Energy transfer and lasing in $\text{LiYbF}_4\text{:Ho}$, $\text{LiYbF}_4\text{:Ho,Tm}$ and $\text{KYb(WO}_4)_3$ crystals.

A.V.Sandulenko, V.A.Sandulenko, A.M.Tkachuk, A.N.Titov,
V.M.Reiterov, V.N.Ivanov

All-Russia Scientific Center "S.I.Vavilov State Optical Institute"
Birzhevaja line, 12, St. Petersburg, 199034, Russia, E-mail: alex@tkachuk.spb.su

ABSTRACT

We have studied both theoretically and experimentally the energy transfer processes in $\text{YbLiF}_4\text{:Ho}^{3+}$ (0.4%) and $\text{YbLiF}_4\text{:Ho}^{3+}$ (0.4%), Tm^{3+} (10%) crystals and in the series of crystals $\text{KYb(WO}_4)_2\text{:Tm}^{3+}, \text{Ho}^{3+}$ (0.4%) with the thulium concentration 5; 10; and 20%. The population kinetics of the $^5\text{I}_7$ holmium level was studied under the $1.047\text{ }\mu\text{m}$ Q-switched YLF:Nd^{3+} laser pumping. The efficiency of energy transfer processes in Ho^{3+} doped crystals, codoped with Yb^{3+} and Tm^{3+} , was demonstrated. With an $\text{YbLiF}_4\text{:Ho}^{3+}$ (0.4%) laser rod we have obtained lasing at $2.06\text{ }\mu\text{m}$ with the total efficiency of 4.8% and the slope efficiency of 11%. In the $\text{KYb(WO}_4)_2\text{:Tm}^{3+}$ (10%), Ho^{3+} (0.4%) crystal, lasing was obtained for the first time at $2\text{ }\mu\text{m}$. The pumping threshold being $\sim 150\text{ mJ}$, total efficiency 6% and slope efficiency 9.7% was achieved.

INTRODUCTION.

The task to obtain LD pumped lasing on holmium transitions demands coactivating the crystals with rare-earth ions having their absorption bands corresponding to spectral range of high power (several watts) diodes which are commercially produced nowadays. Thus, studying the processes of energy transfer among coactivators (those are Tm^{3+} and Yb^{3+}) is of great importance.

For the first time the selectively pumped $2\text{ }\mu\text{m}$ lasing in $\text{BaYb}_2\text{F}_8\text{:Ho}$ crystals was reported by B.M.Antipenko et.al.^{1,2}. Neodymium laser was used as a pumping source. The processes of Yb-Ho coupling to influence the population inversion of $^5\text{I}_7 \rightarrow ^5\text{I}_8$ transition were discussed. Up-conversion mechanism of energy migration (Fig. 1a) was suggested to give the main contribution into $^5\text{I}_7$ level populating process. Besides it was proposed that thulium co-doping could improve the lasing properties of this material due to sensitization of $^5\text{I}_7 \rightarrow ^5\text{I}_8$ holmium transition by Tm^{3+} - Ho^{3+} energy transfer (Fig. 1b). But no experiments have been carried out on this matter so far.

In the present work we studied the processes of energy transfer and lasing in crystals co-doped with Yb^{3+} , Tm^{3+} and Ho^{3+} . On one side, this combination of co-doping ions is promising for LD pumping and on the other side, the efficiency of laser properties of $2\text{ }\mu\text{m}$ lasers could be improved. The following groups of crystals were chosen to study: $\text{YbLiF}_4\text{:Ho}^{3+}$, $\text{YbLiF}_4\text{:Tm}^{3+}, \text{Ho}^{3+}$, $\text{KY(WO}_4)_2\text{:Yb}^{3+}, \text{Ho}^{3+}$, and $\text{KY(WO}_4)_2\text{:Yb}^{3+}, \text{Tm}^{3+}, \text{Ho}^{3+}$. We used YLF:Nd^{3+} laser with the wavelength of $1.047\text{ }\mu\text{m}$ to pump the studied crystals as the model source of selective Yb pumping.

The main goal of the present work was detailed study of population inversion mechanisms for holmium $2\text{ }\mu\text{m}$ transition and possibilities of obtaining stimulated emission in $\text{LiYF}_4\text{:Yb}^{3+}, \text{Tm}^{3+}, \text{Ho}^{3+}$ and $\text{KY(WO}_4)_2\text{:Yb}^{3+}, \text{Tm}^{3+}, \text{Ho}^{3+}$.

2. EXPERIMENTAL METHODS.

2.1. Fluorescence kinetics.

The studied crystals were: $\text{YbLiF}_4\text{:Ho}$ (0.4%): Tm (0%, 10%) and $\text{KYb(WO}_4)_2\text{:Ho}$ (0.4%): Tm (0%, 5%, 10%, 20%). They were manufactured as plates 2 mm thick. The samples were pumped by $1.047\text{ }\mu\text{m}$ laser operating in both Q-switch or free-run modes. The lines monitored were - $1.2\text{ }\mu\text{m}$ ($^5\text{I}_6 \rightarrow ^5\text{I}_8$) and $2.07\text{ }\mu\text{m}$ ($^5\text{I}_7 \rightarrow ^5\text{I}_8$), transitions in Ho^{3+} ions, $1.8\text{ }\mu\text{m}$ ($^3\text{F}_4 \rightarrow ^3\text{H}_6$), transition in Tm^{3+} ion, and $1.02\text{ }\mu\text{m}$ ($^2\text{F}_{5/2} \rightarrow ^2\text{F}_{7/2}$), transition in Yb^{3+} ion. The MDR23 monochromator was used for

wavelengths selection. Fluorescence signals were detected by PbS infrared detector. Pumping intensity levels were verified by infrared filters.

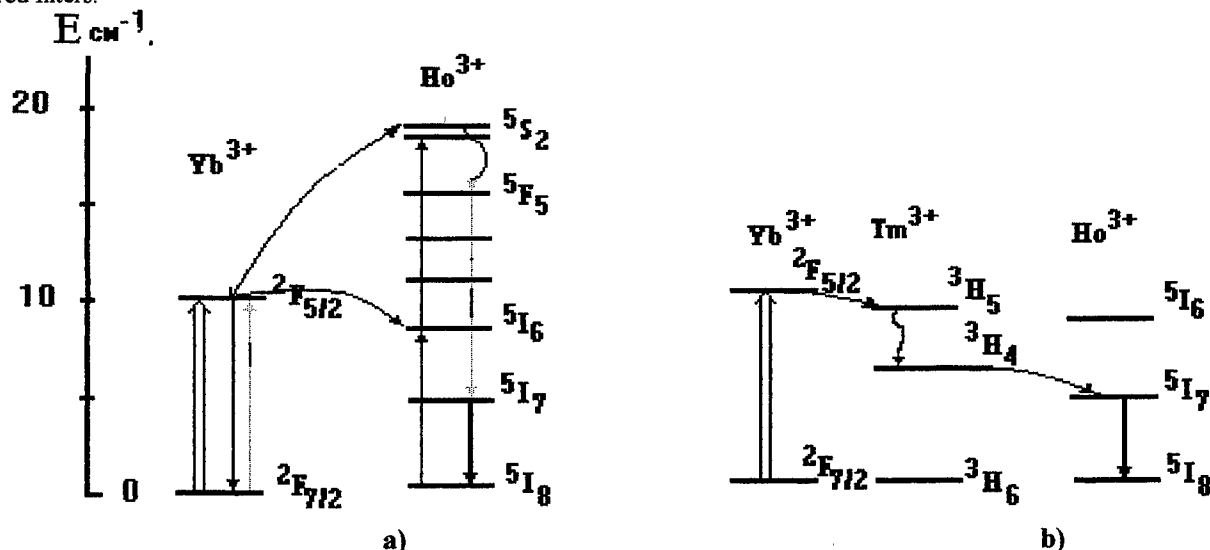


Fig.1 Spectroscopic diagram of 2 μm Ho lasing, a) up-conversion pumping, 1 - energy transfer, 2 - up-conversion b) pumping scheme where Tm^{3+} used as a sensitizer of Ho^{3+} .

We have studied the fluorescence kinetics of pointed above crystals under different pumping conditions: at strong and slight pumping. For strong pumping we used free running mode with pulse energy 0.7 J with pulse duration of 400 μs . Pumping beam was focused on sample with 320 mm lens which permitted us to have 2 mm diameter of pumping beam corresponding to power pump density approximately $I_0=23 \text{ J/cm}^2$. For slight pumping we used the same pump geometry and optical glass filter provided five time decrease in pump intensity.

2.2. Laser experimental set.

1.047 μm YLF:Nd laser operating in free running mode was used as a pumping source. Its output pulse energy was varied up to 1.5 J. Lasing pulse duration was 400 μs . The $\text{YbLiF}_4\text{:Ho}(0.4\%)$ and $\text{YbLiF}_4\text{:Tm}(10\%)\text{:Ho}(0.4\%)$ active crystals were manufactured as rods 30 mm long and 3 mm in diameter. $\text{KYb(WO}_4)_2\text{:Ho}(0.4\%)\text{:Tm}(0\%, 5\%, 10\%, 20\%)$ were 16 mm long and 3 mm in diameter. They were not antireflection coated. Longitudinal pumping scheme was used in the experiment. The cavity was formed with two flat mirrors ($\lambda=2 \mu\text{m}$) and had length of 60 mm. The first mirror had 100% reflectivity at 2 μm and high transmission (about 95%) at pump wavelength 1.047 μm . Output mirror had 80% reflectivity at 2 μm . To provide two-ways pumping of active rod, 100% mirror (at $\lambda=1.047 \mu\text{m}$) was placed behind the output 2 μm mirror. Pumping energy was delivered to active rod through 320 mm lens so as to have slight variation of beam diameter within active rod length. The focus of the lens was behind active rod, beam diameter was 2 mm at the input end of active rod.

3. RESULTS.

3.1 Fluoride crystals.

The kinetic curves of 5I_7 and 5I_6 levels in $\text{YbLiF}_4\text{:Ho}(0.4\%)$ under different pumping conditions (strong and slight pumping) are shown in Fig. 2, 3. Five time increase in pumping power density leads to considerable increase of 5I_7 level populating rate. At the same time kinetic curve of 5I_6 level is deformed in case of strong pumping and its amplitude rises unproportionally to pumping power density. This demonstrates well up-conversion mechanism of 5I_7 level population.

Fig.4 presents kinetic curves of 5I_7 holmium level in $\text{YbLiF}_4\text{:Tm}(10\%)\text{:Ho}(0.4\%)$ pumped by Q-switched 1.047 μm YLF:Nd laser. However, population rate of 5I_7 holmium level in thulium doped crystal is much high than that in $\text{YbLiF}_4\text{:Ho}(0.4\%)$ (5I_7 level population in $\text{YbLiF}_4\text{:Tm}(10\%)\text{:Ho}(0.4\%)$ reaches its maximum within less than 500 μs), and at the same case fluorescence quenching rate of 5I_7 level considerably grows.

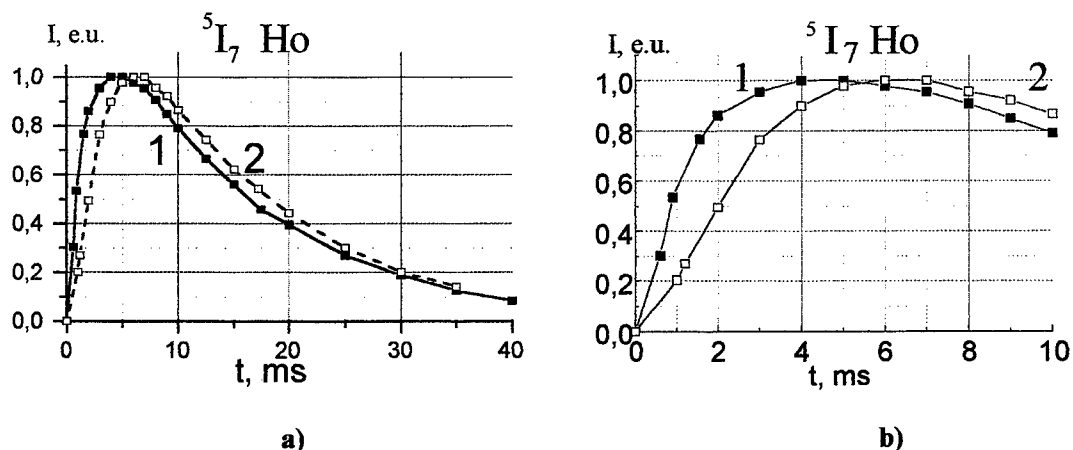


Fig.2. Kinetics of 5I_7 Ho level in $\text{YbLiF}_4:\text{Ho}(0.4\%)$ under free-run $1.047 \mu\text{m}$ laser pumping. Curve 1 - strong pumping, curve 2 - slight pumping. a- total curves, b- initial parts of curves.

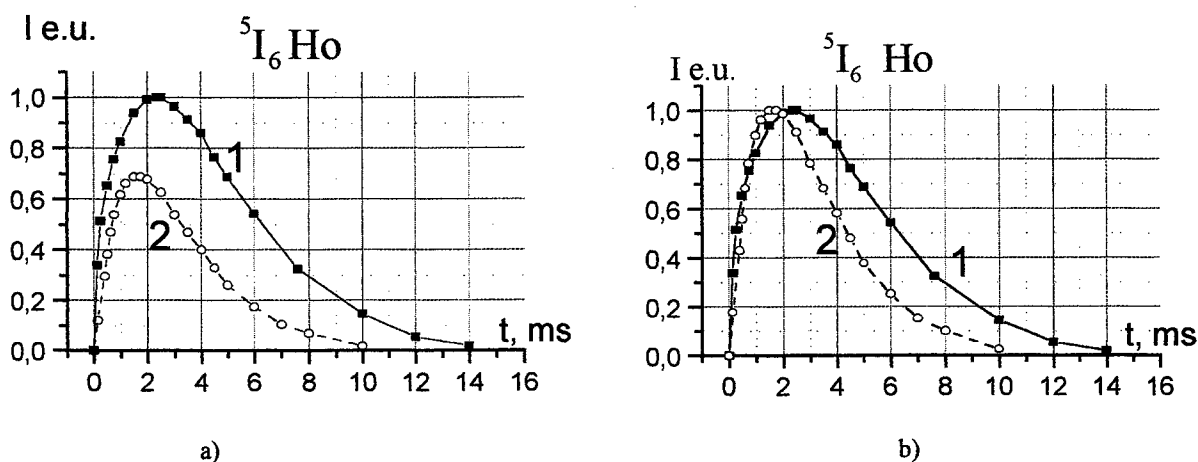


Fig.3. Kinetics of 5I_6 Ho level in $\text{YbLiF}_4:\text{Ho}(0.4\%)$ under free-run $1.047 \mu\text{m}$ laser pumping. Curve 1- strong pumping, curve 2 - slight pumping. a- absolute scale, b- normalized to their maximums.

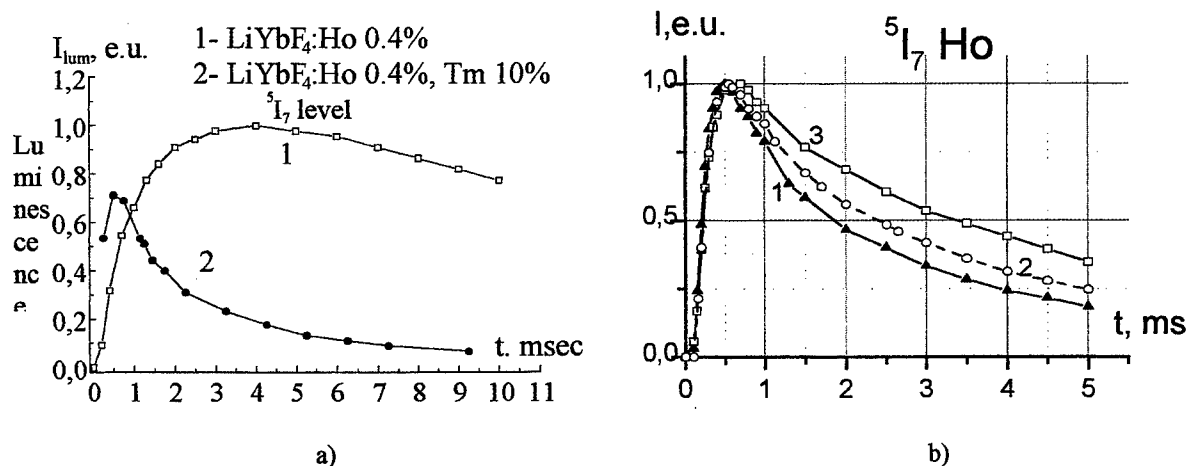


Fig.4 Fluorescence kinetics of 5I_7 level Ho^{3+} in a) in $\text{LiYbF}_4:\text{Ho}(0.4\%)$ (1) and $\text{LiYbF}_4:\text{Ho}(0.4\%):\text{Tm}(10\%)$ (2) under Q-switch $1.047 \mu\text{m}$ laser pumping. (points- experiment, solid curves - calculated), b) in $\text{LiYbF}_4:\text{Ho}(0.4\%):\text{Tm}(10\%)$ at different pumping intensities. 1- strong pumping ($I_0 = 23 \text{ J/cm}^2$), 2 - $0.5 I_0$, 3 - $0.2 I_0$).

Experimental study of the fluorescence kinetics of 5I_7 Ho^{3+} level in $YbLiF_4:Tm(10\%):Ho(0.4\%)$ showed that decay curve was non-exponential in the presence of Tm^{3+} ions and its fast component appeared to be dependent upon pumping power density (Fig. 4b). At the same time no noticeable fluorescence signal was detected within $1.2 \mu m$ ($^5I_6 \rightarrow ^5I_8$) and $1.02 \mu m$ ($^2F_{5/2} \rightarrow ^2F_{7/2}$) spectral regions for $YbLiF_4:Tm(10\%):Ho(0.4\%)$ which shows strong quenching of holmium 5I_6 and $^2F_{5/2}$ ytterbium levels due to the coupling processes.

3.2. Tungstate crystals.

Fig.5 presents kinetic curves for 5I_7 holmium level in $KYb(WO_4)_2:Tm:Ho(0.4\%)$ with different thulium concentrations. In crystal with no thulium 5I_7 holmium level reaches its maximum within 1.5 ms. In thulium doped crystals population rate of 5I_7 holmium level is much higher. Maximum of population corresponds to 300 μs , 150 μs , 120 μs for thulium concentrations 5%, 10%, 20% respectively. At the same time 5I_7 quenching rate grows when increasing thulium concentration (Table 1).

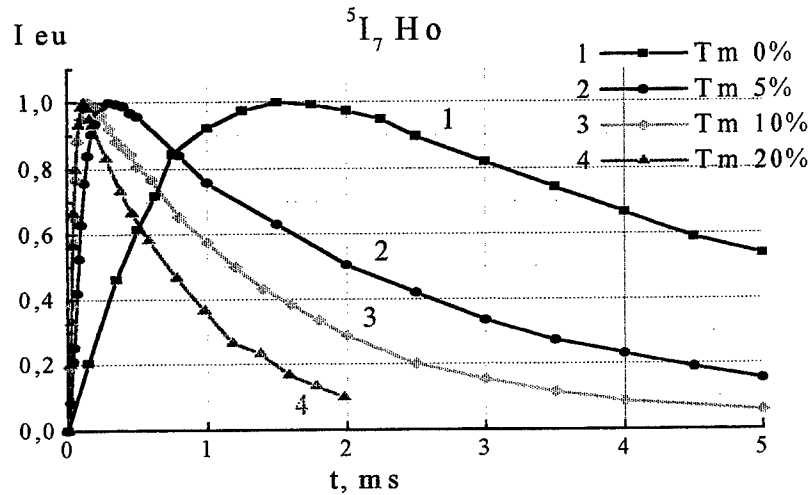


Fig.5. Fluorescence kinetics for 5I_7 level Ho^{3+} in $KYb(WO_4)_2:Ho(0.4\%):Tm$ with different Tm^{3+} concentrations at Q-switch $1.047 \mu m$ YLF:Nd laser pumping.

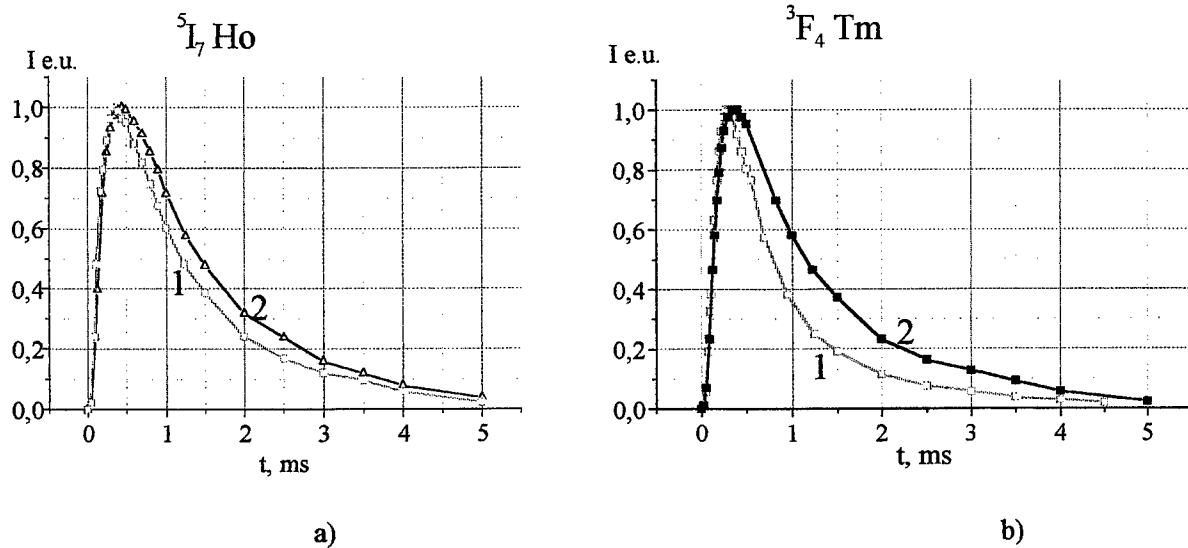


Fig.6. Fluorescence kinetics for 5I_7 Ho level (a) and 3F_4 Tm^{3+} level in $KYb(WO_4)_2:Ho(0.4\%):Tm(10\%)$ under $1.047 \mu m$ pumping at different pump power densities 1- strong pumping, 2- slight pumping.

As it seen from Fig.6 the decay time of the 5I_7 Ho $^{3+}$ level changed slightly with growing of pumping density. No noticeable fluorescence signal was detected on lines $1.2\text{ }\mu\text{m}$ ($^5I_6 \rightarrow ^5I_8$) and $1.02\text{ }\mu\text{m}$ ($^2F_{5/2} \rightarrow ^2F_{7/2}$) in thulium doped crystals.

Table 1. Dependence of 5I_7 holmium level life time on thulium concentration in KYb(WO $_4$) $_2$:Tm:Ho(0.4%).

Thulium concentration %	5I_7 life time, ms
0	4.0
5	2.5
10	1.5
20	1.0

3.3. Lasing experiments

With an YbLiF $_4$:Ho(0.4%) laser rod we have obtained lasing at $2.06\text{ }\mu\text{m}$ with the total efficiency 4.8%, the maximal slope efficiency 11%, the threshold energy being $E_{th} \sim 150\text{ mJ}$ (Fig. 7). One can see the influence of non-linear mechanisms upon inversion population on 5I_7 holmium laser level. It is seen from Fig. 7 that slope efficiency appeared to be dependent on pumping energy. In the Tm-doped crystals, the energy threshold was $E_{th} = 1100\text{ mJ}$.

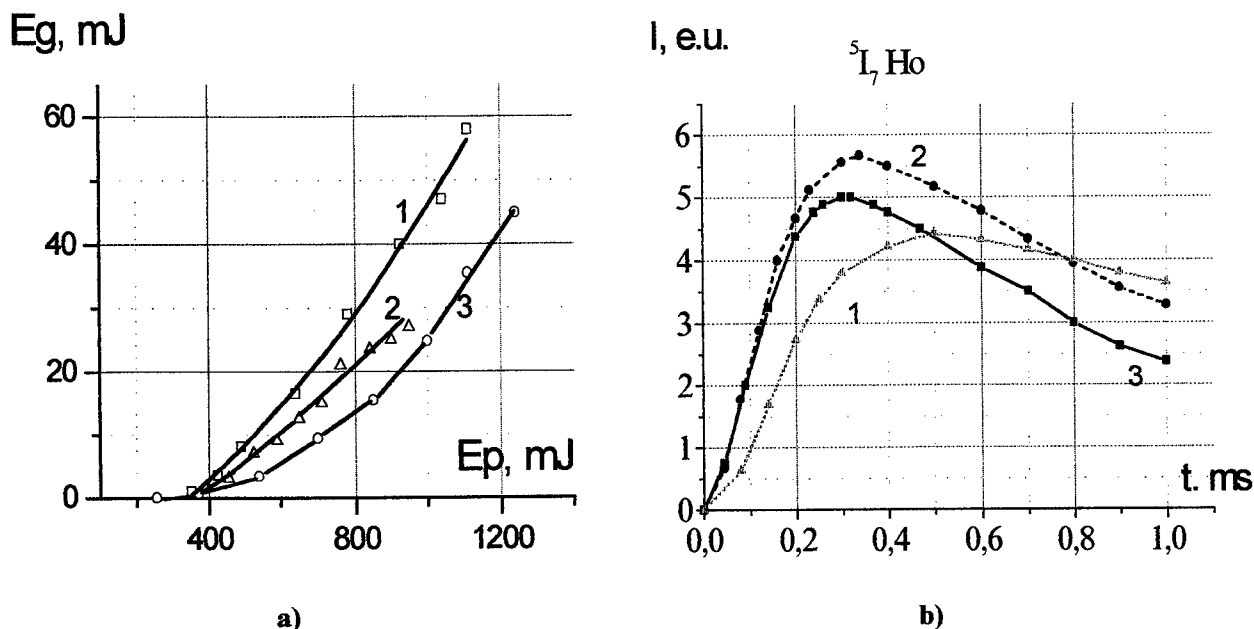


Fig. 7 a) Lasing outputs of KYb(WO $_4$) $_2$:Ho(0.4%):Tm(10%) (curve 1) KYb(WO $_4$) $_2$:Ho(0.4%):Tm(20%) (curve 2) and YbLiF $_4$:Ho(0.4%) (curve 3). b) Kinetics of 5I_7 Ho $^{3+}$ level in KYb(WO $_4$) $_2$:Ho(0.4%):Tm, 1- 5%Tm, 2- 10%Tm, 3- 20%Tm. Pumping by YLF:Nd $1.047\text{ }\mu\text{m}$ laser.

In the KYb(WO $_4$) $_2$:Tm, Ho(0.4%) crystals, lasing was obtained in all Tm $^{3+}$ - doped (5, 10 and 20%) crystals. In the Tm $^{3+}$ - less laser rod stimulated emission was not achieved. In the crystal with 5% of Tm $^{3+}$, the threshold was $E_{th} = 1200\text{ mJ}$. Most efficient laser action was observed in the crystal with 10% of Tm $^{3+}$, the pumping threshold being $\sim 150\text{ mJ}$, total efficiency 6% and slope efficiency 9.7%. Optimum of thulium concentration could be well demonstrated by Fig.7 where behaviour of 5I_7 level population is presented for equal pumping conditions (curves are normalised to equal absorbed energy).

4. DISCUSSION

We have made an attempt to make rate-equation analysis of Yb $^{3+}$ -Tm $^{3+}$ -Ho $^{3+}$ doped systems in fluoride matrix. Theoretical consideration of the population kinetics in YbLiF $_4$:Tm $^{3+}$ (10%), Ho $^{3+}$ (0.4%) and YbLiF $_4$:Ho $^{3+}$ (0.4%) was carried out

by the lack of known microparameters of all coupling processes taking place in the studied system. The processes taken into consideration are shown in the Fig.8. Those are: radiative and nonradiative spontaneous relaxation, non-radiative cross-relaxation energy transfer, nonlinear and cooperative coupling.

4.1. Microparameters for Tm^{3+} - Tm^{3+} , Tm^{3+} - Ho^{3+} , Yb^{3+} - Tm^{3+} and Yb^{3+} - Ho^{3+} coupling.

Energy-level diagram of considered crystals is shown in Fig. 1. All processes involved into consideration, which take place under IR excitation of $\text{LiYbF}_4:\text{Tm}^{3+}, \text{Yb}^{3+}$ crystals are indicated by arrows and pointed as: A_{ij} , B_{ij} and C_{12} - radiative probability from level "i" to level "j" in Ho, Tm and Yb ions accordingly, W_{ij} and W_{21}^m - nonradiative probabilities, α_i - constant of energy transfer (sensitization, selfquenching), β_i - constant of Tm-Yb and Yb-Ho nonlinear coupling (up-conversion at Tm-Yb and Yb-Ho coupling), γ_i - constant of Tm-Tm-Yb and Yb-Ho-Ho cooperative coupling.

Spontaneous radiative and nonradiative probabilities for the $\text{YLF}:\text{Ho}^{3+}$ and $\text{YLF}:\text{Tm}^{3+}$ crystals were studied in ^{3,5}. Optical properties of $\text{YLF}:\text{Yb}^{3+}$ were studied experimentally.

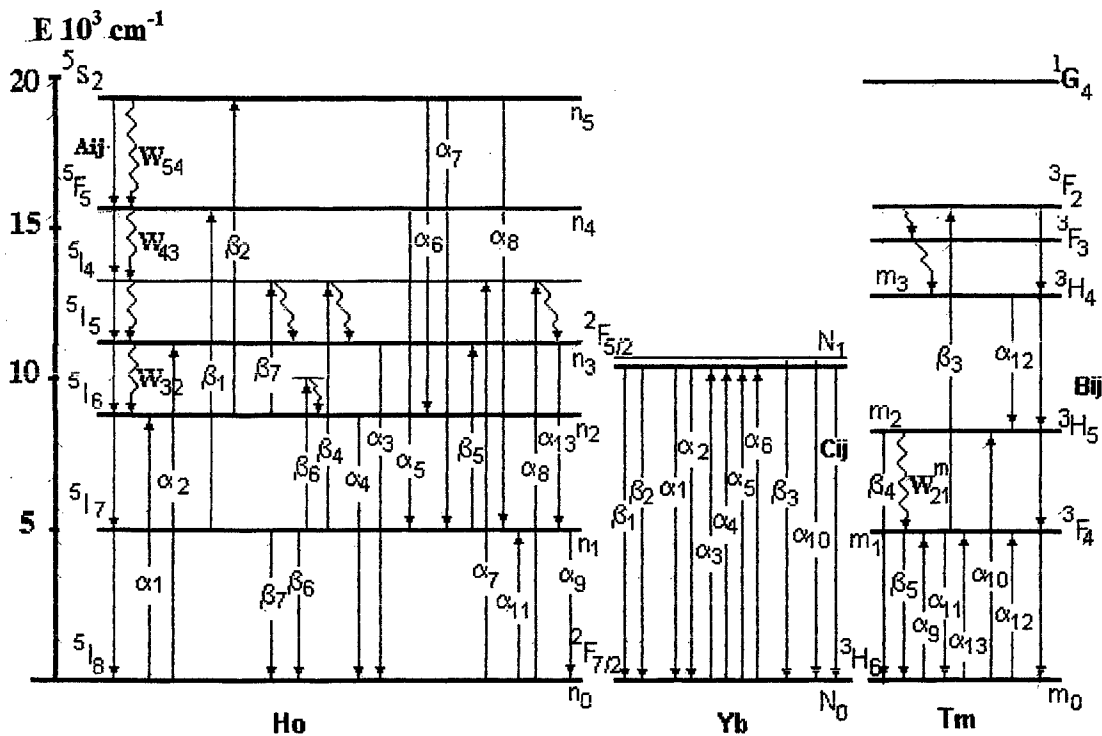


Fig.8. Interior coupling scheme of crystal codoped with Yb^{3+} - Ho^{3+} - Tm^{3+}

The estimation of energy transfer constants was provided on the basis of energy transfer macrorates calculation. It is possible if the values of ET microparameters are known and the mechanisms of ion-ion coupling is determined. For this purpose we provided the experimental and theoretical study of the Tm^{3+} - Tm^{3+} , Yb^{3+} - Tm^{3+} , Yb^{3+} - Ho^{3+} and Tm^{3+} - Ho^{3+} coupling in $\text{LiY}(\text{Yb})\text{F}_4$ crystals codoped with Tm^{3+} and (or) Ho^{3+} . The selfquenching in $\text{YLF}:\text{Tm}^{3+}$ crystals was studied in the series of crystals with different thulium concentration: from 0.5 to 10 at. % ^{6,7}. Energy transfer microparameters of migration (C_{DD}), selfquenching (C_{DA}) and up-conversion (C_{DA}) for Tm^{3+} - Tm^{3+} and Ho^{3+} - Ho^{3+} coupling in YLF crystals were taken from ^{6,8}, for crystals co-doped with ytterbium those were estimated using the method of the model quantum mechanical calculation ^{9,10}. The results for $\text{YLF}:\text{Tm}^{3+}, \text{Yb}^{3+}$, $\text{YLF}:\text{Ho}^{3+}, \text{Yb}^{3+}$ and $\text{YLF}:\text{Ho}^{3+}, \text{Tm}^{3+}$ crystals are summarized in Tables 1 and 2.

The determination of Yb^{3+} - Ho^{3+} energy transfer macrorates in $\text{YLF}:\text{Ho}^{3+}, \text{Yb}^{3+}$ was made taking into account the comparison of the calculated and experimental luminescence decay curves recorded for $^5\text{I}_7$, $^5\text{I}_6$ holmium and $^3\text{F}_4$ thulium levels after its selective pumping into $^2\text{F}_{5/2}$ ytterbium level by $\text{Nd}^{3+}:\text{YLF}$ laser pulses working at free-running and Q-switch modes and effective values of α_i constant were determined.

It is obviously that the full picture of RE^{3+} coupling in $LiYbF_4:Ho^{3+},Tm^{3+}$ can not be understood without taking into account all possible processes of interion coupling. For this purpose we tried to describe the experimental kinetics of holmium levels populations with the system of balance rate equations.

Table 1. Results of microparameter (C_{DD} , C_{DA}) calculations for Yb-Yb migration (DD), Yb-Ho energy transfer (ET1, ET2), Ho-Tm energy transfer (ET3), Ho-Ho selfquenching (SQ), and nonlinear coupling (NQ and NC) in $LiYbF_4:Ho$.

No.	Cross-relaxation scheme	$C_{DD}, C_{DA},$ $10^{-40} \text{ cm}^6 \text{ s}^{-1}$
DD	Yb – Yb migration ($^2F_{5/2} \rightarrow ^2F_{7/2}$) : ($^2F_{7/2} \rightarrow ^2F_{5/2}$)	112
ET1	Yb – Ho energy transfer ($^2F_{5/2} \rightarrow ^2F_{7/2}$) : ($^5I_8 \rightarrow ^5I_5$) – $h\omega$	0.14
ET2	($^2F_{5/2} \rightarrow ^2F_{7/2}$) : ($^5I_8 \rightarrow ^5I_6$) + $2h\omega$	0.42
ET3	Ho – Tm energy transfer ($^5I_7 \rightarrow ^5I_8$) : ($^3F_4 \rightarrow ^3H_6$) – $h\omega$	10.7
SQ	Ho – Ho selfquenching ($^5S_2 \rightarrow ^5I_4$) : ($^5I_8 \rightarrow ^5I_7$)	29
NQ1	Ho-Ho up-conversion ($^5I_7 \rightarrow ^5I_6$) : ($^5I_7 \rightarrow ^5I_8$) + $3h\omega$	0.006
NQ2	($^5I_7 \rightarrow ^5I_5$) : ($^5I_7 \rightarrow ^5I_8$) – $2h\omega$	0.023
NQ3	($^5I_6 \rightarrow ^5I_7$) : ($^5I_7 \rightarrow ^5I_8$)	52
NC1	Yb – Ho up-conversion ($^2F_{5/2} \rightarrow ^2F_{7/2}$) : ($^5I_7 \rightarrow ^5F_5$)	48
NC2	($^2F_{5/2} \rightarrow ^2F_{7/2}$) : ($^5I_6 \rightarrow ^5S_2$)	43

Table 2. Results of microparameter (C_{DD} , C_{DA}) calculations for Tm-Tm migration (DD), Yb-Tm energy transfer (ET1), Tm-Tm selfquenching (SQ), Tm-Ho energy transfer (ET2) and nonlinear coupling (NQ and NC) in $LiYbF_4:Tm$.

No.	Cross-relaxation scheme	$C_{DD}, C_{DA},$ $10^{-40} \text{ cm}^6 \text{ s}^{-1}$
DD	Tm – Tm migration ($^3H_4 \rightarrow ^3H_6$) : ($^3H_6 \rightarrow ^3H_4$)	34.2*
ET1	Yb – Tm energy transfer ($^2F_{5/2} \rightarrow ^2F_{7/2}$) : ($^3H_6 \rightarrow ^3H_5$) + $2h\omega$	0.01
SQ1	Tm – Tm selfquenching ($^3H_4 \rightarrow ^3F_4$) : ($^3H_6 \rightarrow ^3F_4$) + $2h\omega$	0.59
SQ2	($^3H_4 \rightarrow ^3F_4$) : ($^3H_6 \rightarrow ^3H_5$) – $h\omega$	0.011
ET2	Tm – Ho energy transfer ($^3F_4 \rightarrow ^3H_6$) : ($^5I_8 \rightarrow ^5I_7$) + $h\omega$	22.8
NQ	Tm – Tm up-conversion ($^3F_4 \rightarrow ^3H_4$) : ($^3F_4 \rightarrow ^3H_6$) – $2h\omega$	0.009
NC1	Yb – Tm up-conversion ($^2F_{5/2} \rightarrow ^2F_{7/2}$) : ($^3F_4 \rightarrow ^3F_2$)	61
NC2	($^2F_{5/2} \rightarrow ^2F_{7/2}$) : ($^3H_4 \rightarrow ^1G_4$) + $2h\omega$	0.74

4.2. System of balance rate equations

We have considered the system $YbLiF_4:Tm^{3+}, (10\%), Ho^{3+} (0.4\%)$, containing low concentration of Ho^{3+} ions, since we did not need to take into account $Ho^{3+} - Ho^{3+}$ coupling. Additional conditions were as follows: 1) under slight pumping all constants describing nonlinear coupling were equal to zero ($\beta_6 = 0$ and $\beta_7 = 0$), and 2) the parameters depending on the population of excited levels were varied in reasonable limits as well as initial populations.

The system of balance rate equations for normalized populations $n_i = n(Ho)/n(Ho)$, $N_i = N(Yb)/N(Yb)$ and $m_i = m(Tm)/m(Tm)$, where $n(Ho)$, $N(Yb)$ and $m(Tm)$ are concentration of Ho^{3+} , Yb^{3+} , and Tm^{3+} ions accordingly, was:

$$dn_1/dt = -A_{10}x_1 + (A_{21} + W_{21})n_2 + A_{31}n_3 + A_{41}n_4 + A_{51}n_5 + \alpha_5 n_4 N_0 + \alpha_9 n_1 m_0 + \alpha_{11} n_0 m_1 + \alpha_{13} n_3 m_0 - \beta_1 n_1 N_1 - \beta_4 n_1 m_2 - \beta_5 n_1 m_1 + 2\gamma n_0 N_1$$

$$dn_2/dt = -(\sum_{j=0}^1 A_{2j} + W_{21})n_2 + (A_{32} + W_{32})n_3 + A_{42}n_4 + A_{52}n_5 + \alpha_1 n_0 N_1 - \alpha_4 n_2 N_0 + \alpha_6 n_5 N_0 - \beta_2 n_2 N_1$$

$$dn_3/dt = -(\sum_{j=0}^2 A_{3j} + W_{32})n_3 + (A_{43} + W_{43})n_4 + A_{53}n_5 + \alpha_2 n_0 N_1 - \alpha_3 n_3 N_0 - \alpha_{13} n_3 m_0 + \beta_4 n_1 m_2 + \beta_5 n_1 m_1$$

$$dn_4/dt = - \left(\sum_{j=0}^3 A_{4j} + W_{43} \right) n_4 + (A_{54} + W_{54}) n_5 - \alpha_5 n_4 N_0 + \beta_1 n_1 N_1$$

$$dn_5/dt = - \left(\sum_{j=0}^4 A_{5j} + W_{54} \right) n_5 - \alpha_6 n_5 N_0 + \beta_2 n_2 N_1$$

$$dN_1/dt = -C_{10} N_1 - \alpha_1 n_0 N_1 - \alpha_2 n_0 N_1 + \alpha_3 n_3 N_0 + \alpha_4 n_2 N_0 + \alpha_5 n_4 N_0 + \alpha_6 n_5 N_0 - \alpha_{10} m_0 N_1 - \beta_1 n_1 N_1 - \beta_2 n_2 N_1 - \beta_3 m_1 N_1 - \gamma n_0 N_1 - \gamma_1 m_0 N_1$$

$$dm_1/dt = -B_{10} m_1 + (B_{21} + W_{21}) m_2 + B_{31} m_3 + \alpha_9 n_1 m_0 - \alpha_{11} n_0 m_1 + \alpha_{12} m_0 m_3 + \alpha_{13} n_3 m_0 - \beta_3 m_1 N_1 - \beta_5 n_1 m_1 + 2\gamma_1 m_0 N_1$$

$$dm_2/dt = - \left(\sum_{j=0}^1 B_{2j} + W_{21} \right) m_2 + (B_{32} + W_{32}) m_3 + \alpha_{10} m_0 N_1 + \alpha_{12} m_0 m_3 - \beta_4 n_1 m_2$$

$$dm_3/dt = - \left(\sum_{j=0}^2 B_{3j} + W_{32} \right) m_3 - \alpha_{12} m_0 m_3 + \beta_3 m_1 N_1$$

$$n_0 + n_1 + n_2 + n_3 + n_4 = 1, \quad N_1 + N_2 = 1, \quad \text{and} \quad m_0 + m_1 + m_2 + m_3 = 1$$

Initial conditions at pumping into $^2F_{5/2}$ Yb level ($\lambda = 914$ nm) were: $n_0 = 1$; $n_1 = 0$; $n_2 = 0$; $n_3 = 0$; $n_4 = 0$; $N_0 = 0.6$; $N_1 = 0.4$; $m_0 = 1$; $m_1 = 0$; $m_2 = 0$; $m_3 = 0$.

In Fig. 9a the results of rate-equation analysis of the population kinetics of 5I_7 Ho $^{3+}$ level in YbLiF $_4$:Ho $^{3+}$ (0.4%) (curve 1) and YbLiF $_4$:Tm $^{3+}$ (10%),Ho $^{3+}$ (0.4%) (curve 2) crystals are presented as well as experimental luminescence kinetics of 5I_7 holmium level (points - experiment, solid curves - calculations). Similar calculations were provided for YbLiF $_4$:Ho $^{3+}$ (0.4) at different pumping intensities. The results are presented in Fig.9b: curve 1 - strong pumping density, curve 2 - slight pumping density. Comparison of calculated and experimental kinetics for YbLiF $_4$:Tm $^{3+}$ (10%),Ho $^{3+}$ (0.4%) and YbLiF $_4$:Ho $^{3+}$ (0.4%) crystals demonstrated good agreement between theoretical and experimental results.

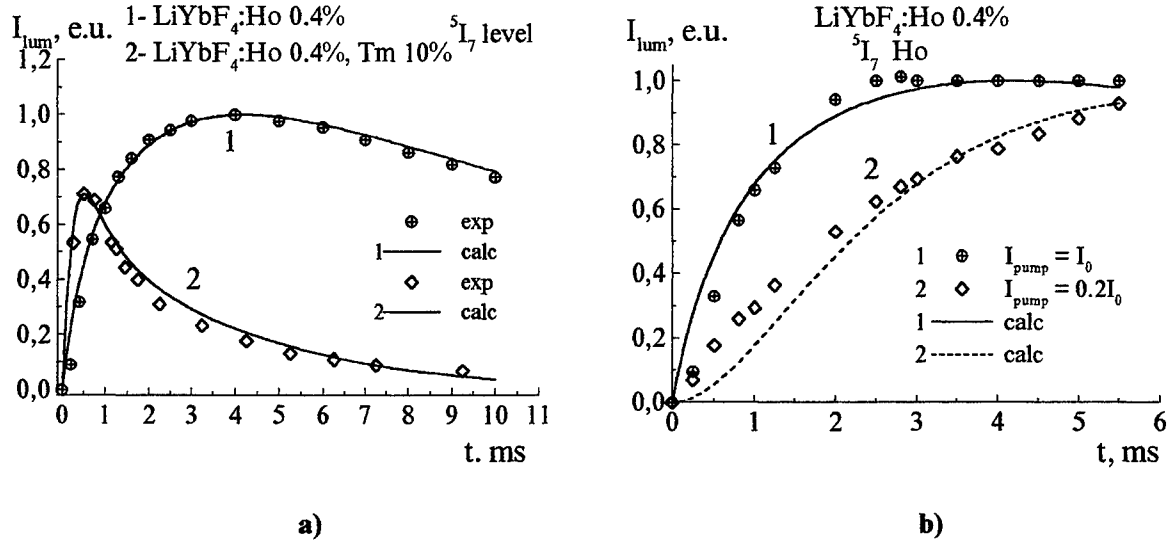


Fig.9 Fluorescence kinetics of 5I_7 Ho level. a) - in LiYbF $_4$:Ho(0.4%) (curve 1) and LiYbF $_4$:Ho(0.4%):Tm(10%) (curve 2) under Q-switch 1.047 μ m laser pumping. Points - experiment, solid curves - calculated. b) - in LiYbF $_4$:Ho(0.4%) at different pumping intensities. 1- strong pumping ($P_0=23$ J/cm 2), 2 - slight pumping ($P = 0.2 P_0$). Points - experiment, solid curves - calculated.

5. CONCLUSION

We have studied both theoretically and experimentally the energy transfer processes in YbLiF $_4$:Ho $^{3+}$ (0.4%) and YbLiF $_4$:Ho $^{3+}$ (0.4%),Tm $^{3+}$ (10%) crystals and in the series of crystals KYb(WO $_4$) $_2$:Tm $^{3+}$,Ho $^{3+}$ (0.4%) with the thulium

concentration 0.5; 10; and 20%. μm The population kinetics of the $^5\text{I}_7$ holmium level was studied under the $1.047\text{ }\mu\text{m}$ Q-switched YLF:Nd^{3+} laser pumping. The efficiency of energy transfer processes in Ho^{3+} doped crystals, codoped with Yb^{3+} and Tm^{3+} , was demonstrated. With an $\text{YbLiF}_4:\text{Ho}^{3+}$ (0.4%) laser rod we have obtained lasing at $2.06\text{ }\mu\text{m}$ with the total efficiency of 4.8% and the slope efficiency of 11%. In the $\text{KYb(WO}_4)_2:\text{Tm}^{3+}$ (10%), Ho^{3+} (0.4%) crystal, lasing was obtained for the first time at $2\text{ }\mu\text{m}$. The pumping threshold being $\sim 150\text{ mJ}$, total efficiency 6% and slope efficiency 9.7% was achieved.

We have made rate-equation analysis of $\text{Yb}^{3+}-\text{Tm}^{3+}-\text{Ho}^{3+}$ doped systems in fluoride matrix. Theoretical consideration of the population kinetics in $\text{YbLiF}_4:\text{Tm}^{3+}$ (10%), Ho^{3+} (0.4%) and $\text{YbLiF}_4:\text{Ho}^{3+}$ (0.4%) was provided for the lack of known microparameters of all coupling processes taking place in the studied system and demonstrated good agreement between theoretical and experimental results.

On the basis of experimental and theoretical spectroscopic studies as well as lasing results of studied systems the following conclusions were made:

- 1) Up-conversion scheme works efficiently in fluoride crystals. Codoping with thulium does not lead to improvement of $2\text{ }\mu\text{m}$ lasing properties due to efficient up-conversion processes.
- 2) On the contrary, $\text{Tm}^{3+} \rightarrow \text{Ho}^{3+}$ sensitizing scheme is more probable within potassium-ytterbium tungstate crystals.

6.ACKNOLEGEMENTS

The work was supported by Russian Foundation for Basic Researches. Grant No. 97-02-16439

7.REFERENCES

1. B.M.Antipenko, A.A.Mak, O.B.Raba et.al. *Sov.J. "Quantovaja electronica"* 1983, V.10 p.889-892
2. B.M.Antipenko, B.V.Sinitzin, T.V.Uvarova. *Sov.J. "Quantovaja electronica"* 1980, V.7, N9 p.2019-2021
3. A.M.Tkachuk, A.V.Chilko, M.V.Petrov. *Optica and Spektr.* **58**, (1), pp. 91-97. 1985.
4. I.Razumova, A.M.Tkachuk, D.Mironov, A.Nikitichev. *Optica and Spektr.* **81**, (2), pp. 230-239. 1996.
5. C.Li.Y Guyot., C.Linares, R.Moncorge, M.-F.Jubert. *OSA Proc.* **15**, pp. 91-95. 1995.
6. I.Razumova, A.M.Tkachuk, A. Nikitichev, D.Mironov. *J. Alloys and Compounds.* **225**, pp. 129-132. 1995.
7. I.Razumova, A.M.Tkachuk, D.Mironov, A.Nikitichev, M.-F. Joubert, R. Moncorge *Optica and Spektr.* in press.
8. A.M.Tkachuk. *Opt. Spektrosk.* **68**, (6), pp. 1324-1336. 1990. [*Opt. Spectrosc.* (USSR). **68**, (6), pp. 775-783. 1990].
9. S.I.Klokishner, A.M.Tkachuk. *Opt. Spektrosk.* **68**, (4), pp. 745-751. 1990. [*Opt. Spectrosc.* (USSR). **68**, (4), pp. 434-438. 1990].
10. A.M.Tkachuk A.M., S.I.Klokishner. *Opt. Spektrosk.* **61**, (1), pp. 84-90. 1986. [*Opt. Spectrosc.* (USSR). **61**, (1), pp. 55-61. 1986].

Spectroscopic and laser properties of $\text{LaSc}_3(\text{BO}_3)_4\text{:Cr,Yb,Er}$ -crystals

O.V.Kuzmin, S.A.Kutovoi, V.L.Panyutin -

SPA "Firm" Krasnodar, Russia

S.T.Durmanov, Yu.P.Rudnitskiy, G.V.Smirnov -

TRINITI, Troitsk Moscow reg., Russia. E-mail: smirgen@fly.triniti.troitsk.ru

ABSTRACT

Spectro-luminescent characteristics were determined for $\text{LaSc}_3(\text{BO}_3)_4$ -crystals, activated by ions of the ytterbium and the erbium. Quantum efficiency of nonradiative transfer from the ions Yb^{3+} to the Er^{3+} is closed to 80% for concentration of ions $[\text{Yb}]=10^{21} \text{ cm}^{-3}$, $[\text{Er}]=5 \cdot 10^{19} \text{ cm}^{-3}$. Quantum efficiency of energy transmission from the Cr^{3+} to the Er^{3+} is about 90%. Having achieved population inversion in the Er-ions the efficiency of energy transmission decay to 70%. We have fulfilled comparison of generation properties for lasers with active elements made of LSB-crystal, that contents $[\text{Cr}^{3+}]=0.5 \text{ at. \%}$, $[\text{Yb}^{3+}]=10 \text{ at. \%}$, $[\text{Er}^{3+}]=0.5 \text{ at. \%}$, and phosphate glass that contents $[\text{Cr}^{3+}]=0.3 \text{ wt. \%}$, $[\text{Yb}^{3+}]=20 \text{ wt. \%}$, $[\text{Er}^{3+}]=0.2 \text{ wt. \%}$.

Key words: luminescence, absorption, $\text{LaSc}_3(\text{BO}_3)_4$ -crystals, rare-earth scandium tetraborates.

1. INTRODUCTION

An intensive luminescence of Er^{3+} ions from $^4\text{I}_{13/2}$ level at wavelength $\sim 1.54 \mu\text{m}$ is observed in phosphate and silicate glasses and crystals where maximum energy of phonons is close to 1200 cm^{-1} . Luminescence from $^4\text{I}_{11/2}$ level is quenched by non-radiate transitions $^4\text{I}_{11/2} \rightarrow ^4\text{I}_{13/2}$ with birth of phonons. In garnets where energy of phonons does not exceed 810 cm^{-1} an intensive luminescence is also observed from the $^4\text{I}_{11/2}$ level at 2980 and 980 nm. In absorption spectrum of rare-earth scandium tetraborates in the near IR range an absorption is observed even at 2500 cm^{-1} which is stipulated by the multi-phonon transitions and that is why the luminescence from the $^4\text{I}_{11/2}$ is quenched completely but luminescence at $1.54 \mu\text{m}$ from the $^4\text{I}_{13/2}$ level is observed.

Non-radiate energy transfer from Cr^{3+} and Yb^{3+} ions to Er^{3+} ions is widely used for sensitization of Er^{3+} luminescence because Er^{3+} ions have low intensive absorption bands.

Because of the considerable minimal distance between rare-earth ions in tetraborates ¹ ($\sim 5.9 \text{ \AA}$ versus $\sim 3.5 \text{ \AA}$ in garnets and glasses) there exists a low efficiency of non-radiate dipole-dipole energy transfer to Er^{3+} ions. A proved method of an increase of the efficiency of energy transfer in the $\text{Cr} \rightarrow \text{Yb} \rightarrow \text{Er}$ chain in phosphate and silicate glasses is a maximum possible increase of Yb^{3+} ions concentration till the value determined by Yb^{3+} solubility in glasses or crystals. Energy transfer between Yb^{3+} and Er^{3+} ions in this case is considerably accelerated by migration of excitation along Yb^{3+} ions ².

As the experience showed, maximum Yb^{3+} ions concentration in lanthanum scandium borate (LSB) is 10 at.% of Sc concentration or $1.35 \cdot 10^{21} \text{ cm}^{-3}$. At such concentration optically homogenous crystals with an even distribution of rare-earth ions and chromium in the volume are obtained.

2. LUMINESCENCE AND ABSORPTION SPECTRA

Fig.1,2 shows absorption and luminescence spectra of Yb^{3+} ions in LSB. The short wave band is stimulated by transitions to the upper Stark component of the $^2\text{F}_{5/2}$ level. Absorption cross-section at the wavelength of laser diode pumping 980 nm equals $1.5 \cdot 10^{-21} \text{ cm}^2$. The bands stipulated by transitions between lower components of metastable level and Stark levels of the ground state $^2\text{F}_{7/2}$ are distinguished in the luminescence. The lifetime of Yb^{3+} -ions equals 900 μs . The luminescence exited by a short light pulse extinguishes exponentially.

Although fig.1,2 shows absorption and luminescence spectra of Er^{3+} for ions concentration in the crystal $6.75 \cdot 10^{20} \text{ cm}^{-3}$. The lifetime of Er^{3+} -ions equals 700 μs . Radiation (spontaneous) lifetime of the excited level $^4\text{I}_{13/2}$ of Er^{3+} calculated on the basis of the value of absorption in the range of overlapping with the luminescence spectra is ~ 7 ms. That is the quantum output of luminescence is close to 10%. The comparison of absorption and luminescence spectra of Er^{3+} ions gives a basis to think that the intensive band with a maximum at $\lambda=1534$ nm corresponds a transition between lower Stark levels of the ground and metastable states.

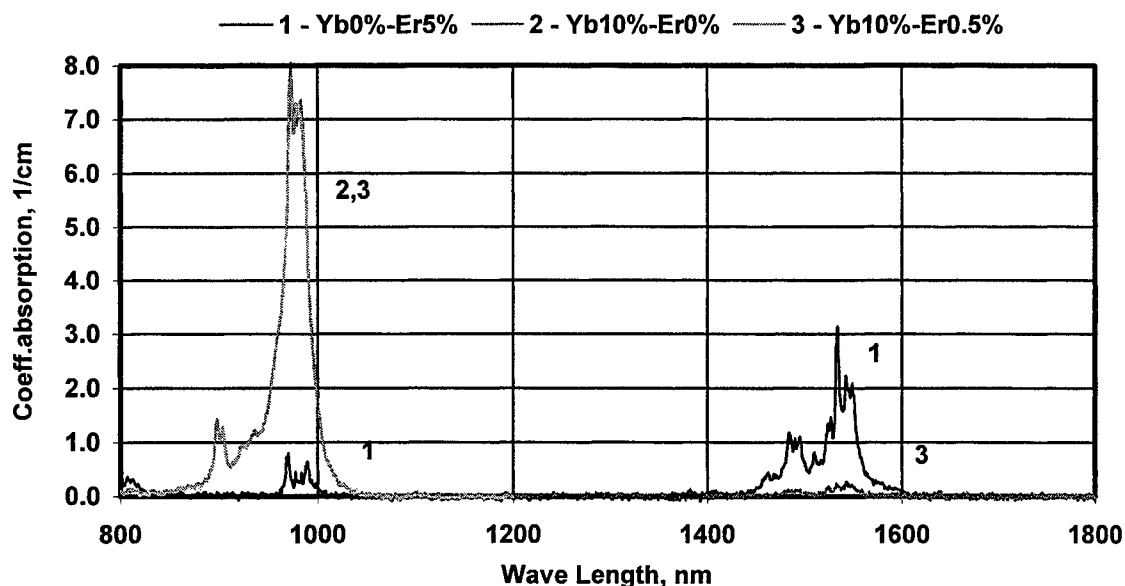


Figure 1. Absorption spectrum of the LSB-crystals

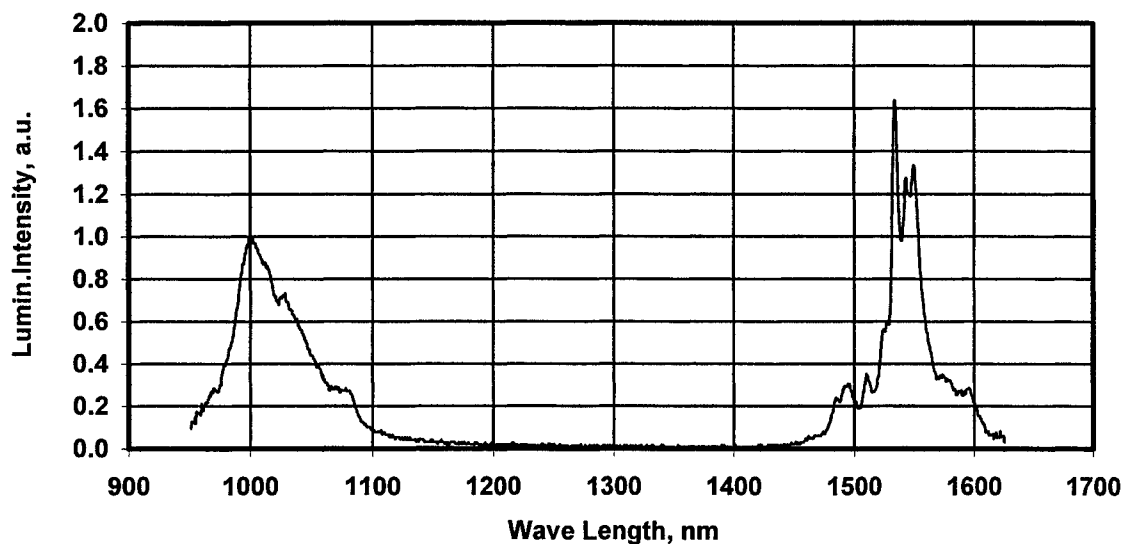


Figure 2. Luminescence spectrum of the LSB:Cr[1.5%]Yb[10%]Er[0.5%]-crystal

Bands with the wavelengths 1545 and 1550 nm correspond to transitions between Stark levels of the $^4I_{15/2}$ state which are 60 and 65 cm^{-1} apart from the lower level and lower component of the $^4I_{13/2}$ level. Bands with the wavelengths 1475-1525 nm seemingly correspond to transitions between Stark components of $^4I_{15/2}$ and $^4I_{13/2}$ levels. Cross-section of the induced radiation at $\lambda=1550$ nm calculated on the basis of the absorption spectrum equals $4 \cdot 10^{-21} \text{ cm}^2$.

2. MEASURING KINETICS OF LUMINESCENCE

We investigated several crystal samples in order to study sensitization of erbium luminescence by chrome and ytterbium ions. The data of ions concentration in the samples and measured efficiency of energy transfer are given in the table.

Table 1

Yb ³⁺ concentration, cm^{-3}	Er ³⁺ concentration, cm^{-3}	Yb ³⁺ lifetime, μs	Quantum efficiency of transfer, η
$5 \cdot 10^{20}$		900	
$5 \cdot 10^{20}$	10^{20}	320	0.66
$10 \cdot 10^{21}$	$5 \cdot 10^{19}$	190	0.79
$10 \cdot 10^{21}$	10^{20}	98	0.90

An intensive chrome luminescence quenching by ytterbium and erbium ions is observed in LSB crystals. Quantum efficiency of energy transfer from Cr^{3+} to Yb^{3+} equals 0.9. Ytterbium luminescence quenching by erbium is less intensive than in phosphate glasses. One can see in the table that minimal possible erbium concentration is close to $5 \cdot 10^{19} \text{ cm}^{-3}$.

A noticeable decrease of population of the $^4I_{15/2}$ state at reaching an inverse population must lead to a decrease of probability of energy transfer from Yb^{3+} ions to Er^{3+} ions and an increase of lifetime and intensity of Yb^{3+} luminescence.

Population of metastable levels of ions participating energy transfer to Er^{3+} ions is described by the following kinetic equations:

$$\frac{dN_3^{Yb}}{dt} = \sigma_p I_p(t) (N_2^{Yb} - N_3^{Yb}) - N_3^{Yb} [1/\tau_{Yb} + W_{tr}(N_1^{Er})]$$

$$N_2^{Yb} = N_1^{Yb} \exp(-E_{12}/kT) = \text{const} \ll N_{Yb}$$

$$\frac{dN_2^{Er}}{dt} = N_3^{Yb} W_{tr}(N_1^{Er}) - \frac{N_2^{Er}}{\tau_{oEr}}$$

$$\frac{dN_1^{Er}}{dt} = \frac{N_2^{Er}}{\tau_{oEr}} - N_3^{Yb} W_{tr}(N_1^{Er})$$

$$N_1^{Er} + N_2^{Er} = N_{Er}$$

where

$I(t)$ - temporal dependence of pumping,

- σ_p - effective cross-section of absorption of Yb at pumping frequency,
 N_2^{Yb}, N_3^{Yb} - populations of the absorbing and metastable levels of ytterbium,
 N_1^{Er}, N_2^{Er} - populations of the ground state $^4I_{15/2}$ and metastable $^4I_{13/2}$ levels of ytterbium,
 N_{Yb}, N_{Er} - concentrations of ytterbium and erbium ions in the crystal,
 τ_{oYb} - luminescent lifetime of Yb^{3+} ions at zero Er^{3+} concentration in the crystal ($\sim 900 \mu s$),
 τ_{oEr} - luminescent lifetime of $^4I_{13/2}$ level of Er^{3+} ($\sim 700 \mu s$),
 $W_{tr}(N^{Er})$ - probability of a non-radiate energy transfer from Yb^{3+} to Er^{3+} -ions as a function of Er^{3+} -ions concentration in ground state.

It should be noted that energy transfer occurs to the $^4I_{11/2}$ level with a quick further relaxation of Er^{3+} into the metastable state $^4I_{13/2}$.

The probability of energy transfer from Yb^{3+} to Er^{3+} is determined by the ratio:

$$W_{tr}(N_1^{Er}) = \frac{1}{\tau_{Yb}} - \frac{1}{\tau_{oYb}},$$

where τ_{Yb} - Yb^{3+} lifetime in LSB at Er^{3+} concentration 0.3 at.% and set pumping level.

In our case radiation of the lamp mainly pumps Cr^{3+} ions which with a probability $\sim 3 \cdot 10^5 s^{-1}$ non-radioactively transfer the energy to Yb^{3+} ions with quantum efficiency close to a unit. That is why for simplicity of kinetic equations one may consider that temporal dependence of excitation of Yb^{3+} ions reiterates pumping.

The analyses of kinetic equations shows that Yb^{3+} ions luminescence quenching after pumping is switched off occurs at actually constant population of the $^4I_{13/2}$ level of Er^{3+} ions. And the ratio of intensities of luminescence of ytterbium and erbium at different levels of pumping is determined by a change of transfer probability W_{tr} .

We used a cylindrical active element from an LSB crystal with dimensions $\varnothing 3 \times 26$ mm doped with Cr^{3+} - 0.5, Yb^{3+} - 10 and Er^{3+} - 0.5 at.% for measuring kinetics of luminescence of Yb^{3+} and Er^{3+} ions. The same element was used for studying Er^{3+} generation at lamp pumping.

We used a miniature silver coated pumping cavity and an INP-3/45 lamp to excite the active element. The electrical circuit allowed to shunt the discharge in the lamp at a specified moment and switch off pumping radiation for the time not exceeding 50 μs . This allowed to measure the intensity and kinetics of luminescence of Yb^{3+} ions at practically constant population of the $^4I_{13/2}$ level of erbium because Er^{3+} lifetime is $\sim 700 \mu s$ and Yb^{3+} lifetime is $\sim 160 \mu s$. One may consider also that at threshold pumping energy $E_{threshold}$ in a resonator with practically 100% reflecting mirrors population of the metastable Er^{3+} level equals population of the ground state level, i.e. half of erbium content in the crystal.

Radiation from end surfaces of the active element was imaged into the entrance slots of the monochromators MDR-3 by means of fiber-optical cables (Fig. 3). The signals at $\lambda = 1.53$ and $1.01 \mu m$ were registered by means of photodiodes FD-9E111B and FD-24K, correspondingly, at a two-channel oscillograph Tektronix TDS-360.

Fig. 4 shows typical oscillograms of lamp radiation, luminescence of Yb^{3+} and Er^{3+} ions in the LSB crystal and, for a comparison, in an erbium phosphate glass doped with Cr^{3+} - 0.3, Yb^{3+} - 20 and Er^{3+} - 0.2 at.%

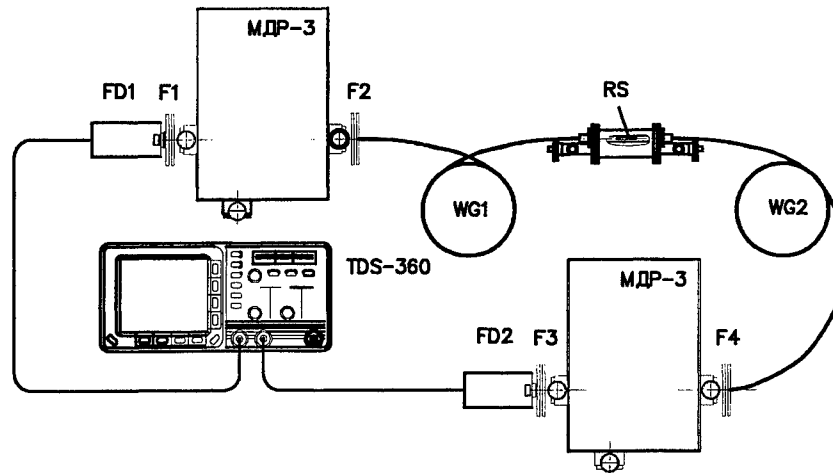
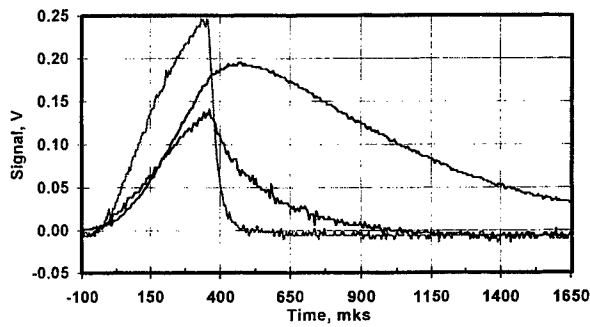
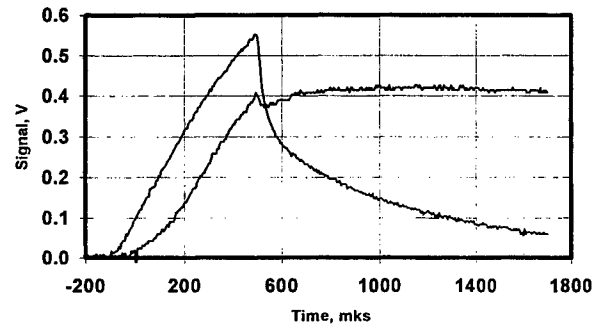


Figure 3: Optical scheme of luminescence measurements: RS - rod sample, $WG_{1,2}$ - fiberoptic cables, $F_{1...4}$ - optical filters, $FD_{1,2}$ - photodiodes



a



b

Figure 4: Typical oscillograms of kinetic processes in the crystal (a) and the glass (b);

- 1 - intensity of radiation of the pumping lamp
- 2 - Yb-ions luminescence at wavelength $\lambda=1.01 \mu\text{m}$
- 3 - Er-ions luminescence at wavelength $\lambda=1.53 \mu\text{m}$

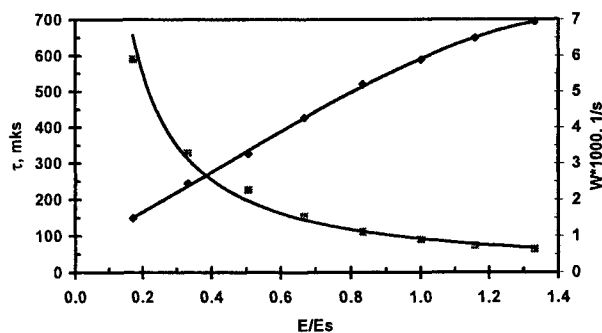


Fig. 5: Dependence of lifetime of ytterbium ions (1) and probability transfer of $\text{Yb} \rightarrow \text{Er}$ (2) in a phosphate glass from pumping energy (in threshold units)

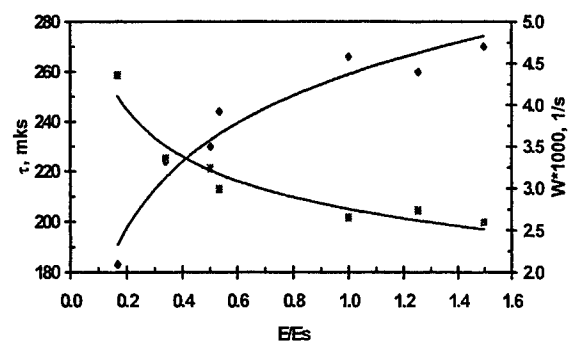


Fig. 6: Dependence of lifetime of ytterbium ions (1) and probability of $\text{Yb} \rightarrow \text{Er}$ transfer (2) in LSB:Cr,Yb,Er crystal from pumping energy (in threshold units)

The results of measurements of the efficiency of $\text{Yb}^{3+} \rightarrow \text{Er}^{3+}$ energy transfer at the inverse population of the $^4\text{I}_{13/2}$ level of Er^{3+} in LSB crystals and a phosphate glass are shown in figures 5 and 6.

One can see that the probability of energy transfer in the crystal at pumping $\sim 1.3E_{\text{threshold}}$ decreases from $\sim 4.4 \cdot 10^3 \text{ s}^{-1}$ to $2.4 \cdot 10^3 \text{ s}^{-1}$ but quantum efficiency of transfer at this is rather high (0.7 versus 0.8 at low pumping levels).

The probability of energy transfer to Er^{3+} ions in the glass is more substantial and quantum efficiency of transfer at pumping $1.3E_{\text{threshold}}$ decreases from 0.9 to 0.6. In fact, it is a limit value of quantum efficiency for laser usage.

The obtained data may be explained by a difference in spatial distribution of doping ions Yb^{3+} and Er^{3+} in the crystal and the glass.

The minimal possible distance between rare-earth ions in LSB is 5.9 \AA . It is obvious that at a maximum solved concentration of Yb^{3+} in the crystal all possible crystallographic sites for Yb^{3+} and Er^{3+} ions are occupied and that is why substantial deviations of distances between Yb^{3+} and Er^{3+} ions from an average value are hardly probable.

The decrease of a probability of excitation energy transfer at $E_{\text{pumping}}/E_{\text{threshold}} > 1$ between Yb^{3+} and Er^{3+} ions ensembles is mainly determined by the change of population of the $^4\text{I}_{15/2}$ state.

In contrast to LSB a minimum possible distance between rare-earth ions in a phosphate glass is 3.5 \AA . The structure of the glass allows substantial deviations from an average distance between Yb^{3+} and Er^{3+} ions. That is why the change of a probability of energy transfer in the glass is also stipulated by the fact that Er^{3+} ions which are at minimal distances from Yb^{3+} ions at $E_{\text{pumping}}/E_{\text{threshold}} > 1$ first of all pass on to the metastable state and Er^{3+} ions which interact weakly with the ensemble of Yb^{3+} ions stay in the ground state.

3. LASER PROPERTIES OF CRYSTALS

For generation tests of LSB:Cr,Yb,Er active elements with dimensions $\varnothing 3 \times 26 \text{ mm}$ we used two types of pumping cavities: one with a pulse lamp INP-2/35 and silver plated elliptical cavity and the other with a pulse lamp INP-3/45 and silver plated cylindrical cavity. Pumping pulse length was $\sim 1 \text{ ms}$.

For comparison purposes we also obtained generation on a $\varnothing 2.5 \times 40 \text{ mm}$ active element from erbium glass. Generation threshold on the LSB active element in the cavity with INP-2/35 lamp was 40 J and was close to a maximum lamp load while generation threshold on the glass element in the same cavity was 8 J. The resonator of Fabry-Perot type had an output coupler with reflectivity coefficient 90%.

Though the efficiency of the cavity with INP-3/45 lamp is lower, the admissible energy supplied to the pulse lamp is substantially higher. Here generation threshold energy on the LSB:Cr,Yb,Er was 60 J and at pumping energy 100 J the laser radiated $\sim 10 \text{ mJ}$ (in the resonator with mirrors $R_1=100\%$ and $R_2=96\%$). The generation threshold energy on the erbium glass element increased to 25 J.

The difference in the threshold energies of the lasers on LSB crystal and phosphate glass may be explained by the following factors:

- threshold inverse population of the metastable Er^{3+} level in the LSB (taking into account thermal population of the lower laser level) is $3 \cdot 10^{19} \text{ cm}^{-3}$ and in the phosphate glass it is $\sim 0.7 \cdot 10^{19} \text{ cm}^{-3}$;
- quantum output of luminescence of Er^{3+} in the LSB crystal is $\sim 10\%$ while in the phosphate glass it is close to 100%;
- optical quality of the active element from the glass is substantially higher than that of the LSB element.

Generation at threshold pumping energy is observed at the end of pumping pulse, i.e. approximately 750 μs after the pump lamp is fired. When pumping energy is $\sim 1.5E_{\text{threshold}}$ generation starts after $\sim 650 \mu\text{s}$ and lasts for $\sim 450 \mu\text{s}$ (Fig. 7). When pumping by $\sim 2.0E_{\text{threshold}}$ the delay in generation is $\sim 500 \mu\text{s}$ and it lasts for $\sim 700 \mu\text{s}$.

The decrease of pumping duration till 500 μs does not change substantially the threshold generation energy but this leads to a decrease of duration of generation and when threshold generation energy is exceeded by 50-100% generation lasts for $\sim 300 \mu\text{s}$. The delay of generation of the induced radiation relative to pumping maximum is explained by two factors: the time of energy transfer from Yb ions to Er ions and accumulation of population on the metastable level $^4I_{13/2}$ of Er^{3+} .

Generated wavelength was determined by means of a diffraction monochromator MDR-3 (the inverse linear dispersion of the instrument with grid 300 lines/mm was 5.2 nm/mm). The induced radiation was registered by a photodiode at the output slot of the monochromator. The measured radiated wavelength was equal to 1548 nm. Its comparison with the luminescence spectrum shows that the generation occurs at the intensive long wave band of luminescence.

The induced radiation cross-section at $\lambda=1548 \text{ nm}$ is evaluated to be $\sim 4 \cdot 10^{-21} \text{ cm}^2$ assuming a 100% insertion of Er^{3+} ions from the melt into the crystal. A relatively small change of quantum efficiency of transfer from the ensemble of Yb^{3+} ions to Er^{3+} at high pumping levels shows that a laser on LSB:Er will be stable in a Q-switch mode at lamp and diode pumping.

The carried-on investigations showed advantages and disadvantages of lasers on LSB:Cr,Yb,Er compared to erbium phosphate glasses.

ACKNOWLEDGMENT

This work was supported by the International Science and Technology Center under contract #251-96. The authors express gratitude to Dr. Yu.B. Kondratenkov for assistance.

REFERENCE

1. Y. P. Main «New material for mini solid state lasers», Ph.D. Doctor Theses, Hamburg, 1994
2. «Phosphate laser glasses», ed. by M.E.Zhabotinski, Moscow, Nauka, 1980

Effect of temperature on absorption and fluorescence spectra of Er-doped laser glasses

Sergei G. Lunter ^a, Nikolai V. Nikonorov ^b, Alexander K. Przhevuskii ^a

^a Vavilov State Optical Institute, 193171, St. Petersburg, Russia;

^b Corning Scientific Center, 199034, St. Petersburg, Russia

ABSTRACT

The absorption and fluorescence spectra of Er-doped phosphate and silicate laser glasses were investigated in temperature range of 20-300°C. The heating resulted in 5-10% decrease of oscillator strengths of spectral bands. On the base of temperature variations of spectral profiles we proposed an energy level model, which allowed to explain the thermal variation of spectrum of Er-laser at 1.54 μm.

Keywords: Er-doped laser glasses, absorption and fluorescence spectra, effect of heating.

1. INTRODUCTION

The active laser elements made of Er-doped glasses heat up considerably with the pumping, especially in case of flash lamp radiating in a broad spectral range. An application of codoping ions (Cr^{3+} , Yb^{3+}) increases the pumping efficiency, however it does not settle the heating problem. In any case a lot of pumping energy transforms in heat. A manifestation of this heating is variation in lasing spectra that can be understood from considering of Stark structure of the ground $^4I_{15/2}$ and the excited $^4I_{13/2}$ terms between which laser transitions occur.

In glass, the low symmetrical atom configurations around Er^{3+} ions disturb Er^{3+} ions states so that the ground $^4I_{15/2}$ state splits into 8 Stark sublevels and the excited $^4I_{13/2}$ states splits into 7 sublevels. Thus, the absorption and fluorescence spectra in "laser" region 1.45-1.60 nm is result of overlapping 56 (7x8) of the $^4I_{15/2} \longleftrightarrow ^4I_{13/2}$ elementary optical transitions between particular sublevels. The thorough analysis of such complicated Stark structure is unsolved problem. The absorption and fluorescence spectra measured at low temperature exhibited that values of the $^4I_{15/2}$ sublevel energy varied in range 10 - 500 cm^{-1} , and the values of the $^4I_{13/2}$ sublevel energy varied in range 10 - 300 cm^{-1} , ¹.

The amplification coefficient $k(\nu)$ for such complicated case can be written in the form:

$$k(\nu) = \sum_{i,k} \sigma_{ik}(\nu) [n_i^{\text{ex}} - n_k^{\text{gr}}] \quad (1)$$

Here, $\sigma_{ik}(\nu)$ is stimulated emission cross section for transition from "i" sublevel of the excited $^4I_{13/2}$ manifold to "k" sublevel of the $^4I_{15/2}$ manifold, n_i^{ex} and n_k^{gr} are corresponding populations.

The heating of Er-doped glasses leads to a redistribution of populations n_i^{ex} and n_k^{gr} . From (1) it follows that such redistribution results in a variation of $k(\nu)$ function and thus the generation spectrum.

Particularly, Kuchma I.G. *et al.*,² observed the heating effect on lasing spectra of Cr-Yb-Er - phosphate glasses. They demonstrated that the generation occurs simultaneously at two wave-lengths, 1.536 μm and 1.545 μm ., with intensity ration depending on the pumping and the temperature of active element. The authors qualitatively explained these results. They supposed that these generation lines corresponded to the optical transitions from the single lowest Stark sublevel of the $^4I_{13/2}$ state to the two sublevels of $^4I_{15/2}$ state with energy gap $\approx 40 \text{ cm}^{-1}$.

Because of complexity of generation where there are many optical transitions, the lasing data are insufficient to get reliable quantitative interpretation of temperature effect on generation. To gain a better understanding, there is a need of experimental study of heating effect on absorption and fluorescence spectra of Er-laser glasses. These data are called for consideration of heating influence on pumping, "broadening and flattening" of amplification spectrum, as well. Thus, the objective of our paper is an investigation of heating effect on fluorescence and absorption spectra of Er-doped glasses.

2. EXPERIMENT

The sample of Er- doped glass was placed in a thermocell having windows made of fused silica. A heater was able to increase the temperature in thermocell up to 400 °C. A thermocouple was located at surface of sample. Using a special scheme with feedback, we were capable to stabilise temperature within 5 degrees.

Absorption spectra were taken with use a single-beam scheme. We applied a grating monochromator, a photodiode, a lock-in-amplifier, and a digital voltmeter. Obtained data were treated with PC.

Fluorescence was excited with radiation of Ar laser, LG-106. The fluorescence spectra were taken with the set-up applied for determination of the absorption spectra, which provided accuracy in comparison of absorption and fluorescence spectral contours in resonance region.. All spectra were measured several times, and obtained data were averaged. An accuracy was usually less than 1 %.

We studied Er-doped glasses of two different matrices: phosphate ($\text{BaO-K}_2\text{O-P}_2\text{O}_5$), and silicate ($\text{Nb}_2\text{O}_5\text{-ZrO}_2\text{-SiO}_2$). In samples for measurement of absorption spectra concentration of Er^{3+} ions varied in range $(3\text{-}10) \cdot 10^{20} \text{ cm}^{-3}$. In samples for

measurement of the fluorescence spectra, the concentration of Er^{3+} ions was only $\approx 1 \cdot 10^{19} \text{ cm}^{-3}$ in order to minimise the reabsorption effect on the fluorescence spectra. For the same reason, the samples for fluorescence measurement had only 1mm in thickness.

3. EXPERIMENTAL RESULTS AND DISCUSSION

The measurements exhibited, that the heating variously effected on the different regions of the absorption contour of the $^4\text{I}_{15/2} - ^4\text{I}_{13/2}$ transition. The differential spectrum, a difference of the absorption coefficients measured at high (T) and room temperature, $k(\lambda)^T - k(\lambda)^{20}$, gives a pictorial example of the absorption contour variation. The typical absorption and differential spectra for phosphate glass are shown in Fig. 1. Within the accuracy of the measurements, the form of the differential spectrum does not change on heating. The amplitudes of this spectrum are growing with increasing temperature.

It is significant that in the lasing spectral range, the variations of the absorption coefficients are different. At a maximum of the first band, $\lambda = 1532 \text{ nm}$, the absorption essentially decreases with a rise in temperature, whereas at the second band of the lasing, 1545 nm , the absorption slightly increases (Fig. 1). From temperature variation of ratio of absorption coefficients, $k(1533) / k(1545)$, we determined that effective energy gap between final state of laser transition was equal $\sim 100 \text{ cm}^{-1}$ for the ground $^4\text{I}_{15/2}$ manifold.

The variation of fluorescence band contour, $^4\text{I}_{13/2} \rightarrow ^4\text{I}_{15/2}$, has complicated character, as well. There are both areas, where the intensity of luminescence is growing, and ones, where the intensity shows a decrease. For analysis of the heating effect on luminescence, the differential spectra were made in the same manner as the analysis of the absorption spectra, $f(\lambda)^T - f(\lambda)^{20}$. In this case, the fluorescence spectra were normalized to square of contour. The typical fluorescence and differential spectra for phosphate glass are shown in Fig. 2. The fluorescence intensity variations are different for two spectral lasing ranges. The different influence of temperature on luminescence signal for two ranges of the lasing can be explained by cause, when the optical transitions occur with different excited Stark levels, namely, the heating changes the relation of populations of these levels. We found a linear temperature dependence for the logarithm of ratio of fluorescence intensities for two ranges of lasing (Fig. 4). From slope of the line, we determined that the effective energy gap between initial states of laser transitions was equal $\sim 50 \text{ cm}^{-1}$.

The integral intensity of the $^4\text{I}_{15/2} \rightarrow ^4\text{I}_{13/2}$ absorption decreases monotonically, when sample is heated. These variations can be related to a small drop of relative energy of the lasing on heating ².

Same drop of the integral intensity on heating was observed for absorption bands at 795 and 970 nm , as well, which are used for Er-laser pumping. This behavior of oscillators strength on heating allowed us to conclude that the static mechanism is responsible for optical transitions in Er-doped glasses. In case of vibration mechanism, the heating of samples would be

resulted in an increase of the oscillators strength, rather than a decrease.

The absorption spectra of silicate Er-glasses were investigated for 20 - 300°C. In general term, the character of variation of spectral contours for silicate glasses was the same as for phosphate ones. This result shows that the character of Stark structure, position and relative intensity of Stark component, for silicate and phosphate glasses are similar. The typical absorption and differential spectra for silicate glass are shown in Fig. 3.

Thus, the results of present investigation allowed us to suggest energy level model for laser transitions. It differs from the model of Kuchma I.G *et al* ² in the following points: (a) laser transitions originate from two different Stark sublevels of the $^4I_{13/2}$ state and (b) the energy gap between sublevels of the $^4I_{15/2}$ ground state is twice as large as the one in Kuchma's model (Fig. 5).

4. CONCLUSIONS

The contours of the absorption and fluorescence bands of Er-doped laser silicate and phosphate glasses vary with temperature. These variations is determined by the redistribution of the population throughout the Stark sublevels of the $^4I_{15/2}$ ground and the $^4I_{13/2}$ excited terms.

On the base of temperature variations of spectral profiles of phosphate glasses, we proposed the energy levels model, which allowed to explain the thermal variation of spectrum of Er-laser at 1.54 μm . According to this model, the transitions in two range of lasing (1533 and 1545 nm) come from two Stark sublevels of the $^4I_{13/2}$ manifold to two Stark sublevels of the $^4I_{15/2}$ manifold. Effective energy gaps are equal to 50 cm^{-1} and 100 cm^{-1} for the $^4I_{13/2}$ and $^4I_{15/2}$ manifolds respectively.

There is quality similarity of temperature variations of spectrum contours for Er-doped phosphate and silicate glasses. However, absolute values of variation are different. This may result in essential difference of heating effect on laser properties.

5. REFERENCES

1. N.E.Alekseev, V.P. Gapontsev, M.E. Zhabotinskii, V.B.Kravchenko, and Yu. P. Rudnitskii, "Laser Phosphate Glass", Nauka, Moscow, 1980.
2. I.G. Kuchma, A.A. Petrov, and V.A. Fromzel "Effect of temperature of active medium on properties of erbium glass laser", *Opt. Spektrosk.* (in Russian) Vol.71, N1, pp.180-187, 1980.

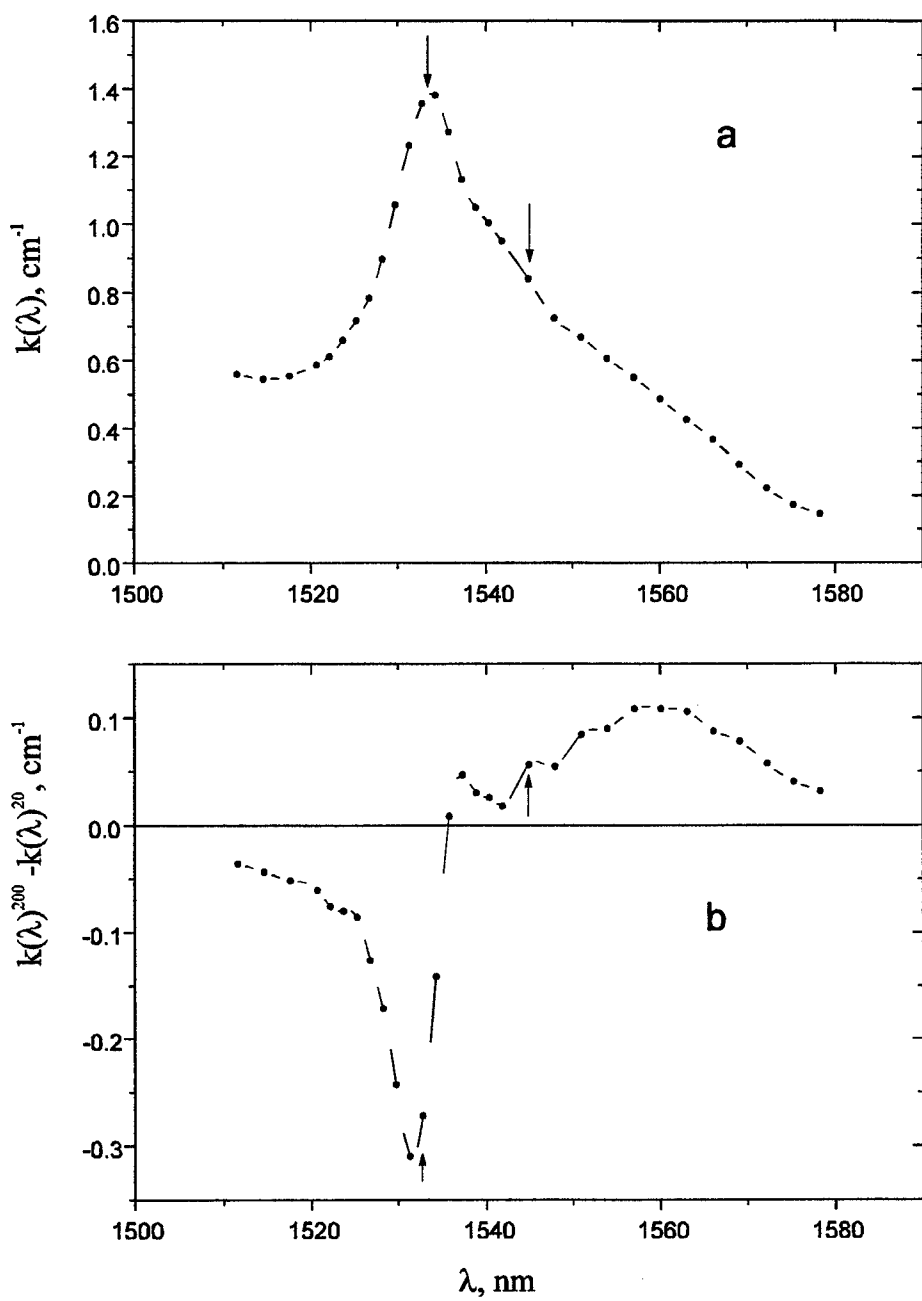


Fig. 1 Absorption spectrum (a) and differential absorption spectrum (b) of phosphate glass. Arrows indicate the lasing ranges.

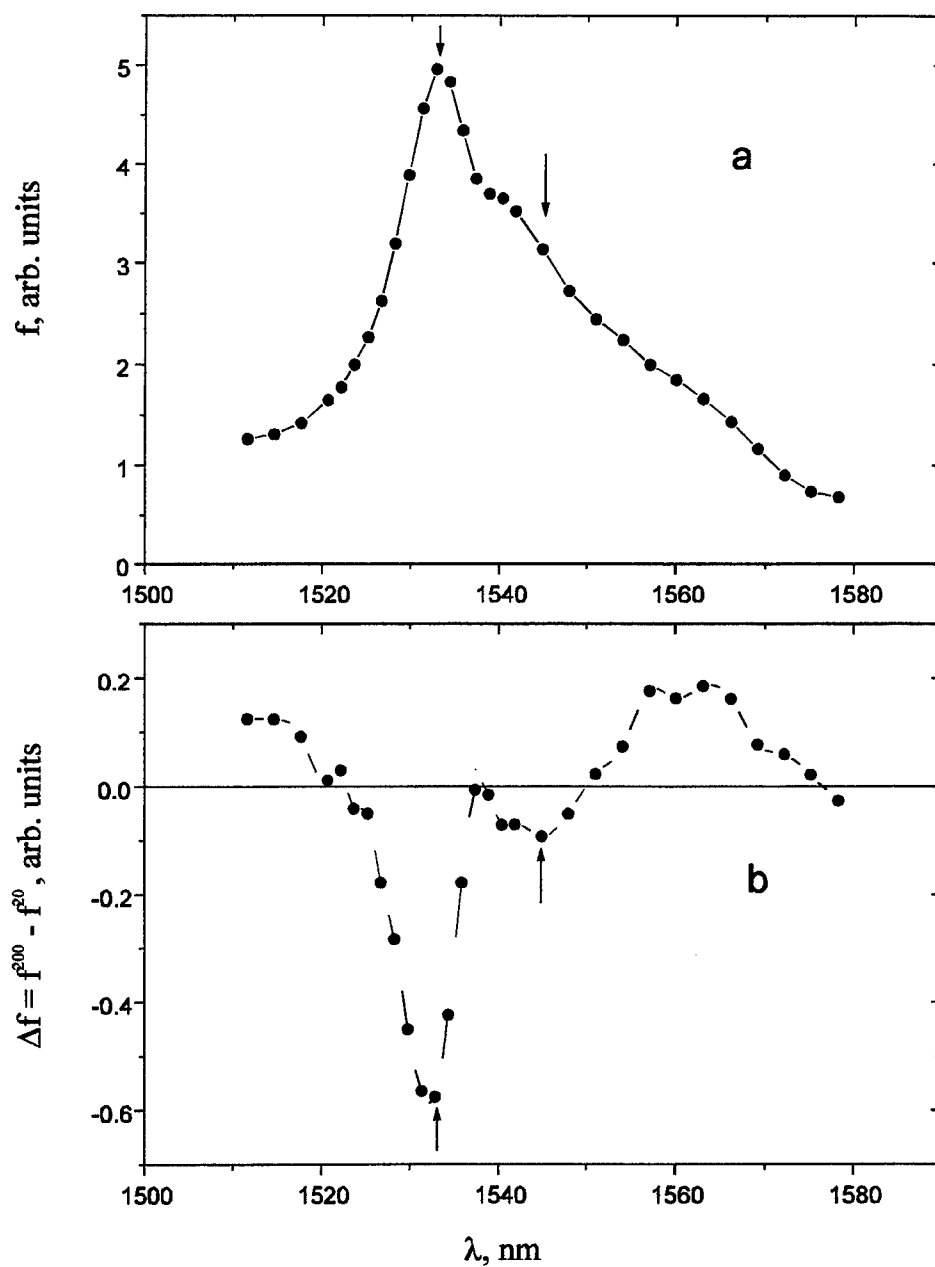


Fig. 2 Fluorescence spectrum (a) and differential fluorescence spectrum (b) of phosphate glass. Arrows indicate the lasing ranges.

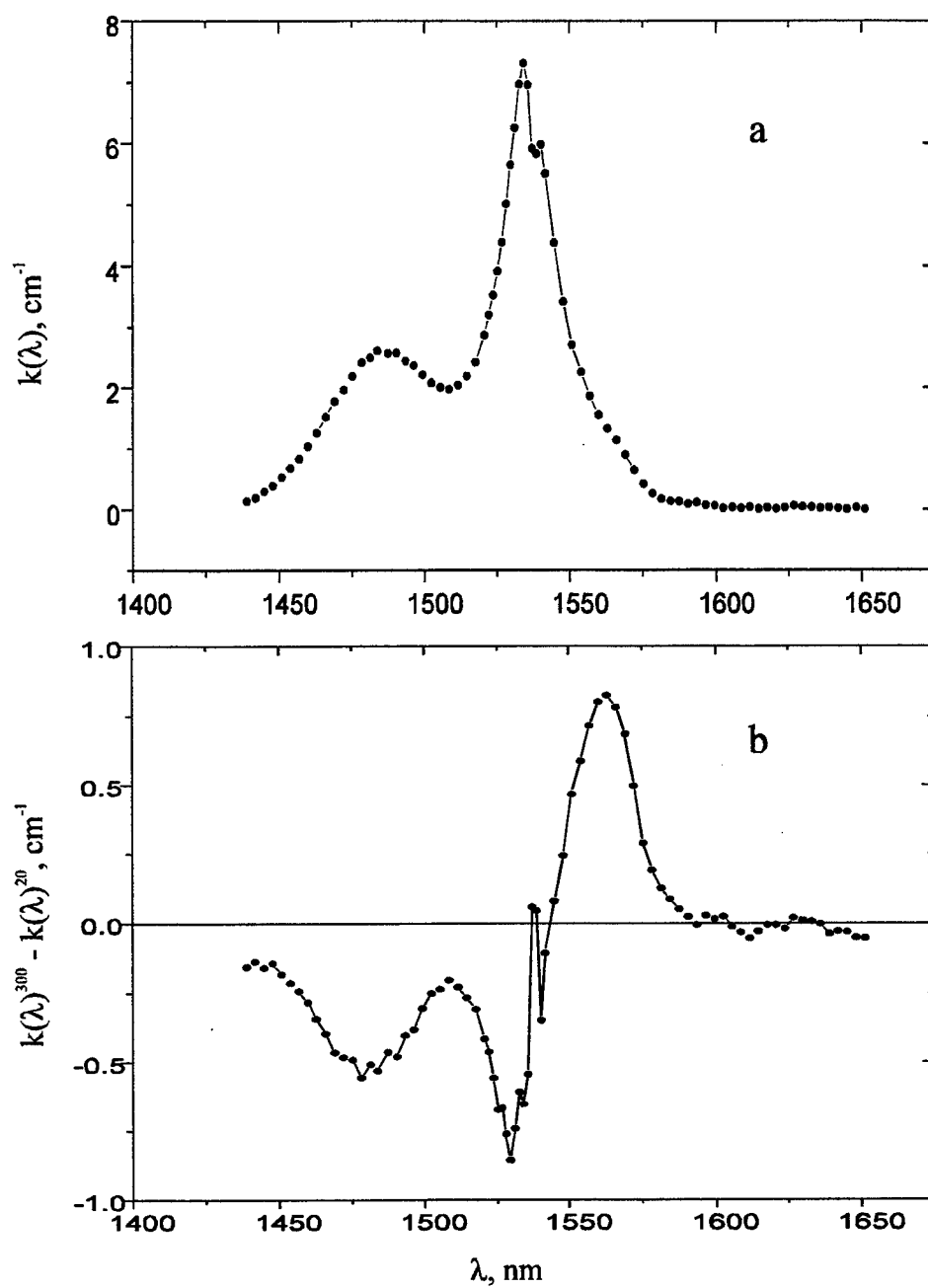


Fig. 3 Absorption spectrum (a) and differential absorption spectrum (b) of silicate glass.

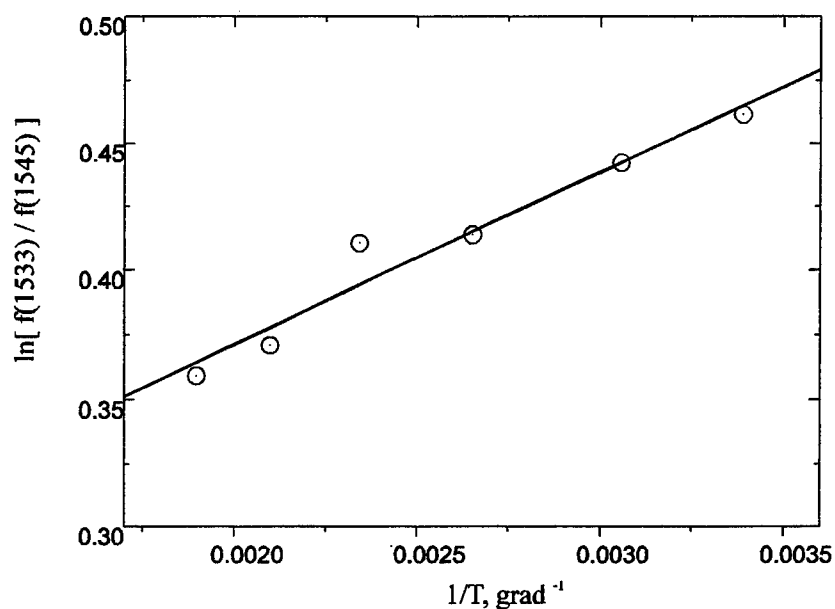


Fig. 4 The determination of energy gap between Stark sublevel of $^4I_{13/2}$ state from the temperature dependence of ration of fluorescence intensities at the two lasing ranges.

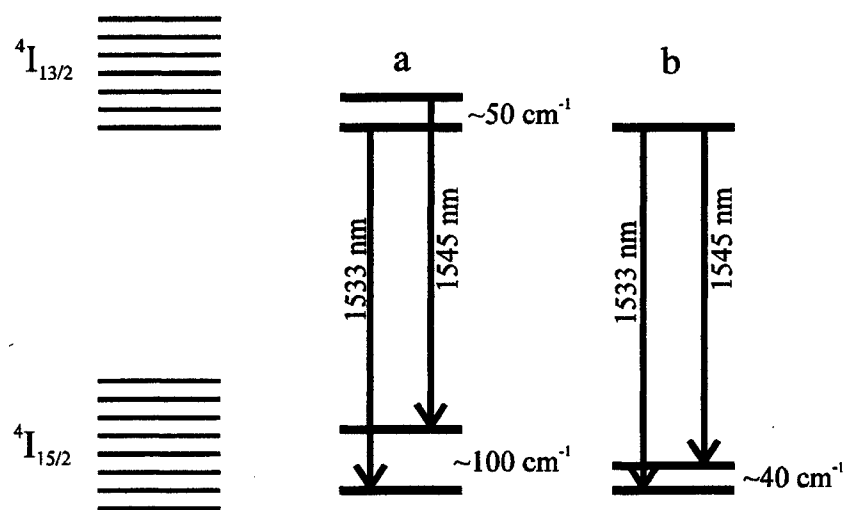


Fig. 5 The models of laser transitions in Er-doped phosphate glasses. a - the model of present paper, b - the model of I.G.Kuchma et. al.²

SESSION 3

Laser Applications for High-Precision Measurements

LINGRAN-100: laser middle-base interferometric gravitational antenna

Valentin N. Rudenko, Vadim K. Milyukov, Victor V. Kulagin, Andrey V. Gusev,
and Alexander Kopaev^a

^aSternberg Astronomical Institute, Moscow State University,
Universitetsky prospect 13, 119899, Moscow, Russia

ABSTRACT

The goal of the project is the construction of a wideband gravitational gradiometer based on a laser 100-m Fabry-Perot-Michelson interferometer on free masses in deep rock surroundings. The device is aimed at registering bursts of gravitational radiation with an amplitude of the dimensionless metric variations as small as 10^{-21} in the frequency range $10^2 - 10^3$ Hz. The auxiliary purpose is to measure low-frequency variations of the Earth gravity gradients bearing information on the internal dynamics of our planet.

The deep under-rock position of the installation inside tunnels of Baksan Neutrino Observatory provides a two-order of magnitude decrease in the geophysical noise level which allows the combination of parallel astrophysical and geophysical studies. For geophysics, the long-based interferometer with hanging mirrors presents a new type of geophysical instrument - an angular gravity gradiometer at low frequencies $10^{-4} - 10^{-5}$ Hz with a resolution of $10^{-8} - 10^{-10}$ rad, which is enough to register weak geodynamical perturbations due to oscillations of the Earth interiors.

Keywords: Longbase laser interferometric gravitational detectors

1. INTRODUCTION

At present time, the experimental detection of gravitational waves from cosmic objects is based on constructing sensitive ground-based antennas of two kinds: supercryogenic resonance bar detectors and wide-band laser interferometers on free masses. The leading world countries (USA, Germany, UK, France, Italy, Japan) are in the process of building long-base laser interferometric gravitational wave antennas with a sensitivity of $10^{-21} - 10^{-23}$ in dimensionless metric variations, which must be completed in 5-10 years.

For reliable registration of gravitational radiation it is principally necessary to construct an international network of gravitational wave antennas working on the coincidence scheme. The global gravitational network would allow one not only to select gravitational wave signals with a sufficient accuracy, but also to probe their astrophysical sources. Russian science can join this network already during next 3-5 years by constructing an optical gravitational detector with 100-m base and a number of reflections 10^3 capable of registering metric variations with an amplitude of 10^{-21} in the frequency range $10^2 - 10^3$ Hz. A similar project is being now under construction in Japan (TAMA-300).

A wide frequency range of the laser interferometer ensures the possibility to observe, in an optimal way, gravitational radiation emitted by various cosmic sources. The sensitivity of the antenna should allow detection of gravitational wave bursts not only from the sources inside our Galaxy, but also from nearby galaxies (within ~ 10 Mpc). The expected rate of such bursts can be a few events per year as a minimum.

In addition to the main use as a gravitational wave detector, the interferometer with suspended mirrors may serve as a high-sensitivity angular gradiometer capable of registering weak variations of the terrestrial gravity field caused by internal dynamical processes due to, for example, the internal terrestrial core perturbations. The first experience of realisation of these ideas using a 100-m installation would be of a significant interest with a prospect of solving fundamental issues of global geodynamics.

However the realization of the "geophysical application" of the antenna on free masses is possible only provided that the device is located in a deep underground surroundings where low-frequency geophysical noises are strongly suppressed. The location of the gravitational detector nearby the neutrino scintillation telescope is also advantageous in pursuing the program of simultaneous "looking for collapse" by two radiative channels.

Other author information:
V.V.K.: E-mail: kul@sai.msu.su

2. RESEARCH TEAM

The LINGRAN-100 project is assumed to be mainly realized by scientific groups from Sternberg Astronomical Institute (SAI) of the MSU, Moscow, and from Institute of Laser Physics of Russian Academy of Sciences (NILP RAS), Novosibirsk, with the participation of the Nuclear Research Institute of RAS (NRI), Moscow, through its Baksan Neutrino Observatory (BNO), (Baksan, North Caucasus).

The SAI group should provide astrophysical and geophysical theoretical base of the project, the general engineering and construction of the project, including the system of suppression of seismic, acoustic and thermal noises, the system of autotuning and operational regime keeping, electronic systems of data read-out and processing.

The NILP group should provide the laser and optical parts of the project, including the construction of a stabilized laser pumping source, the mode selector, mirrors, the interferometry, as well as opto-electronic transformation of the signal in the channels of read-out and operational regime keeping.

NRI (BNO) group should provide installation of the antenna inside the underground channels of BNO, the access to communications and other infrastructure elements required during the period of mounting and exploitation of the device.

3. EXPECTED RESULTS

The successive realization of the project should result in the construction of a multipurpose gravitational gradiometer serving as:

(a) a gravitational wave detector on free masses with 100-m base and the number of reflections 10^3 capable of registering signals from astrophysical sources with an amplitude of 10^{-21} in the frequency range 300 – 500 Hz from distances up to 10-30 Mpc;

(b) a low-frequency angular gradiometer capable of measuring gravity gradients induced by global geodynamical perturbations with a sensitivity of $10^{-8} - 10^{-10}$ rad/Hz^{1/2} in the frequency band $3 \times 10^{-4} - 3 \times 10^{-5}$ Hz, which allows registration of motions of the terrestrial core and studying their correlation with positional variations of the Earth rotational axis;

(c) a tool for searching for correlations between gravity-gradient and neutrino backgrounds in the problem of "looking for the collapse" in the Galaxy and its nearby surroundings.

4. ASTROPHYSICAL MOTIVATION OF THE PROJECT

The promisable astrophysical sources of gravitational radiation in the frequency range 10 – 1000 Hz are mainly thought to be coalescing binary neutron stars, binary black holes, and core collapse supernovae. The GW waveforms and the total energy release in GW from merging binaries at the inspiral phase are known to a very high accuracy, while for GW from supernovae this is not the case. Oppositely, the rate of type II and Ia supernovae is derived from astronomical observations to within a factor of two, while for the rate of compact binary mergers it is known to worse than an order of magnitude.

A typical GW amplitude from coalescing binary neutron star or black hole is

$$h \approx 3 \cdot 10^{-23} M^{5/3} (100/r)$$

where M is the characteristic mass of the components in solar units, r is the distance to the source in Mpc.

The GW waveform from a coalescing binary has a quasi-harmonic shape and the signal-to-noise ratio on the detector can be increased, using the optimal matched filtering, by $n^{1/2}$ times, where $n = f^2 / \dot{f}$ is the number of periods coming through the detector bandwidth $\Delta f \approx f$. Thus the signal-to-noise ratio may be defined by a characteristic amplitude $h_c = h_{amp} \sqrt{n} \approx M^{5/6} f^{-1/6} / r$. This means that at a given signal-to-noise ratio the detector will be more sensitive to massive stars ($\propto M^{5/6}$), therefore massive black holes (with a typical mass of $10M_\odot$) will be more preferable in comparison to less massive neutron stars (with a typical mass of $1.4M_\odot$). The number of events registered during one-year integration is thus

$$(N_{bh}/N_{ns}) = (V_{bh}/V_{ns}) (M_{bh}/M_{ns})^{15/6}$$

where V_{ns} and V_{bh} are merging rates of neutron stars and black holes per unit proper volume of space, respectively. The rate of binary neutron star mergers can be derived from the existing binary pulsar statistics and is $\sim 8 \times 10^{-6}$ per year per Galaxy. As for binary black hole merging rate, it can be estimated only from theoretical studies of binary stellar evolution. The recent studies show that this rate is very sensitive to such evolutionary parameters as critical mass of the main sequence star yielding a black hole as a result of the collapse, the black hole mass, and the mode of stellar wind losses during normal evolution of the progenitor star. However, for a wide range of evolutionary parameters, the resulting binary black hole merging rate was found to be only an order of magnitude smaller than V_{ns} , which has led, considering the high mean mass of the forming black holes, to an optimistic conclusion that binary black holes may be registered during one year integration at frequency 100 Hz with LINGRAN-100 GW-interferometer, i.e. at $h_{rms} = 10^{-21}$. The number of binary neutron star mergings registered by such an interferometer falls 10 times short and such coalescences would not be registered at this sensitivity level during one-year integration.

5. OPTICAL SCHEME AND BASIC PARAMETERS OF LINGRAN-100

The optical scheme of the interferometric gravitational antenna LINGRAN-100 is typical for such installations and includes two symmetric perpendicular Fabry-Perot cavities 100 m in length tuned to the pumping laser frequency and forming a Michelson-like interferometer (fig.1). The number of reflections of Fabry-Perot cavities is $N = 1000$, so the resulting optical length of each arm is 100 km. The incoming mirrors of the cavities are much more transparent than the end ones.

Optical elements of the installation are located inside vacuum chambers connected by vacuumized tubes several tens cm in diameter. The Fabry-Perot mirrors are attached to "free masses" (low-frequency pendulums) and isolated from seismic noise with the help of multi-link antiseismic filters.

The laser pumping can be provided by a high-stable Nd:YAG laser. To increase the effective pumping power, the recycling light scheme have to be used.

The output fields of Fabry-Perot resonators are phase-modulated by the gravitational wave signal. These fields are subtracted from each other in Michelson interferometer, therefore compensation of the pumping laser frequency noises and doubling the useful signal amplitude take place.

The project assumes achieving the following parameters:

- Lower frequency of the antenna's operating range $f_{min} = 300$ Hz
- Upper frequency of the antenna's operating range $f_{max} = 2000$ Hz
- Interferometer arm length $L = 100$ m
- Front mirror reflection coefficient $R = (1 - 1/N) = 0,999$
- Pumping laser wavelength $1,06\mu m$ (or $0,63\mu m$)
- Pumping laser power $W = 3$ W
- Quantum efficiency of photodetector $\eta = 0.5$
- Mass of the mirrors $m = 50$ kg
- Lowest internal mode frequency of the mirrors $\omega_e = 5 \cdot 10^4 s^{-1}$
- Quality factor of the mirror lowest internal mode $Q_0 \approx 10^5$
- Residual air pressure inside beam tubes $p = 10^{-6}$ torr
- Maximal beam diameter $D = 10$ cm
- Mirror suspension frequency $\omega_\mu = 3 s^{-1}$
- Mirror suspension quality factor $Q_\mu = 10^7$.

The realization of these parameters will allow to achieve the sensitivity $h \approx 3 \cdot 10^{-21}$ in the frequency range 300 Hz \div 1300 Hz.

6. SIGNAL-TO-NOISE RATIO AND SENSITIVITY

6.1. Signal

The transmission function of the antenna has the form

$$H_{gwa}(\omega) = 2\alpha\omega_e \exp(-i\gamma) \sin \gamma/\omega (1 - R_e R e^{-i2\gamma}),$$

where ω_e is the pumping laser frequency, R_e, T_e and R, T are reflection and transmission coefficients for the end and front mirrors respectively, $\alpha = T^2 R_e / (-R + (R^2 + T^2) R_e)$, $\gamma = L\omega/c$.

In the one-mode approximation the change of the field phase at the Fabry-Perot interferometers output is (tuning "on top")

$$\Phi(\omega) \approx -[(\omega_e/2)/(\delta_e - i\omega)] h(\omega)$$

where $h(\omega)$ is the gravitational wave spectrum, $\delta_e = c(1 - R)/2L$ is the effective damping for Fabry-Perot interferometer resonance curve.

This relation shows that δ_e should be decreased in order to increase the antenna's sensitivity. However, the whole spectrum of the gravitational wave signal must fall inside the transparency band of the Fabry-Perot cavity, that puts the lowest boundary on the possible value of δ_e .

6.2. Noises

The noise in a laser gravitational antenna is mostly due to the photon shot noise of photodetector, thermal noise of the suspension pendulum mode, thermal noise of the suspension violin modes, thermal noise of the mirror internal modes, seismic noises, amplitude and frequency laser noises, the fluctuations of the refraction coefficient of residual gases along the beam path, the beam orientation fluctuations, gradient noises caused by the motion of large masses, and other noises (for example, those caused by the action of cosmic rays, variable electric and magnetic fields, etc.).

6.2.1. Photon noise

When only the photon noise is present, the sensitivity of a gravitational antenna for short bursts of gravitational radiation with central frequency inside the frequency band of Fabry-Perot cavities is

$$h_{\min} = \lambda_e (4\pi LN)^{-1} (h\omega_e/2\pi\eta W\tau)^{1/2}$$

where $\tau = \Delta f^{-1}$ is the minimum duration of the signal.

A numerical estimate for the assumed parameters of LINGRAN-100 antenna yields $h_{\min} = 5 \cdot 10^{-21}$ which is worse than the required value. So to reach the sensitivity 10^{-21} it is necessary to use the light recycling scheme (coherent adding of the pump laser field at the interferometer input using an additional recycling mirror) with an effective power amplification coefficient about 30-40 (which have been achieved in modern experiments).

If the recycling mirror has the reflection coefficient R_{in} , then the effective pumping power is $W_{eff} = W/(1 - R_{in})$. Thus the required value of the reflection coefficient of the recycling mirror proves to be $R_{in} \geq 0.96$. The spectral density of photon noises in this case has the minimum value

$$G^{1/2} = h_{ph} = 3 \cdot 10^{-23} Hz^{-1/2}.$$

6.2.2. Seismic noise

The spectral density of seismic noises on the Earth surface in terms of the equivalent metric perturbations for $L \approx 10^2$ m is determined as

$$S_h \approx 2L^{-2} (A/f^4) \cong 2 \cdot 10^{-16}/f^4 [Hz].$$

In the operational frequency band $f > 300$ Hz, the signal-to-noise ratio, without applying special antiseismic filters, is very small, of order $\rho \approx 10^{-9}$ for the assumed signal amplitude $h \approx 10^{-21}$. So a minimum seismic noise suppression coefficient $T(f)$ must be not less than $T_{\min} \approx 10^9$. Passive vibration isolation of the laser gravitational antenna is ensured by using a three link mechanical high-frequency filter with a transmission function (TF)

$$G(i\omega) = G_1(i\omega) G_2(i\omega) G_3(i\omega), \quad |G(i\omega)|^{-1} = T.$$

where $G_k(i\omega)$ is the TF of a separate basic link of the construction.

A preliminary filter of seismic noises of "Stack" type can be realized as a multilink mechanical system with three supports. Each support contains several mechanical cells with equivalent dynamical parameters. In the frequency range $f > 10^2$ Hz the transfer function of such support is $T_1(f) \propto f^8$ so for the lower boundary frequency $f_1 \approx 300$ Hz the seismic noise damping coefficient for the "Stack" filter can be made as high as $T_1(f_1) \approx 10^6$.

The following basic element of the antiseismic filter could be a pendulum suspension with the characteristic X-like attachment. TF of such a mechanical system is determined as $G_2(i\omega) \approx (\omega/\omega_0)^{-2}$, where ω_0 is the system's main

mode resonance frequency. For typical parameters of the device one can achieve an oscillation period for X-like suspension of about 10 s therefore the seismic noise suppression coefficient T_2 at frequency 300 Hz can be about 10^5 . The resulting seismic noise reduction by first two links of the antiseismic filter is 10^{11} . Since estimates of the spectral density of seismic noises are very approximate, an additional mechanical system of two coupled mechanical pendula with partial frequencies f_1 and f_2 can be used in the antiseismic filter design. The TF of such a suspension at non-resonance frequencies $f \gg f_1, f_2$ is determined as $G_3(i\omega) \approx (\omega_1/\omega)^4$.

With the use of the three link antiseismic filter the influence of seismic noises at the low frequency 300 Hz turns out to be negligibly small: $h_s \sqrt{f} \leq 10^{-23}$. The use of the "stack"-type antiseismic filter and the X-like suspension provides $h_s \approx 0.5 \cdot 10^{-22}$, which allows to consider the possibility of using in the experiment a simplified version of the antiseismic filter (without the last unit).

6.2.3. Thermal noise

The spectral density of the thermal noise of the lowest internal mode is $G_{in} = 2kTH_i/\pi$, where k is the Boltzmann's constant, T is the temperature, H_i are equivalent losses of the lowest internal mode of the mirrors. For the conventional model of the intrinsic losses we have $H_i = m_i\omega_0\Phi/\omega$, where ω_0 and $\Phi^{-1}(\omega_i) = Q_0$ are the frequency and quality factor of the lowest internal mode of the mirrors, respectively, m_i is the equivalent mass of the lowest internal mode oscillator. The effective thermal shift of the interferometer's mirrors is $|x(\omega)|^2 \cong 2kT\Phi/\pi m_i\omega_0^2\omega$ at frequencies $\omega \ll \omega_0$. The deformation noise spectral density $h(\omega)$ is

$$h(\omega) = |x(\omega)|/2L = (2kT\Phi/\pi m\omega)^{1/2} (2\omega_0 L)^{-1}.$$

The precise value of $h(\omega)$ is dependent upon the low-frequency behaviour of the function $\Phi(\omega)$. To an order of magnitude, one may accept $Q_0^{-1} = \Phi(\omega) = \text{const}$. Then for the low frequency 300 Hz we obtain $h(\omega) = 2.5 \cdot 10^{-23} \text{ Hz}^{-1/2}$ that is less than the photon noise spectral density, i.e. the thermal noise of the lowest internal mode of mirrors will not limit the sensitivity.

The thermal noise spectral density of the mirror suspension is $G_s = 2kTm\omega_\mu/\pi Q_\mu$ where ω_μ and Q_μ are the frequency and quality factor of the pendulum mode of the mirror suspension respectively, and m is the mass of the mirror. The deformation noise spectral density is

$$h(\omega) = (L\omega^2)^{-1} (2kT\omega_\mu/\pi m Q_\mu)^{1/2} = 1.1 \cdot 10^{-23} \text{ Hz}^{-1/2},$$

where the numeric estimate is made for the lower frequency 300 Hz. Thus the thermal noise of the mirror suspension pendulum mode will also not limit the sensitivity of the device in a given frequency band.

Thermal noises of the mirror suspension violin modes are somewhat different from the mirror internal modes and pendulum mode. Indeed, the frequencies of the lowest violin modes fall within the antenna frequency band (usually, 3-4 violin modes). Numerical estimates of the spectral density of thermal noises of the suspension violin modes show that at resonant frequencies thermal noise peaks exceed by three orders of magnitude the spectral density of photon noises, which cannot be accepted. The equivalent antenna sensitivity has the form of a comb-like filter. In order to decrease thermal noises of the suspension violin modes, it is necessary either to use systems with intermediate masses, in which string mode frequencies are shifted to high-frequency domain, or to exploit modified suspension designs without violin modes (e.g., a combined pendulum, cross-like suspension, etc.). In this case the interferometer sensitivity will not be limited by the mirror suspension violin modes.

6.2.4. Technical laser noises

Fluctuations of the laser pump can notably decrease the sensitivity of a gravitational antenna. The conventional mean of suppressing such noises is making a symmetrization of the interferometer arms and using a photodetector in dark port. The laser amplitude noises can be also decreased by the standard Drever's phase modulation method. The laser pump power fluctuations do not decrease the sensitivity at $f > 300$ Hz for the laser power stabilisation at a level of $\Delta W/W < 10^{-6} \text{ Hz}^{-1/2}$ at frequency 1 kHz.

The frequency noise of the laser pump plays the major role when the interferometer arms are not highly symmetrical. Let the length of the arms differ by ΔL and the mean sharpness for the both arms differ by ΔF . Then we have $h(f) = (\delta\omega_e/\omega_e) [(\Delta L/L) + (\Delta F/F)]$. Assuming that the sharpness for the both arms are tuned such that the

second term in this expression is much smaller than the first one, the allowed frequency fluctuations for $\Delta L \approx 10^{-2} m$ are

$$\delta\omega_e < \omega_e \alpha G^{1/2} / \Delta L = 10^{-3} Hz / \sqrt{Hz}$$

which determines the necessary frequency stabilization of the laser pump. In addition, the total laser frequency deviation should not exceed the resonance width, i.e. $\Delta f_e \ll 1$ kHz.

Fluctuations of the laser beam direction in the input should be better than 10^{-8} rad/Hz^{1/2} near the frequency 1 kHz. The stabilization of the beam geometry can be made either with the help of the active methods (modulation of the mirror motion) or passive methods (filtration through a diaphragm, resonator, or a wave-guide). The Ward-Drever scheme of the mirrors position stabilization can also be used.

6.2.5. Other sources of noise

Fluctuations of the residual gas refraction coefficient due to imperfectness of vacuum along the beam may be estimated as follows. The mean number of atoms along the beam is $N_{at} = \rho L \pi D^2 / 4$, where ρ is the mean density of atoms. The variance of the number of atoms is $\delta N = (N_{at})^{-1/2}$, the refraction coefficient is $n = 1 + \alpha \rho$, where α is the polarization. Then the linear spectral density of this noise for $p = 10^{-6}$ Torr is $h(f) = 2\alpha (\rho / L \pi D v)^{1/2} = 2.3 \cdot 10^{-23} Hz^{-1/2}$, (v is the mean velocity of atoms across the beam). Therefore this noise also does not limit the sensitivity of the gravitational antenna.

6.3. Effective Sensitivity of the Antenna

All noise sources considered above are non-correlated, so they are summarized quadratically and the effective noise of the whole antenna is $h_{eff}(f) = \left(\sum_{i=1}^k h_i^2(f) \right)^{1/2}$. Fig. 2 shows the dependence of the sensitivity on frequency for short bursts of gravitational radiation with a frequency band $\Delta f \approx f$, where f is the mean frequency of the signal. From this figure one may conclude that the effective antenna frequency band at the sensitivity level $h \approx 3 \cdot 10^{-21}$ is 1 kHz (from 300 Hz to 1.3 kHz). At the same time there is a frequency band where the antenna sensitivity is higher than $1 \cdot 10^{-21}$ – from 350 to 500 Hz. The maximum sensitivity is $8 \cdot 10^{-22}$ near the frequency 370 Hz.

The sensitivity of the LINGRAN-100 gravitational antenna at the lowest boundary frequency $f \approx 300$ Hz is predominantly determined by the seismic noises (without utilizing additional chain like coupled pendula in the antiseismic filter). To study signals with lower frequencies, it is possible to use additional units in the "stack"-type antiseismic filter. But the main hope to solve this problem is the underground location of the setup where the seismic noise has to be suppressed at least by two orders of magnitude. The limitation on the upper operational frequency is due to the shot noise of the pump laser. Shift toward higher frequencies is possible with the use of a more powerful laser or by increasing the light recycling coefficient in the gravitational antenna design.

7. ADVANCED SENSITIVITY

The LINGRAN-100 sensitivity level 10^{-21} in terms of metric perturbations at the lowest frequency 300 Hz is close to the so called "standard quantum limit" for measuring a free mass (particle) position. In fact $h_{SQL} \approx L^{-1} (\hbar \hat{\tau} / m)^{1/2} \approx 5 \cdot 10^{-22}$ for $m \approx 50$ kg, $L = 10^2$ m and $\hat{\tau} = (2f)^{-1} \approx 10^{-3}$ sec. If a deep underground location were provide some suppression of seismic noise and a more power optical pump provide a decrease of the photon noise, then the advanced sensitivity of gravitational antenna would be limited by SQL. In view of this problem, a development of a special QND-technique is foreseen using a correlation of the quadrature components of the interferometer output light. In SAI MSU, a vector filtration of quadrature components based on quantum measurement theory was proposed. The procedure utilizes phase-sensitive amplifiers with a frequency dependent amplification coefficient as a measuring device. In this case the information about correlation of the quadrature components is used in the optimal way and the sensitivity increase. A cornerstone of this methodic is the compensation of quantum noise in two quadratures. If we assume that the compensation coefficient is of the usual value ($10^2 \div 10^4$), then the increase in sensitivity amounts to two-four orders of magnitude.

8. SITE

The interferometric gravitational antenna is planned to be installed in the underground tunnels of Baksan Neutrino Observatory (BNO) of Nuclear Research Institute of Russian Academy of Sciences located in Baksan Valley (Kabardino-Balkariya). The coordinates of the observatory are: the latitude is $43^{\circ} 12'$, the longitude is $42^{\circ} 43'$. The underground facilities of BNO consists of a number of tunnels about 4 m in diameter, two of which, the "Main" and "Auxiliary", are perpendicular to each other. These tunnels are worked into the mountain massive (Andyrchi) up to 4200 m. The thickness of the mountains in this site is 1500-2000 m (the altitude above the sea level is 1800 m). The angle between the "Main" tunnel and the direction to the south (azimuth) is 135° .

The location of the planned device at a deep ≈ 4000 m tunnel in rocky surroundings allows one to use it as a low-frequency gradientometer to study relatively slow ($T \approx 3 \div 20$ hrs) geodynamical processes induced by dynamics of the liquid and hard Earth cores, since coherent temperature and other geophysical interferences will be suppressed by 2-3 orders of magnitude at such a depth.

9. DATA PROCESSING AND STORAGE

The necessary signal discretization frequency for the design frequency band of the interferometric gravitational antenna is about 10 kHz. Having 2^{16} discretization levels, the storage of one count requires 2 bytes. Thus, $2 \cdot 10^4$ bytes of information will be read-out per second. One-year integration would require to store 200 Gbyte of information. Such value is not unreachable with the modern information storage devices. For example, relatively cheap hard magnetic disks have a capacity of 3-4 Gbytes and can provide 2-3 day's demand in data storage and preliminary on-line processing of the output signal with the aim of discovering "suspicious" events. Strimmers or magneto-optical disks, which have optimal characteristics from the point of view "price-capacity", can be used for a long-term storage of information.

If Pentium-like PC are used, their total number connected in a network must be not less than 8. The total number of central computers can be decreased down to 2-3 by using more powerful modifications (like SUN workstations etc.)

To process the output signal from the gravitational antenna, the modern methods of numerical data analysis will be used, such as fast Fourier transformation, correlation analysis, method of regressive models, etc. The data exchange with other gravitational antennae and other astrophysical devices, like gamma-ray satellite monitors, neutrino detectors, etc., will be made via INTERNET network, in order to find possible coincidence signals (such coincidences are predicted in the framework of some modern astrophysical theories).

10. GEOPHYSICAL APPLICATION

At ultra-low frequencies $10^{-4} \div 10^{-5}$ Hz the interferometric antenna on free masses can be a novel geophysical tool for observations and measurements of global geodynamical processes induced by both internal energy sources and external tidal potential. These frequencies lie far away from the design sensitivity level of the antenna as a gravitational wave detector. Mechanical shifts of testing mass-mirrors on pendulum suspension in this zone are compensated by a feedback keeping the interferometer at the "working point" – in the middle of the dark band. The corresponding compensational tension, the so-called "signal of error", can bear the useful information on gravitational potential low-frequency variations of geodynamical character.

The sensitivity of the new tool can potentially be much higher, by two-four orders of magnitude, than the sensitivity of traditional geophysical devices, such as gravimeters, tiltmeters, and strainmeters. The differential character of tiltmeter measurements on a long-base interferometer significantly enhances the filtration of searches for global geodynamical effects against the background of local coherent interferences.

A differential tiltmeter formed by two remote test masses – mirrors of the gravitational interferometer – should in principle be independent of motions of the local normal and can measure relative deviations of local plumb lines of two spatially separated pendula. The local normal variations can change the orientation of the device "cover" (support of suspensions) but not the relative orientation of spatially separated "plumb vertical lines". The useful signal value must be proportional to the base length. Essentially, such a device will be a gravitational gradientometer, which measures angular gradients of the gravity force vector on the device length. Coherent interferences could only produce a shift of significant mass in the nearby underground zone of the terrestrial crust and mantle, which can be minimised by working deeper, or accounted for due to additional information.

The results of calculations of some global geodynamical perturbations forecast the maximum effect of the mutual mirror deviation on the base of ~ 100 m at a level of $10^{-10} \div 10^{-13}$ rad for outer and inner cores and even more depending on the unknown amplitude of perturbations. The calculations show that from the point of view of instrumental limitations of the "new tool", these effects can be measurable.

11. LOW-FREQUENCY GEOPHYSICAL NOISES

The main advantage of the LINGRAN-100 project (in comparison with other similar projects) is its location in a deep hard rock underground. It is the deep underground that permits to include also geophysical goals in scientific program of the set-up. The natural fact is that geophysical noises strongly decrease in deep underground.

Analysis of the power spectra of horizontal deformations shows that for the most "quiet" places (rocky mountains, the working depth is 10^3 m) it can be well approximated as $S_\epsilon = (10^{-23}/f^2) \text{ Hz}^{-1}$ meanwhile for the "surface" installation (i.e. the working depth is about several meters) the numerical coefficient in this formula increases to 10^{-19} . Thus for a period of 7 hours ($f = 4 \cdot 10^{-5} \text{ Hz}$), with signal selection band Δf inversely proportional to the period, the characteristic noise deformations of the base will be: $\epsilon = 5 \cdot 10^{-10}$ for a "quiet" place and $5 \cdot 10^{-8}$ for a "surface" installation.

Tilt noises are, to an order of magnitude, similar to deformations. So, using above estimates and considering that in the worst case the tilts at the ends of the base are not correlated, we obtain for the characteristic frequency $f = 4 \cdot 10^{-5} \text{ Hz}$ and the same frequency band the tilt noises about $5 \cdot 10^{-10}$ rad for a "quiet" place and $5 \cdot 10^{-8}$ rad for a "surface" installation. Correspondingly, for the tilt angles of the pendula we arrive at $\alpha \approx 2 \cdot 10^{-11}$ for a "quiet" place and $\alpha \approx 2 \cdot 10^{-9}$ for a "surface" installation.

The temperature and atmospheric effects on a device worked deeper into rocky surroundings by more than 1000 m from the day-light surface are much smaller than for surface destination of the installation. The same holds for the "noise" gravitational gradients caused by the tunnel deformations, underground water level variations, etc. Therefore one can conclude that the mounting of the device in the tunnels of BNO makes it possible to register global geodynamic effects.

12. PRELIMINARY STUDIES

The SAI MSU group possesses a working interferometric device in operation – a 100 m laser deformograph installed in the Main tunnel of the BNO. The device represents an asymmetric Michelson interferometer with prism reflectors hardly mounted on a rocky base. The system is completely vacuumized with a permanent vacuum level of $p \approx 10^{-4}$ Torr. The optical system is a delay line with a maximum possible number of reflections ~ 30 . The information on the length variations of the working (long) arm of the interferometer is read-out using two channels: a "geophysical" one at frequencies lower than 0.1 Hz, and an "astrophysical" one at frequency 1.6 kHz. The spectral density of the total deformation noise in the geophysical and astrophysical channels are $\sim 10^{-11} \text{ Hz}^{-1/2}$ and $\sim 3 \cdot 10^{-16} \text{ Hz}^{-1/2}$, respectively. The deformograph is provided with parallel control indicators of temperature, pressure, as well as with a geophysical unit consisting of a "tidal gravimeter" with the sensitivity level $\Delta g \sim (1 \div 10) \mu\text{Gal}$ and a tiltmeter with a resolution of 10^{-4} arc seconds.

The NILP RAS group possesses a working multistep complex for optical laser source frequency stabilization at wavelength 1.06μ and 0.63μ with the residual fluctuation spectral density $\sim 3 \cdot 10^{-4} \text{ Hz}^{-1/2}$ at frequencies $10^2 \div 10^3 \text{ Hz}$. The source power can be as high as $1 \div 3 \text{ W}$.

13. CONSTRUCTION PERIOD, LIFE TIME AND PRELIMINARY COSTS

A construction time for LINGRAN-100 is supposed to be three years including the ultimate adoption of the infrastructure (underground rooms, interior of tunnels, power supply, communications, etc.), and the assembling of the set-up. Then a two-year period is assumed for preliminary exploitation to reach the best project sensitivity. Continuous duty phase of the LINGRAN-100 is planned to be $10 \div 15$ years. In the case of positive results, LINGRAN-100 would provide a serious argumentation for building of a $(1 \div 3) \text{ km}$ underground device.

An economical advantage of the LINGRAN-100 is in the fact that the most expensive components of the project – underground tunnels and vacuum tubes (light guide) – already exist (BNO RAN worked out tunnel in the past for other purposes; SAI MSU purchased 300 m of 0.3 m diameter stainless vacuum pipes). Therefore the total cost of LINGRAN-100 is supposed to be not larger than 5 000 000 USD.

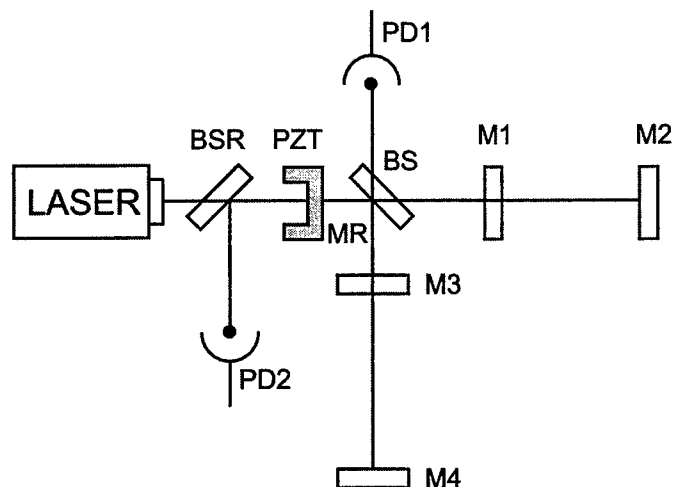


Figure 1. Principal scheme of the gravitational antenna «Lingran-100»: M1,M3 - front mirrors, M2,M4 - end mirrors, MR - recycling mirror, BS, BSR - beam splitters, PD1, PD2 - photodetectors, PZT - piezoceramics

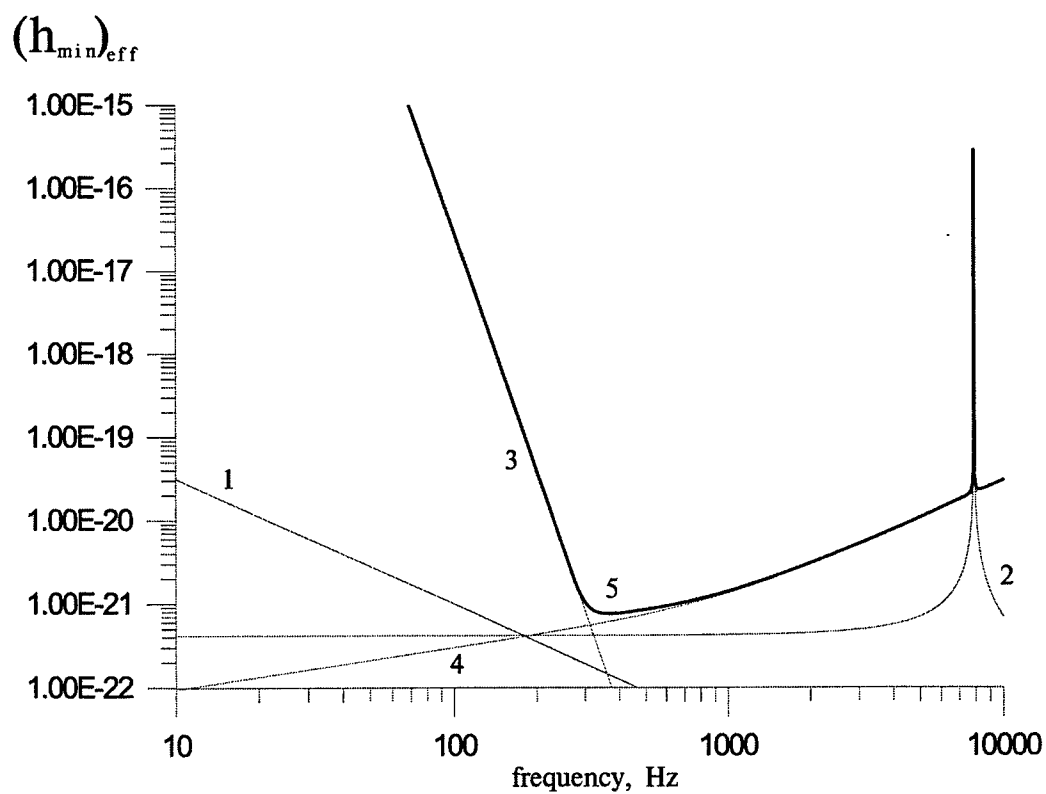


Figure 2. Effective sensitivity of the gravitational antenna «Lingran-100»: 1 - Thermal noise of pendulum mode, 2 - Thermal noise of mirror's inner mode, 3 - Seismic noise, 4 - Photon noise, 5 - Resulting sensitivity

Wide-band laser interferometer for monitoring the Earth strains

V. K. Milyukov, V. N. Rudenko, B.S. Klyachko, A.M. Kart, and A. V. Myasnikov

Sternberg Astronomical Institute, Moscow State University,
Universitetsky prospect 13, 119899, Moscow, Russia

ABSTRACT

The wide-band laser interferometer with a measurable armlength of $75m$ has been installed in an underground tunnel (the North Caucasus), in one of the most active in geodynamic respect region of Russia. The optical scheme of the interferometer is the two passes ($N=2$) Michelson-type interferometer with unequal arms working in regime of space separated beams which is realized by use of the corner reflectors. The mirrors, the beam-splitter and the optical passes are placed in vacuum ($5 \times 10^{-5} mbar$). The long-term monitoring strains of the Earth is provided in two frequency bands: below $0.1Hz$ and in the bandwidth of $0.5Hz$ around frequency of $1.62kHz$ (the monitoring of quadrature components). The sensitivity in the high frequency band is about $10^{-15} Hz^{-1/2}$. In the regime of long-term monitoring the Earth strains the interferometer is operating from the beginning of 1993. The observation data, thanks to the unique capabilities of the laser interferometer with respect to both the frequency and the dynamic ranges, are used for studying some geophysical and astrophysical problems.

Keywords: long-base laser interferometer, Earth strains, geophysical medium, gravitational waves

1. INTRODUCTION

Long-base laser interferometers are the most perfect instruments for measuring relative changes of distances between two points. The frequency range of laser interferometers practically begins from zero and is bounded from above only by the fast-response of the read-out system. The dynamic range of long-base laser interferometers is also practically unlimited and the threshold of sensitivity to relative changes in distances exceeds that of other instruments by several orders of magnitude. An imported advantage of laser interferometers is the presence of an internal length standard, which is wavelength of laser radiation with a high degree of accuracy. The above-indicated properties of long-base laser interferometers make possible their use as deformographs for solving different problems of geophysics and astrophysics¹⁻⁶.

Having a goal of a long-term monitoring lithospheric strains in a wide frequency band Sternberg Astronomical Institute of Moscow University has put in operation a laser interferometer-deformograph^{7,8}. The interferometer is disposed in the Baksan Canyon (the North Caucasus).

The area of the Baksan Canyon is located in the fracture zone of the one of the main Caucasian faults. The northern part of the Great Caucasus Ridge is one of the most active in geodynamic respect among the Russian regions characterized by intensive movements of the Earth's crust. Of special interest is the Elbrus Mountains bounded from the North by the Tyrnyauz depth fault zone. The thickness of the crust here is up to $60km$ crossed by a deep fault system, perpendicular to the canyon axis. According to the repeated levelings and repeated high precision gravity surveys this part of the Caucasus uplifts intensively with a rate of about $1 - 1.5cm/year$. On the whole, now the North Caucasus is considered as an active seismological area.

The laser interferometer strainmeter has been installed in the underground tunnel of the Baksan Neutrino Observatory. The observatory is located in Kabardino-Balkaria, in the Baksan ravine, $30km$ to the south-west of Tyrnyauz and $25km$ from the Elbrus Mountains. The interferometer is mounted at the distance $650m$ from the tunnel's entrance, at the depth of $400m$ and at $1750m$ above sea level. The strainmeter's coordinates: latitude is $43^{\circ}12'$; longitude is $42^{\circ}43'$; azimuth is $150^{\circ}37'$.

Other author information:

V.K.M.: E-mail: milyukov@sai.msu.su

2. OPTICAL AND MECHANICAL PARTS

The optical scheme of the interferometer is the two passes ($N = 2$) Michelson-type interferometer with unequal arms working in regime of space separated beams which is realized by use of the corner reflectors. Operation by the space-separated beam scheme somewhat increases the overall size of the optical system and the wave-guide, but the optical bypassing is easily attained, which prevents the reflected radiation to return to the laser. Thus, no additional optical gates are required. The measurable arm of the interferometer lies along the tunnel and has the length of 75m (the length of the optical path is accordingly 150m), the length of the small (reference) arm is 0.3m.

The light source used is the commercial frequency-stabilized He-Ne laser (model LGN-303), the radiation wavelength is $0.63\mu\text{m}$, the power output is 2mW. The relative instability of the laser radiation frequency is not worse than 10^{-9} during 8-hours continuous operation. The radiation of the laser is modulated at the frequency of 60kHz by the electro-mechanical modulation of the laser cavity. The laser with the modulator has been manufactured by the commercial venture "FALCRA".

The general functional scheme of the interferometer is shown in Fig.1. The laser beam (1) passes through the telescopic system (2) formed by two lens. At the focus of this system there is a diaphragm for cutting-off higher diffraction orders. The telescopic system produces a beam waist with a large radius of curvature, gets on the beam-splitter (3) which splits the beam into two parts and directs them toward each corner mirrors (4,5). Two reflected beams are deflected at a small angle with the aid of an optical wedge (6) and recombine at the same beam-splitter. The interference pattern brought about by the recombination of the reference and measuring beams consists of straight-line fringes.

The optical parts of the interferometer are assembled in two vacuum cylindrical chambers (10,11). The chambers are connected by means of three bellows and vacuum tubes of diameter 30cm, which form a light guide. Thus, the optical arms of the interferometer are fully evacuated.

The vacuum pumping system of the interferometer consists of two parallel cells, (18,19) and (20,21), and the vacuum in the interferometer space is provided by their alternate switching on. The total pumped-out volume is of the order of 6m^3 . The pressure in the system under stationary conditions is $5 \times 10^{-5}\text{mmHg}$.

The radiation unit (laser and telescopic system) and the vacuum chambers containing the optical cells of the interferometer are mounted on three independent footings (15,16,17). The optical cells of the interferometer are rigidly attached to the rock by means of mechanical structures and load-bearing foundations and are not in direct contact with the tunnel's floor.

3. READ-OUT SYSTEM

The read-out system provides the monitoring the interferometer output signal in a wide frequency band: from ultra low frequencies up to thousands Herz. The base of such the read-out system is the feedback system of a compensative type. The output radiation of the interferometer (the interferometric pattern) gets on the galvanometer's mirror. After reflection from this mirror the beam goes through an artificial diffraction pattern which period is equal to the interferometric fringes period and falls onto the photo-receiver. The feedback system, based on the galvanometer, keeps the "dark spot" position of the interferometric pattern on the chink of the photo-receiver. Turning the galvanometer's frame is proportional to the flowing electrical current.

The variation of the measurable arm length of the interferometer leads to displacement of the interferometric pattern. The feedback signal, formed by the electronic equipment, compensates this displacement by turning the galvanometer's mirror. This signal is also the interferometer output signal, whose phase and amplitude carry information about the direction and the value of the displacement, respectively. Of course, the dynamic range of the feedback circuit is restricted, however it can be regulated. The typical range of values is one fringe, i.e. $0.3\mu\text{m}$. For larger perturbations, the feedback is destroyed and the system is jumping into a new equilibrium position.

The long term monitoring of the Earth strains is provided in two frequency bands: from 0Hz up to 0.1Hz, this is so-called the "geophysical channel"; and in the bandwidth of 0.5Hz around the frequency of 1.62kHz (the monitoring quadrature components), this is the "astrophysical channel". The high frequency channel of the Baksan laser interferometer contains the two-channel lock-in amplifier with the carrier frequency of 1.62kHz and two low-pass second-order Butterworth filters with the cut frequency of 0.5Hz.

The read-out system provides also the monitoring temperature and barometric informations.

4. OBSERVATIONS

In the regime of long-term monitoring the Earth strains the interferometer is operating from the beginning of 1993. The data base contains the strains information from March 1993 up to now and consists of about 100 quasi uninterrupted fragments divided by the gaps caused usually by the technical reasons. The histogram of the obtained useful data covered the calendar time is shown in Fig. 2. In the Fig. 3 the average estimation of the strain power spectral density in the frequency range from 5×10^{-6} to 10^3 Hz is presented⁹. The estimation were based on experimental data obtained over period from March 1993 to January 1994. The general behavior of spectrum corresponds to a flicker noise in this frequency region. The power spectrum falls from 10^{-12} Hz^{-1} for frequencies of about 10^{-5} Hz to 10^{-28} Hz^{-1} at frequencies of about 10^3 Hz . There are two well-pronounced maxima corresponding to the diurnal and semidiurnal tides components, the spectral peak of the semidiurnal wave being higher. The experimental estimations of magnitudes of these components are equal 1.28×10^{-8} and 1.47×10^{-8} , this being in good agreement with the tidal strain amplitudes recorded in the USA in a region which is also remote from the sea³ (1.2×10^{-8} and 1.7×10^{-8}). The theoretical values of tidal deformation amplitudes calculated for the location of the Baksan interferometer (assuming the Earth to be spherically uniform and the Love and Shida numbers h and l to be, respectively, 0.6 and 0.07¹) are 0.54×10^{-8} for O_1 and 0.97×10^{-8} for M_2 , which is somewhat lower than those observed. This difference may be accounted for by the location of the interferometer near the fault zone.

The frequency range from 5×10^{-5} to 10^{-3} Hz has been in principle studied insufficiently. This range covers the Earth's oscillations which come to be known as super-long-period ones, in particular core oscillations. For the Earth's models with large enough values of density in the center there exist forms of core oscillations with periods longer than one hour. Some calculations predict core oscillations with periods of 75, 85 and 100 min and larger. However, the amplitudes of core oscillations at the Earth's surface must be extremely small¹⁰ and the possible noise sources in this frequency range - such as slight variations of atmospheric pressure, the motion of ground waters, and thermoelastic deformations - may mask the Earth's super-long oscillations.

The noise in the seismic band (from 10^{-3} Hz upward) varies very strongly in time and space. The sources of such noises depend on the frequency. For frequencies ranging from 10^{-3} to 0.05 Hz the appearance of noise is due to deformations of the surface caused by variations of atmospheric pressure². The strongest fluctuations are caused by turbulent phenomena. However, the intensity of these noises is attenuated with depth. It should be noted that the same range covers the spectrum of the natural Earth's oscillations, whose amplitudes considerably increase during powerful earthquakes. In the range of 0.05 to 0.5 Hz , the main noise source is microseisms. For frequencies from 0.5 Hz and higher, the noises are caused by bulk waves and also by local sources of artificial and natural origin. Figure 3 shows that, against the background of the overall decrease of power, its dispersion increases in the frequency range of 10 - 500 Hz , which seems to be accounted for by the technogenic nature of noises in this range.

Because of the long duration of the series of observations (10 months), on which the estimation of spectral density was based, it may be treated as the background level of seismic noise in a wide frequency range. Thus, the resultant estimate of the spectral density established the lower threshold for the possible detection of geophysical signals in the region studied.

Figure 3 illustrates the unique capabilities of the laser interferometer with respect to both the frequency and the dynamic range, which makes its application expedient for the solution of a wide range of geophysical and astrophysical problems.

5. GEOPHYSICS

The long-time observations of strains in the active tectonic area allow to study the dynamic state of geophysical medium. The state of the system inhomogenities (cracks, faults), the degree of their stability control the dynamic state of the lithosphere. Around the instability the geophysical medium becomes strong nonlinearity and deformation response to the external load increases dramatically. Therefore, variations of the strain-stress relation may be considered as the indicator of dynamic state of the medium. The "external" stress caused by tides may be used as a probe process. Thus variations of the tidal strain "response" can be used for monitoring the medium transition to unstable state without knowledge of absolute values of the rock stress.

Another indicator of the dynamic state is connected with variations of the regime of seismic energy emission. It is expressed as variations of seismicity on the upper scales of failure and as variations of acoustic emission on the

lower scales. The broad band of a laser strainmeter allows to study the character of relation between the acoustic emission and the long-period strains and to use the change of this relation for indication of the medium state.

The data of both Baksan interferometer's channels are used for the investigation of this geophysical problem.¹¹ The observed strains and the theoretical calculated tide stresses were filtered by narrow band-pass filter with the goal to select the group of semidiurnal tide waves. Filtered series have been exposed to the regression analysis in the moving windows. Inside each window the cross-correlation function has been calculated and parameters of regression corresponding to the maximum of correlation have been determined. The time variations of the regression parameter with periods close to 7 and 14 days have been found¹². The nature of this variations must be studied.

The relation between the strain variations in different frequency ranges and the searching the physical causes induced such effects were studied. The multy-demension correlation analysis was used for solving these problems. Such statistical approach can give the additional information about parameters of geophysical medium and statistical properties of coherent noises.

6. ASTROPHYSICS

The high-frequency channel of the interferometer can be considered as a free-mass gravitational antenna because the longitudinal elastic eigenfrequency of the mirrors attached to the rock is much less, then 1.62kHz (the carrier frequency of this channel). The estimation of the sensitivity of this channel in terms of deformations is shown in Fig. 4. The sensitivity level is $15 \times 10^{-16}\text{Hz}^{-\frac{1}{2}}$, what is close to the level of room temperature bar detectors.

The data of this channels are used for searching the correlation with gamma-ray events from BATSE experiment. Such a problem was formulated due to the reason that the join analysis of gravitational data with other astrophysical phenomena gives a new view on the general strategy of gravity-wave experiment which is traditionally oriented to search for coincident events of spatial distributed gravitational detectors. In particular, instead of a trivial "null-experiment" for a single detector, it is reasonable to search for gravitational antenna excitations correlated with some astrophysical events, such as cosmological neutrino radiation pulses and gamma-ray bursts, since some of the models of stars collapse, binary coalescence, etc. predict the radiation of gravity-wave pulses accompanied by neutrino and gamma-ray events.

The adaptive algorithm for the detection of an incoherent pulse sequence with unknown but non random parameters was developed and approved on data of the Baksan laser interferometer. As an additional channel of astrophysical information in the developed integrative system the arising times of cosmic gamma-ray events (the 3B BATSE catalogue) were used^{13,14}.

The developed methods for integration of astrophysical detectors in the gravity-wave experiment improve the standard data processing based on the statistical analysis of the coincidence scheme. The new approach eliminates the most important deficiency of the standard model: the absence of the accumulation of a weak gravitational signal.

7. ACKNOWLEDGMENTS

This work is supported by the Russian Foundation for Basic Research under Grant No 96-05-65334, and the State Scientific Program "High-Energy Physics".

REFERENCES

1. L.A. Latynina and R.M. Karmaleeva, *Deformographic Measurements* (in Russian), pp. 1-155, Nauka, Moscow, 1978.
2. D.C. Agnew, "Strainmeters and Tiltmeters", *Rev. Geophys.* **24**, pp. 579-624, 1986.
3. J. Berger and J. Levine, "The Spectrum of Earth Strain from 10^{-8} to 10^2Hz ", *J. Geophys. Res.* **79**, pp. 1210-1214, 1974.
4. V.V. Nesterov, S.L. Golovin, and V.A. Nasonkin, "Measurements of the Earth Long-Periodical Oscillations by Laser Interferometer- Deformographs", *Izv. RAN, Fiz. Zemli* No 4, pp. 72-78, 1990.
5. S.N. Bagaev, V.A. Orlov, Yu.N. Fomin, and V.P. Chebotaev, "The Observation of Variation of Long-Period Microseismic Noise by Precision Laser Interferometry", *Izv. RAN, Fiz. Zemli* No 1, pp.85-89, 1992.
6. S. Takemoto, "Some Problems on Detection of Earthquake Precursors by Means of Continuous Monitoring of Crustal Strains and Tilts", *J. Geophys. Res.* **96**, pp. 10377-10390, 1991.

7. A.V. Buklenskii, A.M. Kart, B.S. Klyachko, V.K. Kravchuk, V.K. Milyukov, I.V. Melezhnikov, A.V. Myasnikov, V.V. Nesterov, and V.N. Rudenko, "The Baksan Laser Interferometer", *Izmeritel'naya Tekhnika* No 10, pp. 5-9, 1995.
8. V.N. Rudenko, V.K. Milyukov, V.V. Nesterov, and I.P. Ivanov, "The Status of the Gravitational Wave Setups at Moscow University", *Astron. Astrophys. Trans.* 5, pp. 93-101, 1994.
9. V.K. Milyukov and V.K. Kravchuk, "Observation of the Earth's Deformation Spectrum by Means of a Laser Interferometer-Deformograph", *Moscow Univ. Phys. Bull.* No 2, pp.60-64, 1996.
10. C.E. Bullen, *The Earth's Density* (Russian Translation), pp.1-378, Mir, Moscow , 1978.
11. A.V. Ponomarev, V.K. Milyukov, and V.B. Smirnov, " The Investigation of Dynamic State of the Lithosphere. Observations and Methods", *Abstr. of the First Congress of the Balkan Geophysics Society, Athens, Greece*, pp. 494-495, 1996.
12. A.V. Gusev, V.K. Milyukov, A.V. Ponomarev, V.B. Smirnov, and M.P. Vinogradov, "Long-Time Observation and Analysis of the Earth Strains in the Northern Caucasus", *Abstr. of the 29th General Assembly of the International Association of Seismology and Physics of the Earth's Interior, Thessaloniki, Greece*, p. 222, 1997.
13. M.P. Vinogradov, A.V. Gusev, and V.K. Milyukov, " Incoherent Accumulation of the Signal in Gravity-Wave Experiment", *Moscow Univ. Phys. Bull.* No 5, pp. 37-40, 1997.
14. M.P. Vinogradov, A.V. Gusev, and V.K. Milyukov, "Experimental Testing the Adaptive Pulse Accumulator in Gravity-Wave Experiment", *Moscow Univ. Phys. Bull.* No 6, pp. 33-36, 1997.

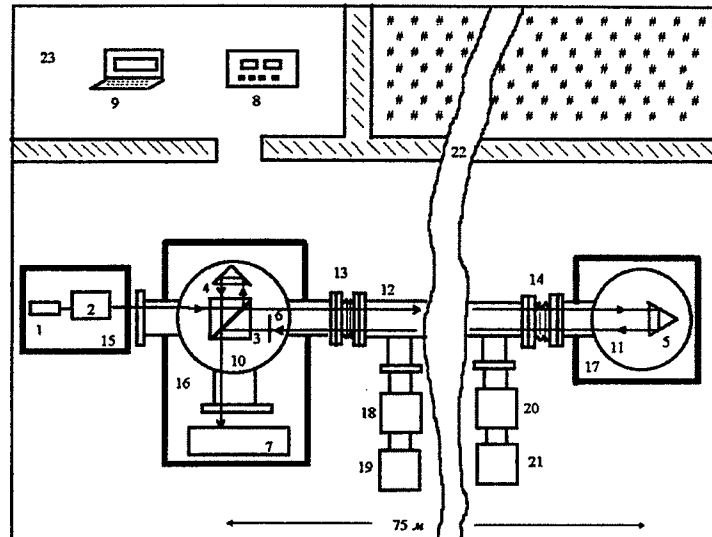


Fig. 1. The Baksan laser interferometer. 1 - He-Ne laser, 2 - Telescopic system, 3 - Beamsplitter, 4,5 - Corner reflectors, 6 - Optical wedge 7,8 - Read-out system, 9 -Aquisition system, 10,11 - Vacuum tanks, 12 - Vacuum tubes, 13,14 - Bellows, 15-17 - Concrete foundations, 18-21 - Vacuum pamps, 22 - Tunnel's wall, 23 - Operator's room.

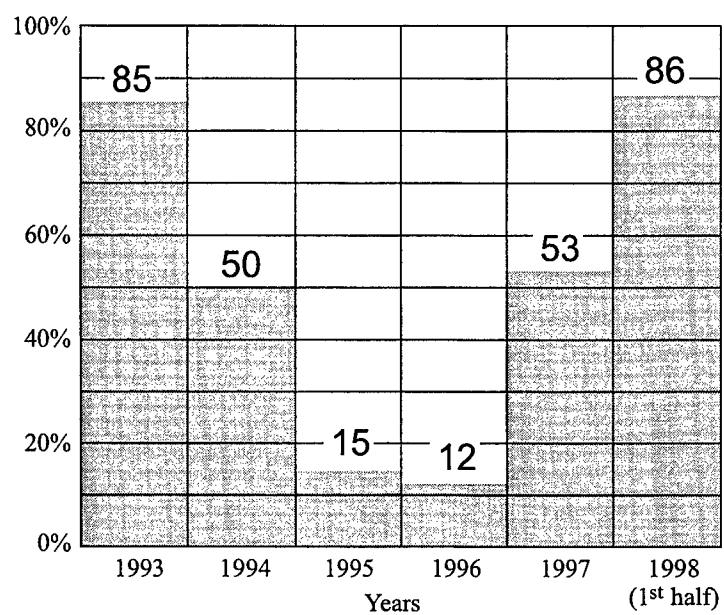


Fig. 2. The time covered by interferometer data to the full calendar time (in percent)

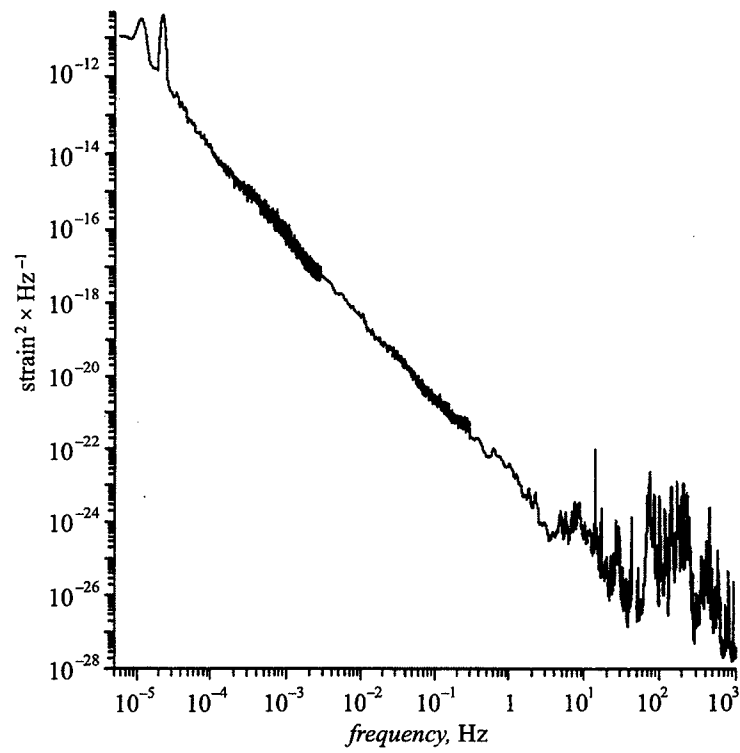


Fig. 3. Average spectral density of the strain power

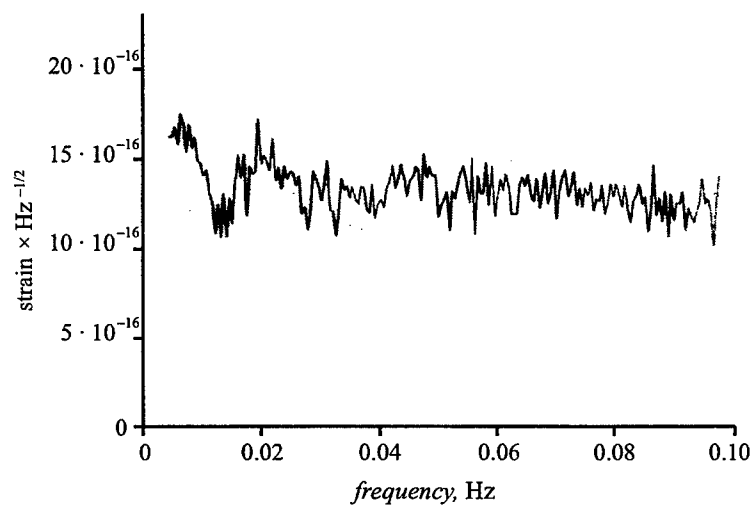


Fig. 4. Amplitude spectrum of the high frequency channel

The Observation of Variations of Long-Period Microseismic Noise by Precision Laser Interferometry

Sergey N.Bagayev, Valery A.Orlov, Sergey V.Panov

*Institute of Laser Physics, Siberian Division of Russian Academy of Sciences, Lavrentiev ave. 13/3,
630090 Novosibirsk, Russia*

ABSTRACT

The results of the study of dynamic peculiarities of deformational oscillations of Earth crust with periods in the range from 10 to 300 sec by He-Ne laser dephormograph placed in underground gallery are presented. The mean square amplitude of deformational noise observed during one month is about 0.01 micrometers. It has constant components and variable one with period 24 hours. A mechanism of the deformational noise generation and a practical implementation of the laser apparatus and observed phenomenon for geodynamic and seismic monitoring are discussed.

Keywords: seismic noise modulation, precision laser interferometry, deformation of Earth crust

1. INTRODUCTION

Great many of theoretical and experimental works were devoted to the investigation of micro-seismic noise for the last 30 years. Continuous improvement of technique for registration of small mechanical oscillations was directed not only to detailed investigations of seismic situation in regions of strong earthquakes but to obtaining of new notions concerning deep structure of the Earth. Earth noises of technogenic and native origin have been investigated in wide enough frequency range from 0.1Hz to some kHz. In particular, as a result of these investigations the general phenomenon of amplitude modulation of noises by deformational processes into Earth crust induced by earthquakes, explosions, natural oscillation of Earth, storms in atmosphere and in ocean was found¹⁻³. It was supposed that tide deformations in lithosphere should lead too to amplitude modulation of micro-seismic noise. The more powerful harmonics of Moon-Sun tide oscillations have periods over the region $T=12$ h and $T=24$ h. In this case amplitude of semi-diurnal component stands out above amplitude of diurnal one in some times. However for experimental envelopes of noise amplitude over the region from 0.1Hz to 2 kHz that relationship was inverse as a rule i.e. in experiments diurnal harmonics were observed well and semi-diurnal ones practically did not register. That is the reason why there were the attempts to explain the phenomenon of long period modulation of noise as a result of technogenic mechanism of the noise generation ascribing to it pure anthropogenic origin⁴. The non-uniqueness of theoretical concept and experimental data pointed to imperfection of notions concerning real mechanisms of excitation of micro-seismic noise^{5,6}.

This problem has aroused our interest in connection with investigations of deformational precursors of earthquakes by precision laser interferometry⁷.

2. EXPERIMENTAL TECHNIQUE

Since 1994, we carry out long time observations in the adit of Talaya station using original He-Ne laser demograph elaborated in the Institute of Laser Physics of Siberian Branch of Russian Academy of Sciences⁸. The scheme of placement of laser dephormograph in adit is shown in fig.1 and heterodyne principle of its operation is shown in fig. 2. The principle of operation of measuring system is based on continuous registration of changing the phase in time due to the Doppler effect at radiation reflection from the moving object. The device is based on the application of two He-Ne lasers with lasing power $P \sim 1$ mW which are phase synchronized by means of a fast response electronic system of phase-frequency offset lock. Owing

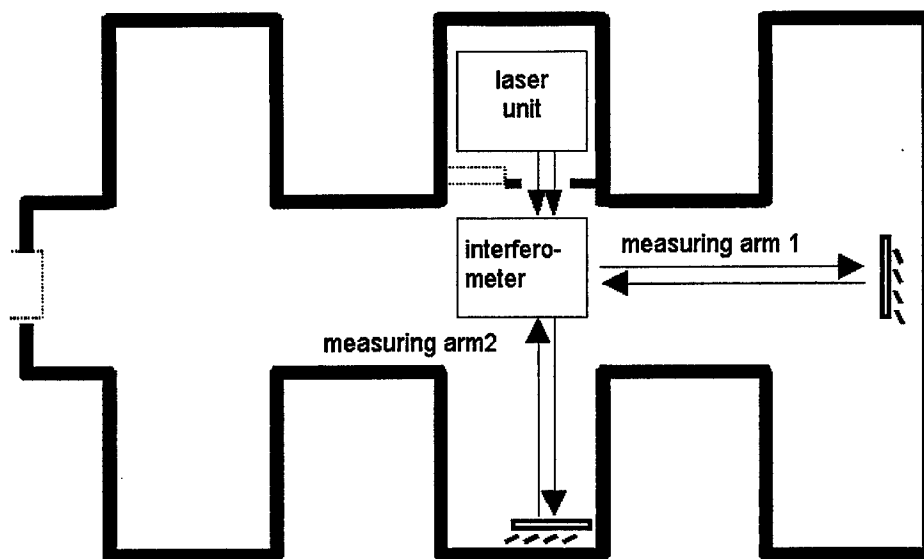


Fig.1 The position of laser deformograph in adit

to this, the beat frequency of lasers extracted on photo-receiver 1 is maintained constant with an accuracy determined by the frequency stability of reference generator. The radiation of probe laser is sent through atmosphere to the moving object, is reflected back from mirror and mixed with radiation of the heterodyne laser on photodetector 2. The value of the object displacement is determined from the analysis of phase difference between two signals. For this purpose, the output signals of photoreceiver 1 and 2 are fed into channels of the phase shift meter having resolution $\pi/512$. The output signal of the device is proportional to a displacement value. The system registers the change of phase difference of 2π as the object displacement

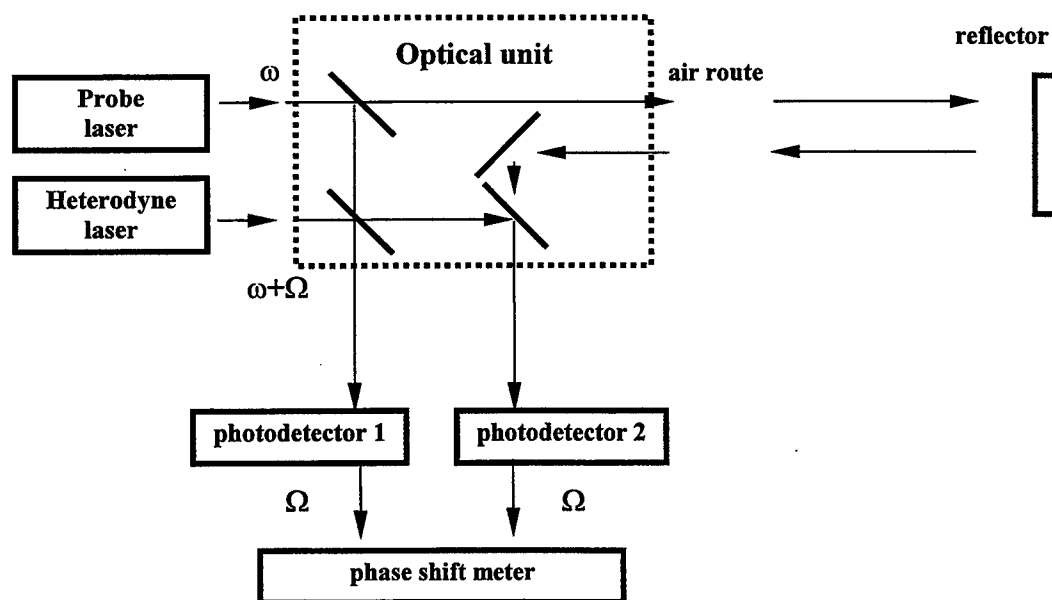


Fig.2 Diagram of laser deformograph

for half of wave length of laser source. The result of measurement was registered by the computer in digital form. The registration of deformations was performed in two mutually orthogonal directions. The length of each measuring arm was $L=25$ m. Using of compensating arm in the interferometer allows to exclude the influence of atmosphere along each of the independent directions in open air.

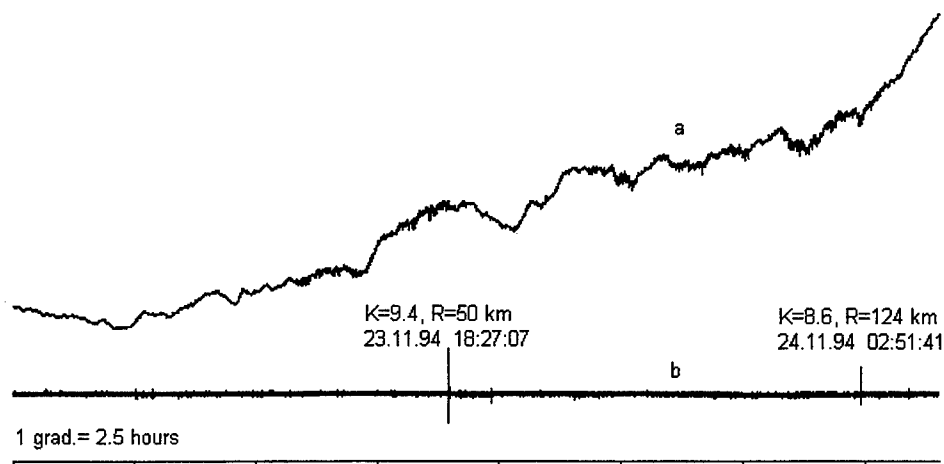


Fig.3 Increase of micro-seismic noise registered by the laser deformograph on the eve of the regional earthquakes in the South Baikal, a – signal of deformograph in one measuring arm, b – signal of seism-detector

A series of phenomena accompanying the earthquakes were observed using that equipment. A heart one of them is a rise of anomalous disturbances in Earth crust deformation some hours or days before strong distant seismic events^{7,9}. The phenomenon manifests itself as a significant deformational disturbance in amplitude about $0.1 - 1 \mu\text{m}$ in the form of “bay” or pulsation over the region of periods from 0.5 to 3.5 hours against a background of natural process of Moon-Sun tide oscillations. The heart of another phenomenon observed in signals of deformograph is increasing of high frequency deformational noise before regional ($S \leq 1000$ km) earthquakes⁸. Typical fragment of deformational record showing this phenomenon is presented in fig.3. Spectral structure of the registered noise is not stationary however has discrete character in the range of periods from tens up to some hundreds of seconds. Amplitude of detected oscillation at a level of $0.01 - 0.1 \mu\text{m}$ depends on distance from earthquake and its energy class. Increase of these oscillations is observed some hours before seismic events. Oscillations of noise components excited before earthquakes have periods 14, 24.8, 35, 41, 54.6, 114, 138 and 273 s and are out of the range indicated in the introduction. The explosions and launching of satellites being exclude from consideration, it is unlikely the existence of constant level of noise and variations of its envelop are attributed to the influence of human activity to the geosphere over mentioned above range of periods. We interpret the generation of registered noise harmonics as a result of resonance excitation of radial (vertical) oscillations of stratified Earth structure that don't contrary well known geophysical notions. However, the question concerning the sources and mechanisms of noise excitation in Earth crust is still open for us. Without answering this question, prognostic value of the noise increasing phenomena before earthquakes is not evident. In this connection, we began to study the long period variation of amplitude of micro-deformations. This paper reports the first results of the study.

3. DETECTION OF VARIATION OF DEFORMATIONAL NOISE AND DISCUSSION OF EXPERIMENTAL OBSERVATIONS

To obtain temporal dependence of microdeformation amplitude the fragments of deformational records were analyzed in long no less than one week obtained at the same time in 3 independent channels with sampling time $\tau=2$ s. Two records belong to two independent orthogonal placed measuring arms of laser deformograph. The third one belongs to short control arm isolated from rocks and registering phase change connected with variation of air index of refraction and prolonged variations of laser wave length. The data of two measuring arms were filtered in frequency band from 0.01 to 0.1 Hz. Then to obtain noise oscillation in every measuring arm coefficient of correlation with data of short control arm were calculated at the time length 5 – 20 minutes. Correlated part of noise oscillations was subtracted and mean square value was calculated. To obtain the value of amplitude in the next point the procedure of calculation was repeated. As a result a plot of noise amplitude versus of time was plotted. Typical fragment of noise amplitude variation observed during 7 days is presented in fig. 4. Plot of the signal obtained in the second measuring arm is identical to the presented one.

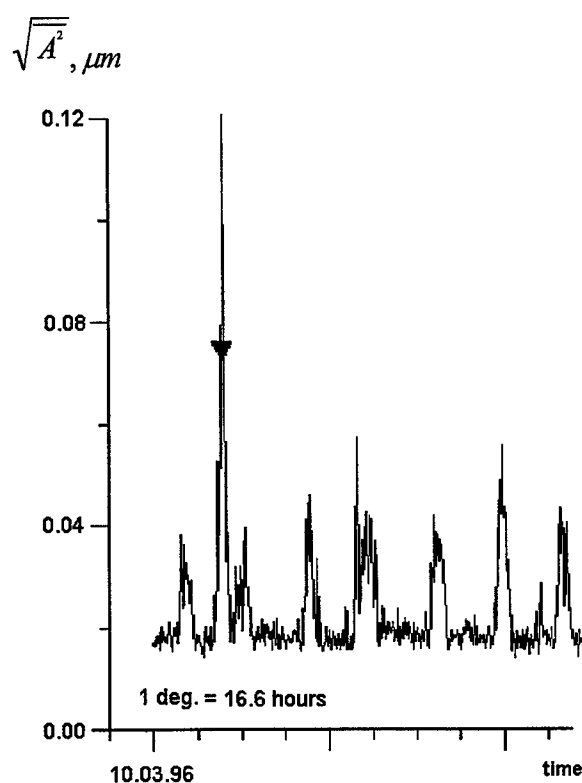


Fig.4 Mean square amplitude of the deformational noises in the range from 0.01 to 0.1 Hz vs time; earthquake is marked by symbol ▼

Since amplitudes of noise in horizontal orthogonal measuring arms are identical this has strengthened the idea that observed micro-deformations are due to vertical oscillations with amplitude of interferometer base sagging $a \leq 500 \mu m$. The main feature of amplitude envelope of micro-deformations is the presence of diurnal periodicity. Maximums of curve correspond to time moments when the Sun is in zenith with respect to geographical place of observational point. It should be emphasized that among variation of noise amplitude there is constant component of noise. The value of this component depends only weak on season of year. The presence in the beginning of curve in fig 4 of high peak corresponds to regional earthquake of the middle energy class $K=10$ which happened March 12 1996 at 20h 47m G.M.T. Distance from the observation point to epicenter of the earthquake was 1090 km. There was a time interval when noise amplitude increased in some times before this event.

Notice that phenomenon of diurnal variation of amplitude of deformational noise found by us has its own noises connected with presence of people in adit, drastic change of meteorological conditions, explosion works and weak earth quakes in the region of observation.

In the first place, notice that there is no correlation between observed effect and Moon-Sun tide oscillation where Moon plays the main role since its gradient of gravitational force in scale of Earth is in some times bigger then Sun's one. The absence of semi-diurnal oscillations on noise envelope in Fig.4 proves that. What is more, the maximums on envelope of noise amplitude repeat themselves strict enough in 24 hours and the fact that noise amplitude has maximum when Sun is in zenith points at main role of Sun in this phenomenon. This relation can be explained if we suppose that generation of noise is due to not variations of gravitational force but potential. Analytical relation for gravitational force operating on element of Earth volume ΔV from Sun can be written as

$$F = -\text{grad}U = -\text{grad}(\Delta V \rho \phi) = -\Delta V \rho \text{grad} \phi - \Delta V \phi \text{grad} \rho$$

where ρ is density of substance in volume ΔV , ϕ is the value of gravitational potential of Sun in the same region. The first term of this relation describes usual gravitational force. The second term is caused by nonhomogeneous distribution of Earth substance. The variable component of noise we connect with existence of this additional force. It is in region of big density jumping the variation of this force become significant. In consequence of Earth rotation, variations of additional pressure connecting with force under consideration have periodicity is equal to twenty-four hours. Estimations have shown that variable diurnal component of pressure amplitude at a depth which is equal to thickness of earth crust at the density jump on the border of lithosphere – mantle 0.3 g/cm^3 is less in two orders of the weight of rocks of this stratum and is determined by relation $P = \rho gh = 10 \text{ kbar}$. The another period which can be detected in this model is equal to one year i.e. is equal to the period of Earth rotation around Sun.

4. CONCLUSION

In our opinion a partly transformation of elastic energy of rocks under the effect of force under consideration leads them to resonance swing. This phenomenon we are going to use for monitoring of strain state of earth crust in order to detect the precursor of earthquakes. Noise response on periodical source of excitation in the general case should depend on the state of rock in point of observation. Before strong earth quakes action of this force in seismic center as a result of elevated sensitivity of rock to destruction can lead to nonmonotone behavior of the power of generated noise for some hours or days before seismic events. We are going to continue such kind of investigations.

5. ACKNOWLEDGEMENTS

The data of deformographical measurements used in the work were obtained with the assistance of Yu.N.Fomin, A.Yu.Rybushkin and V.M.Semibalamut.

6. REFERENCES

1. L.N.Rykunov, O.B.Khavroshkin, V.V.Tsyplakov, *Doklady Akademii Nauk* **238**, N2, pp.303-306, 1976 (in Russian).
2. L.N.Rykunov, O.B.Khavroshkin, V.V.Tsyplakov, *Physics of the Earth*, N1, pp.72-76, 1979 (in Russian).
3. V.N.Tabulevich, *Complex investigation of microseismic vibrations*, "Nauka", Novosibirsk, 1986 (in Russian).
4. E.I.Galperin, A.V.Sitnikov, S.I.Kvetinsky, A.M.Ivanov, A.I.Chesnokov, *Physics of the Earth*, N10, pp.99-109, 1989 (in Russian).
5. L.N.Rykunov, O.B.Khavroshkin, V.V.Tsyplakov, N.A.Vidmont, *Doklady Akademii Nauk* **358**, N2, pp.256 - 256, 1998 (in Russian).
6. A.S.Belykov, V.S.Lavrov, A.V. Nikolaev, L.L.Khudrinskii, *Doklady Akademii Nauk* **348**, N3, pp.383 - 386, 1996 (in Russian).
7. S.N.Bagayev, V.A.Orlov, Yu.N.Fomin and V.P.Chebotayev, *Physics of the Earth*, N1, pp.85 - 91, 1992 (in Russian).
8. S.N.Bagayev, Yu.M.Kirin, S.Yu. Kusnetsov, V.A.Orlov, et.al., *Development of techniques and instrumentation for experimental geophysics. Collection of scientific papers*, 1, pp.52-61, Moscow, 1993.
9. S.N.Bagayev, Z.Vakhrushev, Yu.M.Kirin, S.Yu. Kusnetsov, O.V.Nekipelov, V.A.Orlov, et.al., *Investigation on Creating Scientific Foundation of Prediction of Earthquakes in Siberia*, pp.70 – 71, Irkutsk, 1989.

Contrast enhancement of ESPI addition fringes using real time electronic filtering

Ramon Rodriguez Vera, Carlos Perez Lopez, Fernando Mendoza Santoyo
and Bernardino Barrientos

Centro de Investigaciones en Optica, A.C.,
Loma del Bosque 115, Col. Lomas del Campestre, Leon, Gto.,
Mexico 37150.

ABSTRACT

Optical noise is inherent in fringes obtained with the electronic speckle pattern interferometer (ESPI) system. When used in the subtraction mode the optical noise is readily decreased and high contrast fringes may be seen. However, if fast dynamic events are studied a pulsed laser may be used in order to capture particular moments of such an event. A fast repetition rate, 60 pulses per second, Nd:YAG diode seeded laser is introduced in the ESPI system. This laser has twin cavities allowing the firing of two pulses with a minimum time separation, between them, of less than 10 ns. Thus two pulses can be fired within a single TV frame (TV frame rate is 30 Hz) of the ESPI system, interrogating at two different moments in time the fast dynamic event under observation. This process creates a speckle pattern for each pulse, and since two pulses are fired within a single TV frame an addition fringe pattern is obtained, assuming the event has produced a physical measurable change. This addition fringe pattern has an amount of optical noise that is approximately twice that of a subtraction fringe pattern. Results are presented where the addition fringe pattern contrast may be enhanced by using real time electronic filtering.

1. INTRODUCTION

The first research attempts to use the speckle phenomena in real time metrology led to the development of the ESPI system¹. Since then many research groups around the world have applied this real time optoelectronic system to solve a wide variety of scientific and industrial problems^{2,3,4}. Most of these applications have allowed to further the research and development on ESPI around the automatic acquisition of amplitude and phase data, with the main objective of making ESPI a unique tool for non-destructive optical evaluation in laboratory and other types of environments. Dynamic events are the kind of application that have brought the need to introduce pulsed lasers in ESPI^{5,6}, with the possibility of using the system in any environment.

As is well known, up to date, the ESPI system when used with a pulsed laser renders fringe patterns in two modes of operation: subtraction and addition. A diode seeded twin pulse Nd:YAG laser is able to fire two laser beams that are mutually coherent, and each with a coherence length well within 5 m. A laser like this works at a repetition rate of 60 Hz and may fire two laser pulses separated in time by no less than 10 ns, with any amount of time separation in the upper limit. ESPI images,

see figure 1 for an out-of-plane set-up, are acquired by a CCD camera that relays them to a memory board in a PC. For the addition mode two pulses are fired within a TV field that has a time lapse of 16 ms when working at 30 Hz (two interlaced fields form a TV frame). Each pulse forms its own speckle pattern interferogram (object and reference beams combined), so the two pulses are added forming an addition interferogram. For the subtraction mode only one pulse is fired within a TV frame. The first pulse at t_1 serves as the reference interferogram that will be sequentially subtracted from incoming interferograms at t_{1+n} , with $n = 1, 2 \dots$ serving to number the interferograms captured later in time. ESPI addition interferograms have a higher amount of noise than ESPI subtraction interferograms, and thus subtraction fringe patterns have higher contrast than addition ones. This particular feature allows an easier quantification of amplitude and phase data from subtraction fringe patterns. However, addition interferograms may be digitally and analogically processed to render images with as high a contrast as those obtained in subtraction⁷. This paper presents results where the addition fringe pattern contrast may be enhanced by using real time electronic filtering, taking the ESPI system one step forward towards achieving its full usage as a reliable tool to measure fast dynamic events.

2. THEORY

A brief description of the mathematical model for the formation of addition ESPI interferograms is presented for rotating fan blades. Other approach may be found in, e.g., reference 8. Figure 1 is used throughout. It shows an out-of-plane ESPI set-up.

The case for rotating fan blades will be treated, all equations are (x,y) dependent. The intensity found at the CCD photosensitive plane for pulse 1 is,

$$I_1 = I_o + I_r + 2\sqrt{I_o I_r} \cos(\phi) \quad (1)$$

and for pulse 2,

$$I_2 = I_o + I_r + 2\sqrt{I_o I_r} \cos(\phi + \Delta\psi + \omega_R) \quad (2)$$

where as usual I_o denotes the object intensity, I_r the reference beam intensity, ϕ a random speckle variable dependent on the object surface roughness and optical path differences, $\Delta\psi$ is a variable introduced to denote fan blade deformation due to any cause other than fan rotation, and ω_R is a variable that depends solely on fan rotation. Addition is performed over a single field/frame of the CCD faceplate, thus,

$$I_1 + I_2 = 2(I_o + I_r) + 2\sqrt{I_o I_r} \{\cos(\phi) + \cos(\phi + \Delta\psi + \omega_R)\} \quad (3)$$

The equation shows a twice added noise term $(I_o + I_r)$ that would otherwise disappear along the subtraction process. Hence, this term decreases the contrast and visibility of addition ESPI

fringes. Equation 3 explain well the results obtained for the rotating fan blades presented in this paper.

In the following section a real time electronic procedure will be used to remove this noise term ($I_o + I_r$), thus obtaining a higher fringe pattern contrast. The speed of rotation of the fan blades is high, so subtraction results could not be obtained between two TV frames and hence there is not a direct comparison with the addition fringes obtained.

3. EXPERIMENTAL PROCEDURE AND RESULTS

The experimental set-up for the ESPI is shown in figure 1. It shows an out-of-plane sensitive interferometer in which a mono-mode optical fiber is used to carry the reference beam to its usual conjugate point. The diode seeded twin pulse Nd:YAG laser is frequency doubled to obtain a train of pulsed light, with $\lambda = 532$ nm. The speckle pattern interferograms are acquired by a memory board placed on a pentium driven PC.

A rotating fan with three metal blades was used to obtain addition ESPI fringes. The ESPI set-up includes an external variable pulse generator placed inside a synchronization device (SD). The SD triggers the first laser pulse and then fires pulses at the start of each CCD frame cycle. The pulse generator synchronizes the fan rotation to each CCD field, in such a way that when the laser fires a pulse, both the blade and camera are in synchrony and then the ESPI is ready to take a speckle pattern interferogram. Because of the rotation speed, a second laser pulse is fired in the same TV field. In brief, the external variable pulse generator freezes a particular fan blade during a TV field and with two pulses fired an addition ESPI fringe pattern is formed. Up to this point the noise term ($I_o + I_r$) is still present in the addition fringe pattern. In order to electronically remove it in real time, a filter whose main characteristic is to perform as a DC band pass filter, has been designed. Figure 2 shows the results of applying in real time such a filter. Figure 2a show an addition ESPI fringe pattern where fringes are barely seen. Figure 2b show a rotating fan blade after real time electronic filtering. The latter picture display two features: radial fringes due to fan rotation (ω_R) within the firing time of the two pulses, and blade deformation ($\Delta\psi$) due to, possibly, torsion on the blade.

4. CONCLUSIONS

A real time electronic filter was successfully used to enhance the contrast of addition ESPI fringe patterns. High speed rotating fan blades were used as an example. Results show an increase in contrast for the original addition ESPI fringe patterns revealing fringes on a blade, present but not seen without the use of the real time filter.

5. ACKNOWLEDGMENTS

The research work for this paper was sponsored by CONACYT under grant No. 2318P-A. We would like to acknowledge the comments and suggestions of A. J. Moore.

6. REFERENCES

- 1.- J. N. Butters and J. A. Leendertz, "Holographic and video techniques applied to engineering measurement," Transactions of the Institute of Measurement and Control, **4** (12), pp. 349-354, December 1971.
- 2.- O. J. Lokberg, J. T. Malmo and G. A. Slettemoen, "Interferometric measurements of high temperature objects by electronic speckle pattern interferometry," Applied Optics, **24** (19), 3167-3172 (1985).
- 3.- A. Rowland y F. Mendoza Santoyo, "Evaluation of dynamic volume viscoelasticity using electronic speckle pattern interferometry", Optical Engineering, **25** (7), 865-870 (1986).
- 4.- J.R. Oswin, P.L. Salter, F. Mendoza Santoyo and J.R. Tyrer, "ESPI measurement of flextensional transducer vibration patterns in air and water", Journal of Sound and Vibration, **172** (4), 433-448 (1994).
- 5.- J. R. Tyrer, "Application of pulsed holography and double pulsed ESPI to large engineering vibrating structures," SPIE **599**, pp. 181-188, Cannes, France, December 1985.
- 6.- G. Pedrini, H. J. Tiziani and Y. Zou, "Digital double pulse TV-holography", Optics and Laser Engineering, **26**, 199-219 (1996).
- 7.- N. Alcalá Ochoa, F. Mendoza Santoyo, Andrew J. Moore y C. Pérez López, "Contrast enhancement of ESPI addition fringes", Applied Optics **36** (13), 2783-2787 (1997).
- 8.- R. W. Preater, "Non-contact method of in-plane strain measurement on rotating structures," SPIE **236**, pp. 58-61, Utrecht, Holland, 1980.

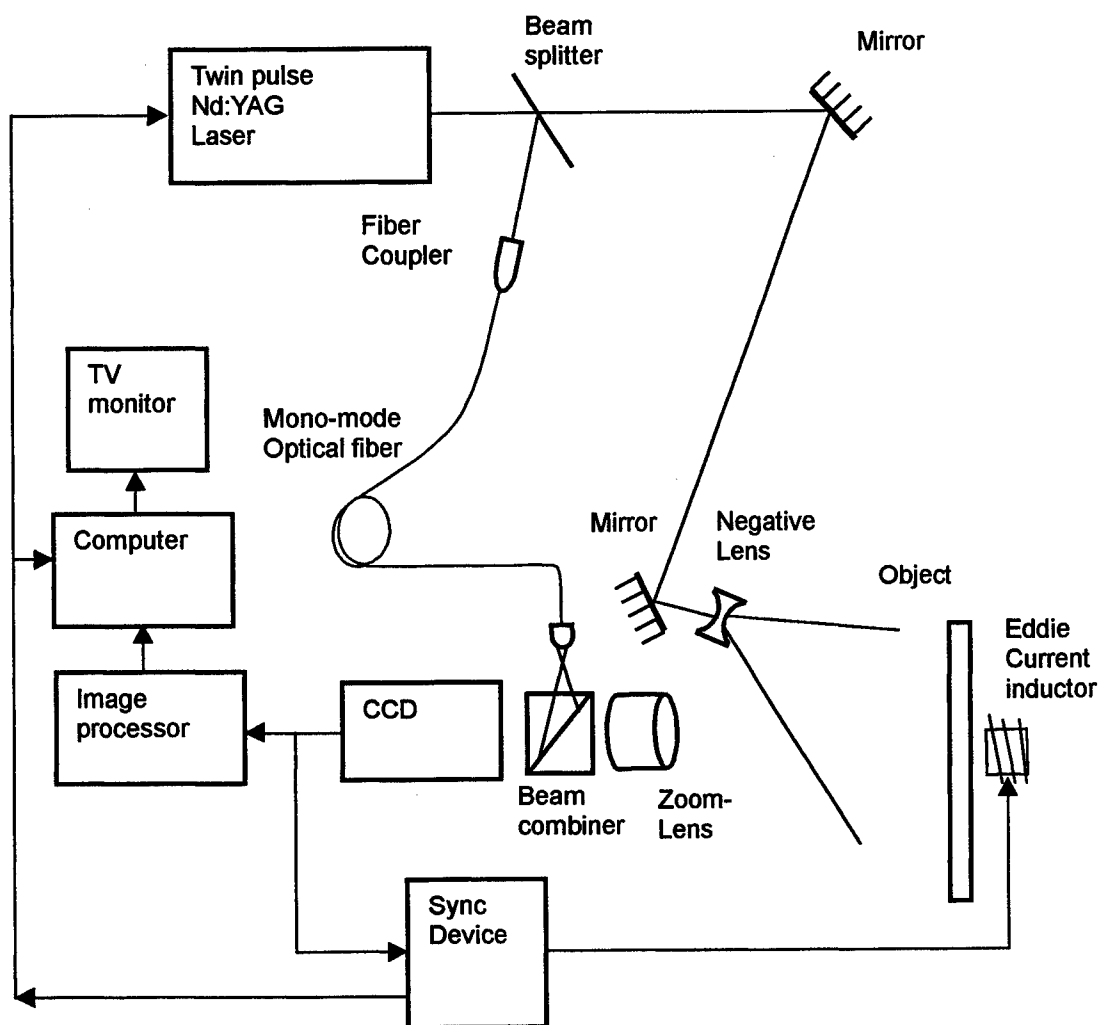
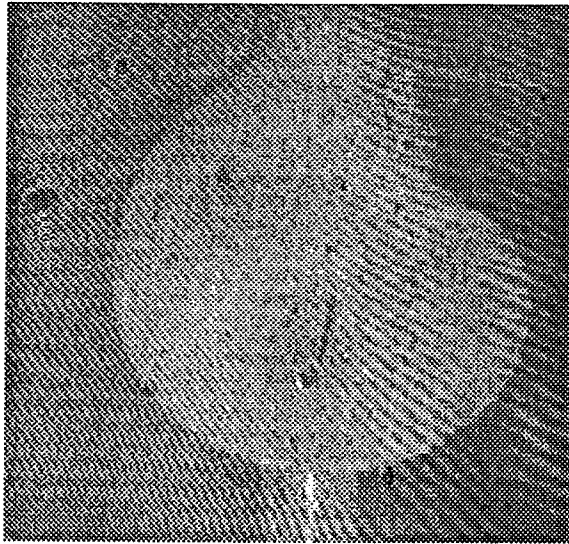
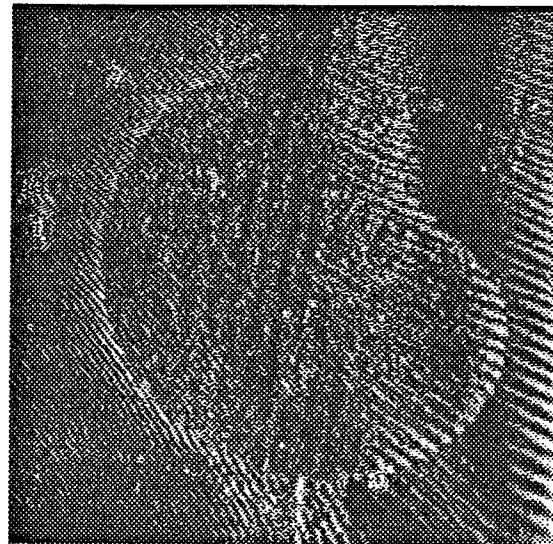


Figure 1. Twin pulse ESPI in the out of plane mode. Set-up as used for studying transient events. For rotating objects, an external pulse generator signal was introduced in the Sync device in order to freeze the object rotation.



(a)



(b)

Figure 2. A frozen high-speed rotating fan blade captured with a twin-pulsed ESPI setup. (a) Addition ESPI fringes (barely seen), (b) Fringes after applying the real time electronic filter.

SESSION 4

Laser Characteristics Control

Transverse mode pattern in distorted resonators

Vladimir V. Lyubimov

Research Institute for Laser Physics of the Science Center

"S.I.Vavilov State Optics Institute", 199034 St.Petersburg, Russia

Ph: +7 812 2189982, fax: +7 812 2185891, E-mail: soms@ilph.spb.su

ABSTRACT

The influence of the wave phase and amplitude distortions on the local angular distribution and on the spatial amplitude distribution of the modes of laser resonator was analysed by the methods of the waveguide theory. The theoretical evaluations are in a good agreement with the experimental data.

Key words: laser adaptive resonator, transverse mode pattern, radiation local angular distribution, spherical aberration

INTRODUCTION

At the field of opened resonators theory the modes of a resonator more complex than a stable one with spherical mirrors are usually calculated by means of computer. It seemed to be correct at the period of time starting from publishing of the paper by A.G. Fox and T. Lee ¹ till L.A.Vainshtein stated the basic principals of opened resonators waveguide theory ².

It is evident that computer calculations are more exact than the result obtained with the use of approximated analytical theory, but it is very difficult to systematise the results of several calculations related to such complex objects as opened resonators.

As an example one can refer to the discussion between R.L.Sandersen & W.Streifer ³ and A.F.Sigmen & A.Miller ⁴ based on the difference in results of the first numerical calculation for unstable resonator modes. As a matter of fact the qualitative difference of their results was due to the aperture influence on the unstable resonators selectivity qualities. It was cleared up within the frame of unstable resonator waveguide theory ⁶.

All the analytical theories present the results in a systemised form. The methodological unity of the waveguide theory has made possible not only to classify the modes in a difficult case of unstable resonators ⁷ but to follow transverse mode pattern evolution from one resonator type to another for all resonators existing in laser practice: plane, tilted, stable and unstable ^{2,7,9}.

In several cases waveguide theory proved to be useful in choosing the way of laser parameters optimisation.

At the present time the papers devoted to modes calculation, when there is not only thermal lens in active medium but also spherical aberration, begin to appear. Perhaps, the waveguide theory would be useful for operation mode optimising for the lasers with adaptive mirror resonators as it states the direct relation between the error of medium inhomogeneity compensation by mirror deformation and the transverse structure of the generated modes.

1. MODES OF THE CAVITIES WITH THE COMPLEX SHAPE MIRRORS

In general case the calculation of the modes in the cavity with symmetrically deformed mirrors can be represented as the solution of the integral equation¹¹:

$$f(\xi, \eta) = \frac{e^{ix}}{2\pi} \iint_s K(\xi, \xi_1; \eta, \eta_1) f(\xi_1, \eta_1) d\xi_1 d\eta_1 \quad (1)$$

where e^{ix} is characteristic value of integral equation,

$$K(\xi, \xi_1; \eta, \eta_1) = \exp i[(\xi - \xi_1)^2/2 + (\eta - \eta_1)^2/2 + kh(\xi, \eta) + kh(\xi_1, \eta_1) - \pi/2],$$

$\xi = x\sqrt{k/2l}$; $\eta = y\sqrt{k/2l}$; $2l$ is the distance between the mirrors or is the cavity effective length in case of lenses present inside the cavity, $k = 2\pi/\lambda$, λ is the wavelength, $h(\xi, \eta)$ is the local deviation of the mirrors from a plane shape.

The solution of the equation (1) will look like:

$$f(\xi, \eta) = \sum_j a_{1j} w_1(S_j^2, \xi, \eta) + \sum_j a_{2j} w_2(S_j^2, \xi, \eta), \quad (2)$$

where the functions $w_{1,2}(S_j^2, \xi, \eta)$ are satisfied to the equation:

$$\frac{\partial^2 w_{1,2}(S_j^2, \xi, \eta)}{\partial \xi^2} + \frac{\partial^2 w_{1,2}(S_j^2, \xi, \eta)}{\partial \eta^2} + [S_j^2 + 4kh_1(\xi, \eta)] w_{1,2}(S_j^2, \xi, \eta) = 0, \quad (3)$$

where $S_j^2 = S_0^2 + 4\pi j$, $e^{ix} \equiv e^{is^2/2}$, $h_1(\xi, \eta) \equiv h(\xi, \eta)$. The relationships between $a_{1,2}$ are defined through the coefficients R_{00}^\pm of the reflection from the resonator edge and transformation coefficients R_{0j}^\pm .

In many important cases it is sufficient to be limited by the consideration of the only one basic wave reflection from the mirror edge. In the cases of the plane resonator² and of the stable one⁹ it is possible because of the transformation coefficient is much less than the reflection coefficient. In the unstable resonator the same is because of the transformed wave amplification is far below than that for the basic wave⁷.

2. WAVE FRONT'S SLOPE IN THE RESONATOR

In the case of the one-dimensional mirrors the equation (2) solutions by the Wentzel-Kramers-Brilluen method are the following:

$$w_{1,2}(S_j^2, \xi) = (S_j^2 + 4kh_1(\xi))^{-1/4} \exp \pm i \int^\xi \sqrt{S_j^2 + 4kh_1(\tau)} d\tau, \quad (4)$$

where $S_j^2 = S_0^2 + 4\pi j$; $j = \dots -2, -1, 0, 1, 2, \dots$ and the equation for modes quantization is:

$$\ln R_{00} + 2i \int_{-\frac{M}{2}}^{\frac{M}{2}} \sqrt{S_0^2 + 4kh(\xi)} d\xi + \ln R_{00}^+ = i2\pi p, \quad (5)$$

From the formula (4) it is easy to trace the evolution of the modes transverse structure from the plane resonator ($h(\xi) = 0$) to the tilted ($h \sim \xi$), stable ($h(\xi) \sim -\xi^2$) and unstable ($h \sim \xi^2$) resonators.

When the caustic point ξ_k in which $\text{Re}S^2 + 4kh(\xi_k, \eta_k) = 0$ is located at the mirror's surface, the integral in formula (5) is taken from the edge of the cavity to the caustic point. If the mode is localised between the caustics, the integral is taken from one caustic to another.

It can be seen from the formula (4) that the local front slope of the waves $w_{1,2}(S_0^2, \xi)$ defined by the value $S_0^2 + 4kh(\xi)$ is the natural characteristic of the mode transverse structure. Such characteristic is more convenient than by the use of the intensity distribution because, at first, it allows to reconstruct the intensity modulation period and, at second, in multiple-modes operating the number of excited modes can be estimated. This result is also obtainable for the two-dimensional mirror.

Really, if we represent

$$w_{1,2}(S_0^2, \xi, \eta) = A(\xi, \eta)e^{iU(S_0^2, \xi, \eta)}, \quad (6)$$

the equation (3) is transformed by WKB-simulation to the following equation:

$$\left(\frac{\partial U}{\partial \xi}\right)^2 + \left(\frac{\partial U}{\partial \eta}\right)^2 = S_0^2 + 4kh(\xi, \eta) \quad (7)$$

It is obviously from the form of the equation (5) that it simulates a cone which surface localises the beams outcoming from the cavity cross-section point with the coordinates ξ, η . The value of the cone angle is as follows:

$$\theta_0 = \text{Re} \sqrt{\frac{S_0^2}{k^2} + \frac{2h(x)}{l}} \quad (8)$$

The beams localised at the surfaces of the cones with angles θ_j will correspond to the waves with another values of S_j^2 . The indicated above local angular distribution discreteness explain the failure of the paper ¹⁰: The point is that Wigner distribution function used in ¹⁰ is not effective for the definition of the fields with a discrete local angular distribution. The use of this function and analogous characteristics is limited by the case of unstable resonator with scattering active medium ^{11,12}.

In many cases the value S_0^2 can be estimated from the condition of absence at the cavity cross-section of the zones at which $\text{Re}(S_0^2 + 4kh) < 0$, since in these zones the generation is practically absent and inverted population accumulation takes place with the Q-factor increase for the modes with more high value of S_0^2 . This fact leads to the estimation: $S_0^2 \cong -4kh_{\min}$ and allows to define the full laser radiation angular distribution as follows:

$$I(\theta) = \frac{|Q|^2}{2\pi\theta} \frac{d\sigma}{d\theta}, \quad (9)$$

where $|Q|^2$ is pumping power distribution, $d\sigma$ is a differential of the area of active medium cross-section taken between the two curve lines:

$$\theta = \sqrt{\frac{2h}{l} - \frac{2h_{\min}}{l}} \quad \text{and} \quad \theta + d\theta = \sqrt{\frac{2h}{l} - \frac{2h_{\min}}{l}} \quad (10)$$

At the consideration of the mirrors deformation and of the active medium optical inhomogeneity the $h(\xi, \eta)$ was supposed as real.

The active medium gain non-uniformity may be taken into account by considering the equality: $\text{Im}kh = (\beta(\xi) - \rho)l_1$, where $\beta(\xi)$ is a local mode gain coefficient, l_1 is the active element length, $\rho = \ln R/2l_1$, R is the output mirror reflection index.

It is easy to see from the formula (4) that the irregularity of the gain coefficient distribution over the active element cross-section leads to sufficient distortion of the waves amplitude distribution $w_{i,2}(S_0^2, \xi)$ when the regions presents where $\text{Im}[S^2 + 4kh] > 0$ takes place. In this case the mode localises at those regions where the condition is inverse: $\text{Im}[S^2 + 4kh] < 0$. In some cases this fact may be used for the decrease of radiation divergence because it is defined by the mirrors local deviation from the plane-parallelism¹³. The occupation of the full active element cross-section by the mode is provided by realisation of the condition: $|\text{Im}S^2| \gg |\text{Im}4k\Delta h|$ i.e. the value of diffraction losses should be greater than the value of the gain non-uniformity in the active medium¹⁴.

When calculating the gain distribution in active medium in the case of the CW lasers the equations (1)-(3) should be supplemented with the energy balance equation. The analytical solution of such equation set was obtained for the case of resonators with high diffraction losses. In these resonators the intensity distribution is formed mainly by the wave travelling towards the more wide edge of the resonator^{15, 16}.

The calculation shows that the wave front shape and the local angular distribution are defined by the equation (7). In order to take into account the influences of the mirrors' deformation and of the active medium inhomogeneity on the generation distribution over the active element cross-section, the local losses ρ_l should be added to the energy balance equation. These local losses ρ_l must satisfy to the equation as follows:

$$\rho_l l_1 \cong \frac{2\text{Re}h'}{\sqrt{S^2 + 4\text{Re}h}} + \frac{\beta_p \sqrt{S^2 + 4\text{Re}h}}{\beta_p - \rho}, \quad (11)$$

where β_p is active media gain coefficient in the lasing absence and thereby characterises the pumping level.

3. USING OF THE ADAPTIVE RESONATOR IN THE CASE OF COMPLEX ABERRATIONS

At the present time the information about the experiments for the thermo-optical aberration compensation in the powerful garnet lasers by means of the mirrors deformation are appeared^{17, 18}. The complexity of this problem is defined by the fact that in the powerful garnet lasers in addition to an aberration of the thermo-optical lens type ($h_l \sim r^2$) the spherical aberration ($h_l \sim r^4$) takes place whose

sign is opposite to the thermal lens sign. It exists because of the temperature dependence of the thermal conductivity.

Let's consider the possibilities of the laser characteristics improvement in the particular case of compensation of thermal lens only. For this partial compensation the $h(w;r)$ function is as follows:

$$h(w,r) = (\alpha(w) - \alpha_c)r^2 + \gamma(w)r^4, \quad (12)$$

where w is the pumping power, $\alpha_c r^2$ is the compensated wave aberration.

It is easy to see that the partial compensation of the thermo-optical lens don't cause to the resonator losses increasing when $\alpha_c r^2$ is increased to the quantity defined by the condition $h'(w,r) = 0$, when $r = r_0$, r_0 is the active element radius (Fig. 1a). In this case the remaining aberration at the active element edge is equal to h_s and mode divergence is described as follows:

$$2\theta = 2\sqrt{\frac{2h_s(r_0)}{l}} \quad (13)$$

When choosing the value α_c to satisfy the condition $h(w,r) = 0$ at $r = r_0$, the maximum value of the $h(w,r)$ would be of $0,25h_s(w,r_0)$ and the mode divergence would be less by a factor of 2 in comparison with the case spoke before. But in this case the zone of unstability in which the local losses $\rho_1 l_1$ defined by the quantity of following order:

$$\rho_1 l_1 = \frac{\sqrt{2h_s(r_0)l/r_0^2}}{\sqrt{2}-1} \quad (14)$$

appears in the region $r_0/\sqrt{2} < r < r_0$ and so leads to the lasing energy decreasing. In

Fig. 1b the local angular distribution structure in such resonator is shown.

It is possible to avoid of the energy decrease at the divergence minimising if the resonator would be adapted to the concentric one. It is because of the concentric resonator with the spherical aberrated mirrors is the equivalent to the plane resonator with the spherical aberration of the opposite sign. The form of such equivalent resonator mirrors is presented at the Fig. 1c together with the local angular distribution structure. From the Figs. 1 b and c comparison one can see that the local structures of angular distribution are significantly different but its full widths are identical.

When the adaptive mirror compensating as thermal lens as the spherical aberrations one controls the mirror by two independent parameters. In this case the control by each parameter is achieved with limited accuracy. One can choose either of the two parameters for the divergence minimisation leaving the error in compensation of the remaining parameter to be of random value. The sign of this error can be taken for the calculations for the resonator of any form presented at Figs. 1 b and c. This configurations and correspondely the signs and values of the compensation errors for both the parameters can be defined from local angular distribution of the laser radiation (Figs. 1 a,b,c) ($h \leq \lambda/2N$, N – Fresnel number).

The very steep dependence of the local angular distribution on the value of aberration compensation error ($\theta \approx \sqrt{2h/l}$) makes possible to measure this error with

the accuracy sufficient for to realise the lasing at the diffraction limit of the divergence.

The useful feature should be noted for the case when the spherical aberration compensation error $\Delta h_s(\xi)$ is positive. When the inequality takes place as

$k\Delta h_s\left(\frac{M}{2}\right) \leq \frac{(3\pi)^3}{4M^2}$ the ground mode divergence will be close to the diffraction limit, even though the intensity distribution may be close to rectangular form.

4. CONCLUSION

The utility of the opened resonators waveguide theory to the numerical calculation systematisation and to the experimental data analysis was demonstrated with the case of the lasers with the complex form mirrors and with the complex termoptycal aberrations in active medium.

5. REFERENCES

1. A.G.Fox, T.Li, Bell System Techn. Journ., Vol. 40, N2, p.453, (1961).
2. L.A.Vainshtein, "Opened resonators and opened vaweguedes", Moscow, (1966).
3. R.L.Sandersen, W.Streifer, Appl. Opt., Vol.8, p.1229, (1969).
4. A.E.Siegman, A.Miller, Appl. Opt., Vol.9, p.2729, (1970).
5. L.Chen, L.B.Felsen, IEEE Journ. of Quant. Electron. QE-9, N11, (1973).
6. G.N.Vinokurov, V.V.Lyubimov, I.B.Orlova, Optika i spektroskopiya, Vol.34, p.741,(in Russian), (1973).
7. G.N.Vinokurov, V.V.Lyubimov, I.B.Orlova, V.F.Petrov, Techn. digest of the V All-union symposium on diffraction and waves transmittance, Leningrad, p.72, (in Russian), (1971).
8. V.V.Lyubimov, I.B.Orlova, Zhurnal Tekhnicheskoi Fiziki, Vol.39, N12, p.2183, (in Russian), (1969).
9. V.V.Lyubimov, I.B.Orlova, Optika i spektroskopiya, Vol.29, p.581,(in Russian), (1970).
10. R.Martinez-Herrero, P.M.Meijas, N.Hodgson, H.Weber, IEEE Journ. of Quant. Electron., Vol.31, N12, p.2173, (1995).
11. V.V.Lyubimov, Trudy GOI, Vol.58, N192, p.135, (in Russian), (1985).
12. V.V.Lyubimov, Izvestiya AN SSSR, Phis. Series, Vol.51, N8, p.1327, (in Russian), (1987).
13. V.V.Lyubimov, A.A.Tarasov, Kvantovaya elektronika, Vol.14, N2, p.394, (in Russia), (1987).
14. B.A.Ermakov, A.V.Lukin, V.V.Lyubimov, , Optika i spektroskopiya, Vol.38, N4, p.776,(in Russian), (1975).
15. O.B.Danilov, A.P.Zhevlakov, V.V.Lyubimov, Kvantovaya elektronika, Vol.10, N5, p.959, (in Russian), (1983).
16. V.V.Lyubimov, Kvantovaya elektronika, Vol.13, N9, p.1933, (in Russian), (1986).
17. N.Kugler, S.Seidel, IX Conference on Laser Optics, Wn A6-04, St.Petersburg, (1998).
18. S.T.Durmanov et al, IX Conference on Laser Optics, Wn A6-05, St.Petersburg, (1998).

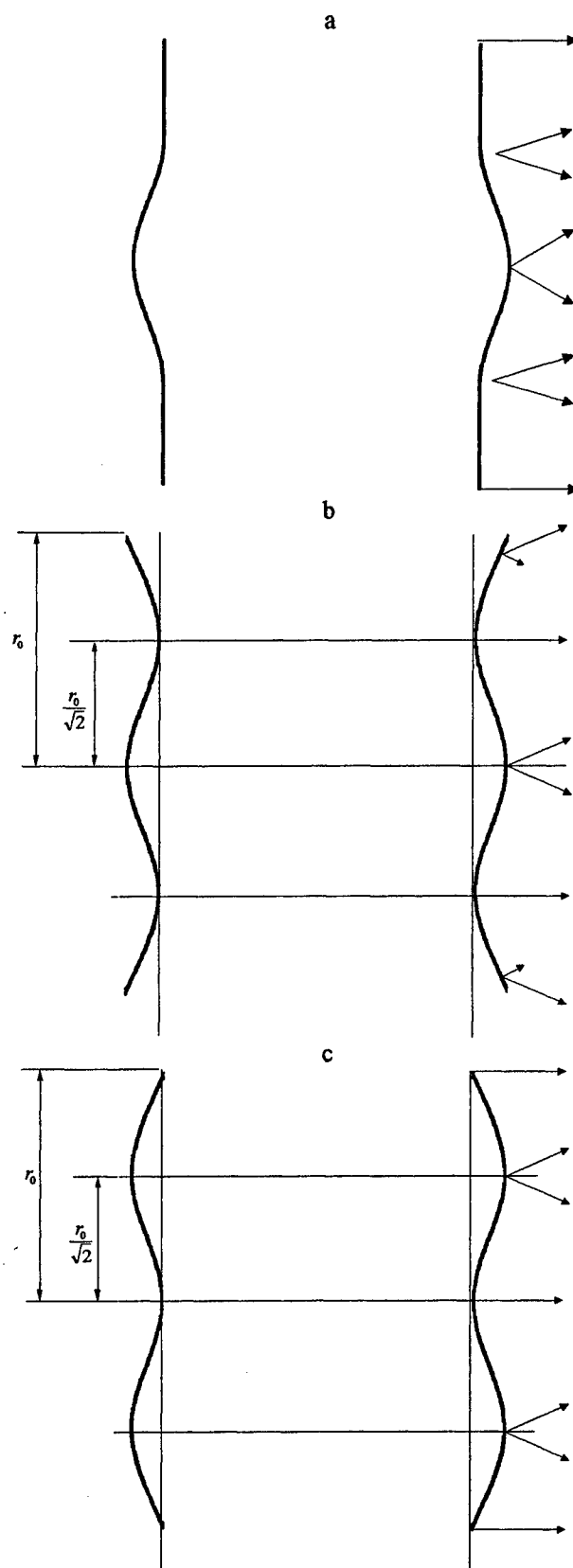


Figure 1. Influence of the total wave aberration on the local angular distribution of laser radiation

High-Power Nd:YAG Laser with Birefringence Compensation and Adaptive HR-Mirror

N. Kugler^a, S. Seidel^a and H. Weber^b

^aLaser- und Medizin-Technologie Berlin gGmbH, Rudower Chaussee 6, D-12489 Berlin

^bOptisches Institut der TU-Berlin, Straße des 17. Juni 135, D-10623 Berlin, Germany

ABSTRACT

In this article we describe an efficient method of the compensation of thermally induced birefringence in high power Nd:YAG rod lasers. Losses at a resonator internal polarizer due to depolarization in the rods are reduced, and a polarized cw laser with an output power of 300 W is realized. Resonators with a small stability range and therefore beam quality near the diffraction limit are introduced. To improve the variability and stability of such resonators an adaptive high reflecting mirror is used as resonator mirror. The maximum average output power of the resonator with adaptive mirror is 145 W at a beam quality of $M^2 \leq 2$.

Key words: Nd:YAG-Laser, Birefringence Compensation, High-Power Laser, Adaptive Mirror, High Brightness.

1. INTRODUCTION

A major goal of laser research is to develop a high-power laser with high beam quality ($M^2 \leq 2$) which operates stable at a variety of output powers. As high power lasers (>100 W) with a beam quality near the diffraction limit require a dynamically stable resonator with a small range of stability the operation regime of such a laser can only be varied by adaptive optics within the resonator. In case of Nd:YAG rod lasers the thermally induced stress birefringence must be compensated if the width of the stability range (in terms of refractive power of the rod) is less than 20 % of the absolute refractive power, otherwise the losses of the resonator increase dramatically. In section 2 our method of birefringence compensation in Nd:YAG rod lasers is described. Hereafter the capability of the compensation scheme to minimize depolarization losses is proved with a high-power polarized cw laser. In the sections 4 to 6 dynamically stable resonators are discussed, an adaptive mirror with a single actuator is characterized and a laser with an adaptive high reflecting mirror is demonstrated.

2. BIREFRINGENCE COMPENSATION

The thermally induced stress birefringence is a limiting factor with regard to polarized output power or fundamental mode output power of Nd:YAG lasers. The stress birefringence in thermally loaded YAG rods causes polarization dependent phase retardation on top of the retardation by the scalar thermal lens and therefore leads to depolarization of a linearly polarized beam in a pumped Nd:YAG rod¹. A polarized top hat beam passing through a thermally loaded Nd:YAG rod is depolarized* to an extend of about 25 %. Additionally the polarization dependent phase retardation is - like the scalar thermal lens - essentially dependent on r^2 , therefore the focal length of the overall thermal lens is also polarization dependent, i.e. it is a bifocusing lens. For Nd:YAG the difference in the refractive power for radially and tangentially polarized light (Fig. 1) is

Correspondence: Nicolas Kugler, Tel.: +49 / 30 / 67053-440; Fax.: +49 / 30 / 67053-440.

* In this context depolarization is defined as part of the power transmitted through the Nd:YAG which is polarized normal to the input beam.

approximately 20%. This results in limitations with regard to the design of stable resonators, because both refractive powers have to be in the limit of stability of the resonator to keep losses small.

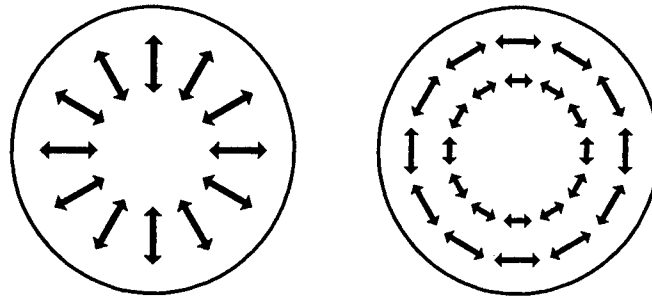


Figure 1. Directions of the field vector \vec{E} for radial (left) and tangential (right) polarized light in the rods coordinate system.

As discussed in Ref. 2 and Ref. 3 in detail the stress induced birefringence in Nd:YAG can be compensated to a great extent when two rods with equal refractive powers are imaged onto each other by a telescope. The distance between the rods and the focal length of the lenses have to be chosen in a way that the principal planes of the thermal lenses are imaged onto each other (Fig. 2). A 90° quartz rotator between the rods swaps amplitude and phase of the radial and the tangential polarization state therefore the polarization dependent phase retardation in the first rod will be compensated in the second rod.

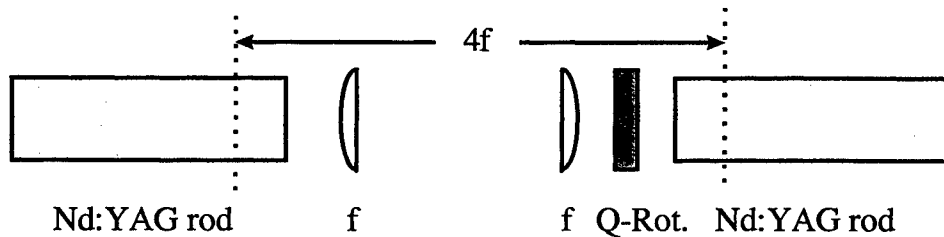


Figure 2. Birefringence compensation scheme with a telescope imaging the principal planes of the thermal lenses onto each other.

For a comparison with the uncompensated situation the quartz rotator was substituted by a quartz glass to preserve the optical path length of the system. Experimental results show that the depolarization of 25% can be reduced to less than 4%. Fig.3 compares the depolarization caused by a system with and without birefringence compensation. In both cases the rods are pumped with a total electrical power of 9.75 kW.

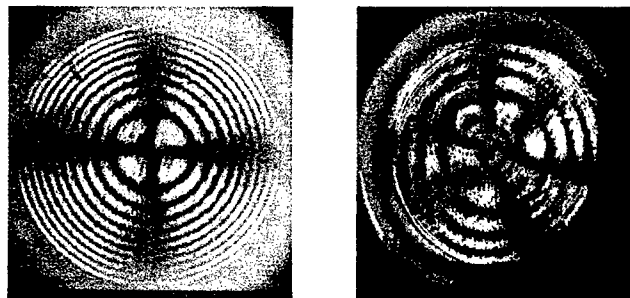


Figure 3. Power transmitted through a thermally loaded two rod system as in Fig. 2 in the middle of a crossed pair of polarizers. Left: without birefringence compensation (quartz glass). Right: with birefringence compensation (90° quartz rotator). The total electrical input power is 9.75 kW in both cases.

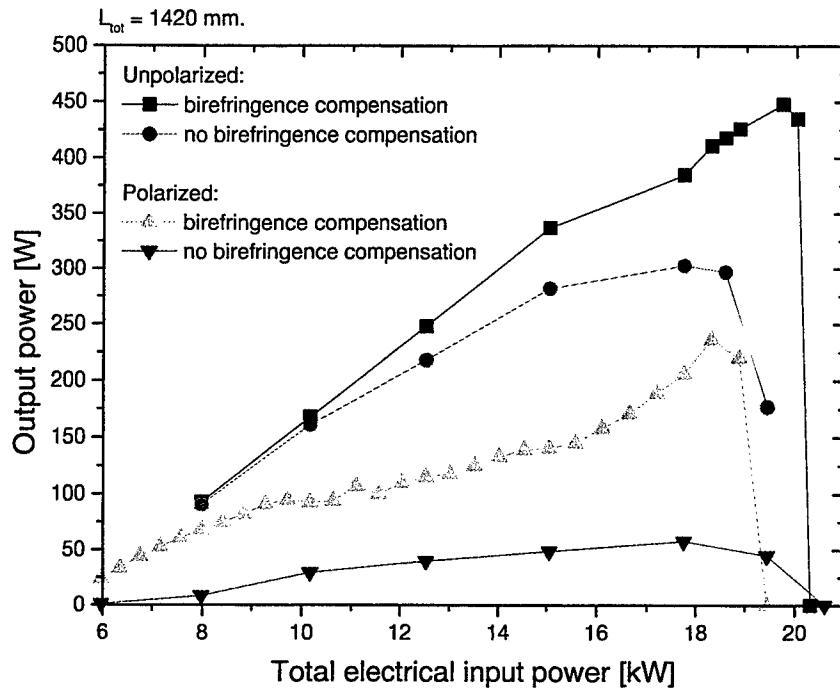


Figure 5. Output power versus total electrical input power in the two rod system with/without birefringence compensation and with/without polarizer.

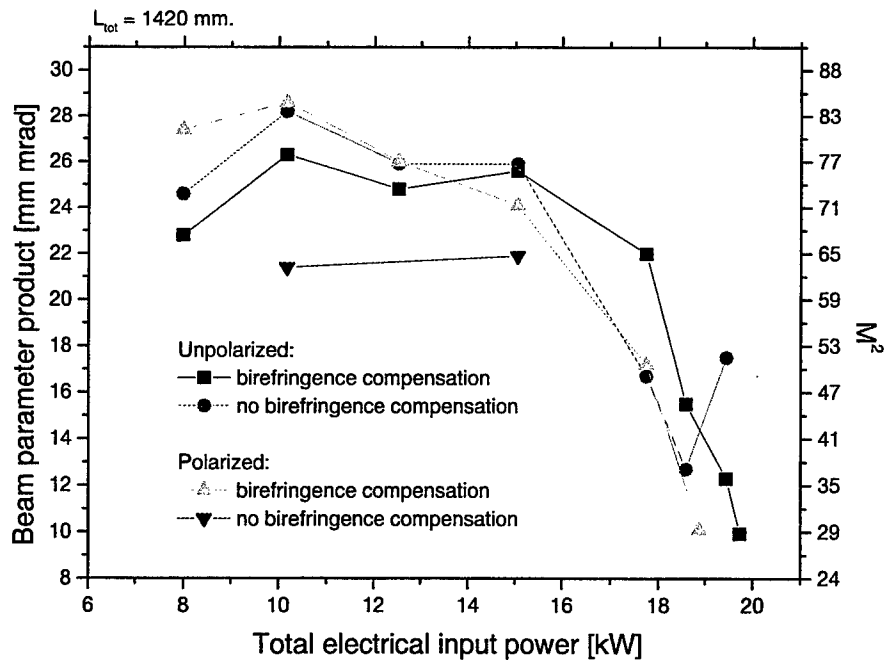


Figure 6. Beam quality versus total electrical input power in the two rod system with/without birefringence compensation and with/without polarizer.

4. DYNAMICALLY STABLE RESONATORS

The beam quality of the symmetric resonator with plane mirrors can be improved by choosing a dynamically stable resonator design⁵⁻⁸. These resonators have a limited range of operation with regard to the refractive power of the thermal lens. The advantage of such lasers is the misalignment insensitivity and the high beam quality at moderate output powers. The beam parameter product $w\theta$ (waist radius times half angle) of a stable resonator has the shape of a parabola with the lowest values occurring at the edges of stability and the maximum in the centre. As long as the limiting aperture in the resonator is given by the rod, the maximum of the beam parameter product is given by⁹⁻¹⁰

$$(w\theta)_{\max} = cr_0^2 \frac{\Delta D}{4} \quad (1)$$

where r_0 is the radius of the rod, ΔD is the width of the stability range in terms of refractive power and c is a constant with $c=1$ if the confocal point of the stability diagram is hit by the resonator, $c=2$ otherwise. To gain a beam quality near the diffraction limit the relative width of the stability range should be in the order of

$$\frac{\Delta D}{D} \approx 3\% \quad (2)$$

where D is the absolute refractive power of the rod. As the difference in the refractive power of radially and tangentially polarized light in pumped Nd:YAG rods is about 20% of its absolute value, it is obvious that such a small stability range can only be realized with a birefringence compensated system. To avoid limitations given by the small range of stability adaptive optics can be used. Two kinds of resonator variations have been investigated:

1. Variation of the position of an internal lens
2. Variation of the radius of curvature of the high-reflecting mirror by an adaptive mirror.

In case of the variable position of the lens the range of input powers at which stable operation can be realized at high beam quality is broad. Fig. 7 shows a sketch of the resonator. The cavities are operated in pulsed mode with a pump pulse duration of $\tau_p=0.5$ ms. The 1.1 at % Nd doped laser rods have a diameter of 9.5 mm and are pumped over a length 156 mm. The distance of the lens L1 to the high reflecting mirror is varied. The focal lengths of the lenses in the resonator are $f_{L1}=30\text{mm}$, $f_{L2}=f_{L3}=f_{L4}=150\text{mm}$ and $f_{L5}=100\text{mm}$. The total length of the resonator is 1.75 m.

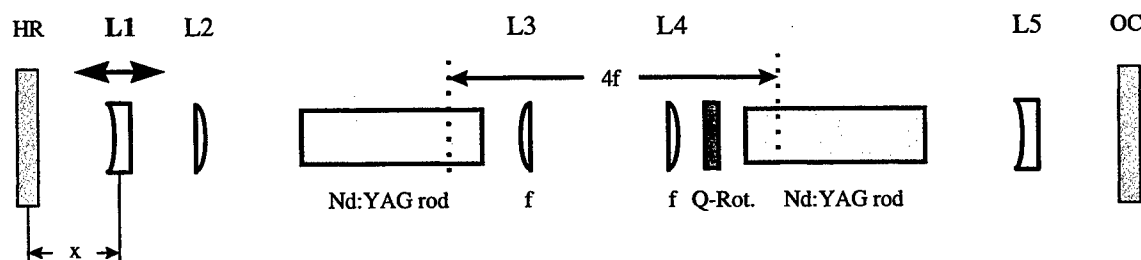


Figure 7. Set-up of a dynamically stable resonator with variable position of the internal lens L1.

In Fig. 8 the output power and the beam parameter product is drawn as a function of the lens position x of lens L1. For each lens position the laser was tuned to maximum output power according to the input power before the beam quality was measured. Due to the small stability range the laser operated approximately in the centre of the stability range. The output power of the laser is tuneable in the range of 40 W to 175 W at a maximum beam parameter product of 1.75 mm mrad ($M^2 \approx 5$). At maximum output power the beam parameter product is 1 mm mrad ($M^2 \approx 2.5$).

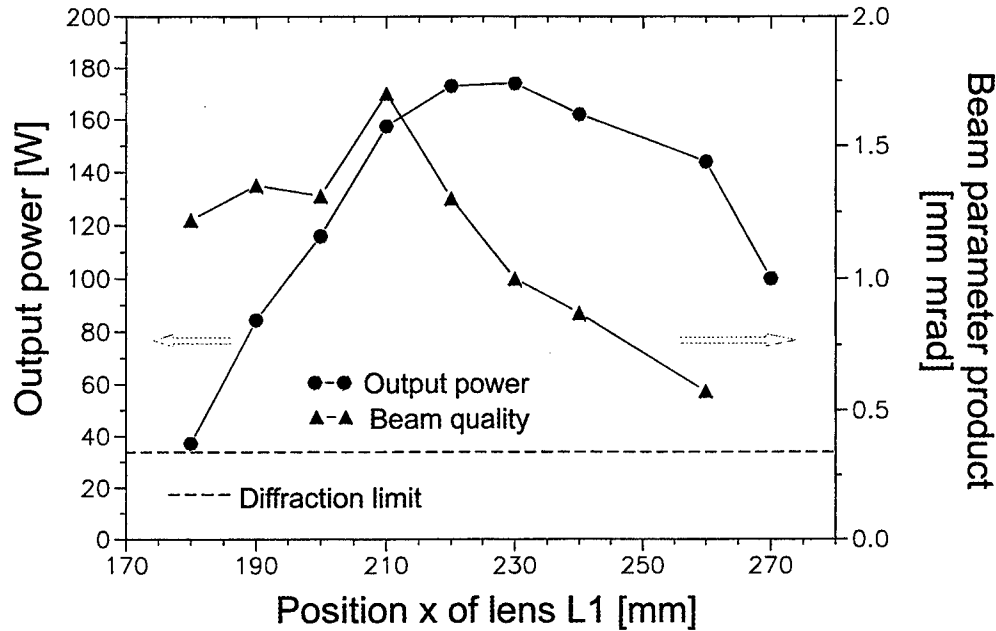


Figure 8. Output power and beam quality of the dynamically stable resonator as a function of the position of the internal lens L1.

5. ADAPTIVE MIRROR

The adaptive mirror consist of a high reflecting coated glass plate with a diameter of 40 mm. The glass plate is fixed at the edge. In the centre of the mirror a piezo-electric actuator bends the plate by an elevation of 40 μm maximum (Fig. 9).

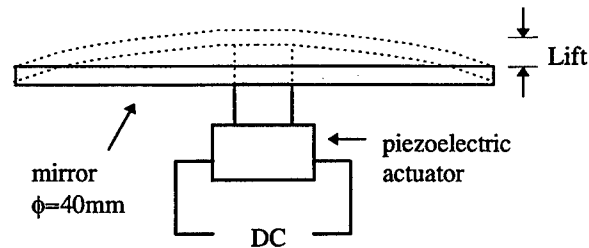


Figure 9. Sketch of the adaptive mirror

The wavefront of a plane wave reflected from the mirror at an elevation of 40 μm is shown in Fig. 10. In the central area of the mirror (diameter of approximately 10 mm) the aberrations are small and the mirror can be regarded as spherical mirror.

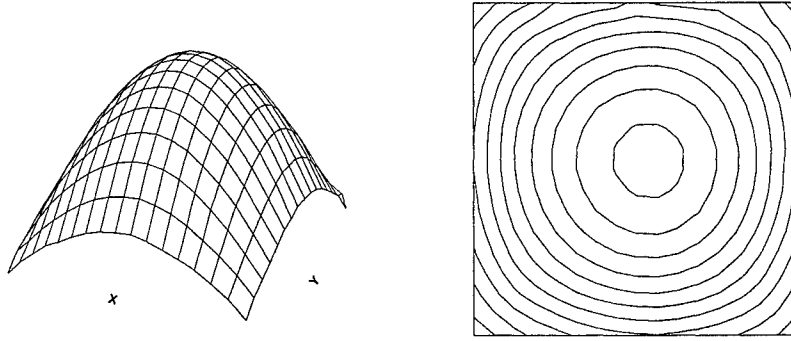


Figure 10. Wavefront of a plane wave reflected from the adaptive mirror at the maximum elevation of the centre of 40 μm .

In Fig. 11 the radius of curvature of an equivalent spherical mirror is plotted as a function of the elevation of the actuator. The radius of curvature of the adaptive mirror can be varied from plane to $\rho=2$ m convex.

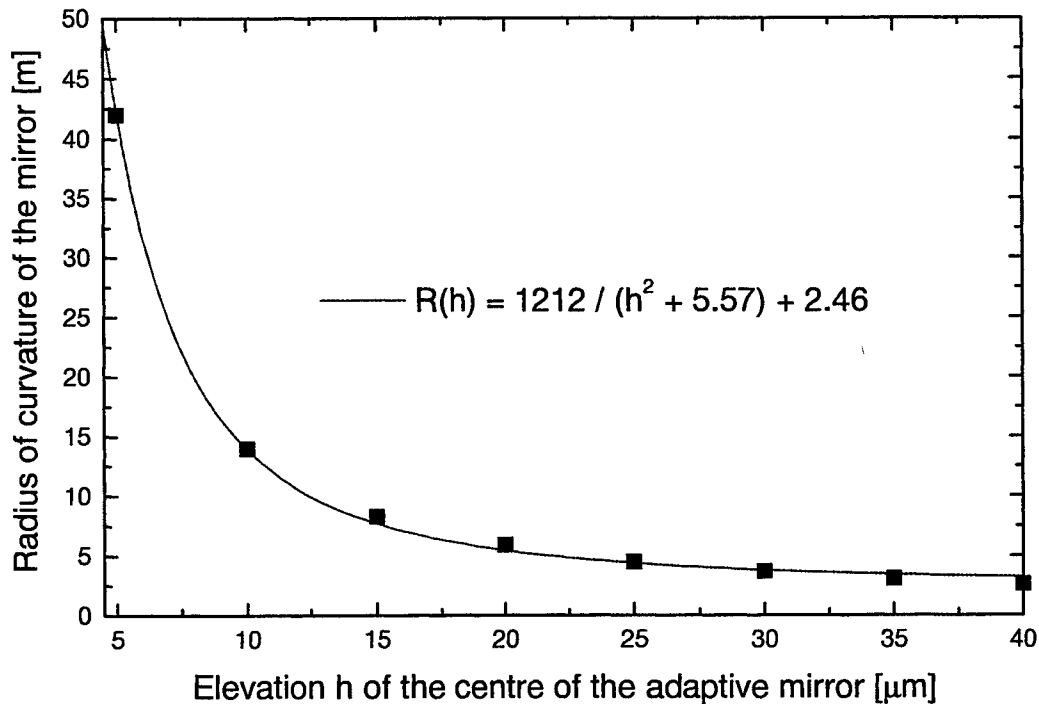


Figure 11. Radius of curvature of the adaptive mirror as a function of the elevation of the actuator.

6. DYNAMICAL STABLE RESONATOR WITH ADAPTIVE MIRROR

To simplify the control of the laser resonator the concept of the variable lens in the resonator is replaced by a resonator design with the adaptive high reflecting mirror described in chapter 5. The two rod system remains unchanged while the Galilei telescope on the side of the HR-mirror in Fig. 7 is replaced but the adaptive mirror. The lens L5 is replaced by a lens with a focal length of $f_L = -30$ mm. The total length of the resonator is reduced to $L_{\text{tot}} = 1.6$ m.

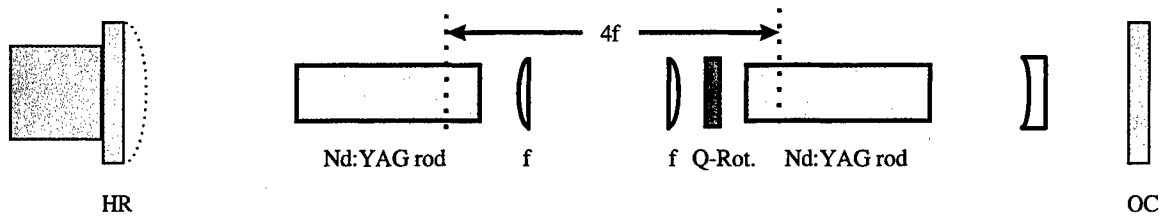


Figure 12. Set-up of the dynamically stable resonator with birefringence compensation and adaptive high reflecting mirror.

Fig. 13 shows the output power and the beam quality of this resonator as a function of the lift of the centre of the adaptive mirror. Four different total electrical input powers are compared. With this resonator an average output power of 145 W at a beam parameter product of 0.6 mm mrad ($M^2 \approx 1.8$) can be realized.

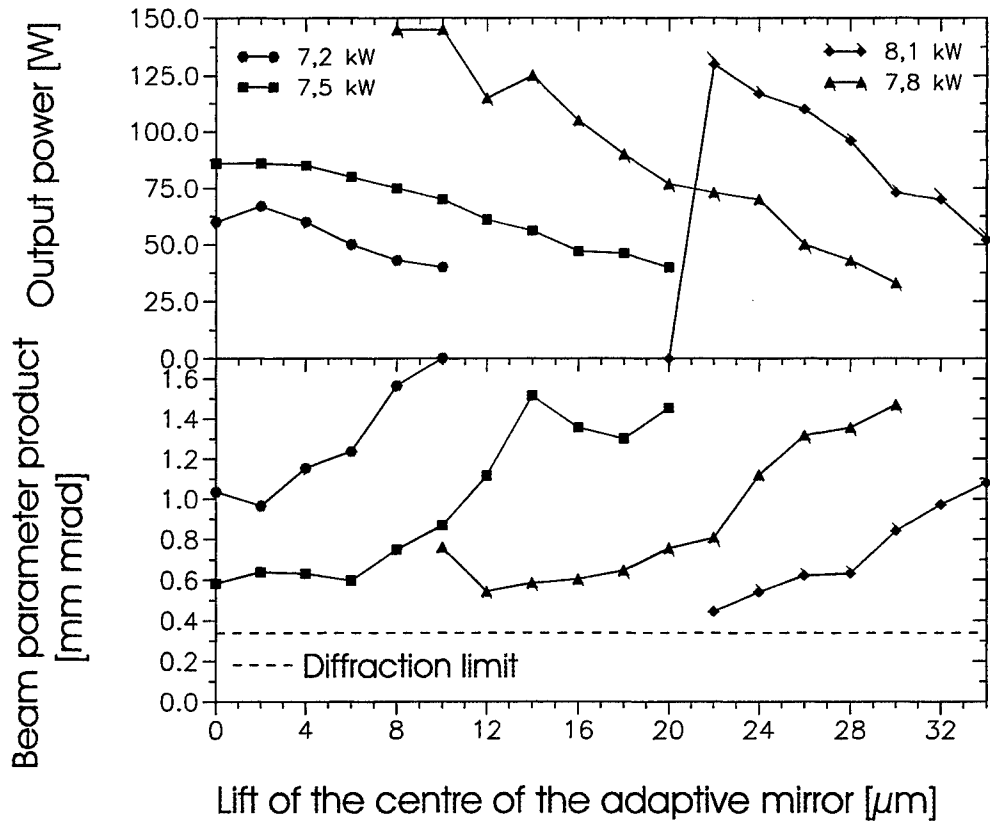


Figure 13. Output power and beam quality of the dynamical stable resonator as a function of the position of the internal lens L1.

7. CONCLUSION

Different resonators with birefringence compensation have been investigated. An output power of 175 W at a beam quality of 1 mm mrad was realized by a resonator with variable internal lens. A resonator with adaptive mirror was designed. The output power of this laser was 145 W at a beam quality of 0.6 mm mrad. For both resonators the compensation of the thermally induced birefringence is necessary.

8. OUTLOOK

To increase the variability of resonator a new mirror concept is investigated. The new mirror is based on SiN and it is fitted with 37 actuators. The mirror will be controlled by a PC which reads the laser parameters, evaluates them and sets the actuators of the mirror accordingly (Fig. 14).

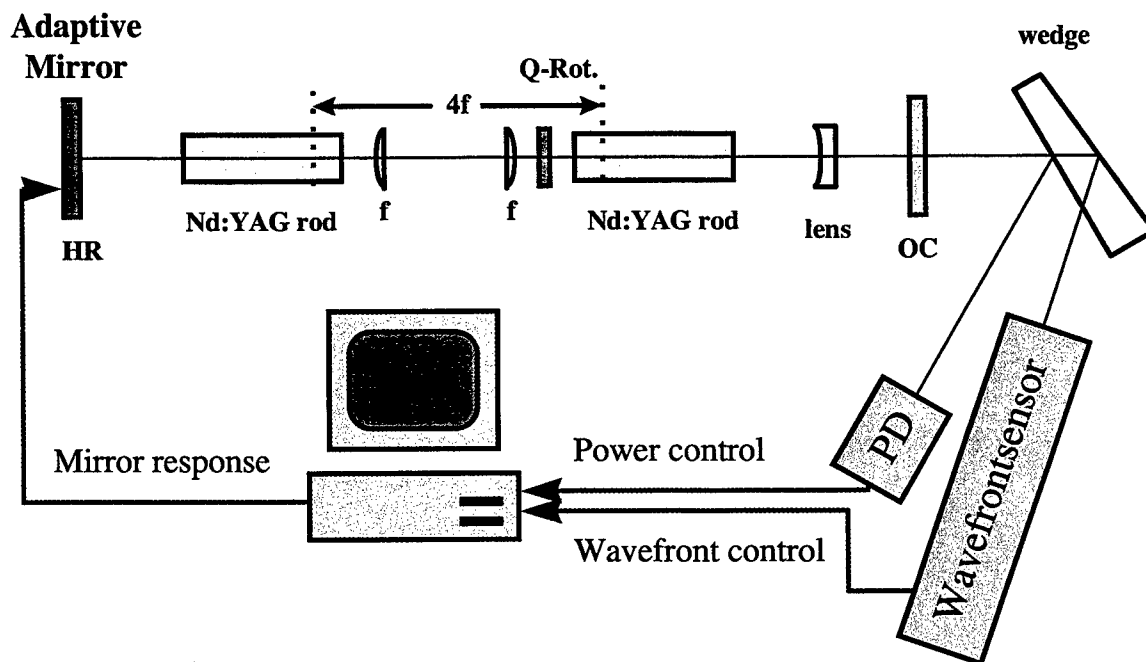


Figure 14. Scheme of a resonator with an adaptive mirror controlled by a PC. The computer reads the beam parameters of the laser and calculates a response function for the mirror.

ACKNOWLEDGEMENTS

This work was partly supported by the European Community within the project LTR 31063 - MOSIS.

REFERENCES

1. W. Koechner, *Solid-State Laser Engineering*, 3rd ed., Springer-Verlag Berlin 1992 (pp.381-400)
2. Q. Lü, N. Kugler, H. Weber, S. Dong, N. Müller and U. Wittrock, „A novel approach for compensation of birefringence in cylindrical Nd:YAG rods“, *Opt. Quant. Electron.*, **Vol. 28**, pp. 57-69, 1996
3. N. Kugler, S. Dong, Q. Lü and H. Weber, „Investigation of the misalignment sensitivity of a birefringence-compensated two-rod Nd:YAG laser system“, *Appl. Opt.*, **Vol. 36**, pp. 9359-9366, 1997
4. S. Seidel and N. Kugler, „Nd:YAG 200-W average-power oscillator-amplifier system with stimulated-Brillouin-scattering phase conjugation and depolarization compensation“, *J. Opt. Soc. Am. B*, **Vol. 14**, pp. 1885-1888, 1997
5. Jürg Steffen, Jean-Pierre Lörtscher and G. Herziger, „Fundamental Mode Radiation With Solid-State Lasers“, *IEEE J. Quantum Electron.*, **Vol. QE-8**, pp. 239-245, 1972
6. D. C. Hanna, C. G. Sawyers and M. A. Yuratich, „Telescopic resonators for large-volume TEM₀₀-mode operation“, *Opt. Quant. Elect.*, **Vol. 13**, pp. 493-507, 1981
7. V. Magni, „Resonators for solid-state lasers with large-volume fundamental mode and high alignment stability“, *Appl. Opt.*, **Vol. 25**, pp. 107-117, 1986
8. G. Cerullo, S. De Silvestri, V. Magni and O. Svelto, „Output power limitations in CW single transverse mode Nd:YAG lasers with a rod of large cross-section“, *Opt. Quant. Electron.*, **Vol. 25**, pp. 489-500, 1993
9. G. Bostanjoglo, R. Dommaschk, Th. Beck and H. Weber, „Stable resonators with variable reflectivity mirrors for multi-kW Nd:YAG lasers“, in *XI International Symposium on Gas Flow and Chemical Lasers and High-Power Laser Conference*, H. J. Baker, ed., *Proc. SPIE* **3092**, pp. 44-47, 1997
10. N. Hodgson and H. Weber, „Influence of Spherical Aberrations of the active Medium on the Performance of Nd:YAG Lasers“, *IEEE J. Quantum. Electron.*, **Vol. QE-29**, pp. 2497-2507, 1993

Compensation of thermo-optical distortions in the active elements of a high power CW Nd:YAG-lasers

S.T. Durmanov, V.V.Lyubimov, Yu.P.Rudnitskiy, G.V.Smirnov -
TRINITI, Troitsk Moscow reg., Russia. E-mail:smirgen@fly.triniti.troitsk.ru
M.A.Kurin, Ya.I.Malashko, A.S.Rumjantsev -
SIC «Systema» Moscow

Abstract

The main purpose of our investigations consists in creation the solid state laser with power ~500 W and high beam quality. The beam quality, as well known [1], is described with parameter M^2 , that characterizes the focusing properties of laser radiation. Notice that the high power technological lasers with lamp pumping have the typical value M^2 from 20 to 100 [2-4]. It could be decreased by means of use the special technical methods of compensation of birefringence [5] and aberrations [6] in the induced thermal lenses of active elements.

Key words: solid state laser, beam quality, M^2 , birefringence, aberrations.

Purpose of investigations

Receiving the output power of the CW Nd:YAG-laser ~500 W with beam quality $M^2 \sim 5$

$$M^2 = (\pi/\lambda) BPP = \pi d_o \Theta / 2\lambda,$$

where $BPP = d_o \Theta / 2$ - beam parameter product,

d_o - output diameter of the laser beam,

Θ - half of divergence angle of the output laser beam

Stages of the work

1. Experimental research of the thermo-optical distortions in the AE Nd:YAG[111]
 $\varnothing 6.3 \times 130$ mm at the pump power up to 13 kW
2. Measurements of the output laser parameters for some resonator schemes
3. Choice of the optimal scheme of the laser resonator with compensation TO-distortions by means of the multisectional adaptive mirror
4. Numerical simulation of the laser generation with the adaptive mirror. Determination the requirements to the adaptive mirror.
5. Investigation of laser properties with the adaptive loop for control of the output beam divergence.

Experimental research of the thermo-optical distortions in the AE Nd:YAG[111] $\varnothing 6.3 \times 130$ mm at the pump power up to 13 kW

For achievement of main goal we was studding the aberration properties of the induced thermooptical lenses in AE Nd:YAG with dimensions $\varnothing 6.3 \times 130$ mm, pumping with two lamps in the double ellipse laser cavity with independent water cooling of AE and lamps (Fig.1). The measurements of the thermo optical properties AE were done in accordance with scheme Fig.2, where the displacement of probe beam in the plane of mat plate was controlled by *Spyricon*-camera in the two orthogonal plane for two polarizations (Fig.2).

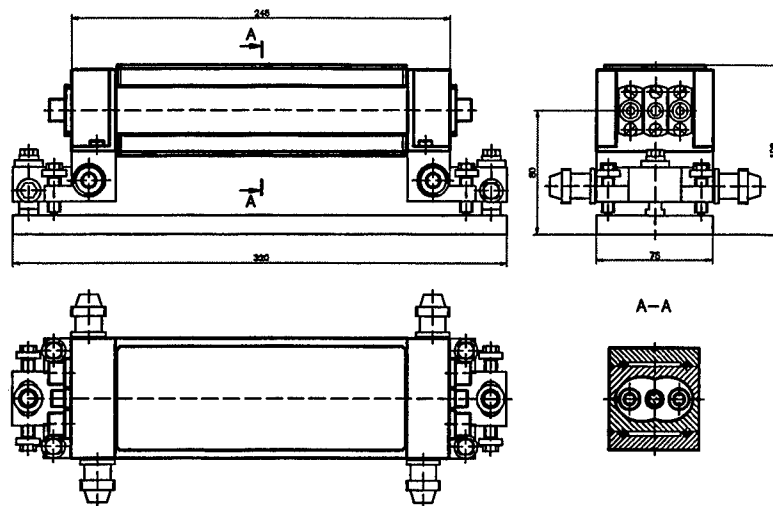


Fig.1. Outside configuration of the two lamps cavity with active element Nd:YAG Ø6.3x130 mm

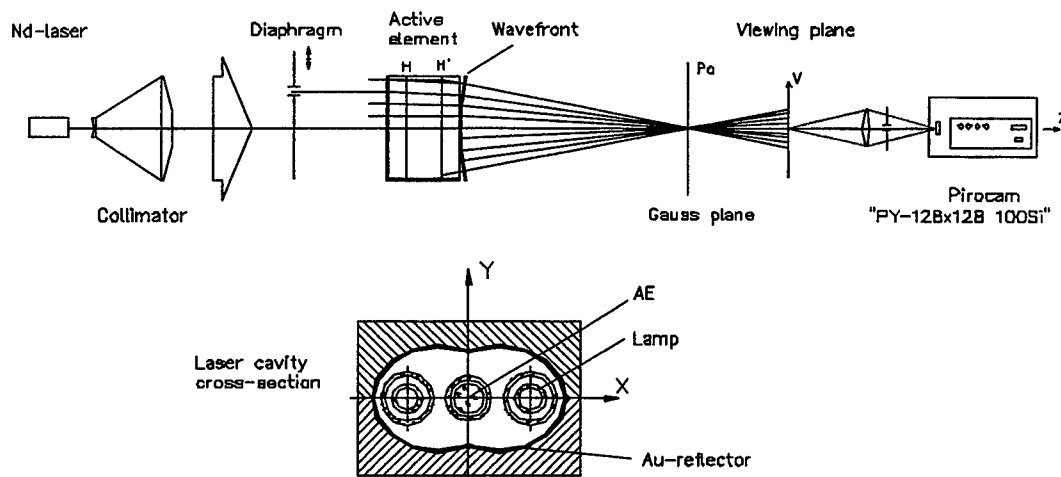


Fig.2. Scheme for the measurement of the geometrical aberrations in the AE Nd:YAG Ø6.3x130 mm

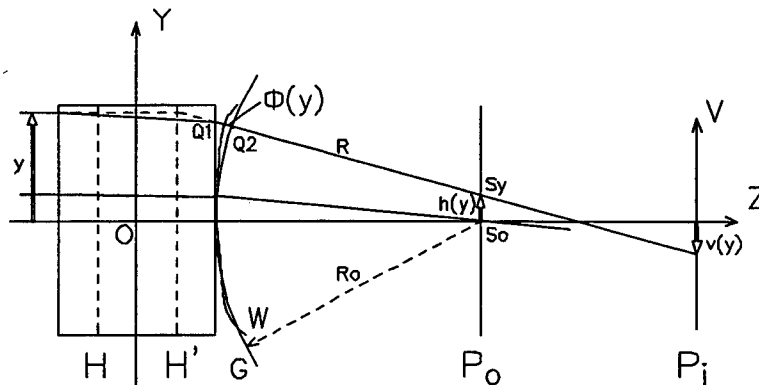


Fig.3. Illustration to the calculation of geometrical $h(y)$ and the wave aberrations $\Phi(y)$ in the AE Nd:YAG Ø6.3x130 mm. $h(y) = R(y) d\Phi(y)/dy$, $R(y) = [Q_2 S_y]$

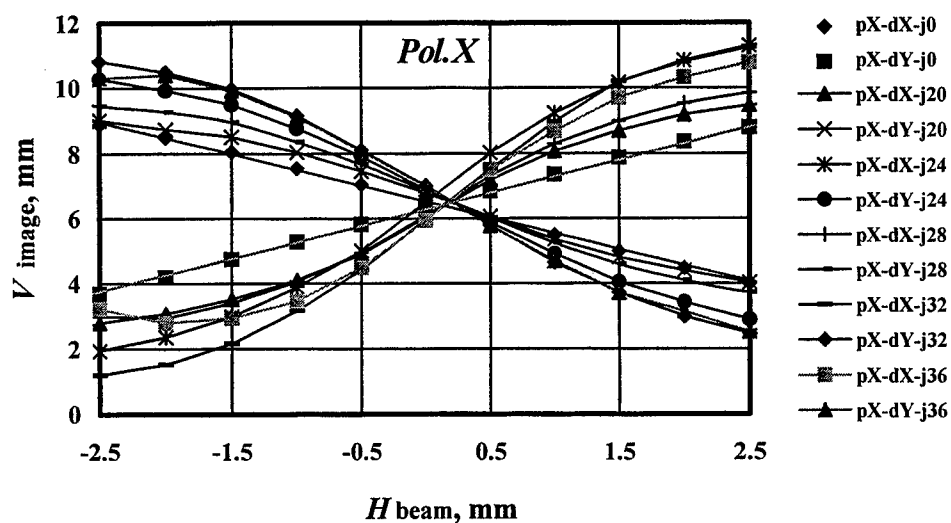


Fig.4. Experimental data of the geometrical aberrations in the viewing plane at the some values of pumping currents. *Beam polarization - horizontal.*

Table 1
Paraxial focuses and wave aberrations of the TO-lenses of the active element for the some pump powers

J, A	P _{pump} , kW	F _{xx} , mm	A _{xx} , μm	F _{xy} , mm	A _{xy} , μm	F _{yx} , mm	A _{yx} , μm	F _{yy} , mm	A _{yy} , μm
20	5.3	171	7.1	221	3.5	214	5.7	217	3.5
24	7.2	137	9.5	173	5.2	149	9.1	142	6.9
28	9.0	102	6.1	126	8.3	114	13.4	109	10.7
32	10.8	81	23.0	99	12.6	92	18.3	87	18.7
36	12.6	72	36.8	82	20.7	73	33.1	72	30.6

F_{ij} - the paraxial focuses of the TO-lens for i-polarization and j- direction

A_{ij} - the amplitude of the wave aberration for i-polarization and j- direction

Table 2
Average data for radial (r) and azimuthal (φ) polarization

J, A	P _{pump} , kW	F _r , mm	F _φ , mm	F _φ /F _r	D _r , 1/m	D _φ , 1/m	A _r , μm	A _φ , μm	A _r /A _φ
20	5.3	194.0	217.5	1.12	5.2	4.6	5.3	4.6	1.15
24	7.2	139.5	161.0	1.15	7.2	6.2	8.2	7.2	1.15
28	9.0	105.5	120.0	1.14	9.5	8.3	13.4	10.8	1.24
32	10.8	84.0	95.5	1.14	11.9	10.5	20.8	15.5	1.35
36	12.6	72.0	77.5	1.08	13.9	12.9	33.7	26.9	1.25

$F_r = (F_{xx} + F_{yy})/2$; $F_\phi = (F_{xy} + F_{yx})/2$;

$A_r = (A_{xx} + A_{yy})/2$; $A_\phi = (A_{xy} + A_{yx})/2$;

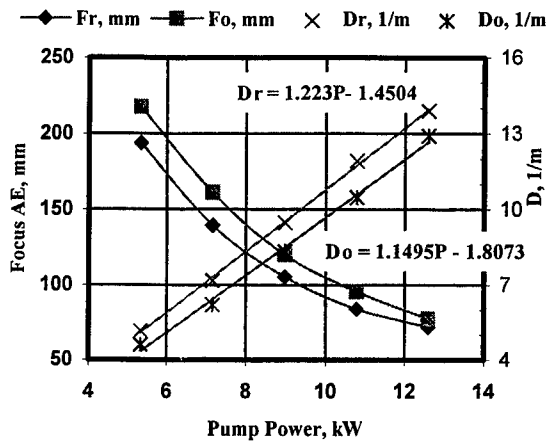


Fig.5. Focuses and optical strengths of AE Nd:YAG[111] $\varnothing 6.3 \times 130$ mm as a function of pump power for radial (r) and azimuthal (φ) polarizations

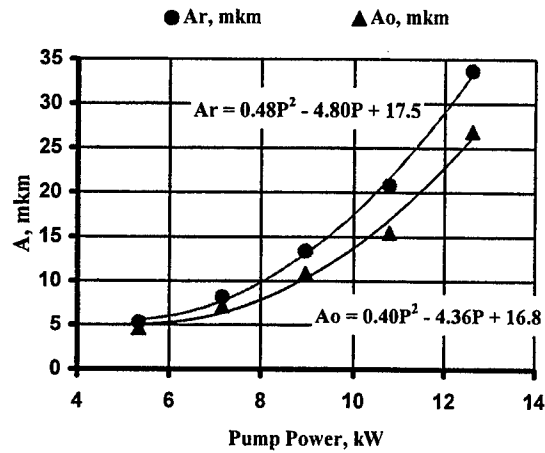


Fig.6. The amplitude of wave aberration $A_s(P)$ in the AE Nd:YAG[111] $\varnothing 6.3 \times 130$ mm as a function of pump power P for radial (r) and azimuthal (φ) polarizations:
 $W_s(r) = A_s(P)(r/R_o)^4, (s=r, \varphi), R_o$ - radius of AE

The Figure 3 illustrates the consistency between the measurement values of high probe beam in viewing plane, transverse spherical aberration in Gauss plane and wave front distortion on relation to base Gauss sphere.

Original data of measurement displacements of probe beam for horizontal polarization are represented on the Figure 4. Here the deflection of points from straight line is a measure of aberration. The Table 1 contents the results of treatment of experimental data for two polarizations, two directions of displacements and some pump power.

The values with parallel vectors of polarization and beam displacements correspond to radial component of polarization and with orthogonal are azimuthal one. This data are presented in the Table 2 and graphically in the fig.5,6.

Measurements of the output laser parameters for some resonator schemes

Figure 7 shows some of studied resonator schemes. The scheme of measurements of the output laser parameters is represented in Figure 8 [1, p.610]. Here the afocal lens system $L1-L2$ transfers the image of output laser mirror in the plane P with scale 1:1 and this image was controlled on the mat plate MP by photodiode matrix (Fig.7A) - in this case it was measured the diameter of laser beam. In case Fig.7A, where the mat plate MP locate in the focal plane of lens $L3$, it was measured the beam divergence.

Dependencies of laser power and beam quality as a function of pump power for some schemes of resonator are shown in the Figures 9-11.

Unfortunately we didn't receive essential improvement the beam parameter M^2 . It means that the more complex compensation schemes for reduction of polarized distortions and spherical aberration in AE must be used.

Now we are going to investigate the scheme of laser is shown in the Figure 12. The changeable negative lenses between the active elements bring the scheme to flat-flat resonator. Adaptive mirror must compensate the wave distortions of TO-lens and the conforming telescope will compensate partially the spherical component of the wave front, incident to the adaptive mirror.

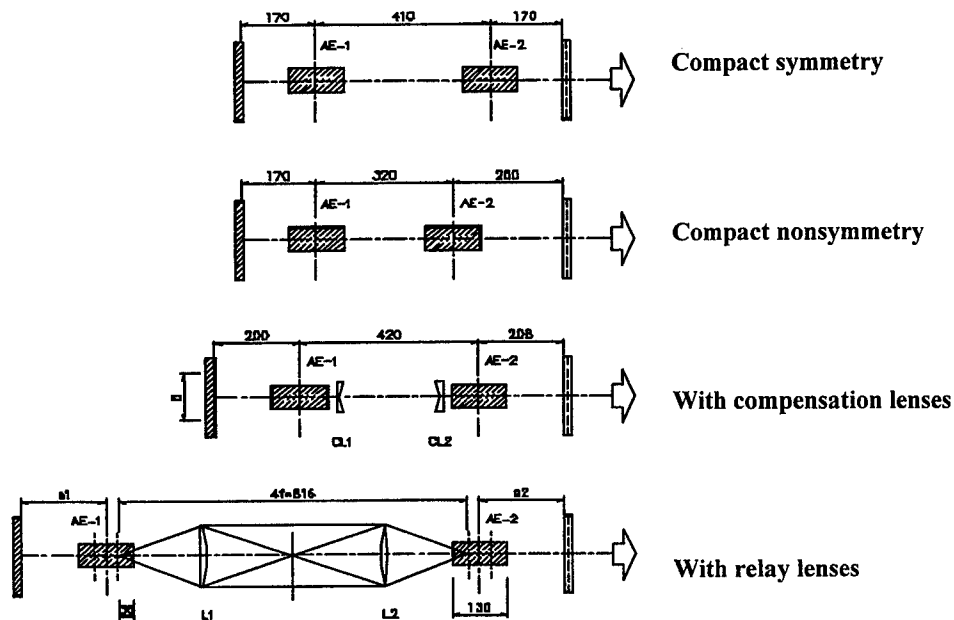


Fig.7. Some of the studied resonator schemes

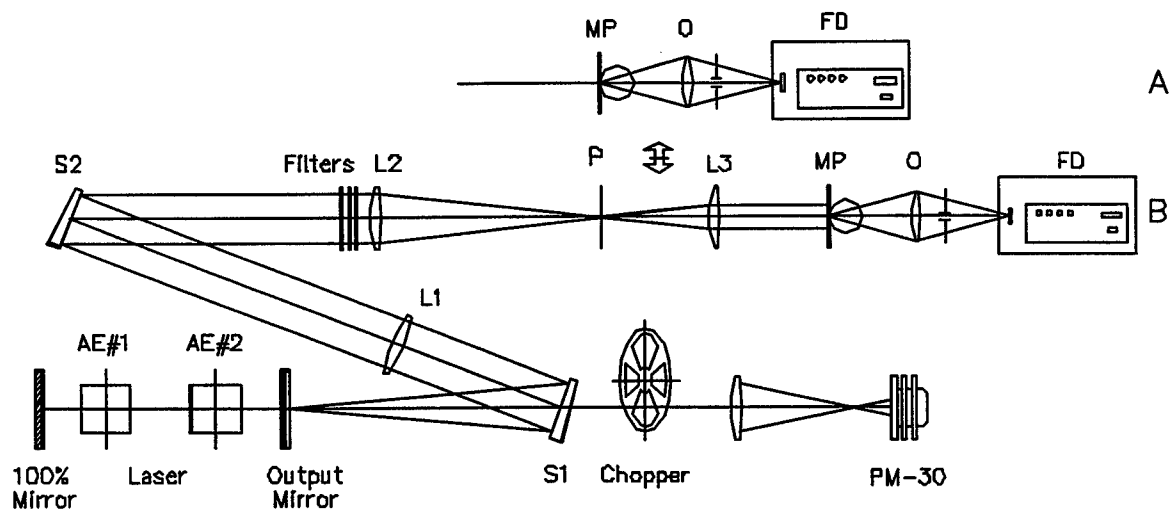


Fig.8. Optical scheme for the measurement of the laser output beam parameters: A - output diameter; B - beam divergence.

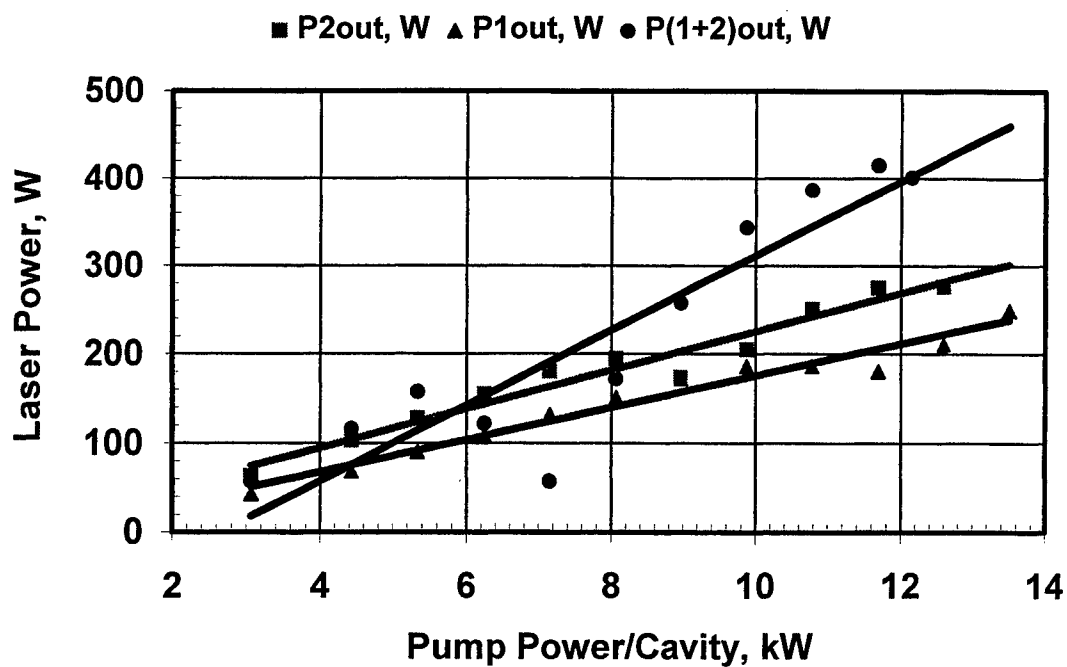


Fig.9. Comparative energy characteristics of laser on the one cavity in compact symmetry resonator ($L=400$ mm, $T=23\%$) and on the two cavities ($L=200+600+290$ mm, $T=38\%$)

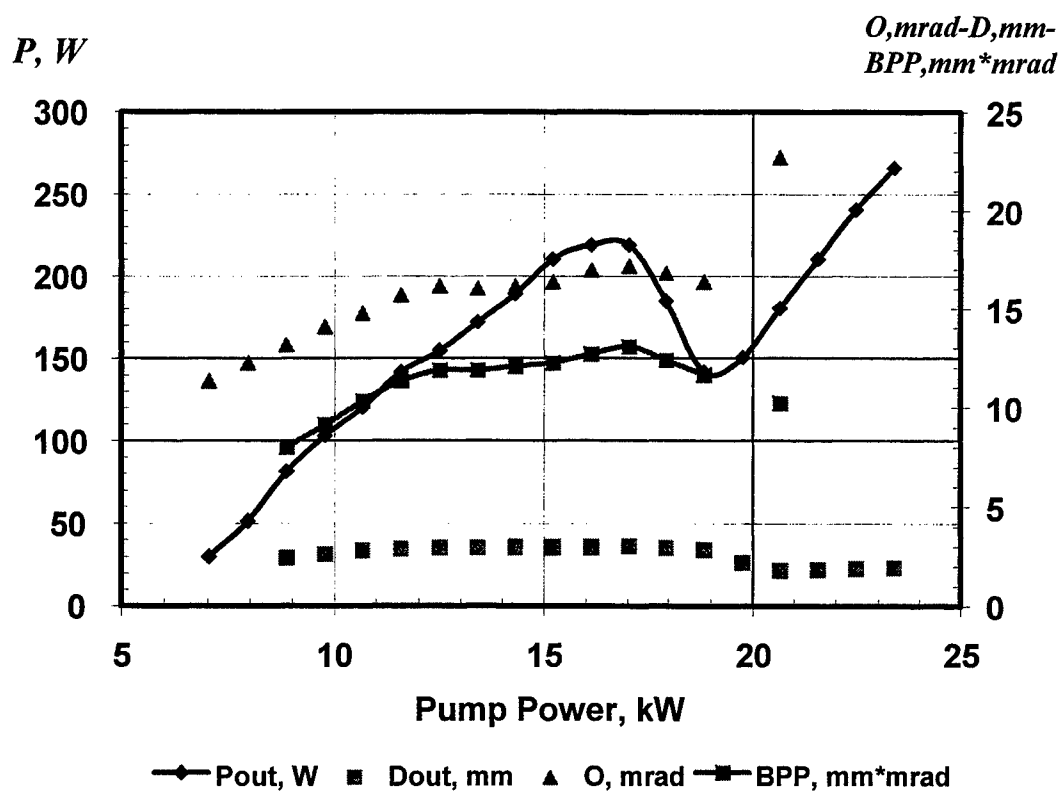


Fig.10. Output parameters of laser with compact symmetry resonator

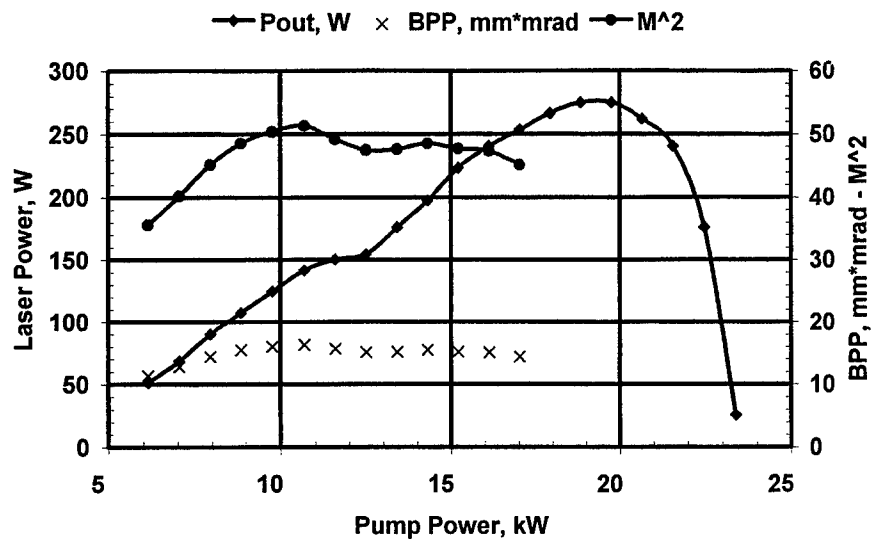


Fig.11. Output parameters of laser resonator with relay lenses

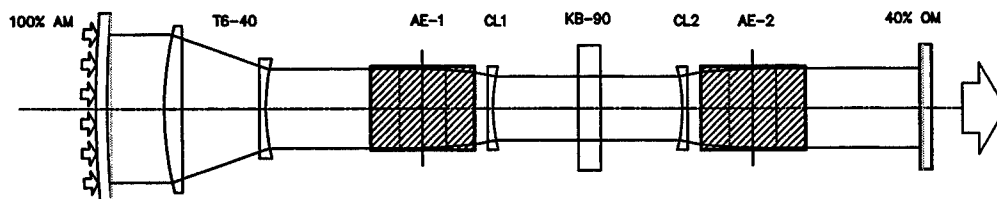


Fig.12. Optical scheme of the laser resonator with the 100%-adaptive mirror: CL - compensation negative lenses, T6-40 - telescope 6^x, AM - correction adaptive mirror.

Conclusions

1. In the studied AE from the crystals Nd:YAG[111] Ø6.3x130 mm in the two lamp cavity at the pump power region up to 13 kW
 - optical strength of the TO-lens achieves to 13 Diopters (for paraxial focus);
 - spherical aberration of the wave front achieves to 30 mm on the edge of the AE;
 - relation of the radial and azimuthal components for TO-lenses is equal to 1.1 and for wave aberrations - 1.2
2. It was received empirical dependencies of the TO-distortions as a function of the pump power
3. Simple schemes of laser resonators with/without spherical compensation lenses inside the resonator don't improve the beam quality considerably (from 30 to 20)
4. It is necessary to compensate the aspherical and polarize components of TO-distortions

Acknowledgment

This work was supported by the International Science and Technology Center under contract #248-96.

Reference

1. N.Hodson and H.Weber, «Optical Resonators», Springer 1997
2. «Laser units for welding and cutting», Product range of HASS-LASER GmbH, Germany 1997
3. «Industrial YAG-lasers», Prospect of Tulamashzavod JSC, Tula, Russia 1997
4. Th.Beck, G.Bostajoglo, K.Richter, H.Weber «Beam Addition of Nd:YAG-High-Power-Lasers», Proc. Of the 6th European Conference on Laser Treatment of Materials (ECLAT'96), Stuttgart 1996
5. N.Kugler and S.Seidel, High power Nd:YAG laser with birefringence compensation and adaptive HR-mirror, IX Conference on Laser Optics, St.Peterburg 1998
6. K.Yasui, Efficient and stable operation of a high-brightness CW 500W Nd:YAG rod laser, Appl.Optics, **36**, 2566-2569 (1996)

The kinetics of laser processes in the multi-cascade optical schemes.

S.G.Grechin^a, member SPIE

E.V.Raevsky^b, V.N.Rojdestvin^a, E.A.Sharandin^a.

^aSRI RL, Bauman Moscow State Technical University, Russia

^bR&DI "POLYUS", Russia

ABSTRACT

The results of investigation and development method for multi-cascade pulsed solid-state lasers optical schemes are represented. The analysis of processes for lasers with active and passive Q-switch was made. It is shown the variation of output laser parameters versus the inter-cascade coupling.

Keywords: laser, multi-cascade laser

1. INTRODUCTION

An important task arising in connection with computation and design of laser systems having solid-state active elements of different types, is to identify the details of physical processes going on in the active medium during population inversion buildup, and to provide an effective energy extraction from the active medium. The purpose of this paper is to provide a comparative analysis of different methods of computational investigation of pulsed solid-state lasers, as well as to identify the factors influencing the power, time, and polarization parameters of the radiation.

For computational modeling of the laser output radiation parameters, nonlinear differential equation systems averaged over the cavity length are commonly used [1] (the "point" model). An oscillator model of such type is widely spread because it needs only a relatively small volume of computational resources to solve the equations. In many cases, a rejection of consideration of partial-derivative equations for the radiation intensities allows, in addition, to obtain the required solution analytically. Using "point" model, one may obtain a relatively good (at least sufficient for the engineering practice) agreement of the output radiation energy calculation results with the experimental data in a wide range of laser parameter variation. But at higher pumping levels, the modeling results show understated values of the output radiation pulsewidths. This is a well-known fact, and it is a principal limitation for such a laser model [1].

A more complete agreement between all the laser radiation parameters may be obtained in models, based on equations of carry and taking into account the real parameters of all optical path components, encounter interaction between amplified radiation flows, the noise buildup in the laser components, as well as the interactions between the laser stages. Because of the imperfection of the laser stage optical components, part of the amplifier radiation returns into the master oscillator causing a variation of its radiation pulse buildup kinetics. By a thorough alignment of the laser components, occurrence is possible of circular closed ray trajectories between the oscillator and amplifier optical com-

Further authors information —

Email: gera@mx.bmstu.ru or shar@mx.bmstu.ru; Telephone: (095) 263-6880; Fax: (095) 333-91-66

ponents. As a result, preconditions arise for a spurious oscillation which in turn may cause a sharp decrease of the stored energy level in the active elements, as well as for their damage at the moment of oscillation in Q-switched lasers. A minor angular misalignment between the amplifier and the oscillator, frequently used in practice, is not always possible - e.g. by using of phase conjugation mirrors in the amplifier path. Particularly important, especially in case of using a harmonic generator at the laser output, are also the polarization characteristics of the radiation.

For these reasons, using of models allowing to analyze and optimize multi-cascade laser systems with an account for the above factors is an actual task important for making the laser design less expensive.

2. THE INVESTIGATION OF MULTI-CASCADE LASERS

The investigation of the output radiation parameter forming in multi-cascade lasers has been made with use of coupling balance system of equations for the power density on all amplification passes (I_i) and gain of active medium (K):

$$\begin{aligned} \pm \frac{\partial I_i(z,t)}{\partial z} + \frac{1}{V} \cdot \frac{\partial I_i(z,t)}{\partial t} &= (K(z,t,\lambda,\theta) - \beta) \cdot I_i(z,t) \\ \frac{dK(z,t,\lambda,\theta)}{dt} &= - \frac{(S+1) \cdot K(z,t,\lambda,\theta) \cdot \sum_{i=1}^4 I_i(t)}{Q_s(\lambda,\theta)} + I_p(t) \cdot G \cdot \eta(I_p) \cdot \chi(\lambda,\theta) \\ &\quad - K(z,t,\lambda,\theta) + \frac{K(z,t,\lambda,\theta) + S \cdot \chi(\lambda,\theta)}{\tau_{ef}(K(z,t,\lambda,\theta))} \end{aligned} \quad (1)$$

where Q_s — the saturation energy density of the active elements ($Q_s = h\nu / \sigma_{21}$),

h — Planck' constant,

ν — frequency of laser radiation,

σ_{21} — radiation cross-section of an active element.

λ — laser wavelength,

θ — angle of rotation around axes,

S — coefficient, which setup the relation between pumping velocity and light power of flash-lamp,

$I_p(t)$ — magnitude of pumping power density,

$\eta(I_p)$ — Efficiency of a flash-lamp in spectral interval of active element absorption,

G — coefficient, which setup the relation between pumping velocity and light power of flash-lamp.

The sign “+” in the first equation used for $i=1,3$, sign “-” for $i=2,4$. The basic feature the considered equation system is that takes into account the active element amplified luminescence caused by the presence of closed ray trajectories within the active element as well as by the amplification of the flash-lamp radiation photons. In [2] it has been proposed to describe the influence of these phenomena as a formal increase of the operation transition upper level decay rate, or as a decrease of its effective lifetime τ_{ef} depending on the inversion grade as well as on the active element geometry:

$$\frac{1}{\tau_{ef}} = \frac{1 + \bar{\xi}}{\tau_{21}} \quad (2)$$

where $\bar{\xi}$ — average number of stimulated transitions at the unit spontaneous transition. The ξ parameter is a function from an active element geometry and level of inversion population.

The anizotropy properties of an active elements are described by the following equation

$$\begin{aligned} \sigma_{21}(\theta) &= \frac{\sigma_{21}(0)}{\sqrt{1 - (1 - M^2) \cdot \sin^2(\theta)}} \\ Q_{sat}(\theta) &= \frac{h\nu}{\sigma_{21}(\theta)} \\ K(\theta) &= \sigma_{21}(\theta) \cdot \Delta \\ \chi(\theta) &= \sigma_{21}(\theta) \cdot n_0 \end{aligned} \quad (3)$$

The generalized dependence of pump spectral efficiency, received on the basis of ordering of numerous experimental dates, was represented in approached empirical kind:

$$\eta(I_p) = \begin{cases} \frac{2}{3} \beta \cdot \exp(1 - \beta) + \frac{1}{3}; & 0 \leq \beta \leq 1 \\ \frac{9 - \beta}{8} & ; \quad 1 \leq \beta \leq 5 \end{cases} \quad (4)$$

where $\beta = I_{sp}/I_0$; $I_0 = 0,15 \text{ MW/cm}^2$ — Effective specific capacity of a lamp in 400-700nm spectral interval.

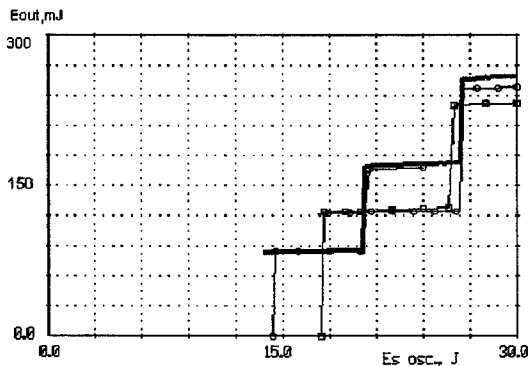


Fig.1. Output radiation energy of a giant-pulse passively Q-switched laser vs. pumping energy. Active element: YAG:Nd³⁺, Ø6.3x65 mm. Q-switch: YAG:Cr³⁺, initial transmission 23% and 46%.

— calculation, —o— experiment.

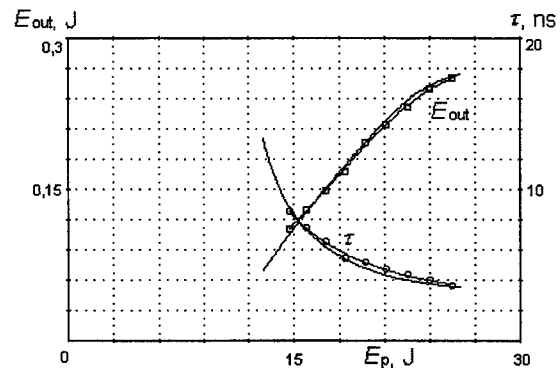


Fig.2. Output radiation energy and pulsewidth of a giant-pulse laser vs. pumping energy. Active element: YAG:Nd³⁺, Ø6.3x80 mm. Cavity: $l_c = 30 \text{ cm}$, $R_{out} = 17.5\%$ — calculation, —o— experiment.

The initial and boundary conditions for this equation system depend on the particular laser optical scheme, and, being very cumbersome, are not presented in this volume-limited paper.

Using the [1] equation system, one may obtain a relatively good agreement of the output radiation energy, temporal and polarization calculation results with the experimental data in a wide range of monopulse laser parameter variation. For illustration, in Fig. 1 the experimental data and calculation results are shown for the output energy of a YAG:Nd laser with passive Q-switching vs. the pumping energy. In Fig. 2 similar dependencies are shown for a giant-pulse laser output energy and pulsewidth. One may see from the plots a good qualitative and quantitative agreement between the calculation results and the experimental data.

Fig.3 illustrates necessity to take into account of interaction between the laser cascades. On this plot computed oscillograms are shown of the radiation pulses generated by a two-stage laser (master oscillator plus a double-pass amplifier). These time dependencies demonstrate an occurrence of a unforeseen oscillation channel between the AM1 - OM1 - OM2 mirrors at the non-fundamental polarization component for the master oscillator. In spite of the relatively high losses (98%) introduced by the radiation polarizes, they are insufficient for compensation of the gain of two subsequently operating active elements. As a result, the master oscillator output radiation has a greater value of depolarization, and the pulsewidth values for the two polarization components are different.

Additional oscillation channels may occur not only after the master oscillator Q-switching, but also during the inversion buildup phase. The result of a spurious oscillation is a freezing of the inversion level in the active elements and, therefore, a decrease of the energy stored in the elements to a level defined by the oscillation threshold. In Fig. 4 computed dependencies are shown of the master oscillator pumping energy corresponding to the spurious oscillation threshold vs. the pumping energy for most frequently used amplifier types. The calculations has been made for a single-mode giant-pulse YAG:Nd³⁺ laser with a Ø5x50 mm active element (an oscillator with a 1.5-mm diameter intracavity aperture and a 30%-reflectivity output mirror) and an amplifier with a Ø6.3x100 mm active element. By calculations, the radiation polarizer contrast ratio has been assumed as equal to 50, the radiation depolarization introduced by the active elements as 0.6%/cm, and the end faces reflectivity as 0.2%. To match the oscillator and amplifier aperture diameters, a matching telescope has been introduced between them.

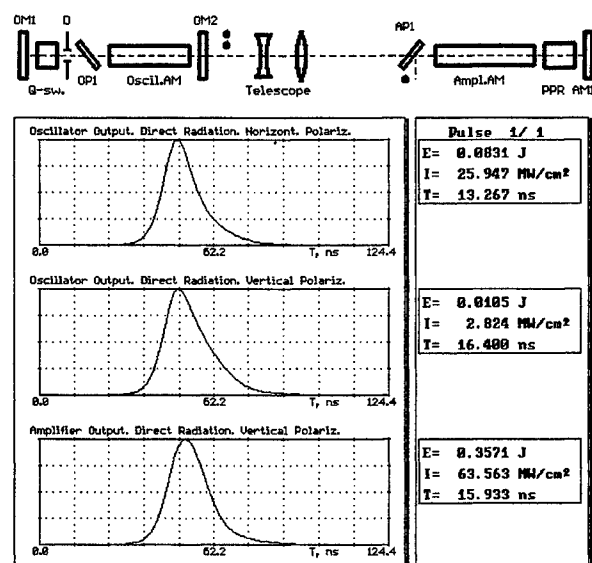


Рис.3. Calculated output radiation pulse oscillograms for a master oscillator / double-pass amplifier laser system.

By calculations, the radiation polarizer contrast ratio has been assumed as equal to 50, the radiation depolarization introduced by the active elements as 0.6%/cm, and the end faces reflectivity as 0.2%. To match the oscillator and amplifier aperture diameters, a matching telescope has been introduced between them.

It can be seen from the presented dependencies that a commonly used double-pass amplifier does not provide high stored population inversion levels in the laser active elements. For the above laser component parameters, at amplifier active element pumping levels higher than 10 J ($KL_{ac} \sim 0.8$) it is not expedient to use an amplifier of such a

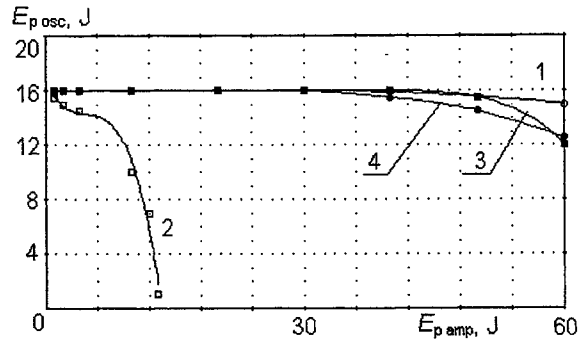


Fig.4. Master oscillator pumping energy corresponding to the starting of spurious oscillation in a giant-pulse laser vs. amplifier pumping energy. 1 - single-pass amplifier, 2 - double-pass amplifier, 3 - double-pass amplifier with an SMBS mirror, 4 - four-pass amplifier with an SMBS mirror.

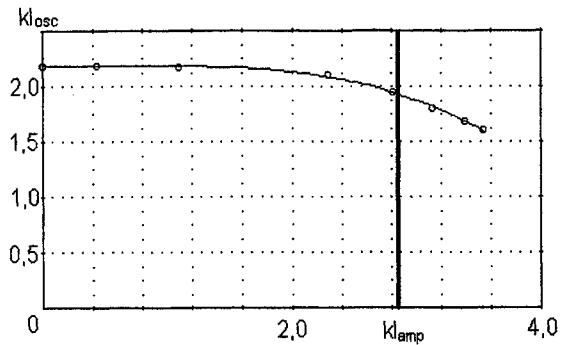


Fig.5. Master oscillator active element gain (at the moment of the radiation pulse buildup starting) vs. active element gain of a double-pass amplifier with an SMBS mirror. The vertical line corresponds to the multi-pulse oscillation starting level.

type. For the other three types of amplifier stages, there is practically no impact of the amplifier on the spurious oscillation starting level up to their element pumping energies of approx. 30 J ($KLac \sim 3.4$).

For passive-Q-switched lasers, for all amplifier types, it is important to take into account their contribution to the total level of noise passing the passive filter. An illustration to this statement is the dependency of the oscillator active element gain by which a radiation pulse generation occurs vs. the gain of a double-pass amplifier with an SMBS mirror (see Fig. 5). The passive filter parameters correspond to a LiF crystal with an initial transmission level of 30% (the other parameters have not been modified). The oscillator pumping energy has been fixed at the 16 J level. It can be seen from the presented dependency that an increase of the amplifier inversion level is leading to a decrease of the oscillator active element threshold gain and, subsequently, to a decrease of its output energy and to an increase of the output radiation pulsewidth. At higher amplifier pumping energy levels, an occurrence of a burst oscillation mode is possible (this level is marked by a vertical line in the figure).

As mentioned before, part of the laser amplifier stage output radiation may return into the master oscillator. Thereby for amplifier stages using phase conjugation mirrors such conditions are not always fulfilled.

In Fig. 6 calculated time dependencies are shown of the output radiation pulse of a double-pass amplifier with an SMBS mirror, exited by single-mode oscillator. The oscillator is optimized for a maximum output energy ($E=13\text{mJ}$, $\tau_{0,5}=13.5\text{ns}$); it is intended thereby that there is no amplifier impact on the oscillator. The middle dependency in Fig. 6 corresponds to the part of the oscillator output energy turned back into the oscillator, which is more than twice its input energy. It is obvious that such a large amount of energy returned into the oscillator will affect the oscillator output radiation pulse parameters as well as the radiation parameters of the laser in general, which is illustrated by Fig. 8. By the computational modeling, the distance between the oscillator and the amplifier has been, for better demonstration, taken equal to 4 m. Attention should be paid to the value of radiation energy passing through the oscillator active element output face (see the second from top plot in Fig. 8): it is more than 50 mJ. Taking into account the intracavity aperture

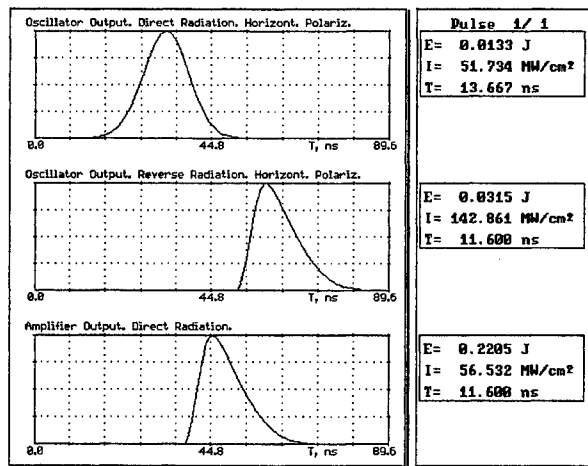


Fig.6. Oscillograms of the radiation pulse at the output of a double-pass amplifier with an SMBS mirror; of the excitation pulse; and of the radiation returned into the oscillator.

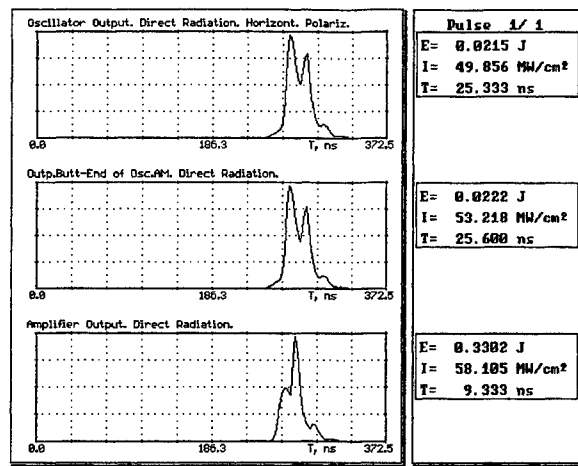


Fig.7. Radiation pulse oscillograms by a combined operation of an oscillator and a double-pass amplifier with an SMBS mirror after a combined optimization of the oscillator and amplifier.

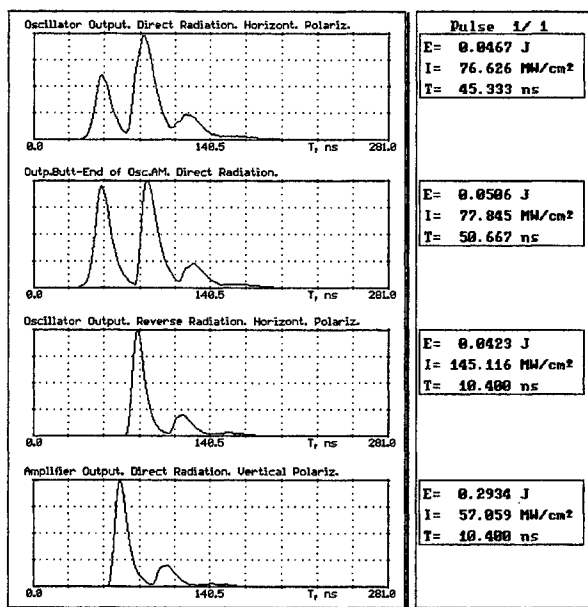


Fig.8. Radiation pulse oscillograms by a combined operation of an oscillator and a double-pass amplifier with an SMBS mirror.

diameter selected for the modeling (1.5 mm), this value corresponds to an averaged over the cross-section energy density of approx. 3 J/cm², which is more than the typical value of the active element optical damage threshold.

The above shows that by designing multi-cascade laser systems it is necessary to take into account the interactions between stages. Usually for reduction of influence of inter-cascade coupling is used optical outcome schemes between cascade. However the necessary effect can achieve by optimization of such lasers as a whole instead of stage by stage. For illustration of the made statement, in Fig. 7 oscillograms are shown of radiation pulses for the above considered laser scheme after a minor modification of the optical layout parameters. Thereby a goal has been set to maximize the output energy, taking into account the maximum limits of energy density of the radiation passing through the active elements. To achieve this, it has been

necessary to decrease the master oscillator output mirror reflectivity by 10% as well as the oscillator pumping energy (to 8 J instead of 16 J), and to increase the amplifier pumping energy from 30 to 36 J. This modification of the system parameters has allowed to increase the laser output energy approx. by 10% while using a slightly less total pumping energy, providing the active elements operation at relatively safe energy density levels.

3. CONCLUSIONS

The laser model used in the given work taking into account the real parameters of all optical path components, encounter interaction between amplified radiation flows, the noise buildup in the laser components and the interactions between the laser stages of the permits with high accuracy to receive agreement with the experimental data of energy, temporal and polarization calculation parameters for multi-cascade monopulse lasers.

The influence of noise properties of the most widespread of laser amplifier schemes on output radiation of master oscillator with active and passive Q-Switch is shown.

The necessity of multi-cascade lasers optimization as a whole instead of stage by stage for achieve of maximum efficiency and for facilitation of its optical elements working modes is shown.

4. REFERENCES

1. A.L. Mikaelyan, M.L. Ter-Mikaelyan, Yu.G. Turkov. "Solid-State Optical Generators", Moscow, Sov. Radio, 1967
2. Yu.A. Ananyev, A.A. Mac, B.M. Sedov. JETP, v. 48, 1965, p.7.
3. A.S. Doynikov. "Spectral Characteristics of Radiation of Tubular Xenon Flashlamps and Arc Lamps". Electronics Reviews, "Vacuum and Gas Discharge Devices" series, Moscow, Central SRI ELEKTRONIKA, 1973, issue 11
4. Optically Dense Active Media. — Moscow: Nauka, 1990. — ISDN 5-02-000774-9
5. A.N. Alpatyev, V.A. Smirnov, I.A. Scherbakov. Preprint N 99, Institute for General Physics of the Russian Academy of Sciences, Moscow, 1990
6. A.A.Mac, L.N. Soms, V.A. Fromsel, V.E. Yashin. "Neodiminm Glass Lasers". Moscow: Nauka, 1990, p.86

*** All the theoretical research has been made with use of the **LID-PSSL** Program Package developed for investigation and development of solid-state lasers.

Feedback Timing Approach to the Pulse Energy Stabilisation in the Actively Mode Locked Laser

V.A.Zaporozhchenko

B.I.Stepanov Institute of Physics Academy of Sciences

F.Skaryna Ave., 68, Minsk 220602, Belarus

Tel.: (017)284-10-23, Fax: (017)284-08-79, E-mail: vzap@dragon.bas-net.by.

ABSTRACT

A high reproducibility of the feedback stabilised prelude dynamics in the actively mode locked and Q-switched laser is shown experimentally. The reliable generation of 65-70 ps pulses with 1 mJ energy at the relative root-mean-square deviation 0.6% is achieved due to the feedback-assisted timing to prelude signal of all cavity Q-control events.

1. INTRODUCTION.

Recent progress both in the femtosecond laser development and diode-pumped laser technology have resulted in almost total displacement of the interest to the actively mode-locked and Q-switched solid-state lasers with flashlamp pumping. Nevertheless such lasers for the present remain the most powerful and less expensive sources of ultrashort light pulses. The basic limitation on pulse duration restricts of course their scope in time-resolved spectroscopy but they can be successfully used as a pumping sources for nonlinear frequency converters, tuneable lasers, and amplifiers of femtosecond pulses. In these fields of applications their main disadvantage in view of contemporary requirements is the relatively high level of fluctuations for amplitude and temporal output pulse characteristics. These fluctuations arise both from the imperfect stability of flashlamp power supply and basic instabilities of intracavity unsteady-state pulse formation.

The most promising approach to the solution of stabilisation problem is based on the two-step ultrashort pulse formation with negative feedback control of laser oscillations on the initial prelude stage¹. Earlier we have shown the reliable bandwidth-limited pulse formation in such conditions with high reproducibility of output parameters². The relative root-mean-square deviation of pulse energy in that experiment was about 2%. Having the objective to improve the laser amplitude stability we have studied the feedback-stabilised prelude dynamics to find the cause of this quite high residual fluctuations.

2. EXPERIMENTAL LASER ARRANGEMENT.

Laser cavity (see fig.1) was formed by the concave ($r=250$ cm) and plane highly reflecting mirrors and contained Nd:YAG laser crystal, $\varnothing 4 \times 65$ mm, mode-locker, thin-film polarizer and two DKDP electrooptic crystals for the cavity Q-control and cavity dumping. The acousto-optic standing wave modulator used as mode-locker was driven with a 30 W power 150 μ s rf-pulse which was formed by the rf-shaping amplifier. Its carrier frequency was obtained by halving the 99.62000 MHz frequency of reference oscillator. The modulator was thermally stabilised (to within 0.2 °C) to maintain its acoustic resonance in the coincidence with rf-pulse carrier frequency. Q-control electronics including high-voltage commutator, feedback signal amplifier and fast avalanche photo-diode have been incorporated with electro-optic crystal and polarizer in single opto-electronic unit with small enough clearance dimensions (bounded with dashed line in fig.1). A rise time of feedback amplifier response was ≈ 5 ns that is less than the cavity roundtrip period (10ns) and fall time was in the range of 30-50 ns. The similar incorporation of electro-optic crystal with high-voltage commutator have been made for the cavity dumper.

Output pulse formation in laser shown in fig.1 includes three steps of cavity Q-control. On the first step a prelude oscillations start at high level of cavity losses provided by an initial bias voltage (≈ 2 kV) applied to an electro-optic Q-control switch which doubles as a fast Q-control device included in the negative feedback loop maintaining the quasi-steady-state behaviour of prelude oscillations. In this feedback loop the optical signal coupled out from the cavity with polarizer due to a presence of dc-bias on the electro-optic crystal is detected by fast avalanche photo-diode which output electrical signal after amplification changes the crystal bias voltage and suppress the rise of intracavity laser oscillations above certain self-consistent level.

After a prelude oscillations reached a quasi-steady-state behaviour resulting in formation of bandwidth-limited ultrashort optical pulse with a reproducible smooth shape cavity Q-switching is produced by means of high-voltage

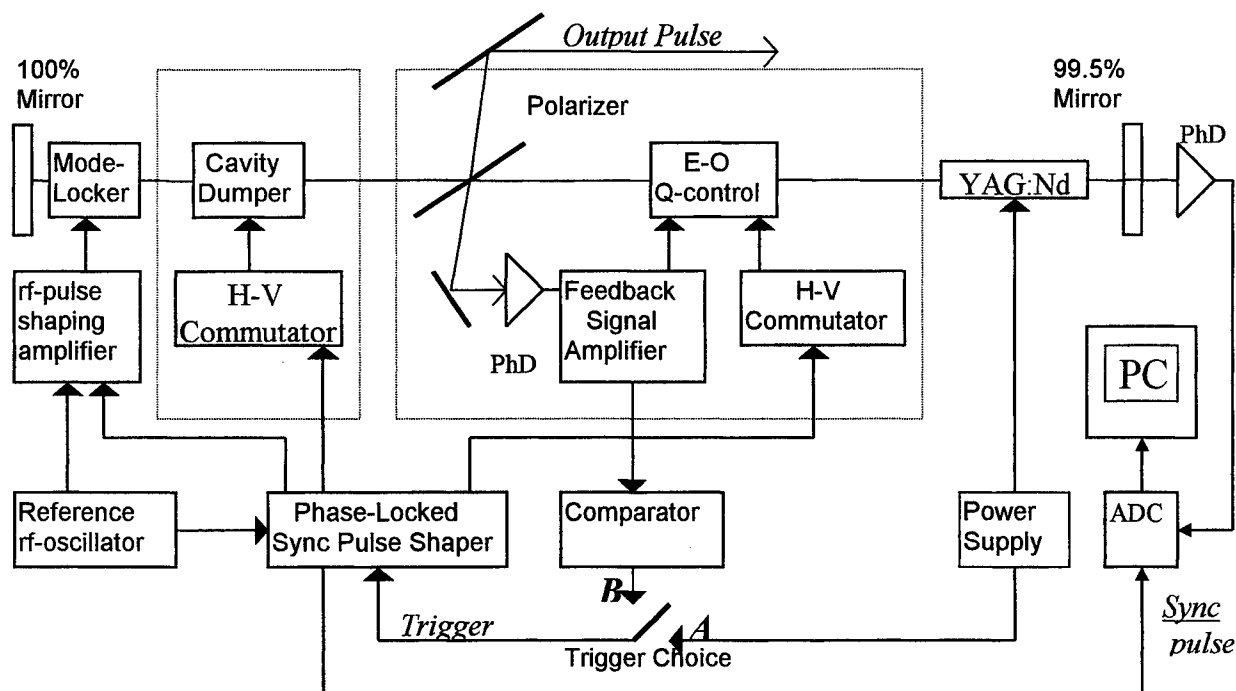


Fig. 1. Schematic diagram of laser circuit.

commutator which reset the crystal bias voltage into zero. The second step of pulse formation is characterised by a fast amplification of optical pulse proceeding in «closed» cavity. Pulse intensity maximum is usually achieved after 15÷20 roundtrips (depends on initial cavity losses). At this instant of time shaped and amplified pulse is extracted from laser cavity via cavity dumping caused by applying of quarter-wave voltage to the second electrooptic crystal.

All Q-control events in laser: mode locking rf-pulse, Q-switching and cavity dumping were monitored by the sync pulse shaper which provided the triggering pulses for the rf-pulse shaping amplifier, two high-voltage commutators and data acquisition electronics. This pulse shaper is a multichannel timer phase-locked to the signal of reference frequency and keeping time in the cavity roundtrip units. Usually, it is triggered by a sync pulse from flashlamp power supply or provide triggering pulse to it (in fig.1 switch of trigger choice in A position). In both these cases the count of time begins simultaneously with pump pulse.

According to described procedure of output ultrashort pulse formation in laser under investigation it is clear that output pulse energy depends on the prelude pulse energy at the instant of Q-switching. Thus the amplitude stability of laser output pulse will correspond to the prelude one being higher that of prelude due to the saturation of amplification in a laser active media.

3. RESULTS AND DISCUSSION.

To study the laser prelude dynamics and its reproducibility the digital oscilloscopic system was made on the basis of CAMAC 8-bit 20 MHz analog-to-digital converter (ADC) and personal computer. It provided the opportunity of prelude envelope recording with the temporal resolution of 50 ns and corresponding statistical data processing. A measurements were fulfilled without Q-switching and cavity dumping to avoid interrupting of a quasi-steady-state prelude oscillations. In fig.2a typical single-scan record is shown. Because of restricted temporal resolution of ADC shown value W of recorded detector signal corresponds to the intracavity ultrashort pulse energy averaged over 5 cavity roundtrips. It is seen that quasi-cw laser operation manifest certain amplitude oscillations arising from the restricted frequency bandwidth, amplification coefficient and dynamic range of real feedback loop. The spectrum and period of these oscillations is dependent on the mentioned loop parameters, laser amplification coefficient and pump rate. As the result the picture obtained at the statistical averaging of

prelase envelope $\langle W \rangle$ over 100 laser shots (fig.2b) is smoothen in comparison with single-scan one and the relative root-mean-square deviation of prelase signal amplitude $\varepsilon = 100\% \sqrt{\langle (W - \langle W \rangle)^2 \rangle} / \langle W \rangle$ is usually in the range of $(5 \div 10)\%$ (see fig.2c).

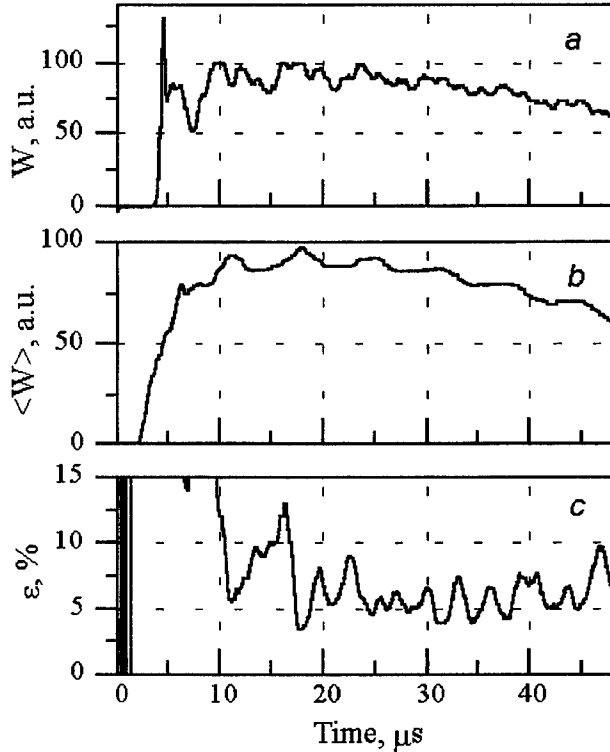


Fig.2. Oscillograms of prelase envelope: single scan - *a* and averaged - *b* ; *c* - standard deviation.

with the period of low depth oscillations of prelase envelope shown in fig.2a the averaging procedure resulted both in smoothing picture and high statistical fluctuations.

On the next step the reproducibility of prelase dynamics have been analysed. For this purpose a simulation of comparator had been included in the data processing procedure and jitter effect was removed by software before statistical averaging. Results are shown in fig.3. It is seen that obtained averaged prelase envelope in fig.3a repeat the single-scan picture (fig.2a) practically in all details. A root-mean-square deviation of prelase amplitude after initial 10μs transient span of time falls down to 2% level. This result can be considered as the evidence of high reproducibility of laser dynamics in the presence of negative feedback loop and suggests a method of additional stabilisation of laser amplitude parameters.

The simplest approach to improve the laser amplitude stability by using a high reproducibility of prelase dynamics

Earlier we have shown³ that 1% fluctuations of pump energy gives rise to 2.5 μs jitter of the prelase envelope. In the present digital oscilloscopic measurements the computer program was used which simulated the operation of fast comparator with adjustable threshold. It provided the opportunity to measure a jitter of prelase starting moment and the results obtained were in good agreement with that of³. Since a jitter value is comparable

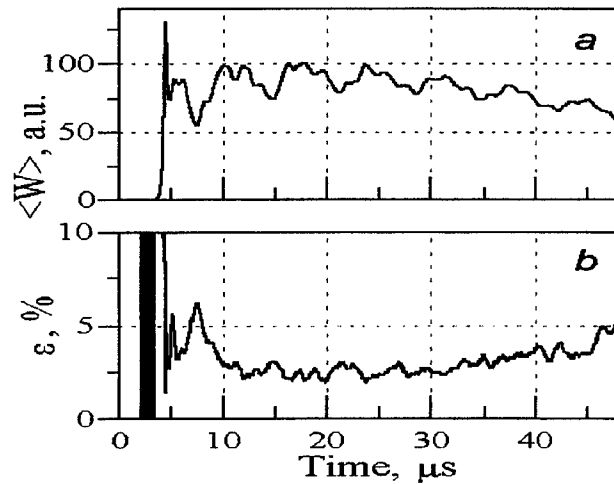


Fig.3. Averaged prelase envelope - *a* and corresponding standard deviation - *b* after jitter removing via data processing.

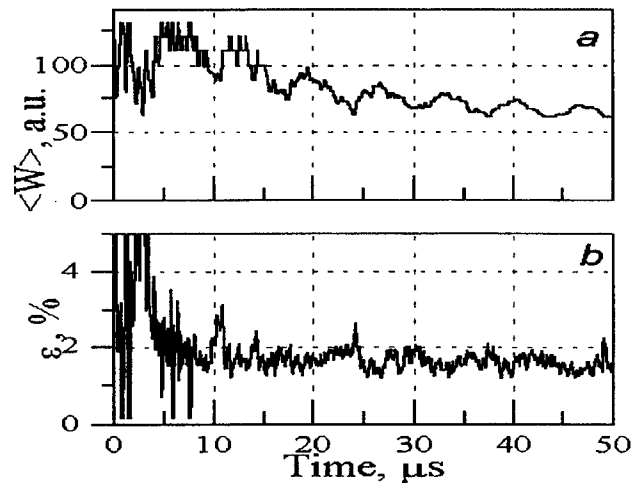


Fig.4. Averaged prelase envelope at jitter removed via comparator timing - *a* and standard deviation - *b*.

consists in the conversion of comparator action simulated in software into the laser hardware. Such fast operating prelate signal discriminator with variable threshold had been designed and included in the laser Q-control circuit. It have closed the additional feedback loop (switch of trigger choice in fig.1 in position B) providing a timing of all cavity Q-control events to the prelate starting moment. The analysing input of comparator is terminated to the control output of feedback signal amplifier and it generates a pulse triggering the sync pulse shaper. At such termination a time count begins from the origin of prelate oscillations providing the reliable timing of a Q-control clock to the prelate dynamics.

Fig.4a demonstrates a prelate envelope obtained by procedure provides the additional stabilisation of prelate dynamics because removes the influence of an imperfection of the straight averaging of records over 100 laser shots and displays the dynamic oscillations of envelope without any distinct smoothing. Its beginning differ from that shown in fig.2a because of the transient acousto-optic mode-locker behaviour on the initial stage of intracavity laser oscillations growth. (In this feedback-assisted timing configuration the trigger of rf-pulse shaper can't be done earlier of prelate origin.) It should be noticed that this feature of new arrangement of Q-controlled mode-locker resonance tuning via synchronisation of the possible rf-pulse envelope beats to the prelate origin. As the result the observed relative root-mean-square deviation of prelate amplitude (see fig.4b) is suppressed down to value of $\approx 1.5\%$ lower that we could obtained by using a software comparator in the experimental data processing (compare to fig.3b).

The final measurements of the laser output pulse characteristics have been fulfilled at the $33\mu\text{s}$ Q-switching delay past a moment of the prelate origin. The cavity dumper was triggered after 18 cavity roundtrip cycles of amplification in «closed» cavity when the maximum of the ultrashort pulse energy had been attained. The mean value of output pulse energy was 1 mJ and the probability distribution obtained from the multichannel analysis of 1000 laser shots is presented in fig.5. The shown distribution corresponds to the relative root-mean-square deviation 0.6% that is at least three times better that obtained without the feedback assisted timing to prelate dynamics. Ultrashort pulse duration have been measured by the autocorrelation method using noncollinear second harmonic generation mechanism in I-type frequency doubling KDP crystal. Experimental points have been obtained by averaging over 50 laser shots and standard deviation of the autocorrelation signal was in the range of 1% that is the evidence of high pulse duration stability. The best Gaussian fit to obtained autocorrelation function corresponded to 62 ps pulse duration.

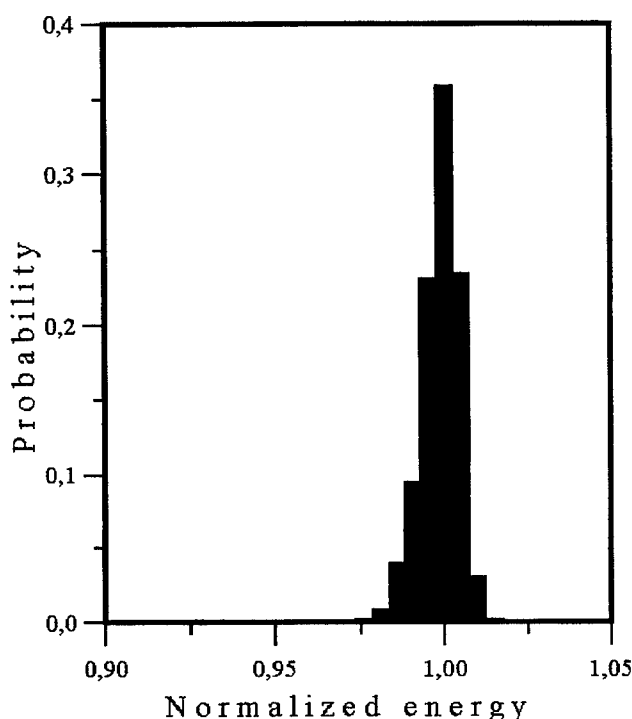


Fig.5. Probability distribution of the output pulse energy.

4. ACKNOWLEDGEMENTS.

Author is grateful for the support of this work in frame of ISTS project B-078-97.

5. REFERENCES.

1. B.Luther-Davies, «An electro-optically Q-switched actively mode-locked Nd:YLF laser with feedback stabilized pre-lase», Opt. Commun., Vol. 57, pp. 345-349, 1986.
2. V.A.Zaporozhchenko, A.V.Kachinskii, I.V.Pilipovich, N.A.Tyletz, «Stabilization of USP parameters in a pulsed actively mode-locked negative-feedback YAG:Nd laser», Sov. J. Quantum Electron., Vol.20, pp.46-47, 1990.
3. V.A.Zaporozhchenko, I.V.Pilipovich, N.A.Tyletz, «Stabilization of the USP timing and duration in an actively mode-locked YAG:Nd laser», Sov. J. Quantum Electron., Vol. 21, pp.1091-1096, 1991.

SESSION 5

Laser Components

Liquid Crystal Modulators with improved laser damage resistance

Fedor L. Vladimirov, Nina I. Pletneva, Ivan E. Morichev
State Optical Institute, 12 Birjevaja linija, St.Petersburg, 199034, Russia
E-mail: vlv@fl.spb.ru

Leonid N. Soms, Vasiliy P. Pokrovskiy
Institute of Laser Physics, 12 Birjevaja linija, St.Petersburg, 199034, Russia

Experimental results have been given on laser-damage resistance of the liquid crystal modulator with longitudinal operating electrical field. It was shown that laser-damage resistance of the modulator is limited by the ITO transparent electrodes and equals $2.5 - 2.9 \text{ J/cm}^2$ at 1.06 nm , $\tau = 15 \text{ ns}$. To improve this parameter we proposed an liquid crystal structure controlled by a transverse electric field in which the ITO electrodes are removed out of the zone intense laser radiation. The main characteristics of this mode liquid crystal modulator are discussed.

Keywords: liquid crystal modulator, laser-damage resistance

Laser damage resistance of Liquid Crystal Modulators with longitudinal operating electrical field

Liquid Crystal Modulators (LCM) are well known and used in a wide range of optical systems. Usually the LCM consists of a number of thin film layers sandwiched between two glass substrates. Transparent electrodes are deposited on the inner surfaces of the glass plates. Initial orientation of the liquid crystal (LC) molecules is determined by alignment layers deposited on transparent electrodes. The thickness of the LC layer is defined by a dielectric spacer. Electro-optical properties of LC layer are controlled by a longitudinal electric field. Light to be modulated passes through all layers of the LCM. Main characteristics of the LCM are:

- maximum modulation frequency;
- speed of response;
- contrast ratio;
- transmission in dark state;
- transmission in light state;
- laser damage resistance.

The last parameter is extremely important in applications of the LCM involving high power laser systems.

We tested laser damage resistance of twisted nematic LCM and its elements: glass substrates, ITO transparent electrodes, alignment and LC layers. We conducted laser interaction experiments using focused output beam a single-mode single frequency Q-switched YAG:Nd laser. Output energy was varied from 15 to 40 mJ, pulse duration was 15 ns, repetition rate - 3 Hz. Special feature of our testing method was use of a probe beam of auxiliary He-Ne laser to visualize damages (Fig. 1). Shlieren picture of tested spot was

observed on a screen. The criterion of laser damage was either optical distortions of the probe beam or laser-induced breakdown. The reference sample of polished glass (K-8) substrate was used for the calibration of laser energy density.

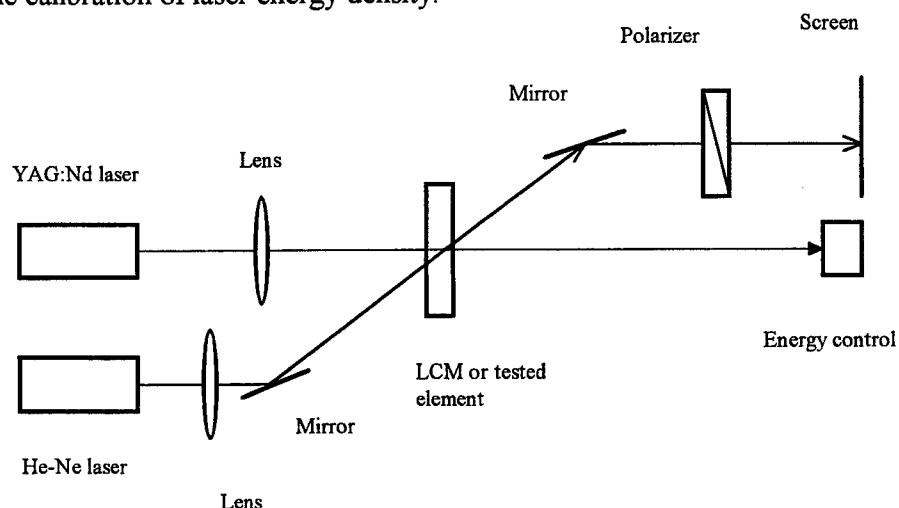


Fig. 1. Experimental setup for measurement of laser-damage resistance.

Table 1. Laser-damage resistance of the LC modulators and its elements.

LC modulator elements	Laser-damage resistance at wavelength 1.06 mcrn and impulse duration 15 ns, J/cm ²
Glass substrate, K-8	> 16.0
Liquid crystal layer $\Delta n = 0.22$; $\Delta \epsilon = + 12.0$; $\Delta t = 0 - 59$ °C	> 16.0
Alignment layer, GeO, d = 300 °A Oblique vacuum deposition	6.9
ITO transparent electrode, cathode sputtering, 90% In ₂ O ₃ + 10 % SnO ₂ , Conductivity - 200 Ω/□	2.5 - 2.9
LC modulator with longitudinal electric field	2.5 - 2.9
LC modulator with transverse electric field	6.7 - 6.9

The results of laser-damage tests are given in Table 1. Glass plates and LC materials based on cyanobiphenyls do not limit laser-damage resistance of the LCMs. Laser-damage threshold of alignment layers was slightly less then 6.9 J/cm². These layers were prepared by resistive vacuum evaporation of GeO. It was found that this value depends on the

conditions of the vacuum process and the thickness of the layer. Transparent ITO electrodes were prepared by standard technological process of cathode sputtering in glow discharge in atmosphere of Ar and O₂. The ITO layers have minimal laser-damage resistance of : 2.9 J/cm². It seems that the reason for the damage was thermal heating owing to absorption of the laser radiation by small metal particles or admixtures. The laser-damage resistance of LC cells tested was about the same. Damage in the LCM was displayed by the formation of gas bubbles. Near the damage threshold we observed dissolution of these gas bubbles. We believe that this reversible process was caused by local heating of the LC material near the ITO layers by absorbed laser radiation. Further increasing laser energy density results in the appearance of indissoluble gas bubbles, degradation of the LC materials and the formation of carbonaceous residues. Laser damage threshold of LC cells tested was 2.5 - 2.9 J/cm². This energy density corresponds to the appearance of dissoluble gas bubbles.

It is obvious that this laser-damage resistance does not meet the requirements of some laser systems and optical devices.

Electro-Optical Characteristics and Laser Damage Resistance of the Liquid Crystal Modulator with Transverse Operating Electric Field

To improve the laser-damage resistance we propose a new LCM structure in which the ITO electrodes are removed out of the zone of intensive laser radiation. In this structure the optical properties of the LC layer are controlled by a transverse electric field.

The LCM configuration is shown in Fig.2. The electrodes are made as thin strip from ITO. The transparent strip electrodes are deposited on one glass substrate only. The other side of the LC layer is limited by a glass substrate without electrodes. Both inner surfaces of

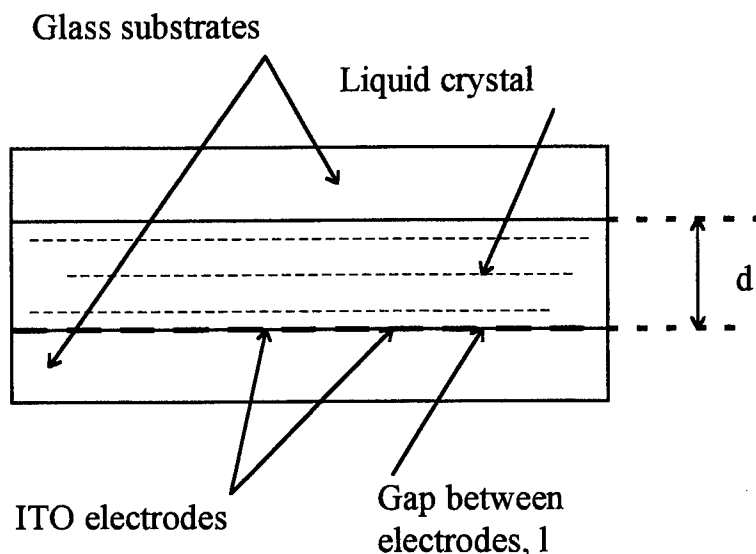


Fig. 2. The LCM configuration with transverse operating electric field.

the glass plates are coated with alignment layers. As alignment layers we used oblique evaporated GeO with thickness 200 - 300 Å. The control voltage is applied to two neighboring electrodes. The laser beam to be modulated passes through the gap between them. We studied the electro-optical properties of the LCMs with two initial alignment of LC molecules (Fig.3):

- homogeneous orientation of LC molecules along the electrodes direction (S-structure);
- twisted structure (T-structure).

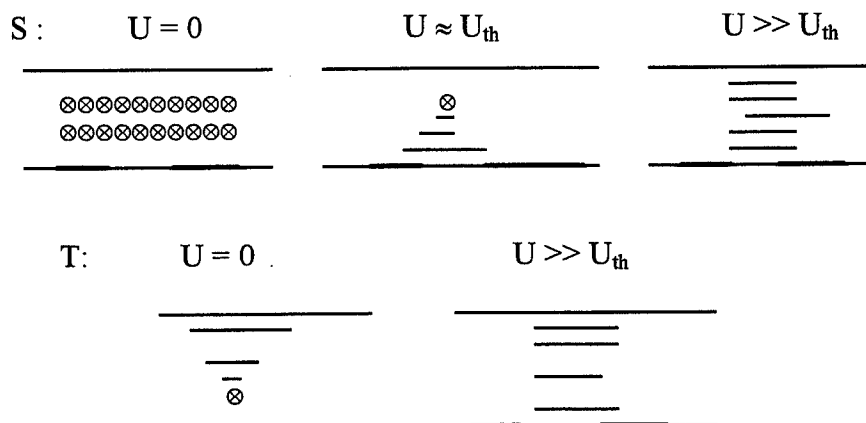


Fig. 3. Electro-optical effects in S- and T-structures

The effect of applied voltage on LC and its optical properties are shown in Fig 3. The electrode width was 1 mm, the gap between electrodes (l) was changed from 10 to 300 μm and LC layer thickness d from 3 to 10 μm . LC materials was used with following parameters : $\Delta n = 0.22$; $\Delta \epsilon = +12.0$; $\Delta t = 0 - 59^\circ\text{C}$. The LCM was driven by a triggered pulse generator giving electrical pulses of variable duration and amplitude. Electro-optical response was measured at 633 nm.

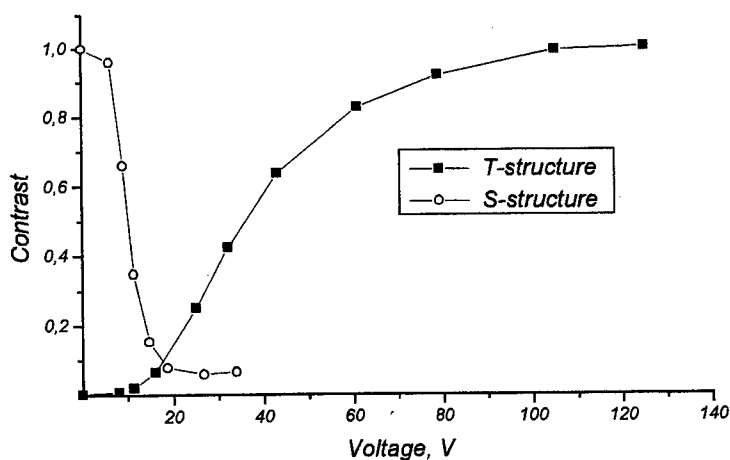


Fig. 4. Contrast ratio as a function of applied voltage for T-structure ($d = 3\mu\text{m}$, $l = 100\mu\text{m}$, parallel polarizes) and for S-structure ($d = 3\mu\text{m}$, $l = 20\mu\text{m}$, crossed polarizes)

Typical electro-optical characteristic for twisted structure is shown in Fig. 4. Transmission of the T-structure in parallel polarization is minimum in the off-state ($U = 0$). Increasing the applied voltage results in untwisting of the initial T-structure and leading to increasing transmission in the gap between the electrodes. The dependence of contrast ratio as a function of applied voltage is monotonic. The contrast ratio for this structure was not less than 400:1. The threshold voltage U_{th} of this electro-optical effect has approximately linear dependence on the gap width l between two neighbouring

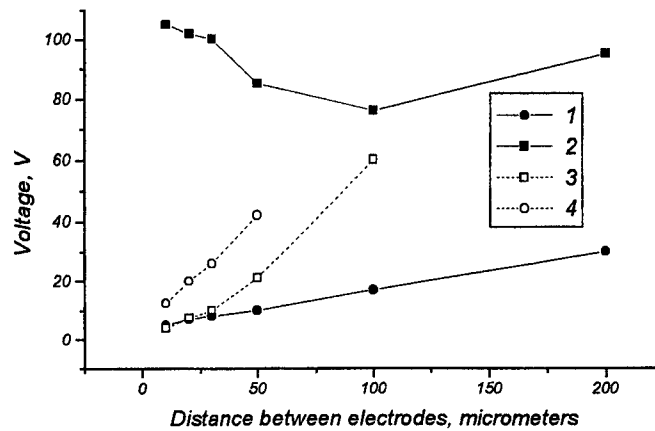


Fig. 5. Threshold voltage and saturation voltage as a function of distance between electrodes: 1 - threshold voltage for T-structure, 2 - saturation voltage for T-structure, 3 - threshold voltage for S-structure, 4 - saturation voltage for S-structure ($d = 3 \mu m$)

electrodes (Fig. 5). This dependence corresponds to the well known expression describing threshold voltage as a function of LC parameters:

$$U_{th} = \frac{\pi l}{d} \sqrt{\frac{4\pi K_{ii}}{\Delta\epsilon}} \quad (1),$$

where d - thickness of LC layer, l - distance between electrodes, K_{ii} - corresponding elastic constant, $\Delta\epsilon$ - dielectric anisotropy. Dependence of saturation voltage U_s on gap width is not monotonic.

In the case of the S-structure (the LC molecules are parallel to the electrodes) the electro-optical characteristics of the effect are also monotonic (Fig. 4). However, the LC molecules are reoriented in a more complicated way (Fig. 3). Voltages that exceed the threshold value result in a spiral twisting; further increasing of voltage leads to untwisting in the opposite direction. The contrast ratio for this case is equal to 20:1. The S-structure also shows an approximately linear dependence of the threshold and saturation voltage vs. gap width Fig. 5, according to equation (1).

Times on for T- and S-structures approximate to a l/U relationship, where l is the gap width and U is the applied voltage. Times on for both S- and T-structures are presented in Fig. 6 and Fig. 7. Minimum time on 0.07 ms was obtained for the T-structure with $d = 3 \mu m$, $l = 10 \mu m$, and the applied voltage 90 V. Time off for the LCM with the T-structure was 20 ms. Time off does not depend on the gap width but only on the LC layer thickness. It

should be noted that LCMs, controlled by a transverse electric field, exhibit better time characteristics in comparison to the analogous devices with a longitudinal electric field. In the latter rise times are usually 0.5...1 ms. The reason for this is that it is possible to use thin LC layers in LCMs with transverse operating electric field without danger of electrical breakdown. Such breakdown is the main factor limiting times on in LCMs with longitudinal electric field. The breakdown voltage is not because of a liquid crystal characteristic but is the result of technological defects (admixture to LC, inhomogeneous profile of conducting layers, etc.). These reasons lead inevitably to variations of electric field in LC layer. For transverse

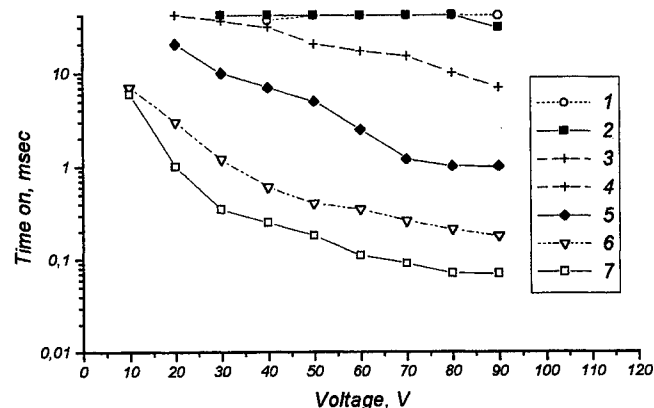


Fig. 6. Time on (T-structure, $d = 3 \mu\text{m}$) as a function of applied voltage at different distances between electrodes: 1 - 300; 2 - 200; 3 - 100; 4 - 50; 5 - 30; 6 - 20; 7 - 10 μm

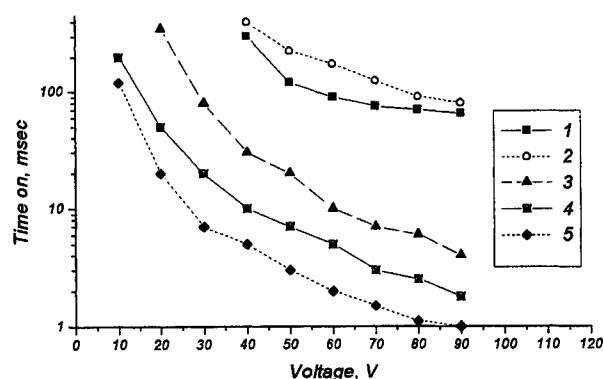


Fig. 7. Time on (S-structure, $d = 10 \mu\text{m}$) as a function of applied voltage at different distances between electrodes: 1 - 200; 2 - 300; 3 - 100; 4 - 50; 5 - 20 μm

geometry, these technological shortcomings are much less important, and one can realize a bigger electric field in LC layer with a smaller thickness, and thus improving the response time of the device.

Laser damage resistance of the LCMs with a transverse electric field was studied in the same setup that was used for testing of the LCM with a longitudinal operating electric field. It was shown that laser damage resistance of the LCM with transverse operating electric field

was $6.7 - 6.9 \text{ J/cm}^2$ at 1.06 nm , $\tau = 15 \text{ ns}$. The improvement of laser-damage resistance was achieved by removing of the ITO transparent electrodes out of the zone of intense laser radiation.

Conclusion

Experimental results have been given on laser-damage resistance of LCMs with longitudinal operating electrical field. It was shown that laser-damage resistance of the LCM is limited by the ITO transparent electrodes and equals $2.5 - 2.9 \text{ J/cm}^2$ at 1.06 nm , $\tau = 15 \text{ ns}$. To improve this parameter of the LCM we proposed an LCM structure controlled by a transverse electric field in which the ITO electrodes are removed out of the zone intense laser radiation. The main characteristics of the LCM are the following: time on - 0.07 ms , time off - 20 ms , contrast ratio - $400:1$ (LC layer thickness - 3 mcrm , distance between electrodes - 10 mcrm , operating voltage - 90 V). The laser-damage resistance of $6.7 - 6.9 \text{ J/cm}^2$ is a promising feature for the LCM with transverse electric field for high power laser applications.

Obtained results allow us to conclude about possibility of use of the LCM with transverse operating electric field as dynamic diaphragm for intracavity laser beam spatial control. The laser systems with internal LCMs can provide swift laser beam scanning, precise addressing of laser radiation and generating of laser beams with complicated spatial structure[3].

References

- [1.] F.L.Vladimirov, N.I.Pletneva, V.P.Pokrovskiy, L.N.Soms "Transverse-electric-field induced electro-optical effects in nematic liquid crystals", European Conference on Liquid Crystals, Science and Technology, Zakopane - Poland, March 3 - 8, 1997, Abstracts, D-8
- [2.] F.L.Vladimirov, E.A.Morozova ,Sov.J. of Opt. Technol.,**10**, 61,(1989)
- [3.] A.F.Kornev, V.P.Pokrovskiy, L.N.Soms, V.K.Stupnikov, J.Opt. Technol. **61**, 1, (1994)

Passive shutter on basis of nonlinear total internal reflection for laser pulse shortening

A.N. Rubinov, I.M. Korda, A.I. Bibik

B.I. Stepanov Institute of Physics, National Academy of Sciences of Belarus

Skariny prospect 70, 220072 Minsk, Belarus

Tel.: 375 (0172) 685-349, Fax:375 (172) 393-131E-mail: rubinov@ifanbel.bas-net.by

ABSTRACT

New device, enabling more than tenfold shortening and smooth variation of a laser pulse duration using repeated nonlinear total internal reflection of the laser beam from a border of transparent and absorbing media, is proposed. The shape and duration of the reflected and transmitted parts of the incident pulse are calculated in dependence on parameters of neighboring media and conditions of the experiment.

2.THEORY

The phenomenon of nonlinear total internal reflection (NTIR), discovered by the authors earlier [1], consists in change of light reflection at the border of transparent dielectric and absorbing medium due to the partial absorption of incident pulse in this medium. (Fig.1). NTIR was successfully employed for laser Q-switching [2] and for some shorting laser pulses outside a resonator [3,4]

$$n_1 = 1,4909 \dots 1,6568 \text{ (glasses)}$$

$$n_2 = 1,3243 \dots 1,5042 \text{ (liquids)}$$

$$\Delta n_2 = 0,002 \dots 0,033$$

$$n_1 - n_2 = 0,0003 \dots 0,2721$$

$$T_2 = 6^\circ \dots 80^\circ$$

$$\alpha_{\text{lim}} - \alpha = 30' - 60'$$

$$E = 0,5 \text{ J} \dots 1,5 \text{ J}$$

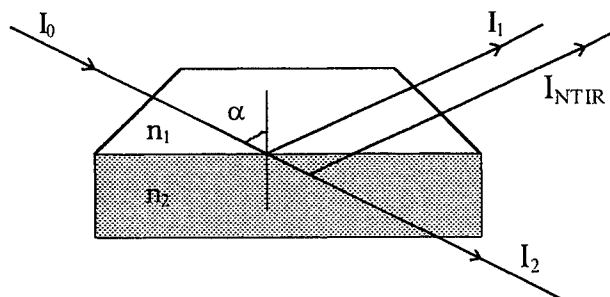


Fig.1

The raise of the medium temperature, caused by light absorption, leads to some change of its refraction index and as a result to change of the limiting angle α_{lim} of the total internal reflection. It means that at fixed angle of incidence α the difference of angles $\alpha_{\text{lim}} - \alpha$ will decrease in the process of the absorbing medium heating. As a consequence essential increase of the reflection coefficient from some initial reflection value up to $R = 1$ may take place. The typical dependence of the reflection coefficient on the difference $\alpha_{\text{lim}} - \alpha$ is shown in Fig.2a.

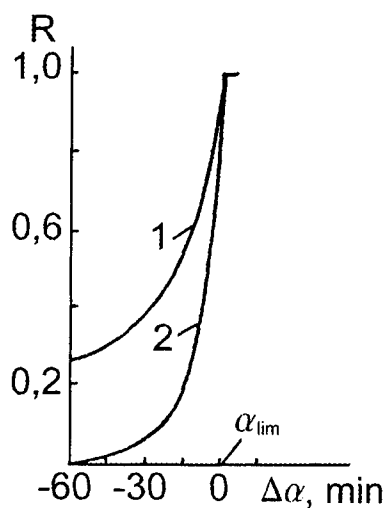


Fig. 2a

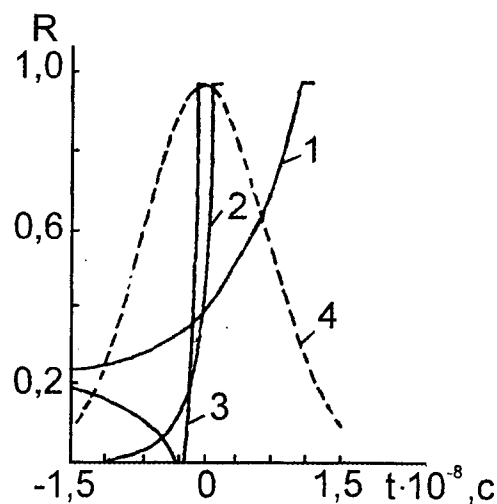


Fig. 2b

On the same picture the time dependence of R induced by incident Gaussian laser pulse is demonstrated. One can see that at the rightly chosen parameters of the both bordering media the range and the speed of reflection modulation due to the NTIR phenomenon can be significant. It means that this phenomenon may be employed for the control of a laser pulse temporal characteristics.

We have studied the potentialities of the NTIR-modulators for interactivity laser Q-switching and for pulse shaping of laser output. We have chosen glass as a transparent dielectric, alcohol dyes solutions as saturable absorber and water solutions of CuSO_4 as linearly absorbing medium. The scheme of experiment with NTIR shutter is shown in Fig. 3a.

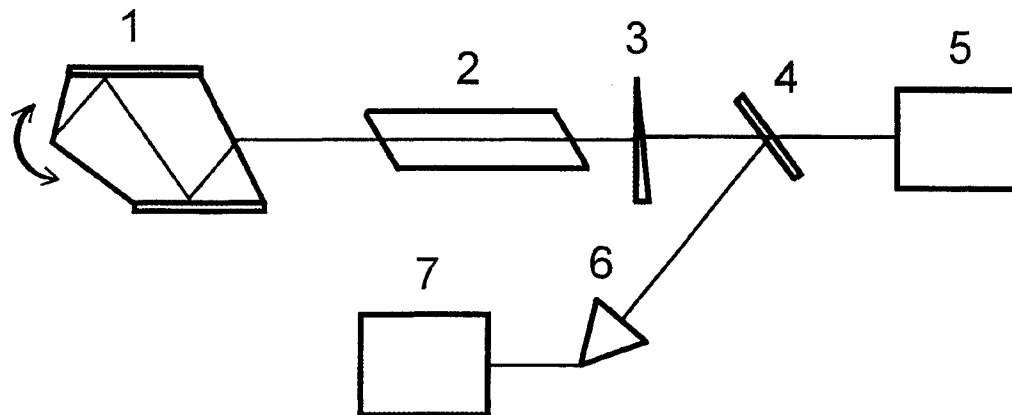


Fig. 3a

In the case when saturable absorber with fast relaxation time was used we observed experimentally two modes of Q-switch modulation. First one takes place under condition, when the initial incident angle is less than TIR limiting angle. In this case the basic role plays thermal change of a solution refractive index, resulting in attainment of a total internal reflection condition. Such mode of the shutter operation provides generation of a smooth giant pulse with duration of $\tau \approx 20$ ns (for ruby laser). Another mode of operation was observed in a case, when the initial incident angle was equal (or slightly exceeded) α_{lim} . In this case the Q-modulation happens due to the bleaching a thin dye layer near the border surface at the "diving" of radiation into the bordering medium in the course of TIR. In such mode the magnitude of reflection modulation is small, but its rate is much higher because here it determined not by the thermal processes but rather by the relaxation time of bleachable dye molecules. Because of the above reason the NTIR in such case results in mode-locking of the laser. Transition from one mode of modulation to another is easily achieved by small change of the angle of incidence α via the appropriate turn of the shutter. The oscillograms of ruby laser output radiation for both modes of modulation are shown in Fig. 3b.

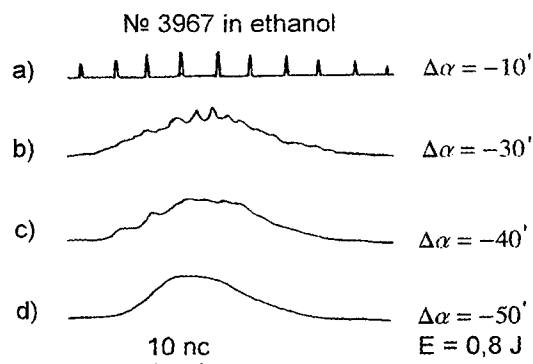


Fig.3b

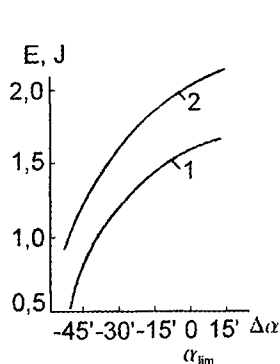


Fig.4a

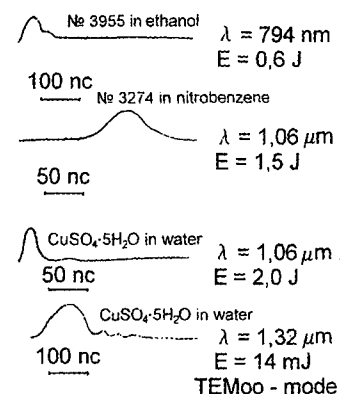


Fig.4b

Fig.4 illustrates results of giant pulses generation in Nd-laser by Q-switching with NTIR in the first modulation mode using both bleachable dyes and CuSO_4 water solution as absorbing media. Comparison of results presented in Fig.4b shows, that the linear absorber performs more efficient Q-switching than bleachable dyes, providing generation of shorter pulses with higher output energy.

Thus, the main advantage of NTIR-shutter in comparison with conventional passive dye Q-switches is that it does employ saturated absorbers. For the first, the use of inorganic substitution instead of dyes greatly increase photostability of a shutter. For the second, it opens simple possibility of Q-switching for IR lasers, for which saturable absorbers are not available. At present our experiments we successfully used NTIR-shutter with water solution of CuSO_4 for Q-switching of the YAG-laser on the wavelength 1.32 micron (see oscillogram at the bottom in Fig.4b). The dependence of giant pulse energy of the laser on the initial angles difference $\alpha_{\text{lim}} - \alpha$ is presented in Fig.4a.

NTIR allows to modulate only one edge of a pulse, leaving the other one without changes, as the shutter after being switched on keeps reflection coefficient R equal to 1 until the absorbing layer is cooled down (i.e. during the time period much longer than the laser pulse duration). If the reflected part of the pulse is utilized then the first part of the pulse will be cut off and consequently the leading edge of it will be sharpened. On contrary, if to pick up the transmitted beam, then the trailing part of the incident pulse will be cut off.

Here we propose the device which allows to cut off both leading and trailing edges of the pulse (Fig.5a).

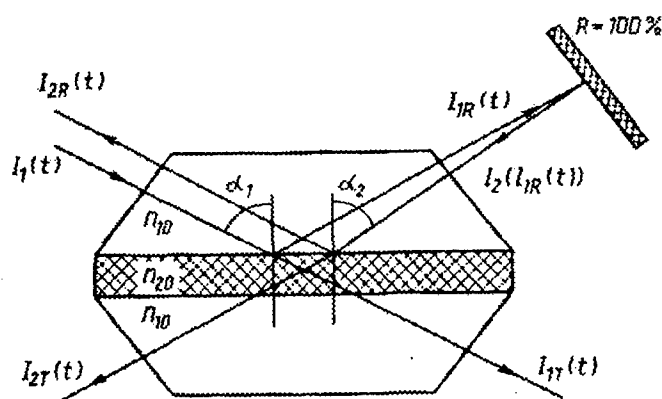


Fig.5a

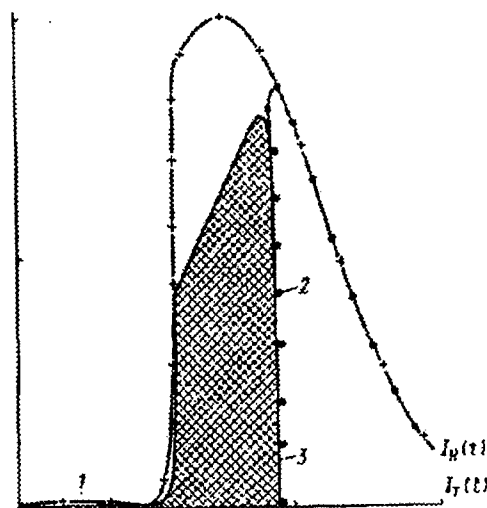


Fig.5b

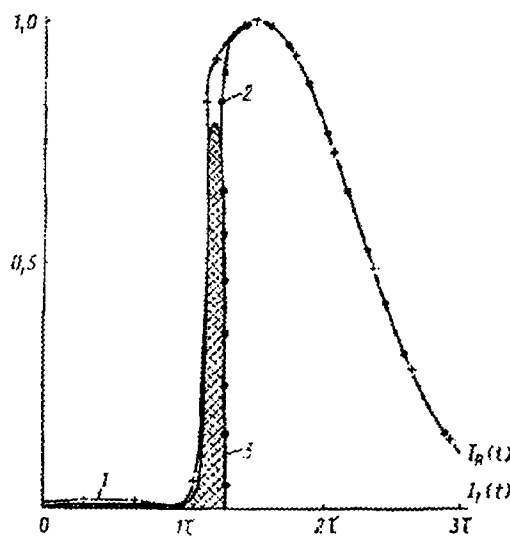


Fig.5c

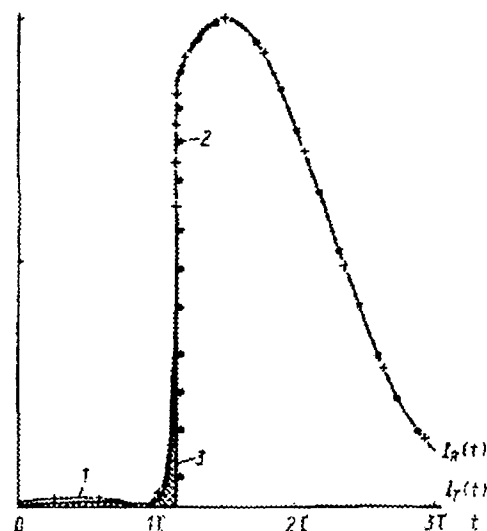


Fig.5d

In such device the absorbing layer should be thin enough to prevent significant losses of radiation at transmission. Due to the use of additional (fully reflective) mirror the laser beam is twice subjected to NTIR at slightly different angles of incidence. At the first reflection the leading part of the pulse is cut off while after the second reflection the transmitted beam I_{2T} experiences the cutting off the trailing part of the pulse. As a result the pulse with shape close to the rectangular one is obtained out of the initial laser pulse. The duration of the rectangular pulse depends on the difference between the angles of incidence by two consecutive reflections and may be easily varied. We have carried out the numerical calculations of the parts of the incident pulse reflected from and transmitted through the proposed device. As it is seen from the obtained results (presented in Fig.5), the new shutter allows not only to receive pulses with abrupt leading and trailing edges, but also to vary duration of the output pulse simply by some tilting the additional mirror. In accordance with our calculations the shutter should allow to receive pulses about 1ns, the duration which is hard to achieve by other means.

3. REFERENCES

1. Rubinov A.N., Korda I.M. " J. of Quantum Electronics (rus) ", №4(16),(1973),96-97.
2. Rubinov A.N., Korda I.M. " J. of Quantum Electronics (rus) ", Vol.1, №8,(1974),1877-1880.
3. Insarova N.I., Olefir G.I. JAS. Vol.42, №2,(1985),255-259.
4. Rubinov A.N., Korda I.M. " Lasers-Physics and applications ", Singapore, (1989). 745.

Biaxial nonlinear crystals for laser radiation harmonic generation.

Valentin G.Dmitriev^a, member SPIE,

Sergey G.Grechin^b, member SPIE.

^a Research&Development Institute "POLYUS", Moscow, Russia

^b Bauman Moscow State Technical University, SRI Radioelectronics and Laser Technology,
Moscow, Russia

ABSTRACT

The results of a comparison analysis of the laser radiation harmonic generation in biaxial crystals for all types of interaction are represented. The calculation of the phase-matching angles, bandwidths (angular, spectral, temperature), "field" of effective nonlinearities, phase-matching curves and etc. have been carried out.

Keywords: nonlinear optics; nonlinear optical crystals; optical frequency conversion.

1. CLASSIFICATION DIAGRAM

It is enough difficult to make a comparison analysis of nonlinear crystals even for so special case as harmonics generation of laser radiation. Hobden [1] has proposed the scheme (diagram) of stereographic projections that de-

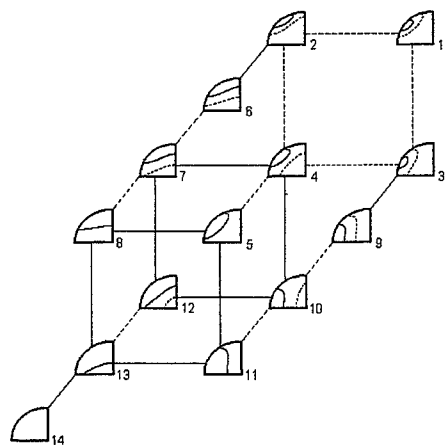


Fig.1. Schematic diagram of the possible loci of direction for Phase-Matching in Biaxial Crystals.

termines the possible phase-matching directions (PMD) in nonlinear biaxial crystals for harmonic generation (fig.1). These projections show the angle distribution of PMD for SSF - (slow-slow-fast, solid curves) and SFF - (slow-fast-fast, dotted curves)-interactions. Axis OZ is directed up, axis OX- to the left, OY-perpendicular to figure plane. The view of concrete angle distribution changes from one to other projections in dependence on birefringence (difference between main indices of the refraction coefficients with laser wavelength variation) and dispersive parameters of crystals; this change takes place on binding lines (fig.1). In this process the change of intersection points' position (of PM-curves with main crystal planes) takes place. These points are corresponding to non-critical PM (for angle dependence). The solid binding curves determine SSF-type, dotted binding lines -

SFF-type. It is important, that transitions between projections is possible only on binding lines. The transitions' sequence determines for crystal or for crystals groupe determines by crystal birefringence and its dispersion. Later this

Further authors information: <http://www.bmstu.ru/facult/rl/lid> E-mail: gera@mx.bmstu.ru Fax: (095) 333-91-66

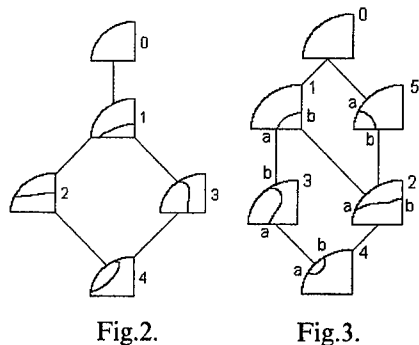


Fig.2.

Fig.3.

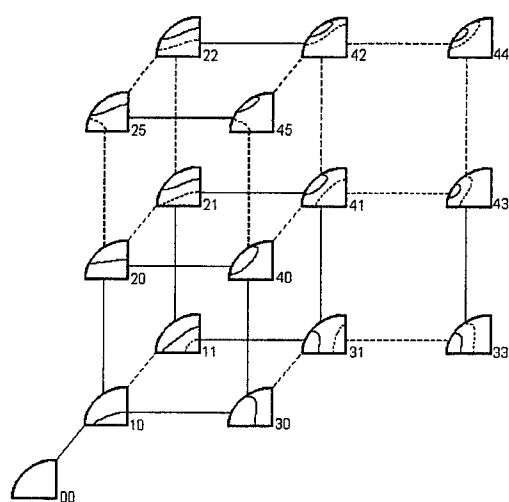


Fig.4. Complete diagram of a phase-matching directions in biaxial crystals.

consideration was developed in [2] for OPO-problems' analysis.

Of course, this scheme can be successfully used for nonlinear crystals' classification, but we have here some problems. The main problem is the fact, that for some crystals we have an angle PMD distributions that aren't corresponding to this scheme. So for RTA crystal with wavelength 3387,3 nm the PM-SFF-conditions are fulfilled strongly in OX-direction, and with wavelength decreasing the PM-cone girdles this axis (see later Table 3); such type of diagram in Hobden's classification (fig.1) is absent.

The scheme on fig.1 is the combination of all possible transitions between projections with wavelength change for two types of interactions- SSF and SFF. The transition diagram for both types is the same fig.2). The SHG process begins along OY-direction, and with wavelength change, in dependence on dispersion, it is possible to have the PM-conditions fulfilling along axes) OX or OZ. The limit state is the appearance of the PM-direction's cone around optical axis (diagram 4 on fig.2).

The detailed analysis of dispersion dependences of crystals shows that the transitions for SSF-type takes place always in accordance with scheme on fig.2. For SFF-type this diagram is shown on fig.3. In this case the SHG can appear with wavelength change along axis OY as well as along OX. The limited position is the same as for SSF-type.

Uniting diagrams on figs.2 and 3, as on fig.1, we can make total transitions diagram (fig.4). We used here the two-indices states numeration (first index - for SSF, and second - for SFF-types).

2. COMPARISON ANALYSIS

Let us use these results for analysis of 16 biaxial crystals' properties for SHG. The crystals list and references for Sellmeier's equations are given in Table 1.

The transitions sequences on stereographic projections diagram for these crystals are shown in Tables 2-9. The wavelengths, that are corresponding to transitions between two projections for both types of interactions, are given also in these Tables. The possibility of creating of single classification is not exists for all possible transitions. The transition way is determining by dispersion crystal' properties. Due to this facts, all results are divided in Tables conditionally in accordance to similarity of these transitions. This results representation allows to have the followings:

1. Transparency diapason of crystal and wavelengths diapasons, for which the PM-conditions fulfilling takes place for each interaction type, are shown.

2. Wavelengths diapasons, for which the angle-noncritical PMD's exist, are shown for main planes XOY, XOZ, and YOZ.
3. Wavelengths, that are corresponding to transition between stereographic projections, are shown. For these wavelengths the noncritical PM takes place for both angles.

Tabl.1. List of Biaxial Crystals.

Point gr. of symm.	Positive/ Negative	Title	Name	Organic/ Inorgan.	Bibl. Ref.
2	Negative	LAP	L-Arginine Phosphate Monohydrate	Organ.	/3/
222	Positive	POM	3-Methyl-4-Nitropyridine-1-Oxide	Organ.	/4/
		BFM	Barium Formate	Inorgan.	/5/
	Negative	α -Iodic Acid	α -Iodic Acid	Inorgan.	/6/
		CBO	Cesium Triborate	Inorgan.	/7/
mm2	Positive	L-CTT	Calcium Tartrate Tetrahydrate	Inorgan.	/8/
		KTP	Potassium Titanil Phosphate	Inorgan.	/9/
		KTA	Potassium Titanil Arsenate	Inorgan.	/10/
		CTA	Cesium Titanil Arsenate	Inorgan.	/11/
		RTA	Rubidium Titanil Arsenate	Inorgan.	/12/
		KB5	Potassium Pentaborate Tetrahydrate	Inorgan.	/13/
	Negative	Potassium Niobate	Potassium Niobate	Organ.	/14/
		Banana	Barium-Sodium Niobate	Inorgan.	/15/
		KLN	Potassium Lanthanum Nitrate Dihydrate	Inorgan.	/16/
		LBO	Lithium Triborate	Inorgan.	/16/
		FMB	Magnesium-Barium Fluoride	Inorgan.	/17/

We can mark some crystals groups: for first groupe (Tables 2-5) the transparency diapason is more wide than wavelength' diapason that corresponds to SHG-PM-conditions fulfilling. With wavelength increasing these conditions are fulfilling firstly for SSF-type, and then for SFF-type, and in the process the transition takes place on projections up to limit position (extremum). With further wavelength increasing we have a transition in opposite direction on the same (or very similar) way in the initial position. For crystals groupe on the Table 2 this opposite transition takes place on the same way (...20-21-22-21-20...). For crystals groupe on the Tables 2-5 we have "loop-like" transition (for example, for LBO crystals: ...31-33-43-41-31...).

For second crystals groupe we have transition from initial position to the finishing position without return to the initial position (Tables 6-9). The finishing position is position 44 on diagram fig.4..The same situation takes place for crystal in Table 9, but transparency band limits the initial position (40 instead of 00).

The existing of the extremums and "loop-like" transits shows that these positions have to demonstrate the wide spectral phase-matching widths. Really, for KTP, CTA, and Potassium Niobate crystals this situation takes place. In Table 10 the dependences of the spectral PM-widths on laser radiation wavelength are shown for two limited angle φ values ($\varphi=0$ and 90°). In Table 10 the stereographic projection' number are given also (these data correspond to these results). The wide spectral PM-width takes place also for crystals RTA, POM, and LBO, which have the "loop-like" transition (see Table 10).

The crystals in the Table 6 have the monotonously increasing dependence of the spectral width on the wavelength. Note that the wide spectral PM-width is possible in the case of small crystal dispersion (for crystals in the

Tabl.6

Crystal	Type	00	00-10	10	10-30	30	30-31	31	31-33	33	33-43	43	43-44	44
KB5	SSF	330	434		471,18									
mm2, Positive	SFF						583		640,13		902		1258,6	1440
MBF	SSF	370	609,25		713,3				998,52		1097,5		1536	5000
mm2, Negative	SFF						839,1				-----			
α -HfO ₃	SSF		-----	700	717,9		849,7		917,7	1600				
222, Negative	SFF										-----			
KLN	SSF		-----	670	694,7		781,3		944,2	1100				
mm2, Negative	SFF										-----			
LAP	SSF		-----	500	502,1		637,3		673,46	1300				
2, Negative	SFF													

Tabl.7

Crystal	Type	00	00-10	10	10-30	30	30-31	31	31-41	41	41-43	43	43-44	44
BFM	SSF	490	656,74		775,58									
222, Positive	SFF						826,7		928,3		1020,9		1246	2200

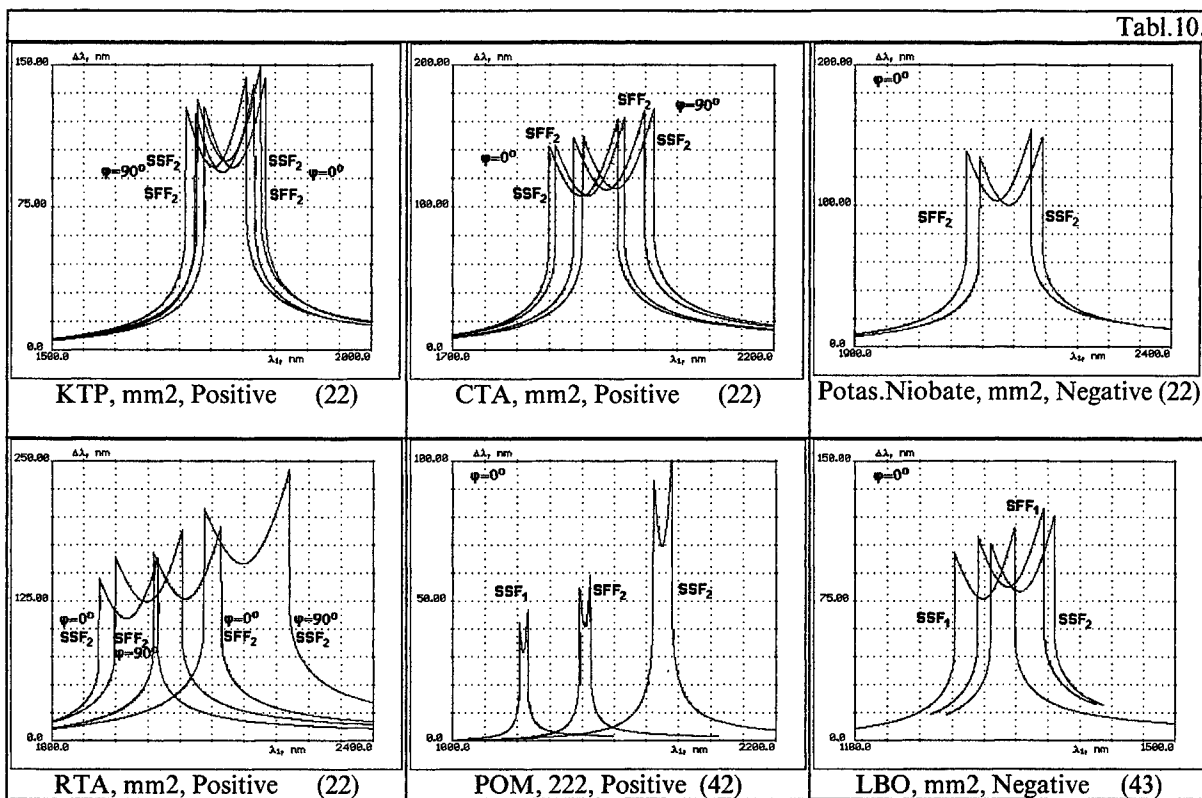
Tabl.8

Crystal	Type	00	00-10	10	10-20	20	20-21	21	21-41	41	41-42	42	42-44	44
L-CTT	SSF	560	697,3		827,5									
mm2, Positive	SFF						945,4		1127,7		1132,7	1400	-----	

Tabl.9

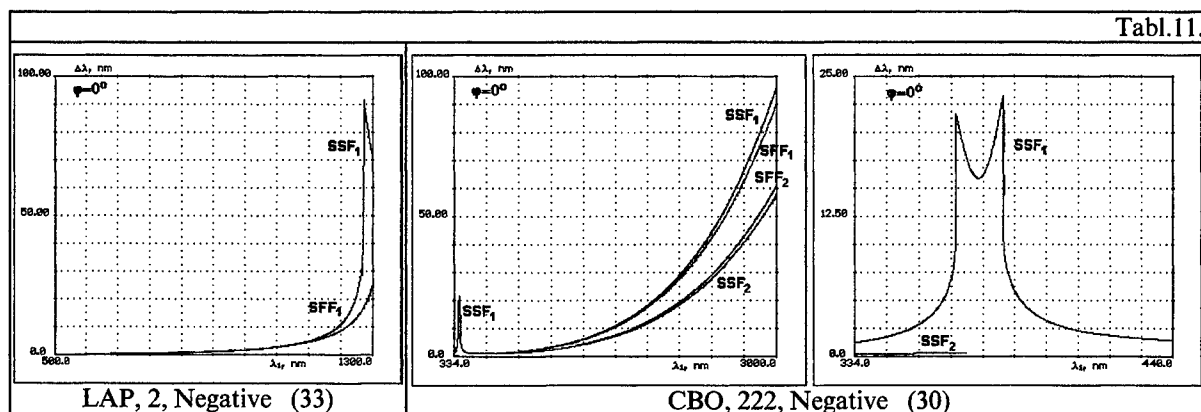
Crystal	Type	40	40-30	30	30-31	31	31-41	41	41-43	43	43-44	44
CBO	SSF	334	370,9				716,4					
222, Negative	SFF				508,7				1017,2		1336,6	3000

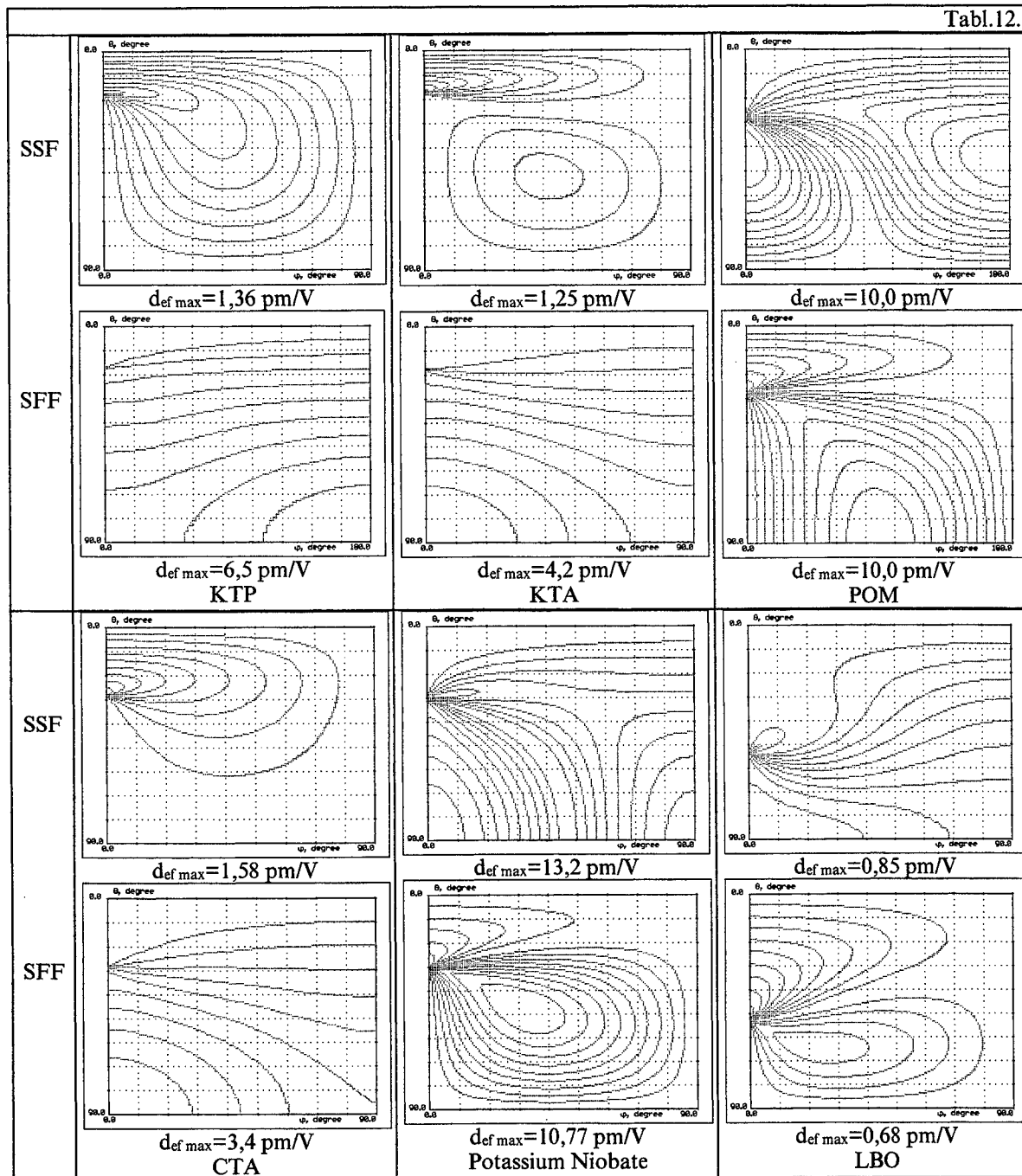
Table 6 it is possible only for LAP crystal, see Table 11). The crystal dispersion is enough small for IR-board of the transparency diapason, that provides the increasing of the spectral PM-width up to 74 nm. The analogous results take place for MAP and NPP-crystals.



The "loop-like" transitions lead to the wide spectral PM-widths for crystals in Tables 6-9. The results for CBO crystal are given in the table 11.

All of abovementioned results were obtained by using of known published data about dispersion of the refraction indices. Unfortunately, these data for middle IR diapason have a bad agreement with experimental results, and

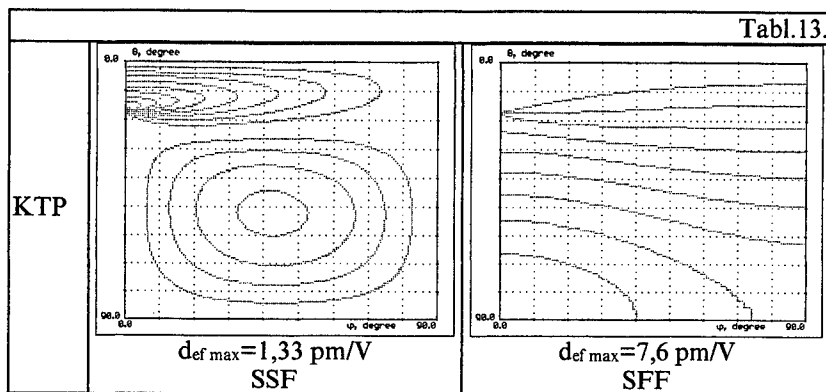




it is possible that some transition have to be modified with verification of the Sellmeyer' equations.

It is very important to calculate the efficient nonlinearity coefficient for the harmonics generation. Traditionally we calculate this efficient nonlinearity for PMD's. The more information can be obtained by calculating of this value for all possible diapasons of the angles φ and θ , that corresponds to the SHG *efficient nonlinearity fields*. This representation allows to find directions of the maximal efficient nonlinearity. By temperature variation or by using

of the applied electrical cw-voltage it is possible to change PMD up to desirable direction. The results of the efficient nonlinearity calculation (Kleinman's conditions are fulfilled) are given in Table 12. For biaxial crystals the position of the maximal SHG efficient nonlinearity is determined not only by symmetry group (that is to say by view of the nonlinear tensor, as for uniaxial crystals), but also by relation between tensor components. Due to this reason, the angle distributions of the efficient nonlinearity will be different for crystals that belong to the one symmetry group. These distributions are most similar for the 222 symmetry group.



In the Table 13 the angle efficient nonlinearity distributions are given for the case, when Kleinman's condition are not fulfilled. It is seen that in this case we have the difference (relatively to the case when these conditions are fulfilled) not only for maximal coefficient but also for distribution view. Note that the question about real Kleinman's condition fulfilling is open, and for

its clearing it is necessary to obtain more accurate measurements of the nonlinear tensor's components.

All presented in this report results were received with help of program facilitates **LID-SHG (Laser Investigator&Designer - Second Harmonic Generation)**. This program set was designed by Bauman MSTU, RDI R&L and R&DI POLYUS (Russia) - <http://www.bmstu.ru/facult/rl/lid>.

3. CONCLUSION

Authors believe that presented in this report results can give the "second life" to the Hobden's classification and will be useful for practical applications.

4. REFERENCES

1. M.V.Hobden. J. of Applied Physics. **38**, pp.4365-4372, 1967.
2. D.U.Stepanov, V.D.Shigorin, G.P.Shipulo. Sov.J. Quantum Electronics. **11**, pp.1957-1964, 1984.
3. D.Eimerl, S.Velsko, L.Davis, F.Wang, G.Loiaconen, G.Kennedy. IEEE J. of Quantum Electronics.**25**, pp.179-193, 1989.
4. J.Zyss, D.S.Chemla, J.F.Nicoud. Journal Chem. Phys. **74**, pp.4800-4811, 1981.
5. B.S.Bechtold, S.Haussuhl. Journal of Applied Physics. **14**, pp.403-410, 1977.
6. H.Naito, H.Inaba. Opto-Electronics. **4**, pp.335-337, 1972.
7. Y.Wu, T.Sasaki, S.Nakai, A.Yokotani, H.Tang, C.Chen. Applied Physics Letters. **62**, pp.2614-2615, 1993.
8. C.Medrano P., P.Gunter, H.Abend. Physica Status Solidi. **143**, pp.749-754, 1987.

9. T.Y.Fan, C.F.Huang, B.Q.Hu, R.C.Eckardt, Y.X.Fan, R.L.Byer et al. *Applied Optics*. **26**, pp.2390-2394, 1987.
10. K.Kato. *IEEE J. of Quantum Electronics*. **30**, pp.881-883, 1994.
11. A.Bianchi, M.Garbi. *Optics Communications*. **30**, pp.122-124, 1979.
12. L.K.Cheng, L.T.Cheng, J.Galperin, P.A.M.Hotsenpiller, J.D.Bierlein. *J.Crystal Growth*. **137**, pp.107-115, 1994.
13. W.R.Cook, L.H.Hubby. *J. Opt. Soc. Amer.* **66**, pp.72-73, 1976.
14. B.Zysset, I.Biaggio, P.Gunter. *J. Opt. Soc. Amer.* **9**, pp. 380-386, 1992.
15. S.Singh, D.A.Draegert, J.E.Geusic. *Physical Review, B*, **2**, pp. 2709-2724, 1970.
16. K.Kato. *IEEE J. of Quantum Electronics*. **26**, pp.1173-1175, 1990.
17. B.S.Bechtold, S.Haussuhl. *J. of Applied Physics*. **14**, pp. 403-410, 1977.

Broadband Spectrum Selective Coatings for Laser Systems

Kotlikov E., Khonineva E.

Department of Physics, State University of Airspace Instrument Making, St. Petersburg, 190000, Russia.

ABSTRACT

To obtain wide-band antireflection coatings for the visible and the middle IR regions of the spectrum transparent optical films with different refractive indexes and small absorption coefficients are required. Promising BaF_2 , CaF_2 , SrF_2 films with optical thickness more than 3-5 micrometers are not transparent in the visible region. Alloyed BaF_2 films, which were transparent in the all mentioned diapason, were obtained and investigated. Spectra selective coatings which based on alloyed BaF_2 were synthesized, made and researched for the visible and the middle IR range. The synthesis was realized on the base of the method of equivalent layers.

1. INTRODUCTION

The producing of broadband interference coatings for the middle IR and the visible region of the spectrum calls for a set of materials with different refractive indexes and small absorption. This set can be obtained if to use fluorides, such as BaF_2 , CaF_2 , SrF_2 , which are promising film-forming materials in the middle infrared region. However, it is known that fluoride films having optical thickness more than 3-5 μm are not enough transparent in the visible spectral region because of losses appearing as a result of scattering. In order to decrease the light scattering it is need to alloy optical films by the molecules of another substance [^{1,2}].

In the present paper the investigation of optical parameters of alloyed barium fluoride films is investigated. It is demonstrated the opportunity of producing of the films, which are transparent in the middle IR, and the visible spectrum diapason.

Spectrum selective coatings including alloyed BaF_2 films were synthesized, produced and explored. It was established that considered coatings might be used for the laser systems not only in the middle infrared region but in the visible region too.

The synthesis was realized based on the method of equivalent layers. These are techniques that allow getting over the restriction of the set of film forming materials with different refractive indexes and to project coatings realized on practice with demanded spectral characteristics [^{3,4}].

2. EXPERIMENTAL PROCEDURE

1. Performance of films and coatings.

Optical films and multilayer coatings of PbTe , GeTe , ZnTe , BaF_2 , CaF_2 , MgF_2 were made using the method of resistant evaporation in vacuum [⁵]. The vacuum of order of 10^{-3} Pa was obtained with the help of oil-diffusion pumps. ZnSe , PbTe and GeTe were evaporated from glass-graphite boats of specific design, which provide the decreasing of the interaction of evaporating substance with boat's material.

The polishing washers with diameter 20 mm of quartz, zinc selenium and potassium bromide are used as substrates. The substrate temperature (T_p) in the course of the evaporation was sustained with accuracy $\pm 5^\circ\text{C}$ in $50\text{-}200^\circ\text{C}$ range.

The checking of evaporated film thickness and of condense precipitate rate was carried out by photometry method through the transmission in the $0.6\text{-}1.1\ \mu\text{m}$ range, in which all films have small absorption.

The evaporation rate was determined through the time that took to evaporate the films with thickness, corresponding to the distance between two neighboring extremes. The distance from the crucibles to the substrates was not more than 150 mm, that provide to coat equally in thickness films on the plate with diameter up to 100 mm. The evaporation rate in this case was equal up to 15 mm/s without breaking of the film stochiometric composition, which can arise due to the overheat of film-forming substance during evaporation.

2. Spectrophotometric methods.

Transmission and reflection spectra of coatings were measured in ranges of value from 0.5 to 1.5 μm and from 2 to 22 μm with the use of the spectrophotometer "Perkin-Elmer". The inaccuracy of measurements was less than 0.2%.

Optical losses on light diffusion and absorption A were calculated using the formula $A=[1-R(\lambda)-T(\lambda)]$, where $R(\lambda)$ and $T(\lambda)$ – values of reflection and of transmission on the wavelength λ . It was possible to estimate magnitudes of energy losses in investigated spectrum diapason and compare the quality of made films and coatings spectrum by building of optical loss curves.

3. Method of the synthesis of interference coatings.

The projecting of interference coatings we performed using the method of the synthesis, which described in details in the literature [3, 4]. The method is based on the minimization of introduced function of quality and on following replacement of the films with found reflective indexes by an equivalent three layers structure. The function depends on construction parameters of a coating – thickness and reflective indexes of layers.

Thus, the task of synthesis is reduced to the decision of the task about the minimization of the function of quality in the defined region of D^{2m} – dimension Euclidean space E^m , where m – the number of layers of interference coating.

The method includes:

1. a choice of the first approach based on the stepped structure,
2. the optimization of stepped coating on reflective indexes of layers,
3. the replacement of layers by equivalent three layers structures,
4. the optimization of the found structure of projected coating on thickness of layers.

Stage organization of the process of the synthesis permits to get over the deficiency of possibilities of personal computers at the present time and the restriction of a set of real film-forming materials.

The calculation of data of transmission, reflection and absorption spectra obtained with the help of spectrophotometric methods can be processed by both analytical and numerical methods. When spectral dependencies are perturbed by strong absorption bands (for example, spectra of BaF_2) the determination of the values of optical constants of coatings is performed by numerical methods only.

3. EXPERIMENTAL AND ANALYTICAL RESULTS

1. The investigation of alloyed BaF_2 films.

We carried out experiments on the alloying of barium fluoride films by calcium and magnesium fluorides. Experiments shown that BaF_2 films alloyed by CaF_2 or MgF_2 possessed small grain structure and dispersed the light weakly in the visible part of the spectrum. Such films stay transparent even being components of the multilayer interference coatings with total thickness more than 3-5 μm .

For the illustration of aforesaid we produced multilayer coatings of pure barium fluoride and the ones of barium fluoride alloyed by calcium and magnesium fluorides. Coatings had the structure $\text{SH}(\text{LH})^3$, where S was the substrate of ZnSe ; L – the layer of pure BaF_2 or the one of BaF_2 with alloying impurity CaF_2 or MgF_2 ; H – the layer of ZnSe . The layer L had smaller refractive index in comparison with layer H . Films having divisible $\lambda/4$ optical thickness were applied to ZnSe substrates. The temperature of which was sustained in 80-90° C range. The value of a wavelength λ was equal 10.6 μm (the CO_2 laser generation wavelength). The one of photometry checking wavelength during the evaporation was 0.768 μm .

Curves of dependencies of optical losses in the visible and near IR spectrum regions of created mirrors are presented on Fig.1. These mirrors consisted of seven layers and were based on: 1 – pure BaF_2 films applied to ZnSe substrate; 2 – BaF_2 films alloyed by MgF_2 with the concentration 2 % and applied to ZnSe substrate. Comparative analysis of figures 1.1 and 1.2 allows to note that the alloyage of BaF_2 films by calcium fluoride or magnesium fluoride decreases essentially optical losses of coatings produced on the base of these materials in the visible range of a spectrum. In the range 0.6-0.8 μm optical losses are caused by absorption substrate of ZnSe too.

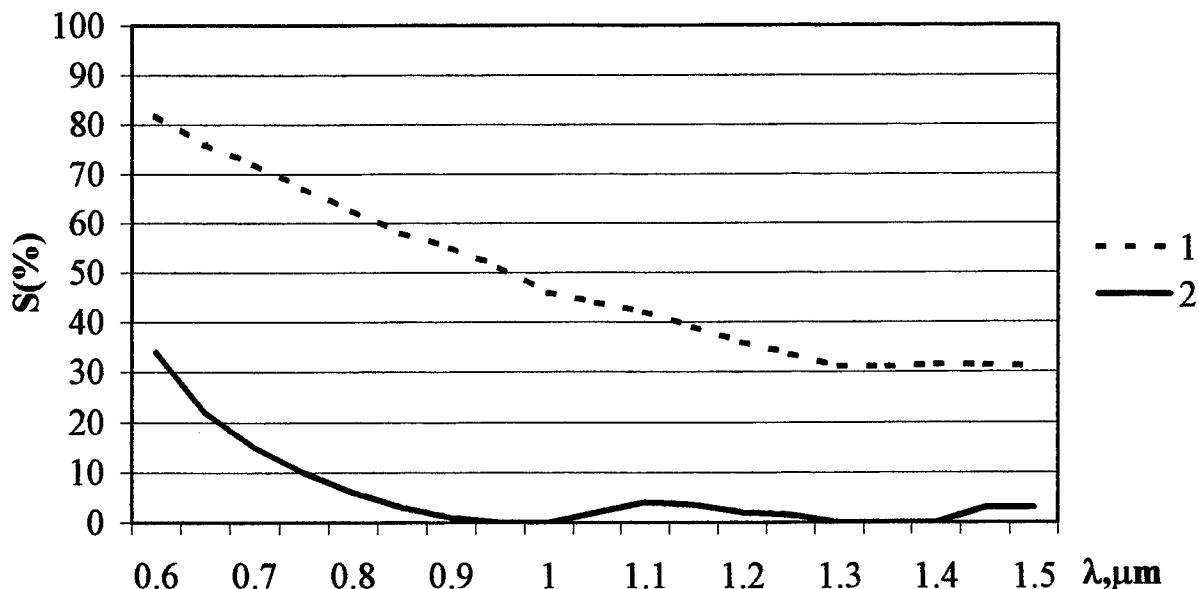


Fig. 1. Curves of optical losses $S(\%)$ of mirrors based on: 1 – pure BaF_2 films deposited onto ZnSe substrate, 2 – BaF_2 films alloyed by MgF_2 deposited onto ZnSe substrate.

We performed the research of optical losses in the case of the using of alloying additions with different concentrations. It was established that concentrations of alloying impurity of the CaF_2 – to 10 % and the one of MgF_2 – to 2 % were optimal. Optical losses decreased when concentrations of these alloying additions increase to the values mentioned above. Further experimental increasing of concentration of the alloying impurity sets up stresses in films and their following breaking.

2. Investigation of the interference coatings on the base of alloyed BaF_2 films.

Used results of the synthesis the set of the spectrum selective coatings was produced. In the first case it was the spectrum selective coating separating radiation of the He-Ne and CO_2 lasers. It was applied to ZnSe substrate and had the structure $S(\text{H3L})^3\text{H}$, where S – the substrate of ZnSe; L – the layer of BaF_2 ; H – the layer of ZnSe. Made coating reflects nonpolarized He-Ne laser's radiation ($\lambda = 0.63 \mu\text{m}$) and is transparent for the CO_2 laser's radiation ($\lambda = 10.6 \mu\text{m}$) in the case of normal incidence. For oblique incidence ($\alpha = 45^\circ$) the reflection coefficient on the wavelength $0.63 \mu\text{m}$ is more than 95 %, the transmission coefficient of nonpolarized radiation with wavelength $10.6 \mu\text{m}$ was more than 99 %.

The reflection spectrum for considered coating in the spectral diapason $0.5 - 1.5 \mu\text{m}$ is presented on Fig. 2.

In the second case, these were spectrum selective coatings working in the spectral diapason $2-20 \mu\text{m}$ and having the ratio of the reflection coefficient to the transmission coefficient $R/T \approx 1$. Coatings were deposited onto the substrate of ZnSe or KBr. Formerly, for this spectral diapason spectra selective coatings have been made on the base of pure germanium films [7]. On the Fig. 3 calculated transmission spectra of elaborated coatings are presented. For the comparison, on the Fig. 3.1 the spectrum of the single Ge film deposited onto the KBr substrate is presented too.

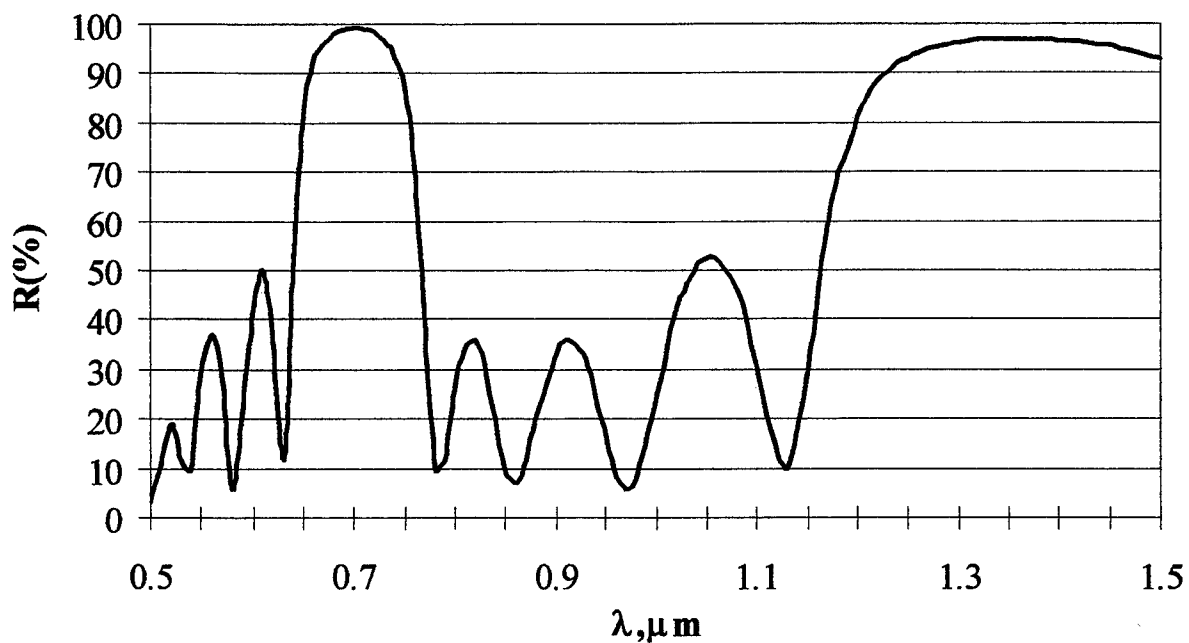


Fig. 2. Reflection spectrum for spectrum selective coating separating radiation of the He-Ne and CO₂ lasers. The coating was deposited onto ZnSe substrate.

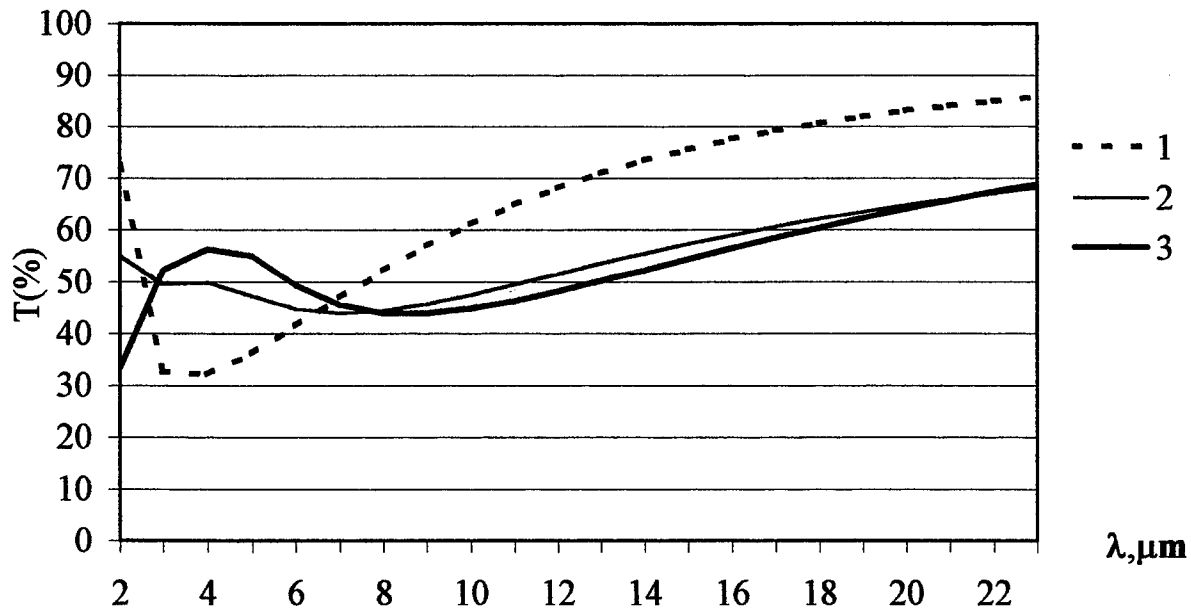


Fig. 3. Calculated transmission spectra of coatings of spectrum selective coatings with the ratio of the reflection coefficient to the transmission coefficient $R/T \approx 1$.

- 1 – the coating based on single Ge film deposited onto KBr substrate,
- 2 – alloyed coating deposited onto ZnSe substrate,
- 3 – alloyed coating deposited onto KBr substrate.

For example of the using of the techniques described by us it was synthesized and studied the antireflection coating. It had mean value of reflection coefficient 2 – 3 % in the diapason of spectra 5 – 12 μm and not more than 6 % in the rest diapason. Calculated spectra of reflection from one border of a ZnSe substrate with deposited coatings and of a pure ZnSe substrate are presented on the Fig. 4.

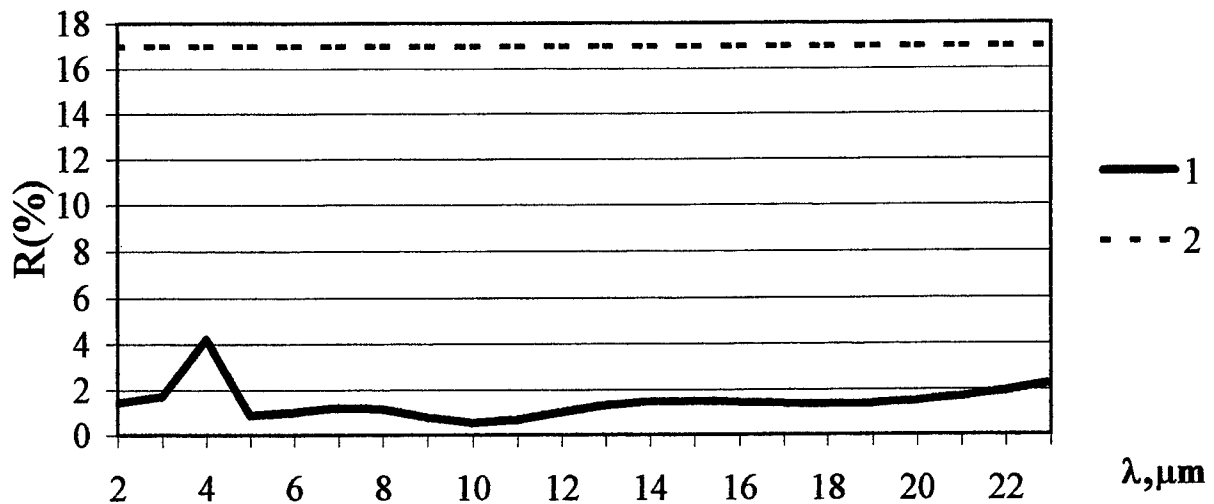


Fig. 4. Calculated spectra of reflection: 1 - from one border of a ZnSe substrate with deposited antireflection coating, 2 - from a pure ZnSe substrate.

4. CONCLUSION

Carried out experimental investigation show that barium fluoride films alloyed by calcium or magnesium fluorides, were promising for producing interference coatings in wide spectrum diapason. Due to the using these films and the method of equivalent layers spectrum selective coatings were synthesized, produced and explored for the middle infrared and the visible spectrum regions.

5. REFERENCES

- [¹]. Golota A.F., Limanskaya A.B., Podkolsina T.M., Khoubieva Z. R., Sbornic tezisov docladov VII Vsesoiousnogo soveshania "Krystallicheskie materialy". Leningrad, 1989, pp. 359-362.
- [²]. Kotlikov E.N., Physical optics, 1990, vol. 69, No 4, pp. 846-850.
- [³]. Kotlikov E.N., Tereschenko G.V., Journal of optical technology, 1997, vol. 64, No 3, pp. 110-115.
- [⁴]. Kotlikov E.N., Tereschenko G.V., Physical optics, 1997, vol. 82, No 4, pp. 603 – 609.
- [⁵]. Ritter E., Physika tonkikh plenok, Moscow, Mir, 1978, vol. 8, pp. 36-556.

FULLERENE-BASED NONLINEAR OPTICAL DEVICES FOR FAST CONTROL OF SPATIAL, POWER, AND TEMPORAL CHARACTERISTICS OF LASER RADIATION

I.M.Belousova, V.P.Belousov, E.A.Gavronskaya, V.A.Grigorev, O.B.Danilov,
A.G.Kalintsev, V.E.Krasnopolsky, V.A.Smirnov, E.N.Sosnov

Institute for Laser Physics
St.-Petersburg 199034 Russia

ABSTRACT

We present the results of experimental and theoretical study of opportunities for improving of spatial homogeneity in the near field of Nd : YAG-laser radiation at λ 532 nm by means nonlinear optical limiting of laser radiation, that take place in fullerene-containing medium (with C_{60}). A scope for the smoothing out a profile of generation impulse was studied. The experiments were performed with fullerene-containing composites C_{60} -solution. The mechanism of optical limiting is discussed.

INTRODUCTION

Fullerenes and fullerene-based materials have strong nonlinear-optical properties related to the structure of the fullerene molecule [1]. In this connection, they can be used for creation of:

- Limiters (attenuators) of high-intensity radiation and optical switches
- Devices for controlling of spatial and temporal parameters of laser radiation.

The most interesting and advanced in practical studies is application of fullerenes as optical limiters for laser radiation that are necessary for protection of eyes and sensors.

We consider more in detail the fullerene-based optical limiters for high-intensity radiation which can be used for protection of eyes and radiation sensors.

To date, the broadband fast-response laser radiation limiting effect has been obtained in such fullerene-containing materials as solutions, polymers, liquid crystals, sol-gel and glass matrices. The mechanism of optical limiting of high-power radiation is being actively studied. In most cases, the nonlinear-optical limiting phenomenon is being studied using fullerene-solvent systems, the C_{60} -solvent systems (with toluene, benzene, hexane, etc.) being examined most fully [1].

Basically, a mechanism involved in the creation of radiation power (energy) limiters is the phenomenon of saturable light absorption from excited electronic-vibrational levels of a fullerene molecule. This phenomenon is referred to as the reverse saturable absorption (RSA).

At high specific powers (energies), the saturable absorption from an excited state is combined with an additional radiation self-defocusing process and the process of photoinduced scattering, which arises from a nonlinear change in the refractive index of a medium.

1. Kinetics of the mechanism of the reverse saturable absorption and the process of photo-induced scattering

Let us consider the RSA kinetics in more detail. Fig.1 shows a simplified diagram of the main energy levels of fullerenes which take part in the optical limiting mechanism [1].

According to the Franck-Condon principle, a laser pulse excites a fullerene molecule from the S_0 ground state to the S_x excited singlet state. We denote the cross-section for this transition as σ_g^S . The S_x -state molecules quickly relax to the equilibrium S_1 state (the relaxation time being τ_2).

A transition from the S_1 state may occur following two ways: $S_1 \rightarrow S_0$ and to the T_1 metastable triplet molecular state. The singlet-triplet interaction has high probability, because the interlevel energy difference is 9 kcal/mol (~ 0.4 eV) and the quantum yield for the transition to the triplet state is close to unity. Therefore, the main triplet-state population mechanism is the intrastructure singlet-triplet excitation energy transfer. Light can be further absorbed via a transition from the S_1 excited state to upper excited states S_n (absorption cross-section being σ_{ex}^S) and from the T_1 triplet to upper triplet states T_n (absorption cross-section being σ_{ex}^T). Relaxation from these states back to the first excited state proceeds very fast, with $\tau_3(S_n \rightarrow S_1) \approx \tau_6(T_n \rightarrow T_1) \approx 1$ fs.

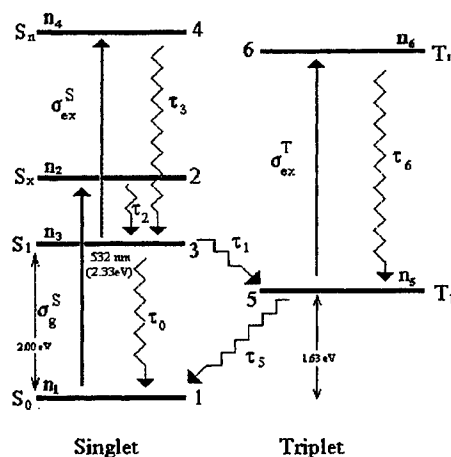


Fig. 1. Energy-level diagram

The radiative transition from the T₁ triplet state to the ground state is forbidden, and the T₁ state decays via intramolecular transitions, or at interactions fullerene molecules or with host-matrix (e.g., solvent) molecules.

If the absorption cross-section for a transition from the ground state to the excited one is larger than that from the excited state upward, $\sigma_g^S > \sigma_{ex}^{S,T}$, saturated absorption from the ground state is observed, that is, a medium becomes translucent when intense light is let pass through it. If $\sigma_{ex}^S \approx \sigma_{ex}^T > \sigma_g^S$, light is absorbed via a transition from an excited singlet or triplet state, the absorption increasing with incident light intensity due to increase in population of excited states. The onset of the RSA phenomenon occurs, and the transmission becomes limited when light is let pass through the medium. If a light pulse is longer than the singlet-triplet interaction time ($\tau_L > \tau_1$), the triplet metastable state acts as an accumulator of the excited molecules, and RSA occurs via the T₁→T_n transitions. If the light pulse is shorter than the singlet-triplet interaction time ($\tau_L < \tau_1$), RSA occurs via the S₁→S_n transitions.

For C₆₀, the RSA and, hence, optical limiting region lies within the 400-700-nm spectral region, because, at $\lambda < 400$ nm, the ground-state absorption cross-section $\sigma_g^S > \sigma_{ex}^{S,T}$ and, at $\lambda > 700$ nm, the absorption cross-section σ_g^S for fullerene C₆₀ becomes very small.

For higher fullerenes C₇₀, C₇₈, and C₈₄, the RSA region shifts beyond 700 nm to the longer wavelengths spectral range.

The population and decay kinetics of the levels involved in optical radiation limiting is adequately described with a six-level scheme. To calculate the level population and to determine the transmission of a sample under high-intensity laser irradiation the value of cross-section and lifetimes were used that present in review of authors [1].

Fig. 2 shows the results of numeric solution of this equation with consideration for the experimental profile of the laser radiation pulse in the conditions of our experiment: the radiation wavelength was $\lambda=532$ nm, $\tau_p=15$ ns, the values of energy density of incident laser radiation E_{in} varied from 0 to 10 J/cm², the cell thickness was $L=3$ mm, the C₆₀ in the solution (toluene) concentration values were 0.6 mM and 1.5 mM. It is seen that nonlinear dependence of E_{out} on E_{in} is observed, in contrast to the case of transmission of radiation with low intensity, because for $c = 1.5$ mM the cell transmission decreases by ~ 12 times at 10 J/cm².

Theoretical and experimental investigations shows that the processes reverse saturable absorption is combined with an additional radiation self-defocusing process and photoinduced scattering connected with photoinduced variations of medium refractive index make considerable contribution in optical limiting at high energy densities [2, 3].

The performed theoretical analysis shows that two factors contribute in the photoinduced variation of the medium refractive index: the medium molecular polarizability and the thermal variation of the medium refractive index. Our assessments show, that thermal variation of refractive index is magnitude higher than the change of refractive index due to the molecular polarizability.

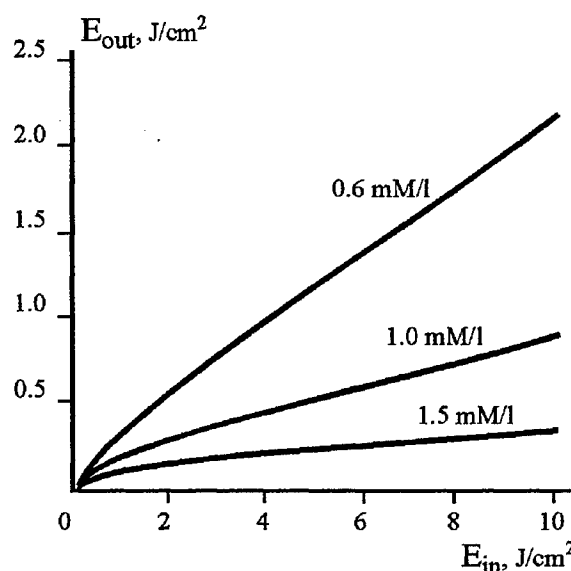


Fig. 2. Calculated dependence of E_{out} on E_{in} with consideration for the mechanism of reverse saturable absorption.

Laser radiation intensity is non-uniform over transverse cross-section of the beam, and the absorbing medium almost always has density fluctuations. Therefore, random transverse variations of the refractive index are present. These variations have thermal character and cause stimulated thermal scattering of light.

In the next chapter we present our experimental results that demonstrate its value and influence on optical limiting.

2. Results of experiments and comparison with the theory

The characteristics of optical limiters of laser radiation were investigated by us in different fullerene-contained medium: solutions of fullerene C_{60} , C_{70} , C_{76-84} , solid-state matrices (sol-gel SiO_2 and porous glasses), and in several films (PMMA, polystyrene, polycarbonate etc.). The opportunity to control the parameters of laser radiation: the homogeneity of space distribution of radiation in close area duration and temporal profile of laser pulses were investigated.

In Fig. 3 presented schemes of set-ups for investigations of optical limiting and the modification of above named setup for the control space-energetic and temporal parameters of radiation.

The main units of the laser system are:

- master oscillator on YAG:Nd;
- system of spatial filtration and decoupling device based on a Faraday cell;
- two-pass amplifier on two YAG:Nd active elements with phase conjugation device;

The parameters of radiation at the output of the facility are:

- wavelength 1.064 μm ; 0.532 μm
- radiation energy in a pulse up to 0.6 J;
- radiation pulse duration 10 ns;
- radiation angular divergence $\leq 0.6 \cdot 10^{-3}$ rad;
- output beam diameter 9 mm;
- spectrum width corresponds to single-frequency radiation.

The pulse energy at the second harmonic frequency was up to 0.35 J.

Measurements were performed in beams 6 - 8 mm and 2 mm in diameter, with application of a telescopic system, and in a focused beam. Fig. 3 shows two variants of general setup of the facility for study of optical limiting: (a) without and with beam collimating by the telescope for obtaining energy densities greater than 1 J/cm², in this case the beam diameter varied from 6 - 8 mm to 1.5 - 2 mm, and (b) the two-pass scheme with radiation focusing at the second pass through the cell that permitted to reach threshold energy densities after the first pass, and thus broaden the dynamic range of radiation transmission. In such a system, we succeeded to vary the density of input energy from 0 to 10 J/cm², and the dynamic range

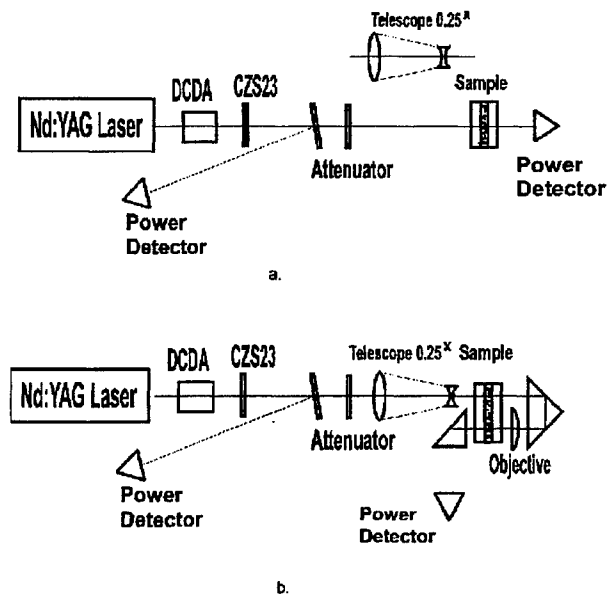


Fig. 3. Layouts of setups for the study of the dynamic range of optical laser radiation limiting .

of the input energy reached $10^6 - 10^7$. We measured energy parameters and pulse profiles of incident and transmitted radiation. To study the contribution of self-defocusing and of photoinduced scattering, we applied special techniques.

It is clear from point 1 that the source of self-defocusing and photoinduced scattering is variation of the medium refractive index on the whole over the beam cross-section and inhomogeneities (fluctuations) of the refractive index over the beam cross-section. Therefore, it was expedient to directly measure these values by means of a laser interferometer, with the sample irradiated by high-intensity laser radiation at $\lambda = 532$ nm in one of its shoulders.

Fig. 4 presents two variants of the interference setup. For measurements of changes in the interference pattern in the

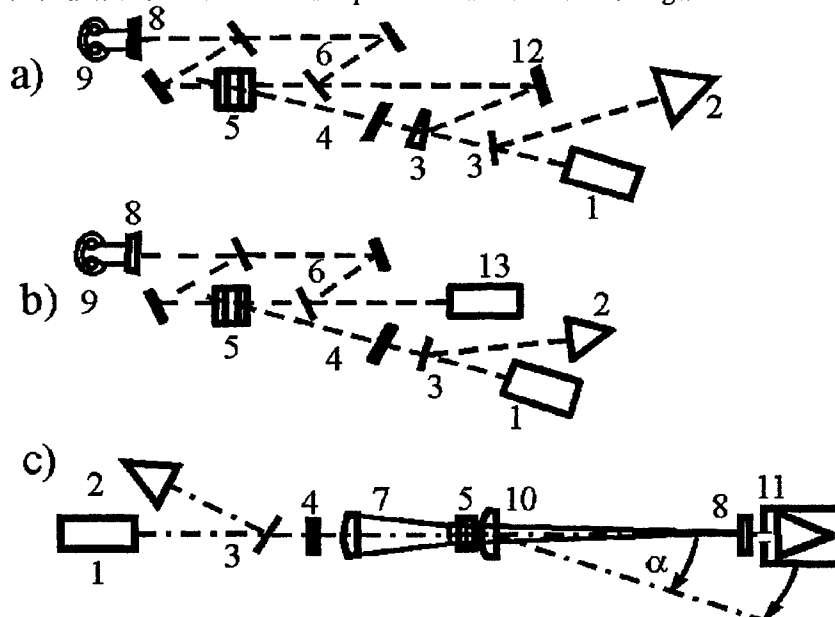


Fig. 4. Experimental setup a) for measuring refractive index variations during laser pulse; b) after laser pulse; c) for measuring indicatrix of photoinduced scattering. 1 - laser ($\lambda = 0.53 \mu\text{m}$); 2 - energy detector; 3 - radiation divider; 4 - changeable filters; 5 - cell with fullerene; 6 - Mach-Zender interferometer; 7 - telescope ($F = 0.33^\circ$); 8 - filters; 9 - photocamera; 10 - objective ($F = 1734$ mm); 11 - energy detector with \varnothing 3-mm aperture; 12 - mirror; 13 - laser ($\lambda = 0.63 \mu\text{m}$).

sample during the process of illumination by a laser pulse during $\tau \approx 8 - 10$ ns, we used the part of the radiation of the same laser (Fig. 4a). For study of variations in interference pattern during and after the pulse acting on the medium, we used a He-Ne laser as the probe one (Fig. 4b).

The study of the contribution of photoinduced scattering was performed with the setup shown in Fig. 4c by calorimetric determination of the transmitted radiation energy in the far zone with small aperture of the field of vision ($\nu \approx 1.8 \cdot 10^{-3}$), with measurements of the scattering indicatrix in angles from 0 to 30° from the beam axis.

Fig. 5 presents the dependencies of the output energy density (C_{60} -toluene for $c = 0.6$ mM and 1.5 mM) on the input energy density [4]. The phenomenon of nonlinear limiting starts approximately from 0.5 J/cm^2 , the level of optical limiting of radiation transmission corresponds to $0.1 - 0.12 \text{ J/cm}^2$ ($c = 0.6$ mM) and 0.05 J/cm^2 ($c = 0.6$ mM). In the single-pass system with the collimated beam, the 60-fold attenuation of the energy density transmitted through the sample was reached. The maximum value of the input energy density was determined by resistance to radiation of the quartz cell, on whose walls soot was formed at high energy densities.

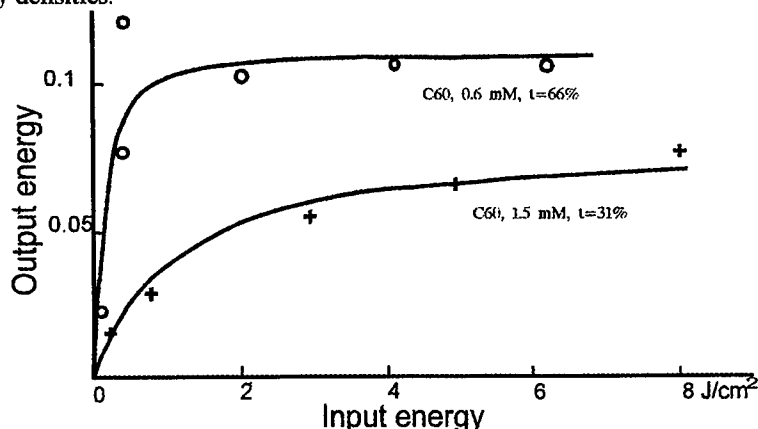


Fig. 5 Dependence of output energy density on input energy density.

The dependence of the level of limiting on the initial fullerene concentration in the solution, on the cell thickness, and on laser radiation wavelength followed the scaling law ML , where M is the molar fullerene concentration in solution, L is the path length in the sample.

Our experimental results show that beam defocusing in the sample (especially in the scheme with focusing the beam in the sample) and nonlinear photoinduced scattering are observed at high densities of input energy besides the RSA effect. We have shown in chapter 1 that these phenomena are connected with variations of the medium refractive index in the domain irradiated by the beam.

The direct measurements that we performed for the refractive index of fullerene-containing medium (C_{60} -toluene) in the collimated beam by means of the interference technique shows the general change of the refractive index over the beam cross-section and local small-scale inhomogeneities. Fig. 6 shows the plot of general Δn change over the beam cross-section during the pulse. It is seen that the Δn value grows and reaches, for example, at $E_{in} = 2.5 \text{ J/cm}^2$ the value $\Delta n \sim 4 \cdot 10^{-4}$. Such general change of the refractive index mainly connected with the thermal mechanism causes small contribution in increase of the angular divergence of transmitted radiation, and, in conditions of our experiment, weakly influences optical limiting. On the other hand, local small-scale variations of the refractive index cause photoinduced nonlinear scattering that strongly grows with increase of the input energy.

Fig. 7 presents the results of measurements of the scattering indicatrix of the output scattered radiation in the solid angles $E_{out} = f(2\alpha)$, where α is a half of the angle at the vertex. The intensity maximum of the scattered radiation is observed in angles $\alpha \sim 1 - 2^\circ$, and further, up to 30° , the field of the scattered radiation is rather uniform (Fig. 7a). The part of scattered radiation decreases with decrease of the input energy.

This scattering is coherent, since the obtained image of the transmitted beam has obviously speckled structure. The spectrum of transverse dimensions of small-scale inhomogeneities obviously lies in the interval $1 - 10 \mu\text{m}$. Fig. 7b presents the angular distribution of the energy transmitted through the cell and the ratio $E_{out}/E_{in}(2\alpha)$. It is seen that the main part of the transmitted energy is within the angle $\sim 40^\circ$, and the energy transmission of the sample in this angle is $E_{out}/E_{in} = 0.3$. Since the transmission is connected only with the RSA mechanism, it may be compared with the calculated value presented in

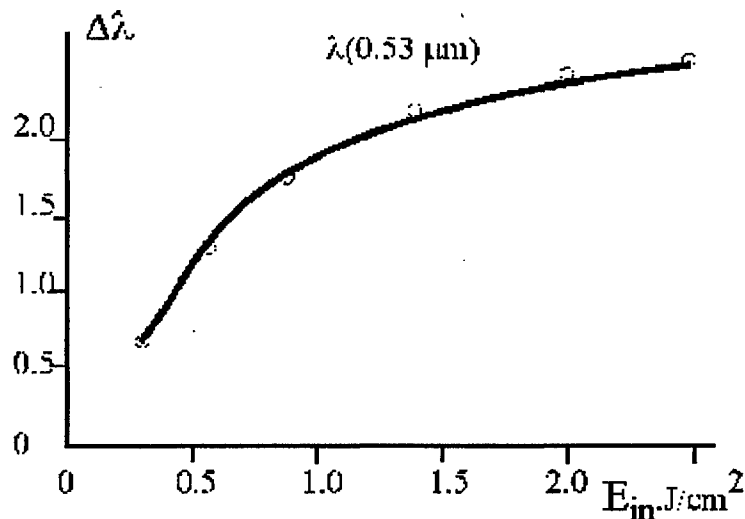


Fig. 6. Influence of radiation on variation of fullerene-containing medium refractive index.

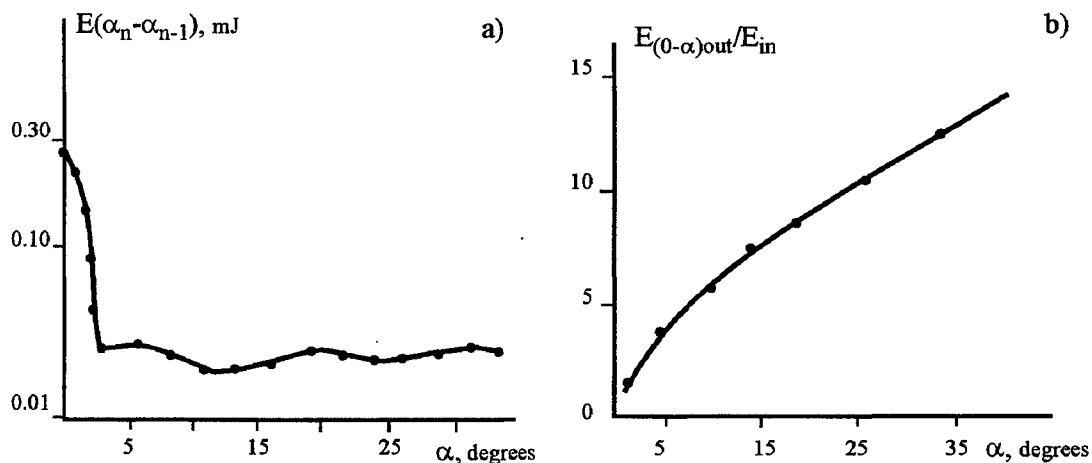


Fig. 7. Measurement results for scattered radiation.

- a) indicatrix of scattered radiation;
- b) dependence of E_{out}/E_{in} on α .

Fig. 2, for the same values $E_{in} = 2.8 \text{ J/cm}^2$, which is $E_{out}/E_{in} = 0.25$. This agrees well with the obtained transmission ratio for the case of the entire collected scattered energy.

The scattered radiation is observed during the entire input laser pulse. The account of contribution photoinduced scattering (at limiting aperture) lead to coincide experimental and theoretical results (Fig. 8). Thus, the performed analysis shows that the mechanism of photoinduced scattering by small-scale inhomogeneities of the refractive index plays significant role in the obtained 60-fold limiting. The contribution of this process strongly grows with increase of the input energy.

Taking into account that practically all observation devices have the angle of field of vision $\alpha \sim 1 - 2^\circ$, we may assume that optical limiters based on fullerene-containing media are photoinduced absorbing phase scattering screen with short response time. This fact significantly changes the value of the energy density in the plane of radiation receivers and the plane of eyes. To widen the dynamic range of optical limiting, it seems of interest to enhance the process of photoinduced scattering.

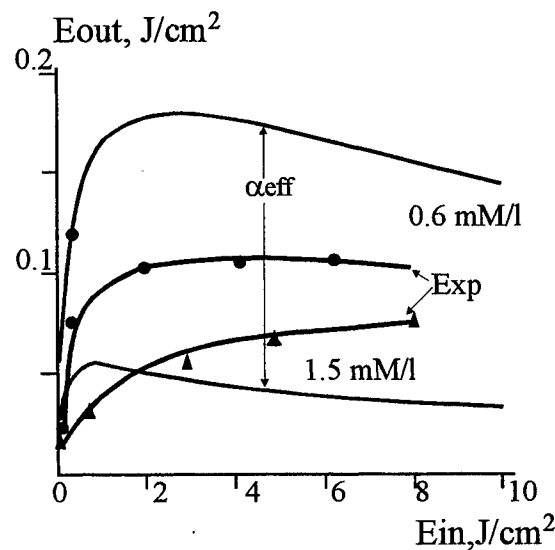


Fig. 8 Experimental and theoretical results E_{out} vs E_{in}

3. Multi-step optical limiter

In this section we will consider the question about possibility of widening the dynamic range of operation of limiters. The upper limit of their operation is determined by resistance to laser radiation of the material used, the lower - by the threshold of nonlinear processes in fullerene-containing media. Experiments show that the resistance to radiation of a limiter is determined by the resistance to radiation of the cell or of the fullerene-containing matrix.

These facts make it expedient to create a multi-step limiter consisting of several elements located in different parts of the beam that decreases in its cross-section.

Fig. 3b shows our experimental setup for the check of the principle of construction of a multi-step limiter (2 steps). The two-step optical scheme with radiation focusing at the second pass through the sample (to reach the threshold of limiting at low input fluences) permitted us to reach optical limiting at the level of $5 \cdot 10^3$ times [4].

Fig. 9 presents the results of our model calculations for radiation attenuation in multi-step limiters based on the theory $\lg T$

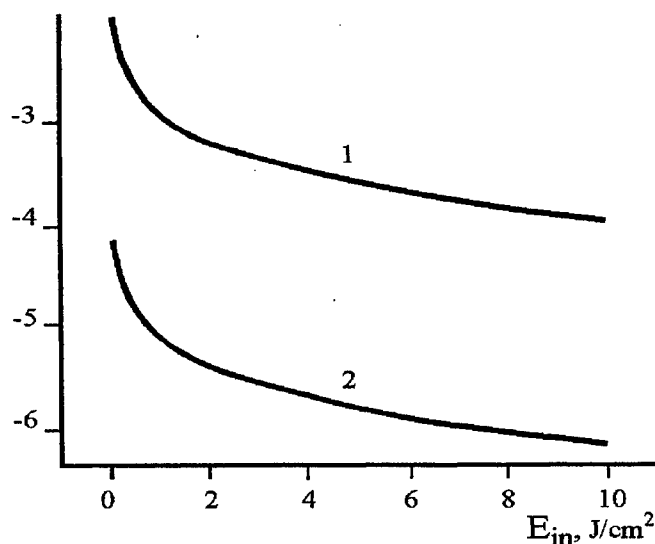


Fig. 9. Simulation of multi-step limiter with changes of input beam area at each step: 1) 0.5%; 2) 0.2%.

developed in chapter 1. These calculations were performed with consideration for contribution by RSA and nonlinear scattering, for the condition $c = 1$ mM of the C_{60} -toluene medium. These model calculations show that the 4-stem limiter permits to obtain the dynamic range $\geq 10^6$ times (from 10 J/cm^2 of the input energy that is determined by the cell resistance to radiation, to some mJ/cm^2 of the output energy). Optimisation of the system (the number of steps, fullerene concentration, location of samples in converging beam) can increase the dynamic range obviously up to 10^7 .

4. Control of space and temporal characteristics of laser radiation

The same mechanisms of optical limiting make available to reduce intensity in close area and also to change the profile of radiation. Fig. 10 and 11 are presented as example experimental and theoretical data on control of space and temporal characteristics of laser radiation for $E_{\text{input}} = 2 \text{ J/cm}^2$. In Fig. 10a the starting space distribution the intensity of laser beam in close zone (inhomogeneous of distribution was artificial made). Local deviation from the mean value reached to 2.5 times. In Fig. 10b the same after passing of radiation through sample C_{60} -toluene ($T=50\%$). You can see the deviation from mean became essential smaller and not exceed 25%. In Fig. 11 it is shown the change the profile of radiation pulse.

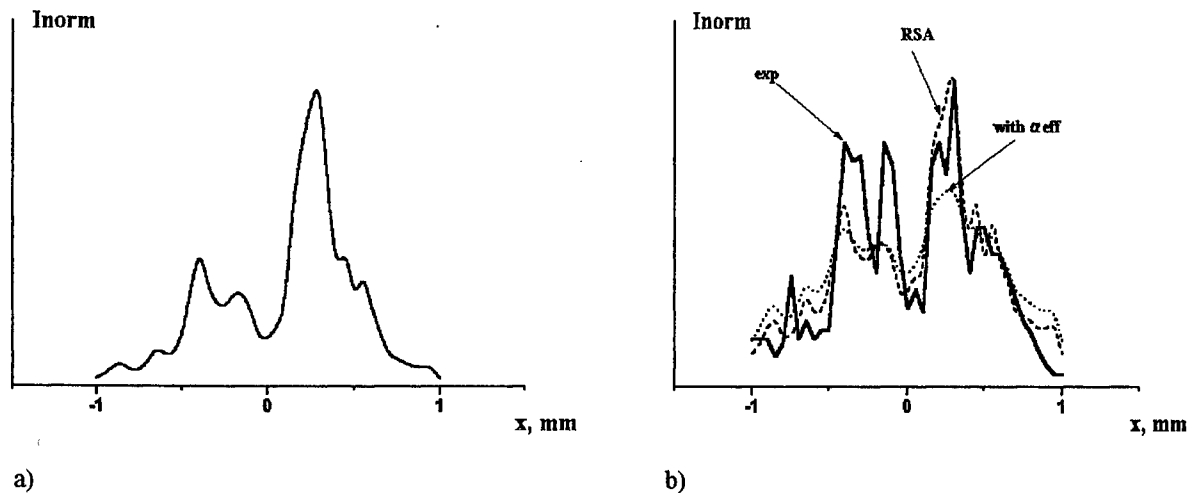


Fig. 10. Space distribution the intensity of laser beam

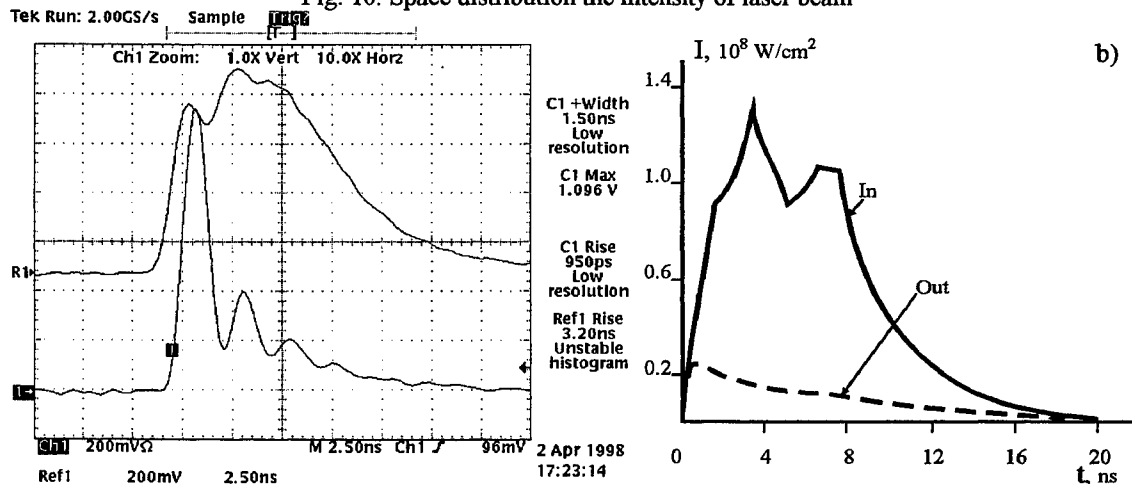


Fig. 11 Laser radiation pulse profile before and after passing through C_{60}

a) experiment: input – upper curve, output – down curve, b) -theory

These results are significant for provision of safe use of laser systems in which take place local inhomogeneity of beam load on optical elements or power sensors.

Conclusion

Our investigation shows that fullerene-containing materials can be used for fast control of power radiation (optical limiters), for control of spatial and temporal characteristics of laser radiation.

References

1. V.P.Belousov, I.M.Belousova, V.P.Budtov, O.B.Danilov, V.V.Danilov, A.G.Kalintsev, A.A.Mak. Fullerenes: structure, physico-chemical and nonlinear optical properties. *Opticheskiy Zhurnal*, 1997, v. 64, N 12, pp. 2-37.
2. S.R.Mishra et al. Optical limiting in C_{60} and C_{70} solutions. *Proc. SPIE*, 1994, v. 2284, pp. 220-229.
3. Y.Song, X.Ban, F.Li et al. Excited state absorption/ random surface scattering optical limiter. *Proc. SPIE*, 1996, v. 2856, pp. 216-219.
4. V.P.Belousov, I.M.Belousova, V.G.Bespalov, V.P.Budtov et al. Nonlinear-optical properties of fullerene-containing media. *Opticheskiy Zhurnal*, 1997, v. 64, N 9, pp. 82-84.

Author Index

- Abazadze, A. J., 50
 Bagayev, Sergey N., 126
 Barrientos, Bernardino, 131
 Belousov, Vlidilen P., 201
 Belousova, Inna M., 201
 Bibik, A. I., 183
 Brand, Thomas, 36
 Clarkson, W. A., 2
 Daiminger, Franz X., 13
 Danilov, Oleg B., 201
 Dmitriev, Valentin G., 187
 Dorsch, Friedhelm, 13
 Durmanov, S. T., 50, 92, 155
 Gao, C., 36
 Gavronskaya, E. A., 201
 Grechin, Sergey G., 163, 187
 Grempele, Hermann, 47
 Grigorev, V. A., 201
 Grudin, M. N., 50
 Gusev, Andrey V., 108
 Ivanov, V. N., 83
 Joubert, Maria-France, 76
 Kalintsev, Alexander G., 201
 Kart, A. M., 117
 Katsavets, Nikolay I., 47
 Khandokhin, P. A., 53
 Khonineva, E., 196
 Klyachko, B. S., 117
 Kolbatskov, J. M., 50
 Kopaev, Alexander, 108
 Korda, I. M., 183
 Kornev, A. F., 63
 Kotlikov, E., 196
 Koval, J. P., 50
 Krasnopolsky, V. E., 201
 Kugler, Nicolas, 36, 145
 Kulagin, Victor V., 108
 Kurin, M. A., 155
 Kutovoi, S. A., 50, 92
 Kuzmin, O. V., 50, 92
 Laporta, Paolo, 24
 Longhi, S., 24
 Lorenzen, D., 13
 Lunter, Sergei G., 99
 Lyubimov, Vladimir V., 138, 155
 Malashko, Ya. I., 155
 Mamaev, Yu. A., 53
 Mendoza Santoyo, Fernando, 131
 Milovsky, N. D., 53
 Milyukov, Vadim K., 108, 117
 Moncorge, R., 76
 Morichev, Ivan E., 176
 Myasnikov, A. V., 117
 Nikonorov, Nikolai V., 99
 Onokhov, Arkadii P., 63
 Orlov, Valery A., 126
 Ovchinnikov, E., 53
 Panov, Sergey V., 126
 Panyutin, V. L., 50, 92
 Perez Lopez, Carlos, 131
 Pfeifer, Egon, 47
 Pletneva, Nina I., 176
 Pokrovskiy, Vasilii P., 63, 176
 Przhhevuskii, Alexander K., 99
 Raevsky, Evgueni V., 163
 Razumova, Irene K., 76
 Reiterov, V. M., 83
 Rodriguez Vera, Ramon, 131
 Rojdestvin, V. N., 163
 Rubinov, Anatoly N., 183
 Rudenko, Valentin N., 108, 117
 Rudnitskiy, Yu. P., 50, 92, 155
 Rumjantsev, A. S., 155
 Sandulenko, Alexander V., 83
 Sandulenko, V. A., 83
 Schmidt, I., 36
 Seidel, Stefan, 145
 Sharandin, E. A., 163
 Shirokov, E. Y., 53
 Smirnov, G. V., 50, 92, 155
 Smirnov, V. A., 201
 Soms, Leonid N., 63, 176
 Sorbello, G., 24
 Sosnov, Eugene N., 201
 Stupnikov, V. K., 63
 Svelto, C., 24
 Svelto, Orazio, 24
 Taccheo, S., 24
 Ter-Martirosyan, Alexander L., 47
 Titov, A. N., 83
 Tkachuk, Alexandra M., 76, 83
 Vladimirov, Fedor L., 176
 von Kopylow, Christoph, 47
 Weber, H., 36, 145
 Zaporozhchenko, Valentin A., 170